Electrical Properties and Structural Disorder in Stannate Pyrochlores

by

Tae-Hwan Yu

B.S., Inorganic Materials Engineering,
Seoul National University, February 1991

Submitted to the Department of Materials Science and Engineering
in Partial Fulfillment of
the Requirement for the Degree of

Doctor of Philosophy
in Ceramics

at the

Massachusetts Institute of Technology
September 1996

Signature of Author_____
Department of Materials Science and Engineering
1996 August 5

Certified by_____
Harry L. Tuller
Professor of Ceramics and Electronic Materials
Thesis Supervisor

Accepted by_____ _____
Linn W. Hobbs
Chair, Departmental Committee on Graduate Students

SEP 27 1996

Electrical Properties and Structural Disorder in Stannate Pyrochlores

by

Tae-Hwan Yu

Submitted to the Department of Materials Science and Engineering
in Partial Fulfillment of
the Requirement for the Degree of
Doctor of Philosophy
in Ceramics

Abstract

The stannate pyrochlores $(Gd_{1-x}Ca_x)_2Sn_2O_7$, $Gd_2(Ti_{1-x}Sn_x)_2O_7$, $Gd_2(Zr_{1-x}Sn_x)_2O_7$ and $Y_2(Ti_{1-x}Sn_x)_2O_7$ were investigated to examine the relationship between intrinsic disorder and oxygen ion conductivity. The ionic radius ratio, r_A/r_B, is known to be an important factor in influencing structural disorder on both cation and anion sublattices in $A_2B_2O_7$ pyrochlores. Stannate pyrochlores were chosen to test the generality of this observation. Electrical conductivity measurements were performed on the stannates as a function of P_{O_2} and temperature to examine the degree of intrinsic disorder and the resultant oxygen ion conductivity. These results were then evaluated by the use of the appropriate defect models.

From electrical conductivity measurements on $(Gd_{1-x}Ca_x)_2Sn_2O_7$, an effective Frenkel constant and oxygen vacancy mobility were established for $Gd_2Sn_2O_7$. The Frenkel constant, K_F, and the oxygen vacancy mobility, μ_i, were found to be $K_F = 1.55\times10^{41}\exp(-0.11\pm0.06eV/kT)$ cm^{-6} and $\mu_i = 1317.7/T\times\exp(-1.54\pm0.03eV/kT)$ cm^2/V respectively. The magnitude of the Frenkel constant at 1000 °C corresponds to ~0.6% disorder on the anion sublattice and the low anion Frenkel defect formation energy, E_F, of 0.11 eV follows the trend of decreasing E_F with decreasing r_A/r_B as observed previously for zirconate-titanate solid solutions. The increasing cation disorder with increasing x in $Gd_2(Ti_{1-x}Sn_x)_2O_7$ was confirmed by X-ray diffraction analysis. The high migration energy of ~1.5 eV, however, resulted in lower ionic conductivity by two orders of magnitude in $Gd_2Sn_2O_7$ than in $Gd_2(Ti_{1-x}Zr_x)_2O_7$ with the same average B site cation radius. This appears to be related to a decreasing dielectric constant in $Gd_2(Ti_{1-x}Sn_x)_2O_7$ with increasing x which results in the lower oxygen mobility. In summary, while intrinsic disorder was found to be correlated

to the r_A/r_B ratio, the mobility was observed to be closely tied to the local cation chemistry.

Disorder was found to increase as the smaller Ti is replaced by the larger Sn ion in $Gd_2(Ti_{1-x}Sn_x)_2O_7$ while the mobility decreased resulting in a broad maximum in the ionic conductivity at $x=0.4$. The ionic conductivity was observed to decrease with increasing x in $Gd_2(Zr_{1-x}Sn_x)_2O_7$ even though disorder remains high regardless of the B site composition. $Y_2(Ti_{1-x}Sn_x)_2O_7$ was found to exhibit a similar ionic conductivity dependence on composition as $Gd_2(Ti_{1-x}Sn_x)_2O_7$. The magnitude of ionic conductivity, however, was higher due, apparently, to the larger disorder induced by the smaller Y relative to Gd ion

$Gd_2(Ti_{1-x}Sn_x)_2O_7$ with $x<0.8$ showed a second conductivity plateau at low P_{O_2}, which could not be explained by the defect model. Short circuit cell measurements were performed on $Gd_2(Ti_{0.8}Sn_{0.2})_2O_7$ to investigate whether this second plateau reflected ionic conductivity by independently measuring the absolute value of the ionic conductivity in the mixed electronic and ionic conduction regime. A P_{O_2}-independent ionic conductivity was obtained from the measurements confirming that the increase in conductivity at low P_{O_2} region is largely electronic. However, a lower magnitude of ionic conductivity, coupled with higher activation energy, were obtained by this method as compared to those derived previously from complex impedance spectroscopy. This was attributed to additional losses due to electrode polarization. Open circuit voltage measurements on $Gd_2(Ti_{0.8}Sn_{0.2})_2O_7$ showed that the ionic transference number, t_i, reached a maximum at intermediate P_{O_2}. This dependence was traced to a decomposition reaction occurring under reducing conditions.

Thesis Supervisor: Harry L. Tuller

Title: Sumitomo Electric Industries Professor of
                            Ceramics and Electronic Materials

3

Table of Contents

5

List of Figures

7

List of Tables

Acknowledgment

I am indebted to all those who have made this thesis possible. First of all, I wish to express my gratitude to my thesis advisor, Prof. Tuller for giving me the opportunity to work in this field and guiding me throughout the years. His passion for research and education will remain in my heart for the rest of my career. I would also like to thank Prof. Ceder and Prof. Wuensch, both of whom were on my thesis committee, for their helpful comments and words of advice.

I would like to extend my thanks to Marlene Spears for guiding me while I conducted experiments which ranged from powder processing to conductivity measurements. I would also like to thank Kevin Eberman and Per Onnerud for providing me with YTS samples and for performing X-ray diffraction refinements on GTS samples. Thanks to Ofer Porat for his advice on the designing of the gas-tight cell, and to Catherine Heremans for her helpful discussion on pyrochlore works. Thanks to Jaedeok Yoo for his friendship throughout the years as well as for his assistance on samples preparations. Also, Yong-Chae Chung's guidance in academic life is unforgettable.

I would like to thank my wife, Won-Jae for her endless love. She has always believed in me ever since we first met seven years ago. Many thanks to my parents-in-law for their support and encouragement. Lastly I would like to thank my parents for their never-ending love. Their unconditional support has enabled me to complete this work.

1 Introduction

1.1 Purpose of Research

Electrically insulating oxides at room temperature can exhibit electrical conduction at elevated temperatures. This electrical conduction involves the migration of mobile electronic and/or ionic charge carriers under a potential field gradient. In the perfect crystalline oxide, these charge carriers are considered as defects controlled by thermodynamic variables such as temperature, P_{O_2} and composition. Electrochemical applications utilizing these properties include oxygen sensors, oxygen membranes, batteries and solid oxide fuel cells.

The pyrochlore structured oxide exhibits a wide range of ionic and electronic conductivities depending on composition. The rare earth pyrochlore $Gd_2(Ti_{1-x}Zr_x)_2O_7$ (GZT) was investigated as a potential electrolyte in a solid oxide fuel cell [Moon, 1988a]. It was observed that at lower Zr content, substantial mixed ionic-electronic conduction (MIEC) exists and as Zr content increases, the oxygen ion conductivity increases sharply. This increase in ionic conductivity was related to the relative increase in anion disorder with Zr content as confirmed by neutron diffraction experiments on the closely related $Y_2(Ti_{1-x}Zr_x)_2O_7$ (YZT) system [Heremans, 1993]. From these observations, it was concluded that one of the important parameters in determining structural disorder in $A_2B_2O_7$ pyrochlores was the cation radius ratio, namely r_A/r_B. As r_B approaches r_A, disorder in the cation and anion sublattices begins to increase reaching the complete randomization characteristic of the fluorite structure in the case of $Y_2Zr_2O_7$ (YZ). As the larger Zr ion replaces Ti on the B site of GZT, anion disorder increases resulting in orders of magnitude increases in the oxygen ion conductivity. In

the case of $Gd_2Ti_2O_7$ (GT) where intrinsic disorder is minimal due to the small ionic radius of Ti^{4+}, the ionic conductivity is dramatically increased by the addition of the aliovalent dopant Ca^{2+} on the A site thereby extrinsically generating oxygen vacancies. A maximum ionic conductivity of 5×10^{-2} S/cm at 1000 °C was obtained for GT doped with 10% Ca [Kramer, 1994].

The ionic radius of Sn^{4+} lies between that of Ti^{4+} and Zr^{4+}. The purpose of this research was to investigate whether Sn^{4+} would also contribute to disorder in pyrochlore as expected from a variation in the r_A/r_B ratio in $Gd_2(Ti_{1-x}Sn_x)_2O_7$. The ionic conductivity of $Gd_2Sn_2O_7$ (GS) was investigated and compared with that in GZT with the same average B site cation radius to examine disorder in the two different pyrochlores. $Gd_2(Ti_{1-x}Sn_x)_2O_7$ (GTS), $Gd_2(Zr_{1-x}Sn_x)_2O_7$ (GZS) and $Y_2(Ti_{1-x}Sn_x)_2O_7$ (YTS) were chosen to examine the compositional dependence of the structural disorder and ionic mobility. The dopant Ca^{2+} was used to obtain a quantitative measure of the degree of disorder in GS.

Key experimental techniques used in this research included electrical conductivity measurements, DC and impedance spectroscopy, as a function of temperature and P_{O_2}. X-ray diffraction measurements assisted in the identification of the phases and their structural disorder. The short circuit cell and open circuit cell measurement were applied to examine their feasibility and limitations with respect to obtaining absolute values of the ionic conductivity from a background of predominantly electronic conductivity. Defect models were used in the analysis of the results.

2 Literature Review

The literature review begins with a description of the pyrochlore structure in relation to the fluorite structure. In particular, the emphasis is placed on order-disorder occurring in the pyrochlore structure leading to intrinsic ionic conductivity dependence on the ionic radii of the A and B site cations. Extrinsic ionic conductivity is also discussed. The next section discusses stannate pyrochlores in terms of the structure, bonding characteristics between Sn and oxygen ion, valence state of the Sn ion, the electrical conductivity and polarizability of Sn ion in comparison with Ti. The final section outlines the proposed work in stannate pyrochlores.

2.1 Pyrochlore Structure and Disorder

2.1.1 Pyrochlore Structure

Pyrochlores can be described by the formula, $A_2B_2O_6Z$ which represents four atoms occupying different crystallographic sites in the unit cell. Z is usually oxygen but can be F, Cl or OH. The space group is Fd3m with eight molecules per cell with a lattice constant of ~10 Å. The possible type of pyrochlores are $A^{3+}_2B^{4+}_2O_7$, $A^{2+}_2B^{5+}_2O_7$, etc. so long as the cation charges add up to +14. The A element can be an alkali, alkaline earth or a rare-earth (Ln) element and the B element can be a transition metal or group IV element.

The pyrochlore structure can be described in relation to the fluorite structure. In the fluorite structure (MO_2), M cations occupy face centered cubic sites and O is located in the tetrahedral sites as shown in Fig. 2.1 for CaF_2. When this oxide is doped with aliovalent cations, A^{3+}, oxygen vacancies are generated to maintain charge balance. When the A/B mole ratio becomes

15
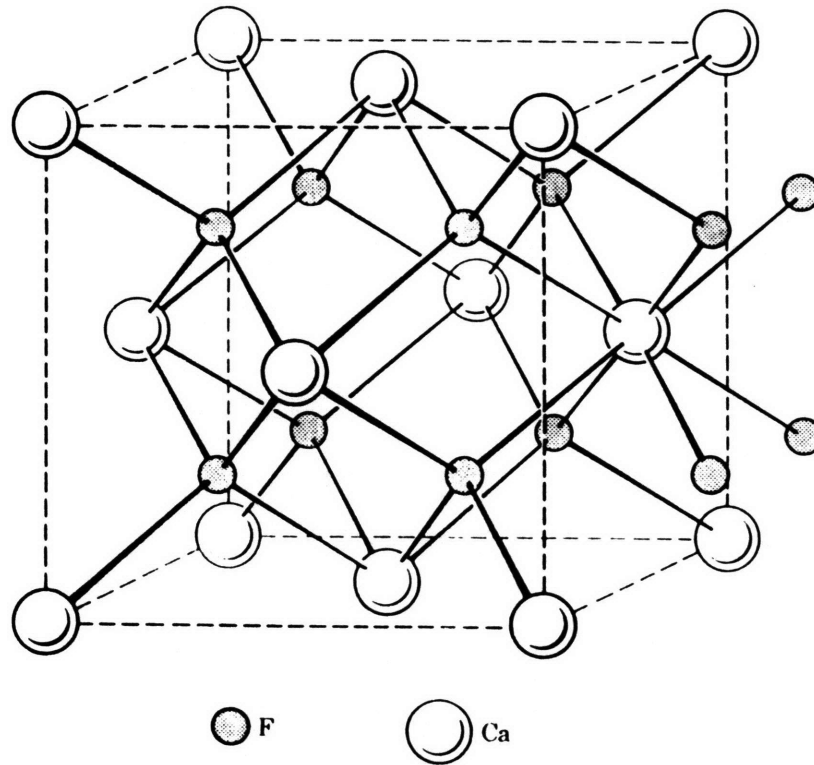
Fig. 2.1 The fluorite structure of CaF₂ [Kingery, 1976].

one, one out of eight oxygen sites are vacant. In this 'defect' fluorite, A and B cations are randomly distributed over face centered cubic sites and oxygen ions and vacancies are also randomly distributed over the tetrahedral sites. In pyrochlores, these cations, anions and vacancies are ordered creating five different crystallographic sites, namely, 16c, 16d, 48f, 8a and vacant 8b. Fig. 2.2 shows the pyrohlore structure derived from a fluorite lattice.

The A cations (radius of ~1 Å) are located in eight-fold coordination (16c) and the smaller B cations (radius of ~0.6-0.7 Å) are in six-fold coordination (16d). Two different anion sites (48f and 8a) and empty sites (8b) exist in the pyrochlore structure due to ordering, whereas there is only one in the fluorite structure (8c). Six oxygen ions in the $A_2B_2O_7$ pyrochlore formula unit occupy 48f sites having two A and two B cation near neighbors. The 8a sites are surrounded by four A cations and the 8b vacant sites by four B cations. Since four B cations surround an oxygen vacancy, they tend to be electrostatically shielded from one another by a displacement x of each 48f oxygen from the center of its tetrahedral interstice towards its two neighboring B cations as shown in the Fig. 2.2. Therefore the pyrochlore structure can be viewed as a superstructure of the fluorite structure with eight molecules per cell and doubling of the lattice parameter in all three directions of the cube. Fig. 2.3 represents the [001] projection of a portion of the pyrochlore unit cell showing five different crystallographic sites.

The 48f oxygen parameter, x, ranges between theoretical limits of 0.4375 and 0.375 resulting in the distortion of the polyhedra around the A and/or B cations. When x=0.375, there is no displacement of 48f oxygen ions from a perfect cubic array and A cations are located in a perfect cubic 8-fold coordination. When x reaches the upper limit of 0.4375, the B cations are in perfect octahedral coordination [Subramanian, 1983]. When the x value ranges between these two limits, each polyhedra is distorted. Fig. 2.4 and 2.5

17
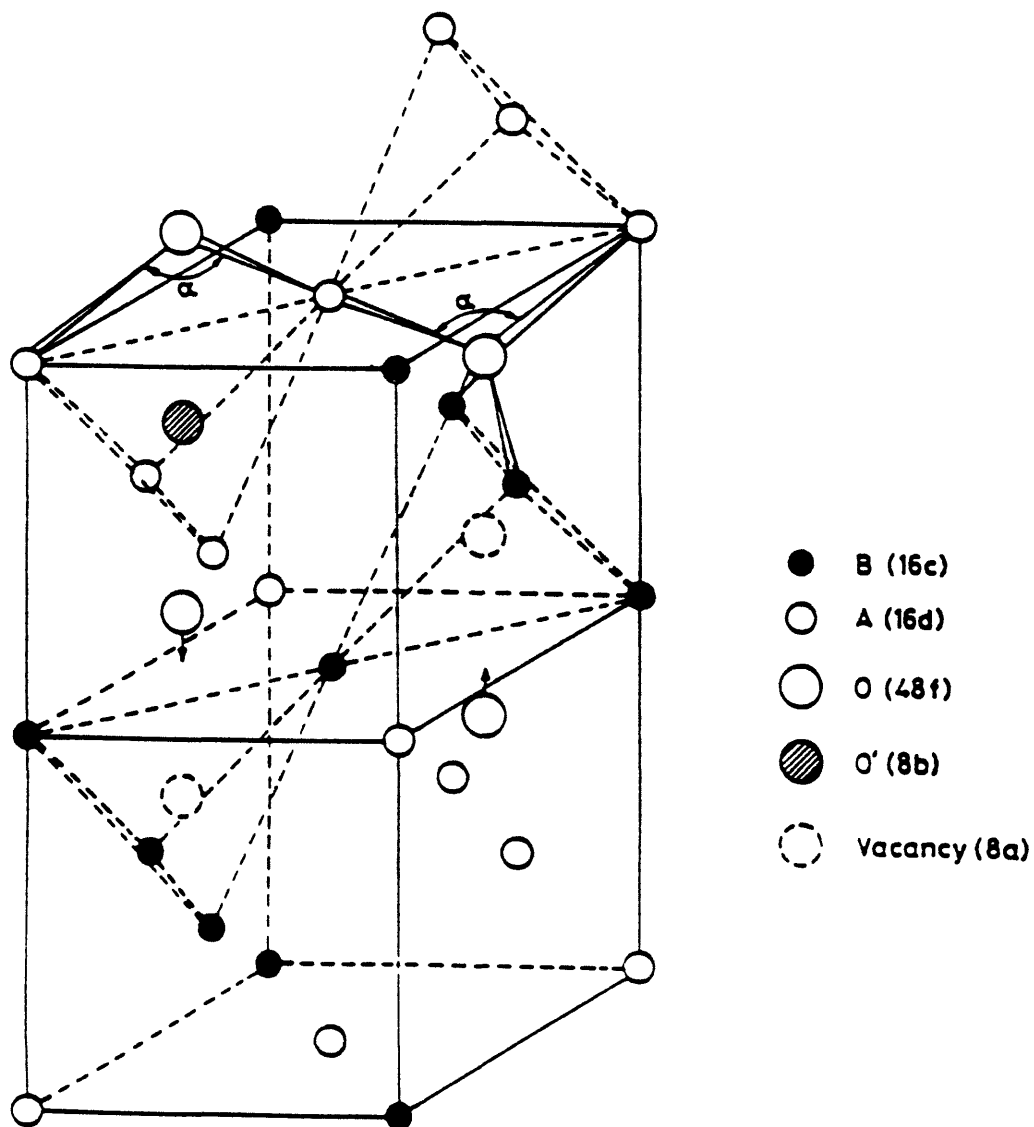
Fig. 2.2 Pyrochlore structure as derived from a fluorite lattice. The cation positions for one quarter of the unit cell are shown. The shifts of 48f oxygen towards the 8a vacancy are indicated [Longo, 1969].

Legend:

- ● B (16c)
- ○ A (16d)
- ◯ O (48f)
- ◉ O' (8b)
- ⦁ Vacancy (8a)

18
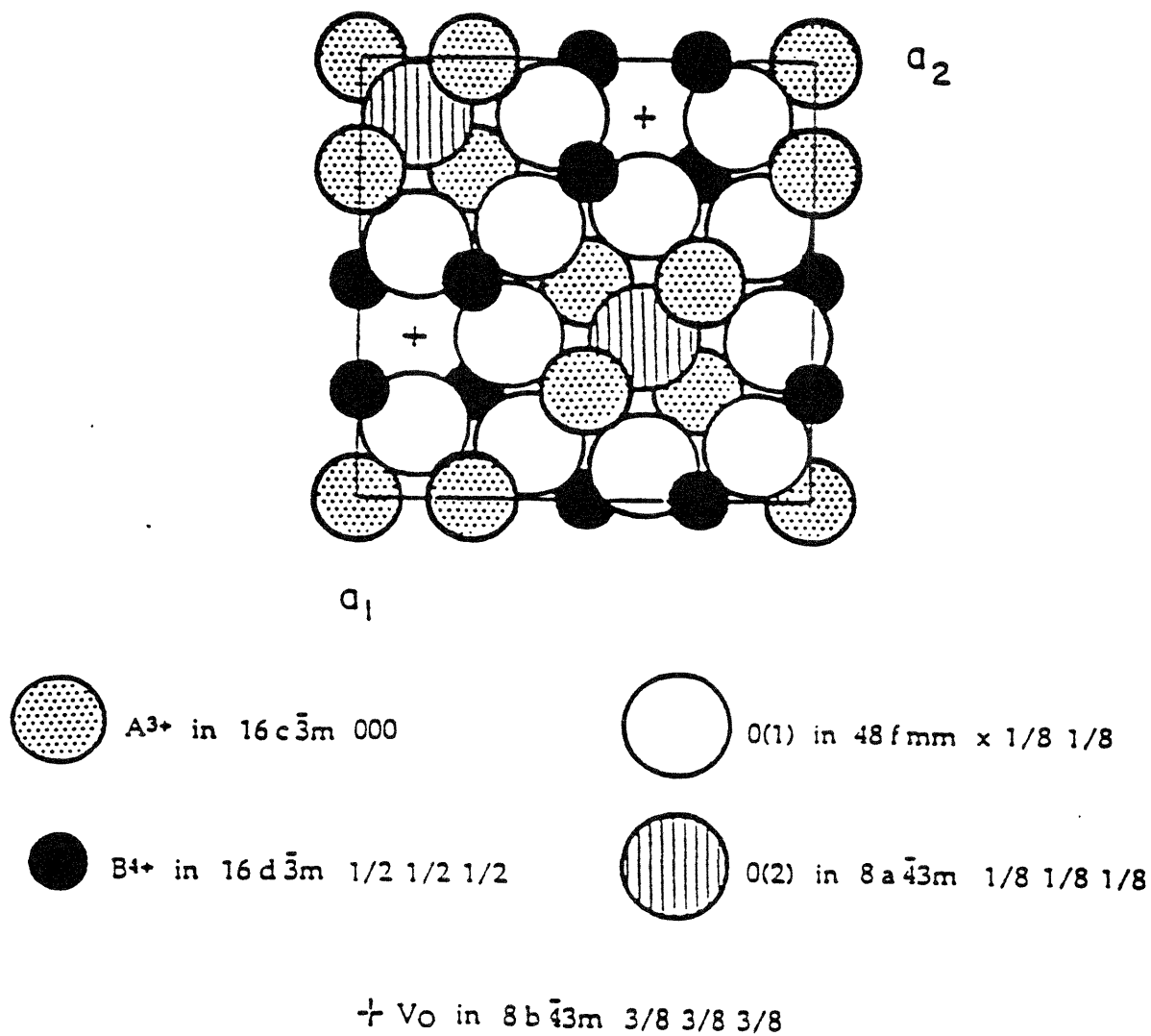
Fig. 2.3 Projection of the pyrochlore cell for $0 \leq z \geq 1/4$ showing the displacement of the O (1) oxygen ion [Haile, 1990; Spears, 1995].
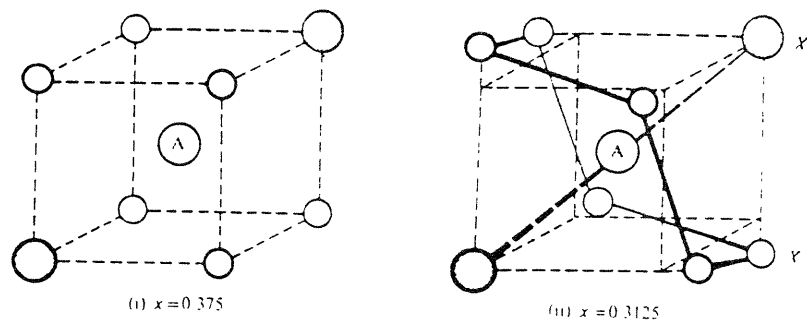
Fig. 2.4 8-fold coordination of the A cation in the pyrohlore structure
[Wells, 1987; Heremans, 1993].
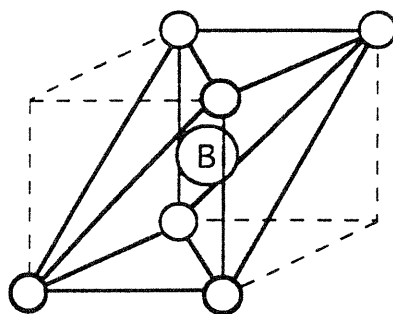
Fig. 2.5 6-fold coordination of the B cation in the pyrochlore structure when
x=0.375 [Heremans, 1993].

shows eight and six fold coordination polyhedra in the $A_2B_2O_7$ pyrochlore structure respectively. The pyrochlore structure is often described as a network structure of corner linked BO_6 octahedra with the A ions filling the interstices. A more complete description of the pyrochlore structure can be found in a review by Subramanian [Subramanian, 1983].

The description above refers to the 'ideal' pyrochlore structure, where every cation and anion is in perfect order. All real pyrochlore compounds exhibit some disorder due to entropy increases associated with defect formation [Moon, 1988a]. In the case of YZT, it has been observed that there is an anion disorder related to the exchange of 48f and 8a oxygen ions with the 8b site (Frenkel disorder) and a cation disorder related to the exchange of 16c (A site) and 16d (B site) ions [Heremans, 1993]. This is called "defect pyrochlore" which is intermediate between the extreme of the ideal pyrochlore structure and the ideal fluorite structure. This structural disorder in pyrochlores will be discussed in detail below and correlated to the intrinsic ionic conductivity in section 2.2.1.

2.1.2 The stability of $A_2^{3+}B_2^{4+}O_7$ Pyrochlore Phase

Thermodynamic variables such as temperature, pressure, deviation from stoichiometry, etc. can determine the stability of the pyrochlore phase. The cation radius ratio, r_A/r_B, in $A^{3+}_2B^{4+}_2O_7$ pyrochlores is known to be one of the important factors in the stability of the pyrochlore phase [Moon, 1988a; Heremans, 1993]. Knop et al. [Knop, 1969; Brisse, 1968] suggested that stability exists for r_A/r_B ratios of 1.22 to 1.47 for titanates and 1.19 to 1.6 for stannates using the 6-fold coordinated radii of Ahrens for both A and B site cations [Ahrens, 1952]. Subramanian [Subramanian, 1983] placed it instead at 1.46 to 1.80 based on Shannon's ionic radii which considers the 8-fold and 6

21

fold coordination in A and B site cations, respectively [Shannon, 1969]. For too small values of r_A/r_B, the defect fluorite forms due to the increase in the exchange of the two cations as in the case of YZ [Moon, 1988a]. On the other extreme, $r_A/r_B > 1.8$, the size difference between the A and B site cations is large enough to lead to a distorted cubic symmetry as observed in $Nd_2Ti_2O_7$ [Roth, 1956]. Fig. 2.6 summarizes such results for the B site cations of Ti, Sn and Zr with a wide range of the A site cations.

Moon demonstrated that a quaternary compound such as $A_2(B'_xB''_{1-x})_2O_7$ forms the pyrochlore phase if the A cation radius and the average B cation radius are within the required limits [Moon, 1988a]. In this case, r_B is the composition-weighted average B cation radius defined as: $r_B = xr_B + (1-x)r_B$. As shown in Fig. 2.6, it is expected that GTS, GZS and YTS solid solution will form the pyrochlore phase. These systems will be discussed in detail in following Section 2.3.

Temperature is another factor which can affect the stability of the pyrochlore phase. Increasing temperatures favors the disordered fluorite phase even though the r_A/r_B ratio lies within the pyrochlore phase boundary. $Gd_2Zr_2O_7$ (GZ), for example, was observed to transform from pyrochlore to fluorite when heated above 1550 °C [Burggraaf, 1981; van Dijk, 1980].

Even though the ideal cation ratio in $A_2B_2O_7$ pyrochlore should be 1:1, a deviation from stoichiometry toward either A excess or B excess can maintain the pyrochlore phase. The Pyrochlore phase diagram in Fig. 2.7 shows that the phase is stable in $GdO_{1.5}$-ZrO_2 system with either Gd excess or Zr excess, which results in an increase of oxygen vacancies or interstitials respectively to maintain electroneutrality [Uehara, 1987; Spears, 1995].
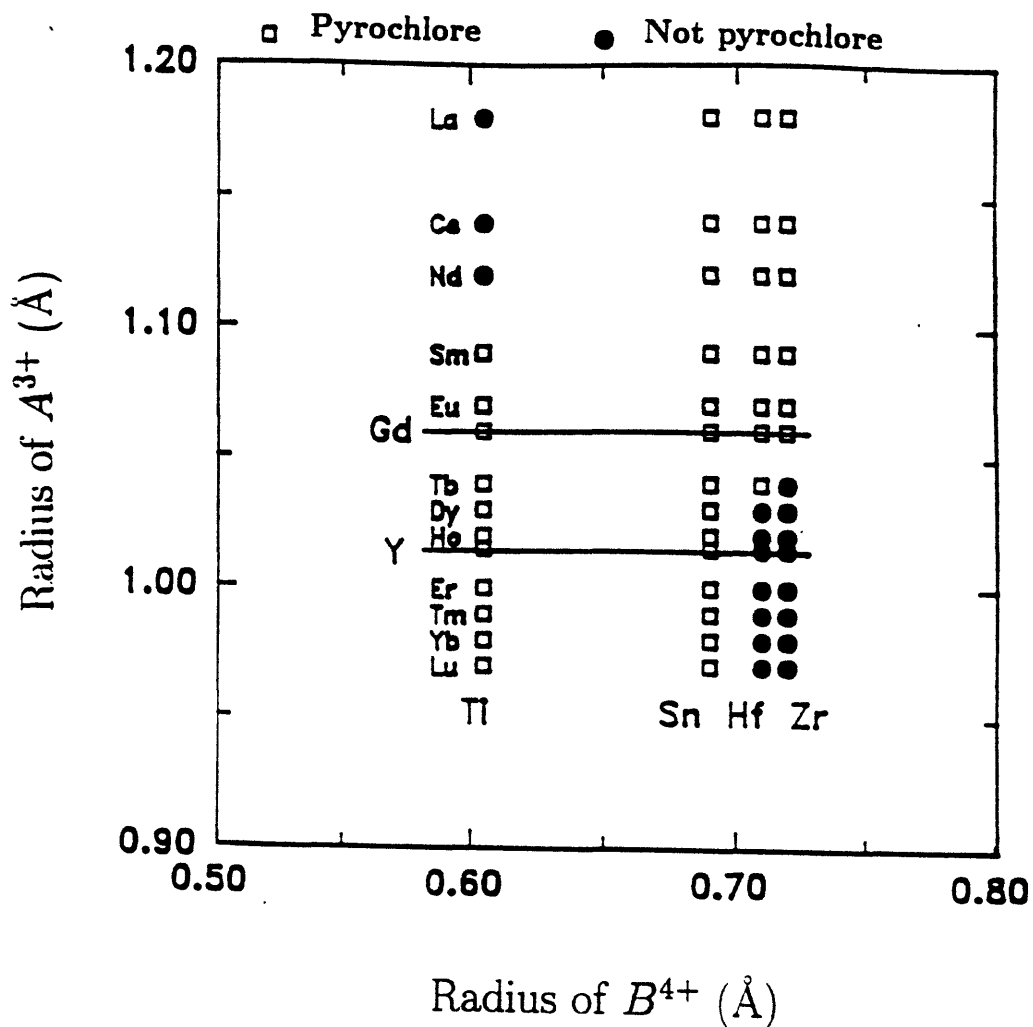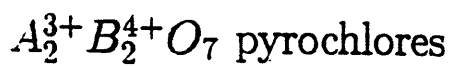
Fig. 2.6 Stability field of the pyrochlore structure as a function of cation radii [Moon, 1988a].

23
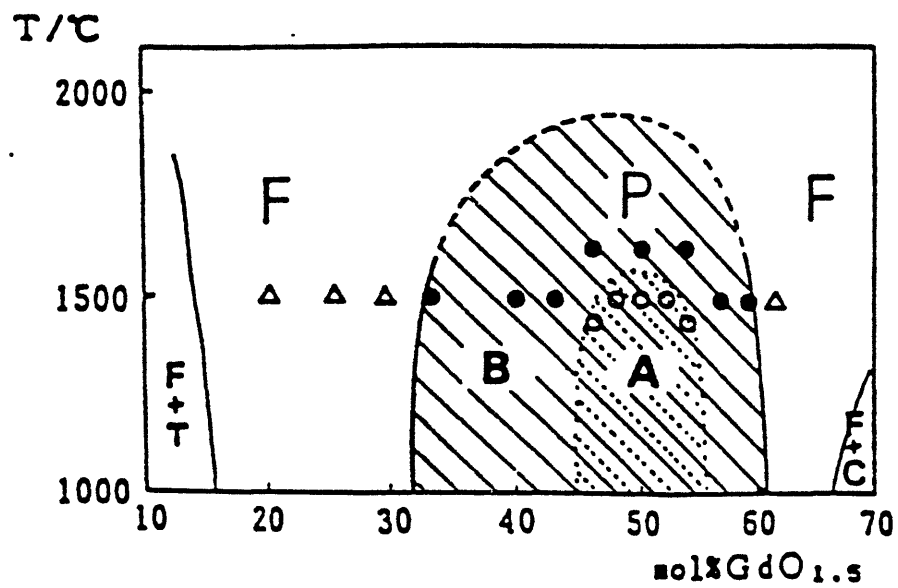
Fig. 2.7 The stability region of the pyrochlore phase (P) [Uehara, 1987].

2.1.3 Structural Disorder

The structural disorder in pyrochlore occurs in the cation and anion lattices respectively [Moon, 1988a; Heremans, 1993]. One of the important factors influencing the degree of disorder in pyrochlores is r_A/r_B. As r_B becomes close to r_A, the enthalpy difference between the completely ordered and disordered state decreases [Moon, 1988a]. On the other hand, the entropy increase associated with an exchange between the A and B cations in the system becomes significant at high temperature leading to increases in the thermodynamic driving force for disorder.

Moon investigated the structural cation disorder in GZT and YZT with X-ray diffraction measurements [Moon, 1989]. The cation disorder was calculated from the relative intensity of the 331 peak with respect to that of the 400 peak. The cation order parameter, Φ_c, is defined by the following equation:

$$\Phi_c = (A_A - A_A^f)/(A_A^p - A_A^f)$$

where A_A^p is the fractional occupation of the A site by A ions for ideal pyrochlore structure and A_A^f is the fractional occupation of the A site by A ions for ideal fluorite structure. Φ_c is one for the ideal pyrochlore structure and zero for the ideal fluorite structure. The cation order parameters in Figs. 2.8 and 2.9 show that the cations disorder progressively with increasing Zr content in both GZT and YZT suggesting increasing disorder in the cation sublattice with increasing average B site cation radius. However, these calculations ought to be considered as a first order approximation because only two peaks were used in the calculation and the intensity between the two peaks depends not only on the disorder of cations but also on the atomic temperature factors and the displacement of the 48f site [Heremans, 1993]

25
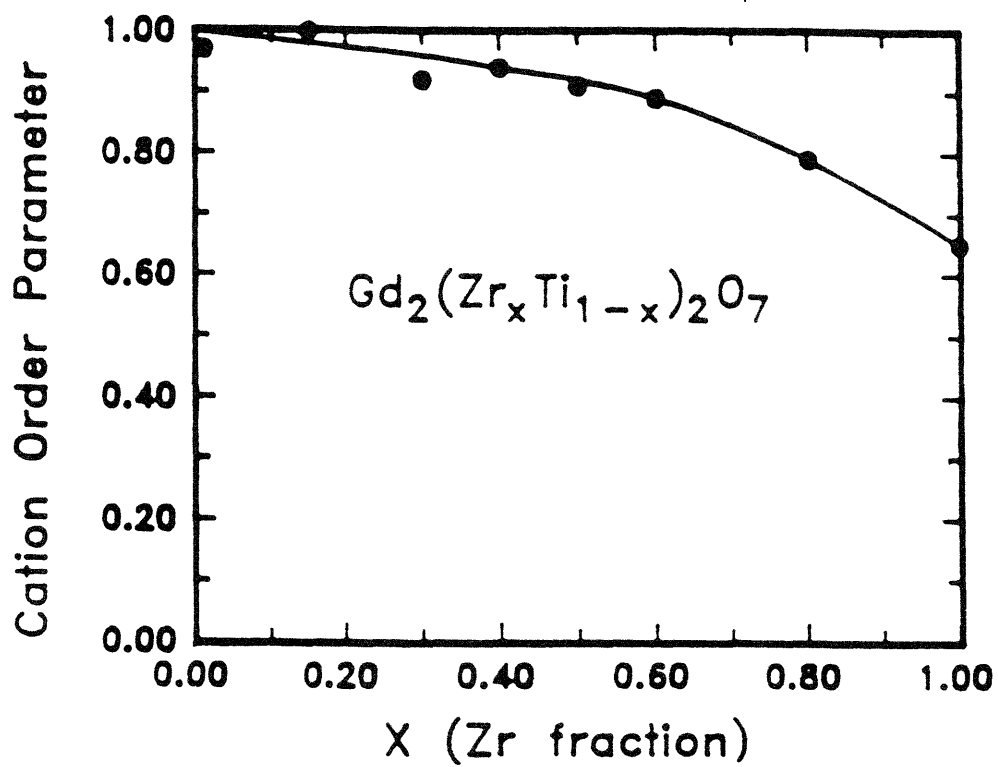
Fig. 2.8 The cation disorder parameter as a function of x for $Gd_2(Zr_{1-x}Ti_x)_2O_7$ from X-ray diffraction studies [Moon, 1989].
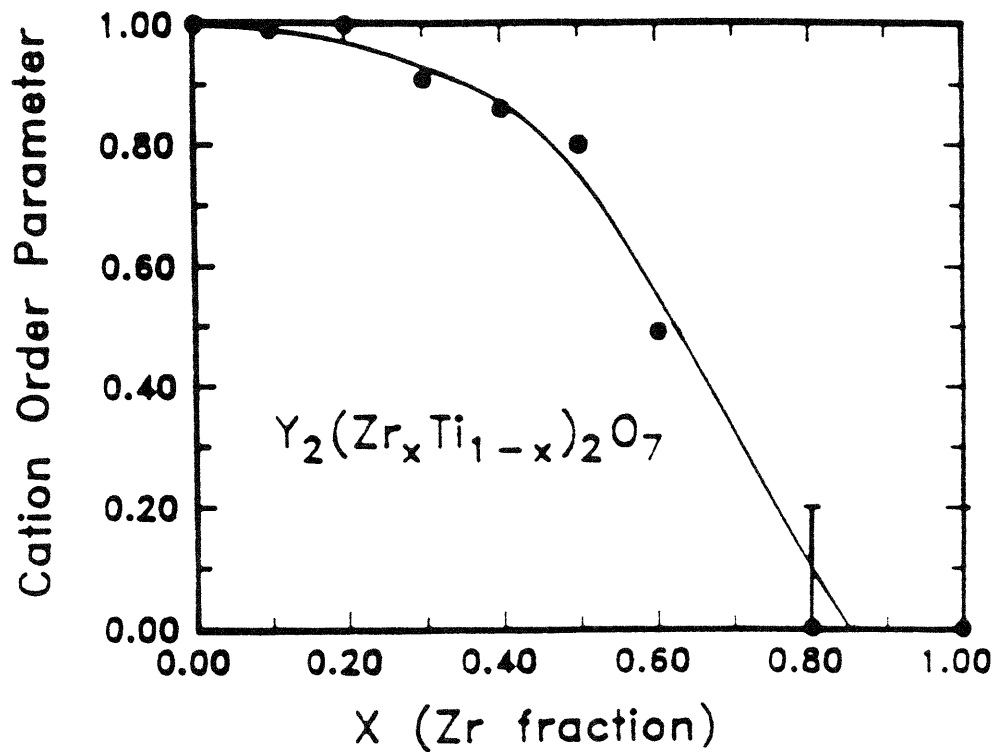
Fig. 2.9 The cation disorder parameter as a function of x for $Y_2(Zr_{1-x}Ti_x)_2O_7$
from X-ray diffraction studies [Moon, 1989].

and more importantly, only a single order parameter was used to describe the disordering of three different cations over two sites. The complete description requires two independent order parameters, which are impossible to obtain from a single X-ray diffraction measurement. These limitations will be discussed in detail in section 5.1. Since the ionic radius of Y^{3+} (1.015 Å) is smaller than that of Gd^{3+} (1.06 Å), the degree of cation disorder is expected to be more significant in YZT than in GZT for a given Zr content as shown in Figs. 2.8 and 2.9.

Anion disorder occurs in the form of an exchange between the occupied 48f or 8a sites and the vacant 8b sites. In this form of disorder, oxygen ions located in the 8b sites are referred to as oxygen interstitials and the vacant 48f or 8a sites as oxygen vacancies. This exchange can be viewed as a Frenkel defect represented by the creation of an oxygen vacancy and interstitial pair. Note that the oxygen interstitial site 8b, is designated as an oxygen vacancy site (8c) in the fluorite structure.

Heremans and Wuensch [Heremans, 1993] investigated the anion and cation disorder in YZT more extensively with neutron diffraction measurements. X-ray diffraction measurements are limited by the identical X-ray scattering density of Y^{3+} and Zr^{4+} and the low scattering density of oxygen ions. Fig. 2.10 represents an anion order parameter as a function of Zr content in YZT. The figure shows that the anion disorder increases at a different rate with Zr content in the three different anion sites 48f, 8b and 8a. Initially, anion disorder arises from the partial filling of the ideally empty 8b sites with oxygen ions from the 48f sites until x reaches 0.45. At larger x, 8a sites also begin to disorder reaching complete randomization characteristic of the fluorite structure at x=0.9. The initiation of anion disorder on the 48f and 8b sites is consistent with the calculations by Wilde and Catlow [Wilde, 1996] where the formation energy of vacancies in 48f was lower than that in 8a sites
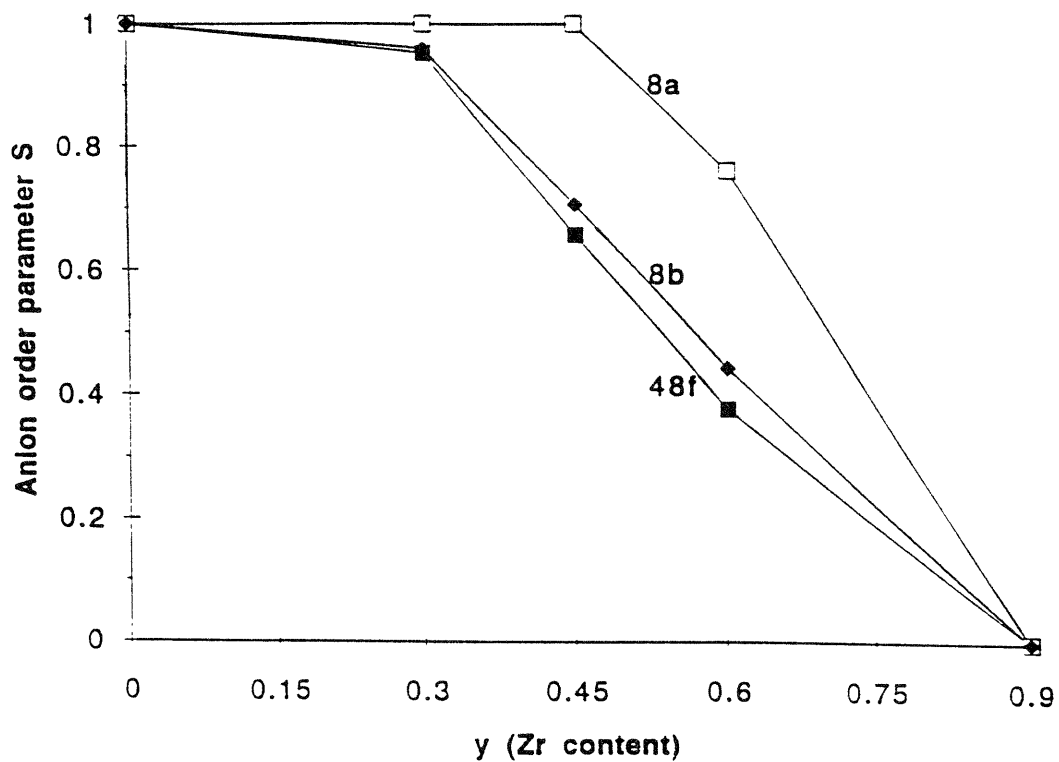
Fig. 2.10 The anion order parameter for the 8a, 8b and 48f sites as a function of y for $Y_2(Zr_{1-y}Ti_y)_2O_7$ from neutron diffraction measurements [Heremans, 1993].

by ~3 eV in both GT and GZ, suggesting that the anion disorder occurs preferentially in 48f over 8a sites. It was also found that cations in this system begin to disorder between x=0.45 and 0.6 which coincides with the onset of disordering of the 8a sites. This shows that the disordering processes in YZT involve, at first, only the oxygen ions closest to the vacant site and subsequently the entire oxygen array and cation array. This structural disorder will be related to the ionic conduction in pyrochlores in the next section.

2.2 Ionic conduction in Pyrochlores

The expression for ionic conductivity can be written as

$$\sigma_i = \frac{\sigma_o}{T} \exp(-E_i/kT)$$

where σ_o is the temperature-independent pre-exponential constant and E_i is the activation energy including both ion formation and migration terms.

Ionic conduction in pyrochlores is believed to occur by the migration of oxygen ions through the continuous channel of 48f sites [Moon, 1988a; Heremans, 1993; Wilde, 1996]. 48f sites form a continuous network of second nearest neighbors of the same type whereas 8a and 8b sites are isolated as shown in Fig. 2.3. From strain energy and potential energy calculations by van Dijk [van Dijk, 1985], jumps between 48f sites are favored over jumps between 48f and 8b or 8a sites. Wilde and Catlow [Wilde, 1996] also confirmed the predominant vacancy hopping mechanism between 48f sites in ionic motion in pyrochlores from their static energy minimization calculations. The examination of intrinsic ionic conduction in YZT along with structural

disorder observed by neutron diffraction confirms that the 48 sites are the major path for ionic conduction as discussed in detail.

Fig. 2.11 presents the electrical conductivity of the Gd_2O_3-ZrO_2 system as a function of composition by van Dijk et al. [van Dijk, 1980]. The figure shows that the maximum in ionic conductivity occurs within the pyrochlore region. From the σ_o and the E_i data as shown in Fig. 2.12 and 2.13, it is observed that this increase in ionic conductivity in the pyrochlore phase comes from the minimum in the E_i indicating improved oxygen vacancy mobility through the ordered structure. The minimum in the σ_o appears to be a reduction of oxygen vacancies due to ordering in the pyrochlore phase. Thus, the increases in the conductivity can be ascribed to the improved mobility of a smaller number of oxygen vacancies in pyrochlore relative to fluorite due to the presence of better pathways for oxygen migration in the ordered pyrochlore phase.

Ionic conduction in pyrochlores can be classified into two cases: Intrinsic conduction where the degree of disorder is largely controlled by intrinsic charge carriers (oxygen vacancies) and extrinsic conduction where charge carriers are extrinsically generated by dopants.

2.2.1 Intrinsic Ionic Conduction

Fig. 2.14 and 2.15 respectively show the measured ionic conductivity as a function of B site composition in GZT and YZT by Moon et al. [Moon, 1989]. These figures show dramatic increases in ionic conductivity with increasing Zr content. Anion disorder in pyrochlores involves the generation of oxygen vacancies in 48f sites. Since these vacancies can migrate by the exchange of nearest-neighboring oxygen ions under an electric field gradient, the ionic

31
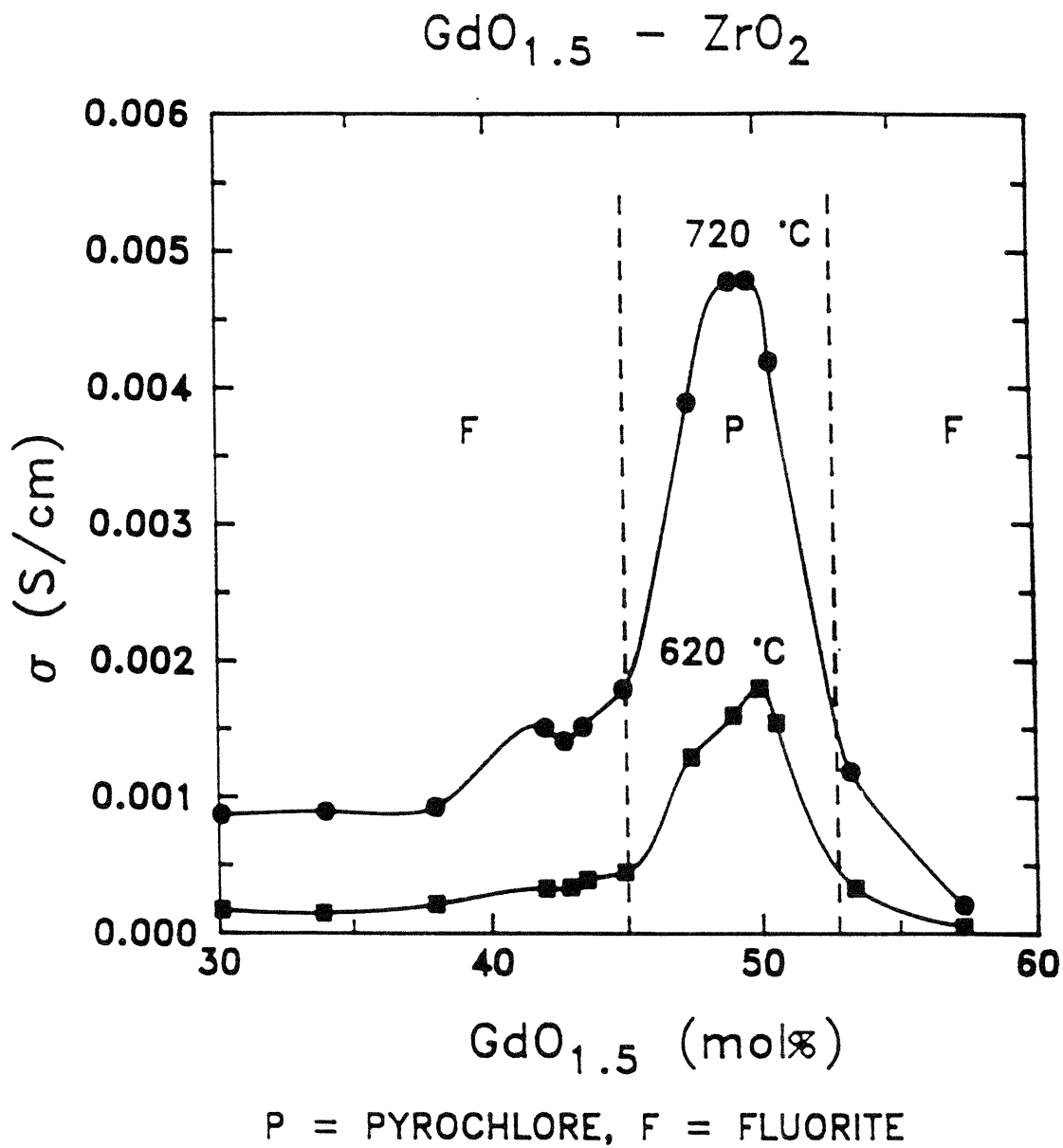
Fig. 2.11 The ionic conductivity as a function of composition in the Gd_2O_3-ZrO_2 solid solution [van Dijk, 1980].
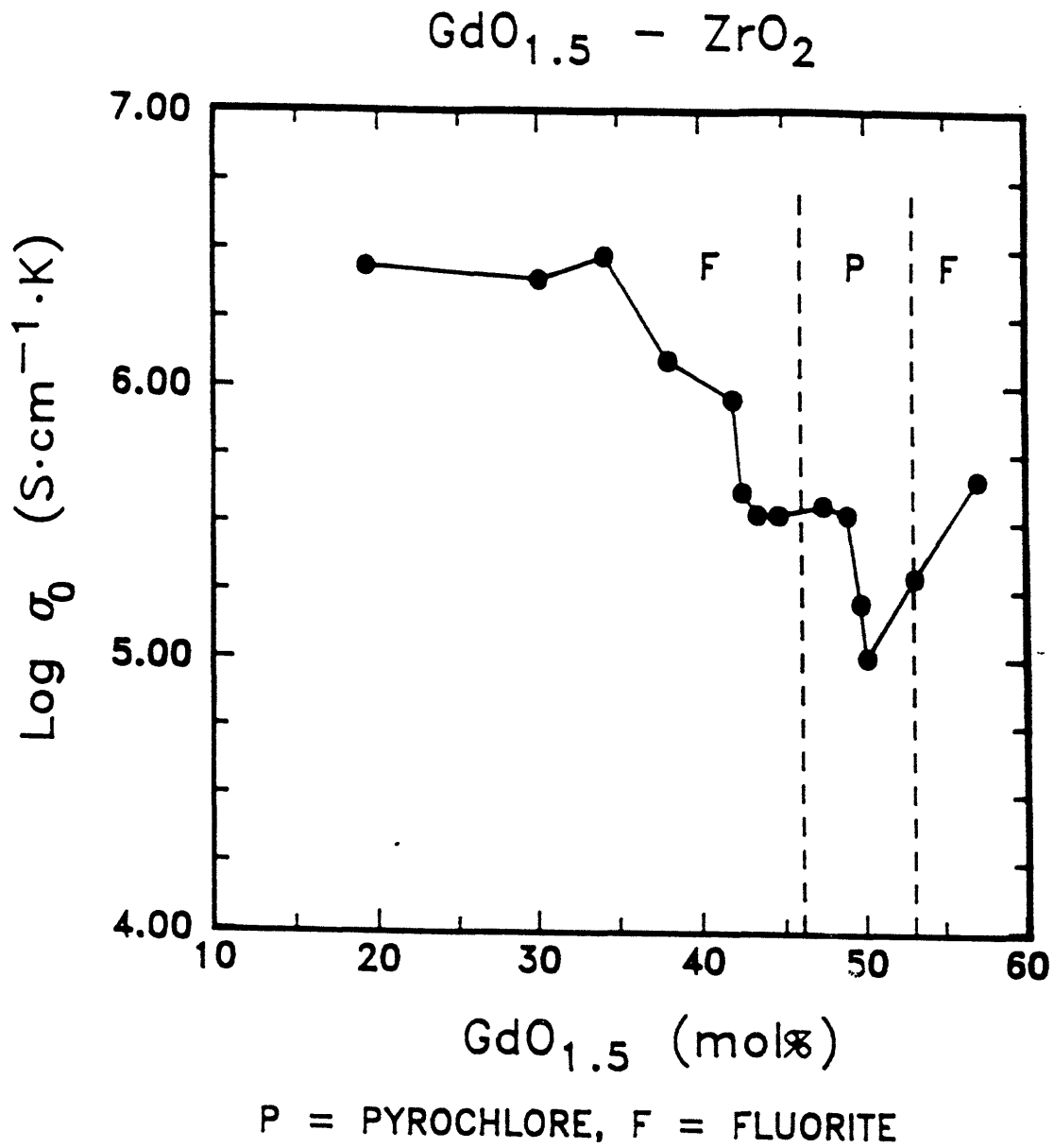
Fig. 2.12 The pre-exponential constant for ionic conduction as a function of composition in the Gd_2O_3-ZrO_2 solid solution [van Dijk, 1980].
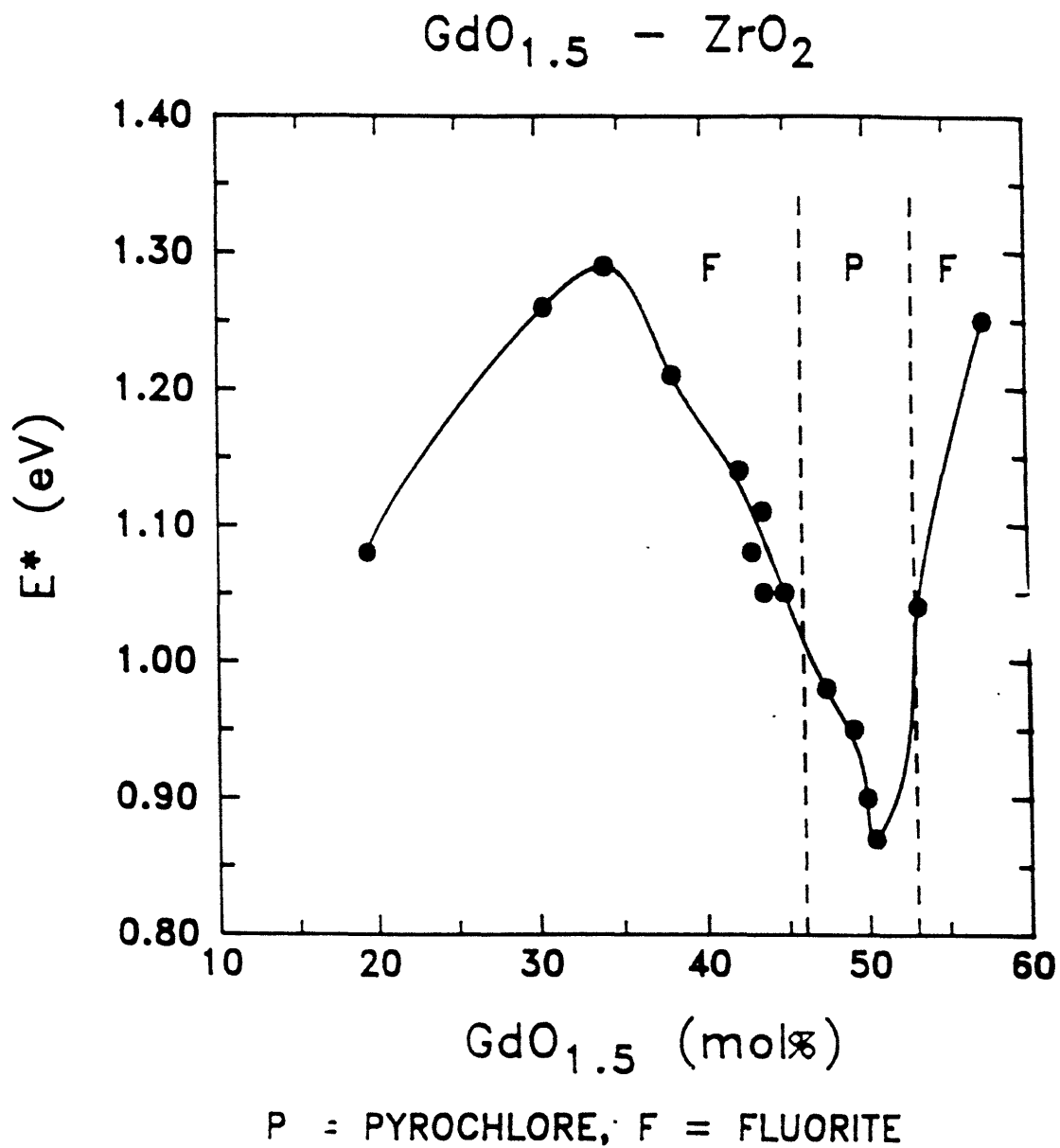
Fig. 2.13 The activation energy for ionic conduction as a function of
composition in the Gd_2O_3-ZrO_2 solid solution [van Dijk, 1980].
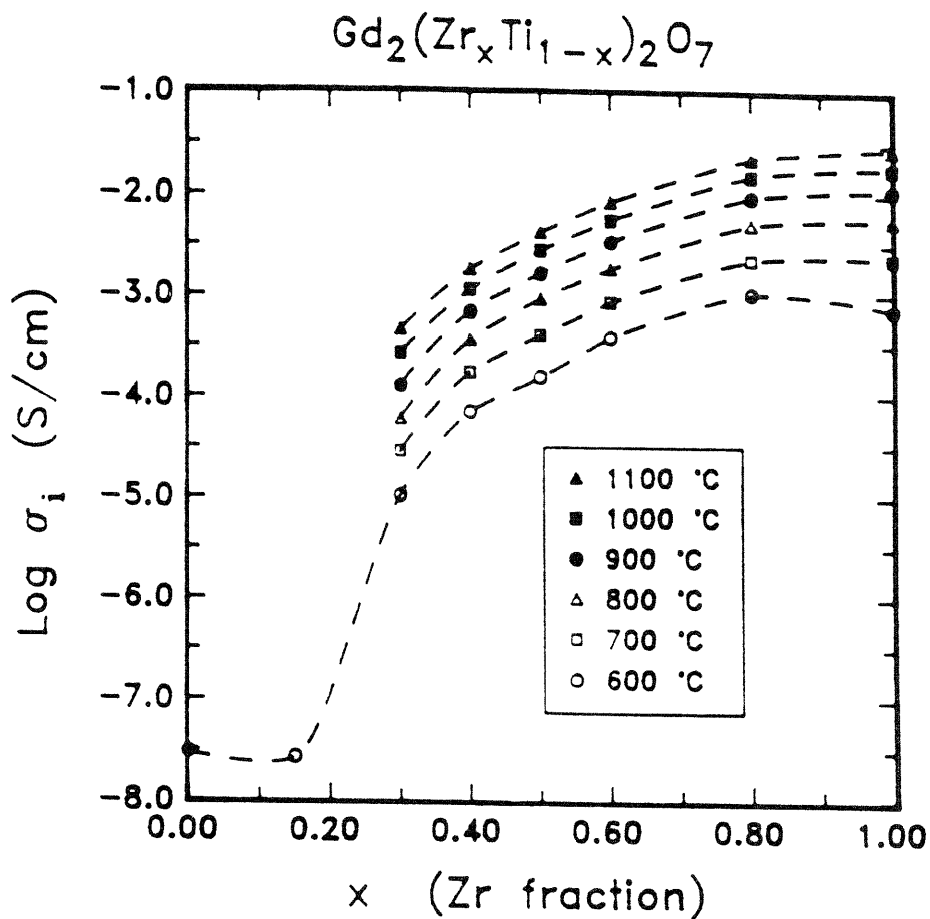
Fig. 2.14 Ionic conductivity of $Gd_2(Zr_{1-x}Ti_x)_2O_7$ as a function of x [Moon, 1989].
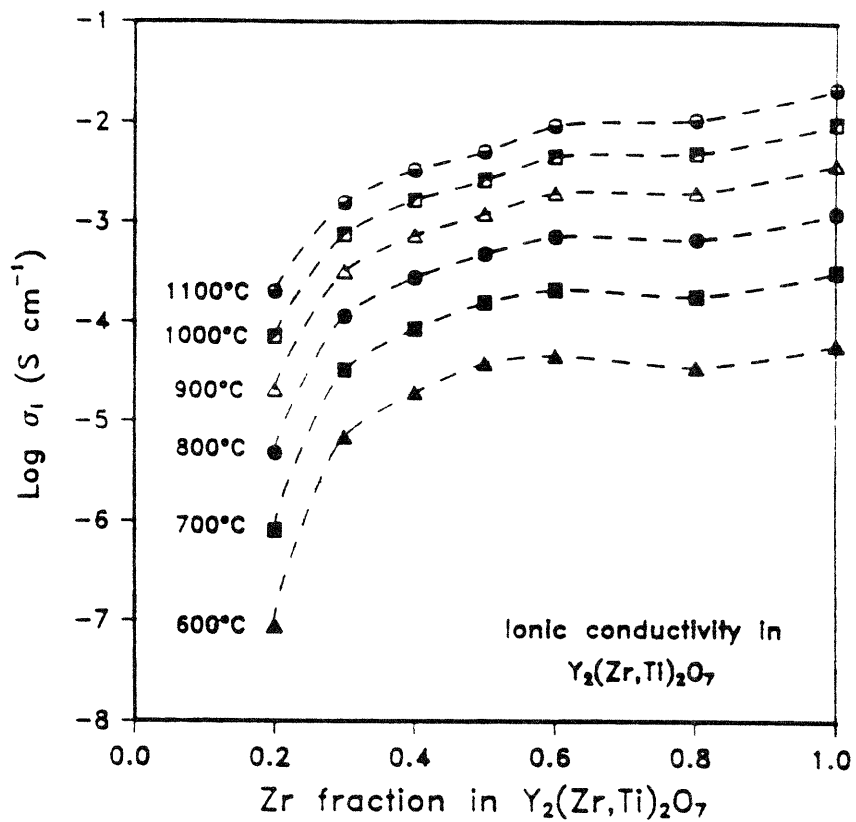
Fig. 2.15 Ionic conductivity of $Y_2(Zr_{1-x}Ti_x)_2O_7$ as a function of x [Moon, 1989].

conductivity can be enhanced by increasing oxygen vacancy concentration. From this stand point of view, the increases in the ionic conductivity in GZT and YZT can be related to the increases in the anion disorder with increasing Zr content thereby generating oxygen vacancies which serve as charge carriers. The corresponding E_i and the σ_0 are shown in Fig. 2.16 and 2.17. From these figures, one can see that increases in the ionic conductivity in these systems comes from increases in the σ_0 rather than decreases in the E_i. Moon attributed increases in the σ_0 with near constant E_i to increases in oxygen vacancy concentration with constant oxygen vacancy mobility.

Increases in ionic conductivity in YZT with higher Zr were well correlated to the anion disorder by the neutron diffraction analysis by Heremans and Wuensch [Heremans, 1993] confirming that the increase in ionic conductivity is due to an enhancement of the defect concentration of oxygen vacancies on 48f sites as discussed in section 2.1.3. Note that the ionic conductivity already increases by more than an order of magnitude from x=0 to x=0.4 in YZT where depopulation occurs only in the 48f sites as shown in Fig. 2.10. This observation confirms the assumption that 48f sites provide the path for oxygen migration. For x less than 0.25 in GZT and YZT, the ionic conductivity appears to be governed by background impurities since the degree of intrinsic disorder is too low to generate a sufficiently high oxygen vacancy concentration.

The larger σ_0 in YZT than in GZT for a given Zr content indicates that the degree of disorder is more significant in YZT due to a smaller r_A/r_B ratio as mentioned previously. The magnitude of σ_i in GZT is, however, larger than that in YZT due to the lower E_i. This suggests that GZT provides better transport pathways for oxygen vacancy migration or less defect association with a more ordered structure relative to YZT.
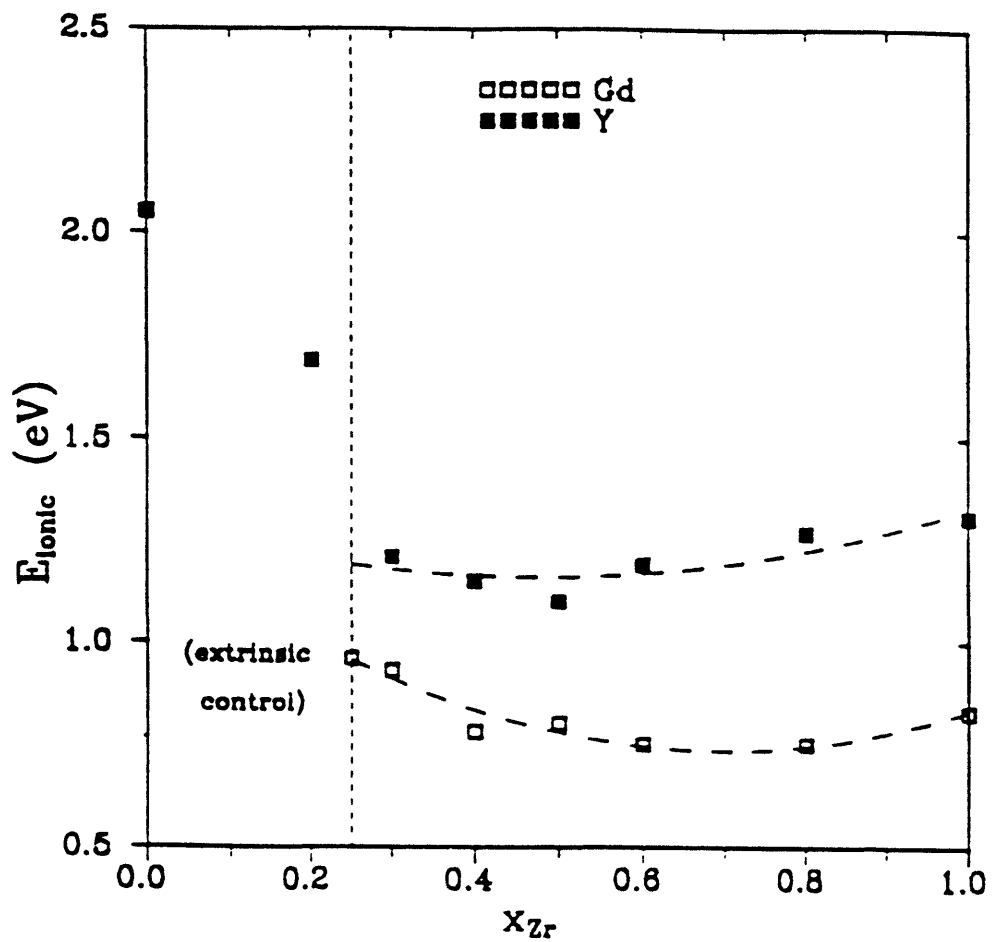
Fig. 2.16 Activation energy for ionic conductivity for $Gd_2(Zr_{1-x}Ti_x)_2O_7$ and $Y_2(Zr_{1-x}Ti_x)_2O_7$ as a function of x. Dashed lines do not indicate parametric fitting. [Spears, 1991].
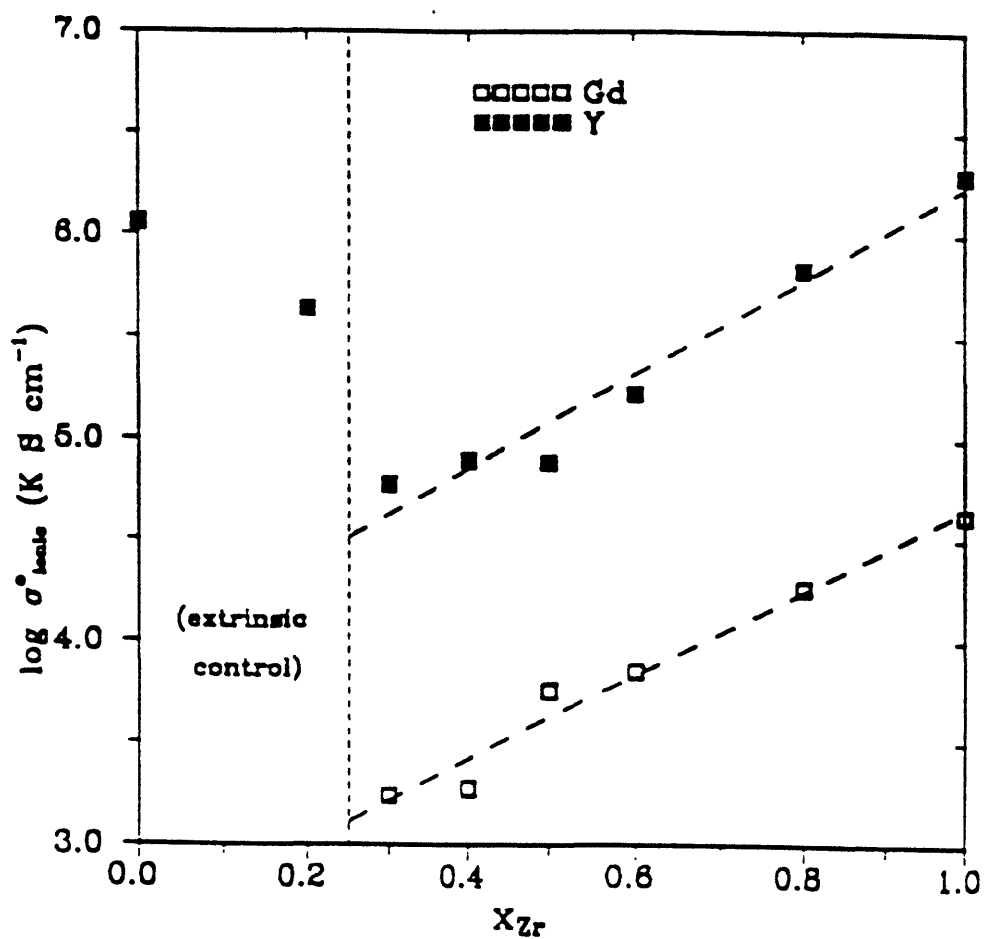
Fig. 2.17 Pre-exponential term for ionic conductivity for $Gd_2(Zr_{1-x}Ti_x)_2O_7$ and
$Y_2(Zr_{1-x}Ti_x)_2O_7$ as a function of x. Dashed lines do not indicate
parametric fitting. [Spears, 1991].

By evaluating the ionic conductivity as a function of net acceptor density in terms of a defect chemistry model, Moon et al. [Moon, 1988b] calculated the Frenkel constant to be 1.0×10^{39} exp(-0.24±0.03 eV/kT) cm^{-6} in GZT at x=0.3. The high Frenkel constant with low activation energy confirms that GZT at x=0.3 is already highly disordered. The corresponding oxygen vacancy mobility was found to be 0.14 exp(-0.78±0.02 eV/kT) cm^2/Vs. At 1000 ^{o}C, an oxygen vacancy mobility of 1.1×10^{-4} cm^2/Vs is calculated while the value for 12% yttria stabilized ZrO$_2$ with the fluorite structure is 5.0×10^{-5} cm^2/Vs [Stratton, 1981]. The slightly higher value for the pyrochlore indicates the better pathway for oxygen vacancy migration in pyrochlores relative to fluorite as discussed earlier in section 2.2.1.

Since the ionic conductivity continues to increase substantially with increasing x in GZT and YZT, one can conclude from both conductivity and neutron diffraction measurements that the intrinsic structural disorder in GZT and YZT becomes larger with relative increases in average B site cation radius for fixed A site cation radius.

2.2.2 Extrinsic Ionic Conduction

In the case of GT where structural disorder is insignificant due to the smaller ionic radius of Ti^{4+} relative to that of Zr^{4+}, the ionic conductivity can be improved by acceptor doping. Kramer et al. [Kramer, 1994] investigated the effect of various acceptor dopants upon substitution in the A and/or B sites in titanate pyrochlores and concluded that Ca^{2+} doping on the A site in GT is the most effective considering the match in ionic radius of Ca^{2+} and Gd^{3+} (Ca^{2+} 1.12 Å and Gd^{3+} 1.06 Å) . As shown in Fig. 2.18, the ionic conductivity increases by over 2 1/2 orders of magnitude with increasing Ca concentration in GT reaching a maximum value of 5×10^{-2} S/cm at 1000 ^{o}C in (Gd$_{1-x}$Ca$_x$)$_2$Ti$_2$O$_7$
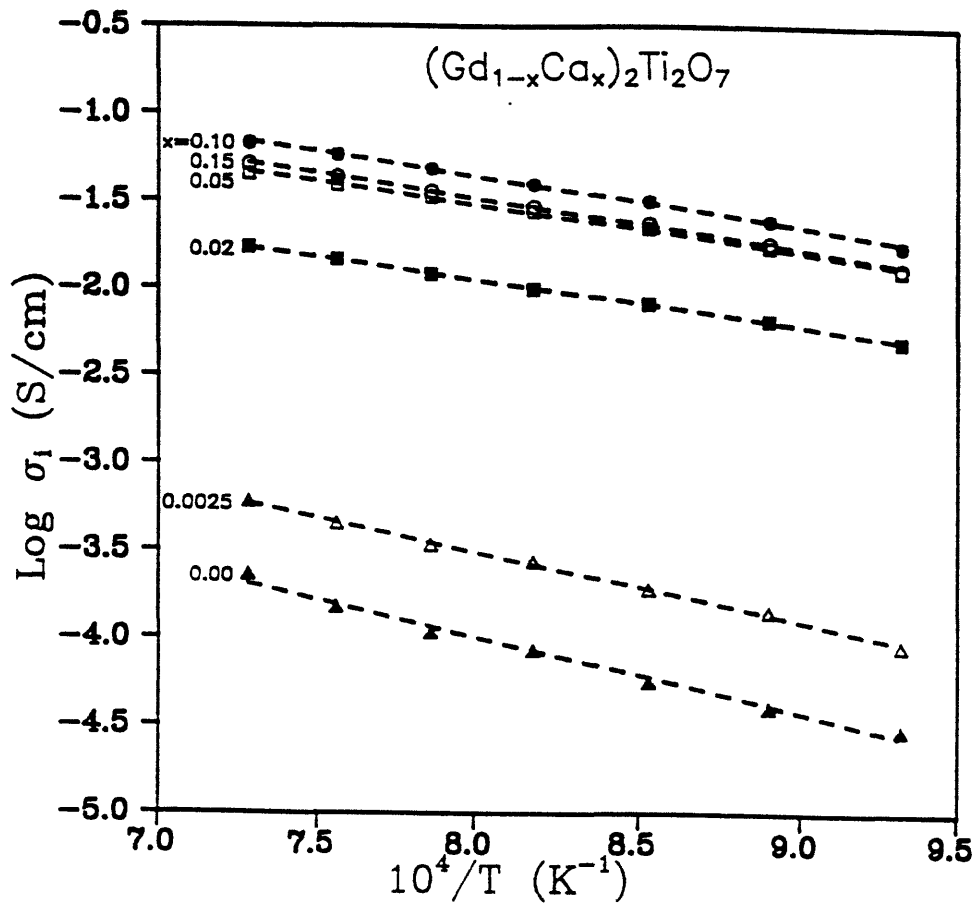
Fig. 2.18 The temperature dependence of ionic conductivity for $(Gd_{1-x}Ca_x)_2Ti_2O_7$ between 1100-800 °C [Kramer, 1994].

with x=0.1, within a factor of two of the conductivity of stabilized zirconia (YSZ). This represents the highest ionic conductivity reported to date for a titanate based material. For x values greater than x=0.1 in $(Gd_{1-x}Ca_x)_2Ti_2O_7$, the formation of the second phase $CaTiO_3$ was confirmed by X-ray diffraction. A more quantitative analysis by wavelength dispersive spectroscopy (WDS) revealed that the maximum bulk Ca concentration in GT was 7 mole %. Fig. 2.19 gives the ionic E_i and σ_0 as a function of Ca dopant concentration in GT. Increases in σ_0 with increasing Ca content is observed due to increases in the extrinsically generated oxygen vacancy concentration. The E_i drops to a minimum value of 0.63 eV at 2 mole% Ca. The initial decrease in E_i is qualitatively similar to those reported in yttria-doped ceria in which the decrease in E_i is attributed to the creation of favorable transport paths between the uncompensated Y'_{Ce} sites and the $(Y'_{Ce} - V_O^{\bullet\bullet})^{\bullet}$ complexes [Wang, 1981]. Kramer suggested that these initial E_i drops in the Ca doped GT system could be related to the electrostatic interaction between Ca'_{Gd} and oxygen vacancies on the 48f sites.

By comparison of undoped GZT (x=0.25) and Ca doped GZT (x=0.25), a value of the Frenkel activation energy of $E_F = 0.44$ eV (compared with 0.24 for GZT (x=0.30)) was obtained. This confirms the trend of decreasing E_F with increasing Zr content in GZT and the fact that the intrinsic disorder increases with decreases in r_A/r_B in $A_2B_2O_7$ pyrochlores.
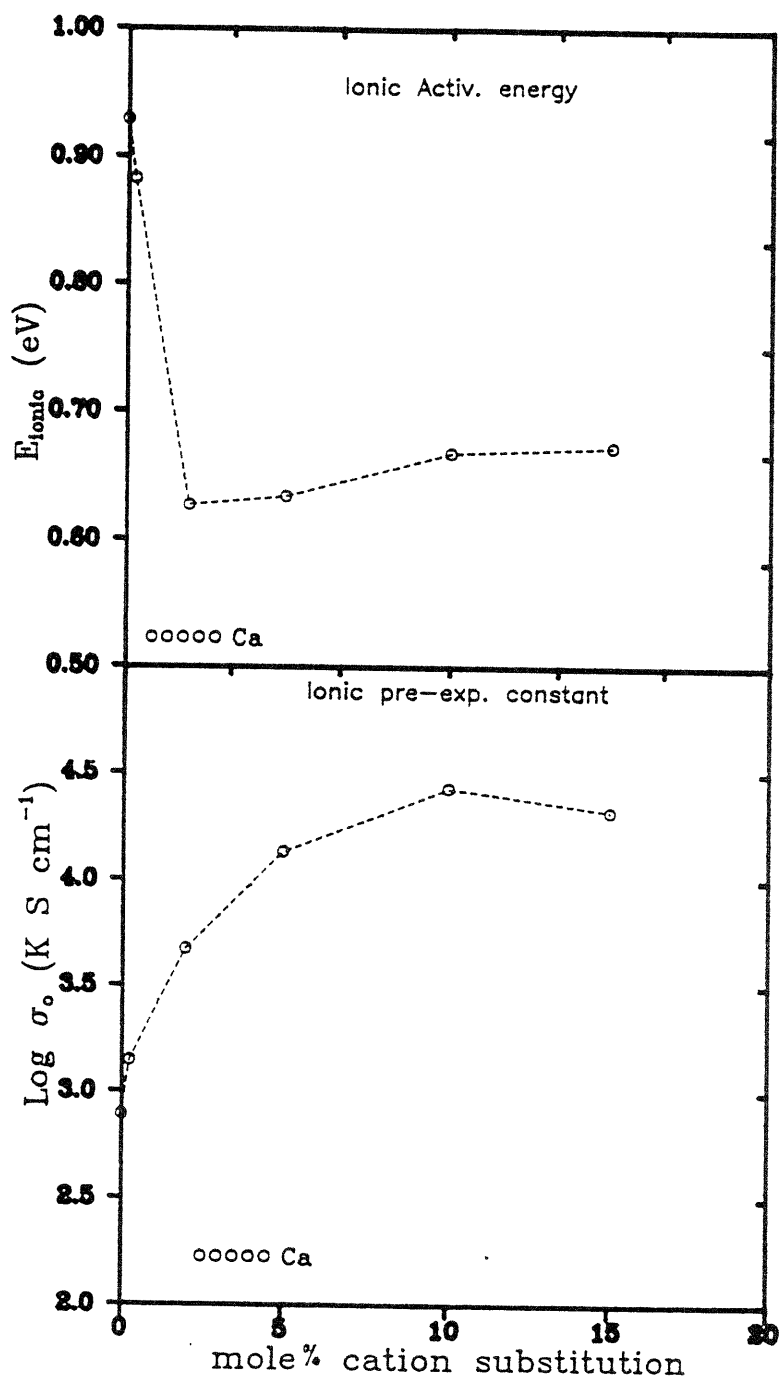
Fig. 2.19 The activation energy for ionic conduction and pre-exponential constant as a function of x in $(Gd_{1-x}Ca_x)_2Ti_2O_7$ [Kramer, 1994].

As shown in Fig. 2.6, the ionic radius of Sn^{4+} is 0.69 Å which lies between that of Ti^{4+} (0.605 Å) and Zr^{4+} (0.72 Å). As discussed previously, it has been observed in GZT and YZT that structural disorder in the pyrochlore structure increases as the average B cation radius becomes closer to the A cation radius. The question arises if the degree of disorder in GS would be comparable to that in GZT with the same average B cation radius. A major purpose of this research is to investigate if the disorder in pyrochlores is a truly a function of r_A/r_B regardless of the chemistry of the B site cation. Choosing ionic radii from Shannon and Prewitt [Shannon, 1969], GZT with x=0.74 has the same average B site cation radius as that in GS. Lattice constant comparisons give a slightly different x value in GZT. From Knop et al.'s data [Brisse, 1968; Knop, 1969; Moon, 1988a], the lattice constant of GT, GS and GZ are 10.181 Å, 10.460 Å, and 10.528 Å. This leads to an x value of 0.80 in GZT which gives the same lattice constant as that in GS. It appears that the lattice constant comparison is more accurate since the derived ionic radii ignored effects such as anion-anion repulsion, irregular coordination and metal-metal bonding as suggested by Shannon and Prewitt. Therefore the x value of 0.8 in GZT will be used in the rest of this thesis regarding the average B site cation radius comparable to that in GS.

2.3.1 The Structure of $A_2Sn_2O_7$ Pyrochlore

Brisse and Knop [Brisse, 1968] investigated the structure of $A^{3+}_2Sn^{4+}_2O_7$ with A = lanthanides or Y with X-ray, neutron diffraction measurements and infrared transmission spectroscopy. All the Ln stannates and $Y_2Sn_2O_7$ were found to be cubic pyrochlores with their lattice parameter increasing linearly with the radius of A^{3+}. The oxygen positional parameter,

x, increased with the ionic size of A^{3+}, indicating a decrease in the distortion of the SnO_6 octahedra. Interatomic distances between Sn and O in $A_2Sn_2O_7$ (A = Y, Sm, La) ranged from 2.048 Å to 2.070 Å which is very close to those reported for six-coordinated Sn^{4+} in SnO_2 and $BaSnO_3$ [Wagner, 1959].

Infrared adsorption spectra of $Ln_2Sn_2O_7$ (Ln = La, Sm, Gd, Yb, Lu; Y) by Vandenborre et al. is shown Fig. 2.20 [Vandenborre, 1983]. The value of the first three higher frequencies (i.e. 640, 454 and 396 cm^{-1} in $Y_2Sn_2O_7$) clearly increases with the decrease of the ionic radius of Ln^{3+} cations. These peaks are identified as lattice vibrations of mainly Sn-O bonding as confirmed in a good agreement with calculated frequencies based on valence force field calculations in stannate pyrochlores. Compared with titanate pyrochlores, they concluded that Sn-O bonding is more covalent and rigid relative to Ti-O bonding and showed that a stronger force is developed between Sn and O in stannates relative to Ti and O in titanate pyrochlores. This characteristic of Sn-O bonding resulted in the sensitive frequency dependence of Sn-O lattice vibration on the change of rare-earth on the A site, while the frequencies due to the Ln-O lattice vibrations remained unchanged. Since ionic conduction occurs by oxygen ion migration in pyrochlores, it is possible that the different bonding characteristics of Sn-O relative to Ti-O might influence the oxygen vacancy mobility in ionic conductivity for stannate pyrochlores. One purpose of this research is to investigate the compositional dependence of intrinsic disorder and oxygen vacancy mobility in solid solution of GTS, which might be related to the different bonding characteristics of Sn-O and Ti-O.

Calage and Pannetier [Calage, 1977] investigated the oxygen positional parameter, x, as a function of A site ionic radius using lattice energy minimization as a constraint. They calculated the total energy, consisting of coulomb and repulsion terms, and allowed the x value to vary so as to minimize the lattice energy. The value of x was calculated to increase with
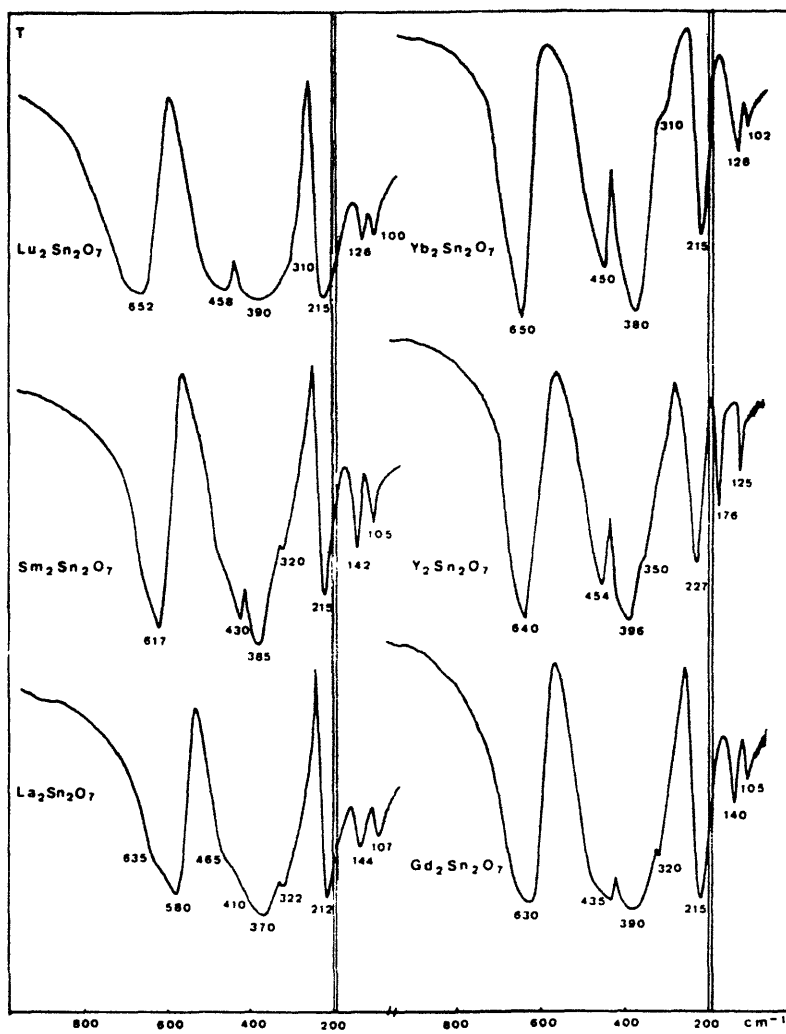
Fig. 2.20 Infrared adsorption spectra of the $Ln_2Sn_2O_7$ compounds (Ln = La, Sm, Gd, Yb, Lu; Y) [Vandenborre, 1983].

increasing A site ionic radius and decreasing B site ionic radius from Zr, Sn to Ti indicating a decrease in the distortion of the SnO_6 octahedra with increasing r_A/r_B ratio. This variation in the oxygen positional parameter, x, is reflected in a linear increase in quadrupole splitting with decreasing lattice constant as observed in Mössbauer measurements on $A_2Sn_2O_7$ (A= Ln, Y), rare-earth stannates [Belyaev, 1969; Loebenstein, 1970]. Calage and Pannetier successfully correlated the Mössbauer quadrupole splitting with the electric field gradient which was calculated from the positional parameter x.

2.3.2 Sn^{2+} containing Pyrochlores

Stewart et al. [Stewart, 1973] reported that $Sn_2Ta_2O_7$ and $Sn_2Nb_2O_7$ form the cubic pyrochlore phase. Birchall and et al. [Birchall, 1975] synthesized and characterized pyrochlores in the Sn-Nb-O and Sn-Ta-O system by X-ray diffraction, Sn Mössbauer spectroscopy, density determination and chemical analysis. The general formula for partially oxidized tin (II) niobate and tantalate, $Sn^{2+}{}_{2-x}(M_{2-y}Sn^{4+}{}_y)O_{7-x-y/2}$, with M = Nb^{5+} or Ta^{5+}, was obtained from these investigations. This formula suggests that pyrochlore phases are possible with Sn/M^{5+} ratio less than and greater than one indicating the existence of both cation and anion vacancies in the lattice.

The Mössbauer spectra established the presence of both Sn^{2+} and Sn^{4+} segregated to crystallographically distinct sublattices -A and B sites- as a consequence of the size disparity of Sn^{2+} and Sn^{4+} ions (Sn^{2+} 1.22 Å and Sn^{4+} 0.69 Å). They reported that Sn^{2+} was found to be located not at the A site with $\bar{3}$m symmetry of the ideal pyrochlore structure but to be displaced from the $\bar{3}$m position by 0.38 Å as evidenced by a relatively large quadrupole splitting and a small isomer shift. They attributed this displacement from the symmetric position to the characteristic of Sn^{2+} which has a lone-pair electron

and thus prefers asymmetric environments as observed in $SnSO_4$ and SnO [Rentzeperis, 1962]. Sn^{4+} was found to be in regular octahedral sites with all six Sn-O distances equal or nearly so with a zero or small quadrupole splitting, whereas Sn^{4+} in $A^{3+}_2Sn^{4+}_2O_7$. is located in distorted octahedral sites as discussed above.

2.3.3 Electrical Conductivity of Stannates Pyrochlores

Chapman et al. [Chapman, 1970] performed electrical conductivity measurements on $A_2Sn_2O_7$ pyrochlores with A = Y, La and Nd. As shown in Fig. 2.21, all these compositions show a small oxygen partial pressure dependence indicating a p-type conduction in oxidizing atmospheres. Compared with the electrical conductivity data on $Y_2Zr_2O_7$ and $Nd_2Zr_2O_7$ pyrochlore by the same group, these stannates exhibited a lower electrical conductivity by a factor of $\sim 10^2$ with a higher activation energy. This is a somewhat unexpected result considering the assumption that the disorder in the stannates would be comparable to that in the zirconates. A more extensive analysis involving ionic conductivity measurements on the stannates as a function of a dopant concentration will provide more insight regarding the degree of disorder in the stannate pyrochlores using appropriate defect models as will be discussed in chapter III.

Wakiya et al. [Wakiya, 1993] synthesized $Ca_{2x}Ce_{2-2x}Sn_2O_7$ (0.35<x>0.43) and $Sr_{0.7}Ce_{1.3}Sn_2O_7$ pyrochlores. From the chemical analysis and the Rietvelt analysis performed on X-ray diffraction data, they suggested that some of the Ce ions on the A site are trivalent to maintain the electrical neutrality of the crystal. The electrical conductivity measurements performed on these systems are shown in Fig. 2.22. The figure shows that $Ca_{0.8}Ce_{1.2}Sn_2O_7$ and $Sr_{0.7}Ce_{1.3}Sn_2O_7$ exhibit higher electrical conductivity than that of $A_2Sn_2O_7$

48
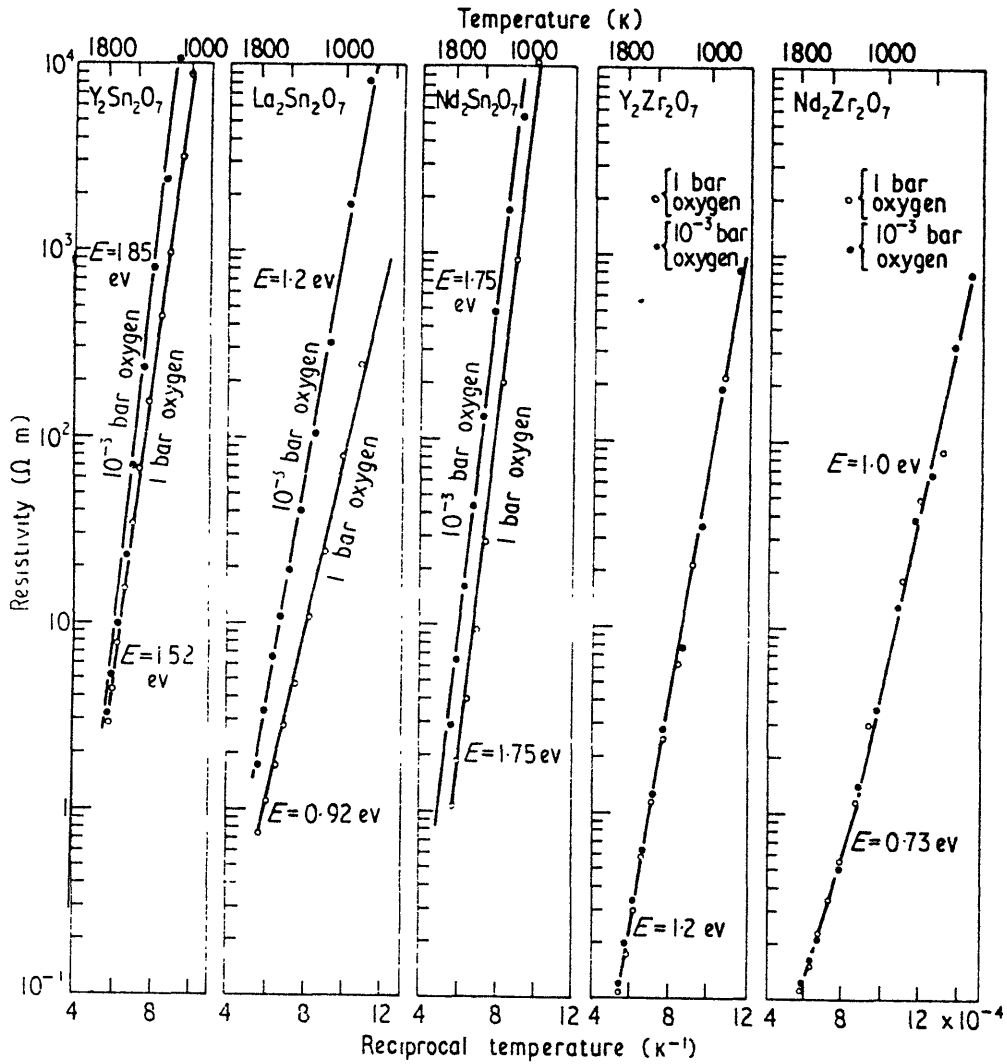
Fig. 2.21 The electrical resistivity plotted against inverse temperature for various stannates and zirconates. The activation energies are for the equation $\rho = \rho_0 \exp(E/kT)$ [Chapman, 1970].
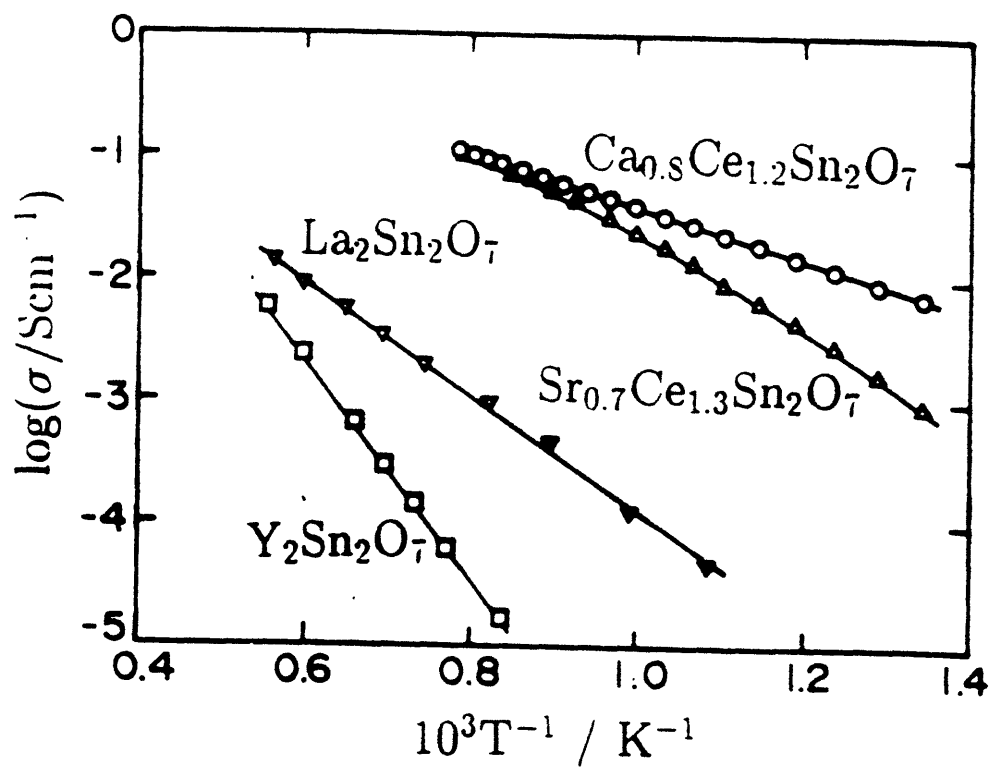
Fig. 2.22 Electrical conductivities of $Ca_{0.8}Ce_{1.2}Sn_2O_7$ and $Sr_{0.7}Ce_{1.3}Sn_2O_7$ as a function of temperature. The conductivities of $La_2Sn_2O_7$ and $Y_2Sn_2O_7$ [Chapman, 1970] are also plotted for comparison [Wakiya, 1993].

with A = La, Nd and Y by 2~4 orders of magnitude depending on the temperature range. From the Seebeck coefficient measurements, it was found that majority carriers in these systems were electrons. They attributed this higher electrical conductivity to the hopping of electrons between Ce^{3+} and Ce^{4+} or Sn^{4+} and Sn^{2+}.

2.3.4 Ti versus Sn

It has been observed that TiO_{2-x} can accommodate a high degree of nonstoichiometry by the formation of crystallographic shear planes. By using computer simulation techniques, Catlow and James [Catlow, 1982] explained this observation in terms of the large cation displacement polarizability. They calculated the lattice energy of the observed structure of Ti_4O_7 and Ti_5O_9 and relaxed all ions in these structures until they were at equilibrium with the TiO_2 potential. They calculated that the relaxation energy for forming shear planes was ~10 eV indicating stabilization of extended defects. This extensive relaxation is necessary if shear planes are to be stable with respect to point defect structures.

In the case of SnO_2, which has the same rutile structure as TiO_2, the formation of extended defects upon reduction was not observed due to a much smaller relaxation energy of ~4 eV [Freeman, 1990]. They attributed this phenomena to a difference in the displacement of the Ti and Sn ion. If cation displacement polarizability is high, cation relaxation in the vicinity of shear plane is sufficiently large to stabilize the shear planes. The difference in cation displacement polarizability is reflected in the high value of the static dielectric constant of ~150 in TiO_2 relative to the much smaller value of ~16 for SnO_2. This difference in ionic polarizability may affect migration of oxygen ions in the pyrochlore structure since cations have to be displaced from

their equilibrium positions when oxygen ions migrate in the lattice. The large difference in dielectric constant between Ti and Sn is well observed in the $Zr_xTi_ySn_zO_4$ (x+y+z=2) system as shown in Fig. 2.23 [Wolfram, 1981]. The figure shows the continuous decrease in dielectric constant with increasing Sn content within the single phase region indicating the difference in the displacement polarizability between Ti and Sn ions.

Assuming the oxygen ion migrates in the continuous channel of the 48f sites in the pyrochlores, the local environment of the 48f sites may play an important role in the oxygen vacancy mobility. Since the nearest neighbors of the 48f sites are two A site cations and two B site cations, the oxygen vacancy mobility can be affected by the ionic polarizability of the cations reflected in the readiness of the cation displacements. It is of interest to investigate the dependence of dielectric constant in the GTS system as a function of Sn content to examine the effect of the relative ionic polarizabilities of the Sn and Ti ions and its consequent effect on oxygen ion mobility.

2.4 Summary and Proposed Work

The literature review revealed several issues to be addressed in this investigation. First, it was observed that the r_A/r_B ratio is an important parameter in determining disorder in the cation and anion sublattices in GZT and YZT. The intrinsic ionic conductivity increase with increasing Zr content was successfully correlated to this structural disorder. The question is whether Sn on the B site can give rise to comparable disorder in GS and $Y_2Sn_2O_7$ (YS). The conductivity data on $A_2Sn_2O_7$ (A = Y, La and Nd) pyrochlores show that the stannate has a lower conductivity than that of the corresponding GZT or YZT systems with x=0.8. We will investigate the conductivity of GS and YS and compare these with that in the GZT and YZT

52
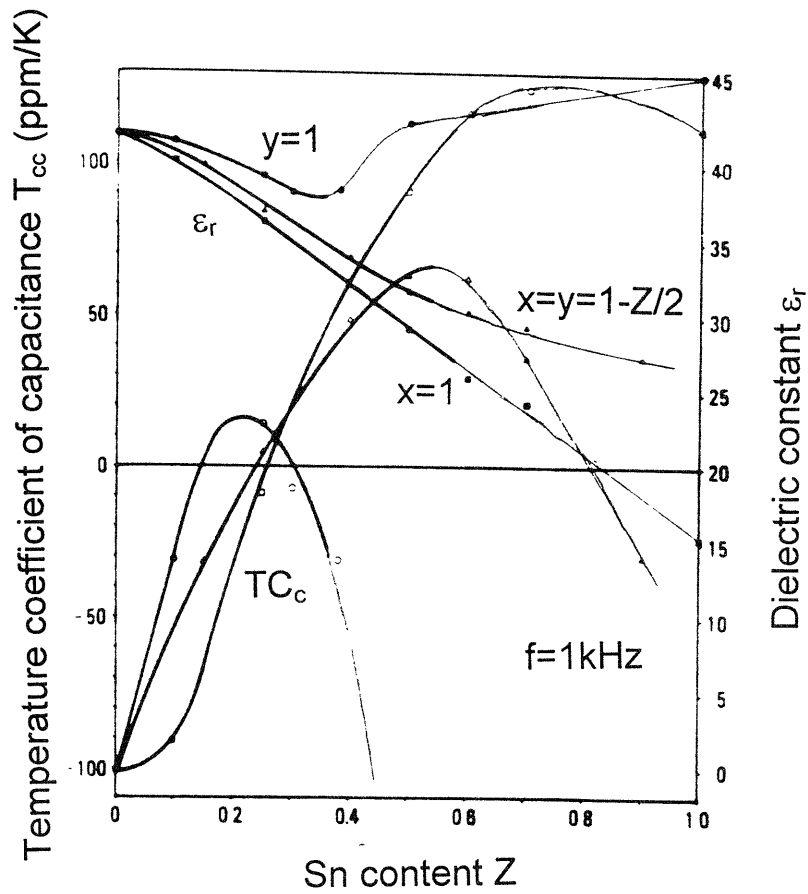
Fig. 2.23 Dependence of the dielectric constant ε_r and the temperature coefficient of capacitance T_{cc} on the Sn content z. The single-phase range is indicated by the bold line [Wolfram, 1981].

systems. Ca doping on the A site of GS will be used to examine the increase in the ionic conductivity and thereby calculate the intrinsic disorder in GS by using a defect model discussed in detail in chapter III.

From the infrared transmission and absorption data, it appears that Sn has different bonding characteristics from that of Ti or Zr. The ionic polarizability of Sn ion appears to be much less that that of Ti. The ionic conductivity of solid solution of GTS, YTS and GZS will be investigated to examine intrinsic disorder and oxygen vacancy mobility as a function of the B site cation composition. X-ray diffraction measurements will be performed on GTS in collaboration with Prof. Wuensch's group at M.I.T. to investigate the structural disorder in cation and anion sublattices in stannate pyrochlores. The dielectric constant of GTS will be measured to correlate the polarizability of the Sn ion with the oxygen ion mobility.

Lastly, two experimental techniques are applied-short circuit cell and open circuit voltage measurements-to separate out the ionic conductivity from the total conductivity. These measurements are used to investigate the ionic conductivity in the region where the simple defect model is no longer valid. The ionic conductivity derived from the short circuit cell measurements is compared with values extracted from the defect model with the limitations of the technique.

3 Theory

In this chapter, the theoretical aspects of electrical conductivity and defect chemistry in pyrochlores are discussed. On this basis, a model for the electrical conductivity as a function of the thermodynamic variables such as temperature, Po_2 and dopant concentration is derived. The second section describes various electrochemical techniques which permit one to measure the ionic conductivity in MIEC. Key equations for open circuit voltage and short circuit cell measurements are explained.

3.1 Defect Chemistry and Electrical Conductivity

Electrical conductivity in oxides can involve both electronic and ionic charge carriers. Since charge carriers are considered as defects in the perfect crystalline lattice, the understanding of defect chemistry is important in the investigation of electrical conduction. This section begins with the basic theory of electrical conduction and relates it to a defect model appropriate for pyrochlores.

The electrical conductivity σ_j of carrier j is defined by:

$$\sigma_j = c_j Z_j q_j \mu_j \tag{3.1}$$

where c_j is the carrier density, $Z_j q_j$ the effective charge and μ_j the mobility of the jth species. As shown in this equation, the carrier density and the mobility are key components in determining the electrical conductivity. The total electrical conductivity of a solid is the sum of the partial conductivities of each type of charge carrier such as the electron, hole and ion and is given by:

$$\sigma = \sum_j \sigma_j \qquad (3.2)$$

Writing the general exponential form for each partial conductivity as:

$$\sigma_i = \frac{\sigma_o}{T} \exp(-E_i/kT) \qquad (3.3)$$

where σ_o includes $Z_j q$ and the pre-exponential terms related to concentration and mobility of the charge carrier and E_i, the energy required for charge carrier generation and migration. The transference number is defined by the fraction of the conductivity contributed by each charge carrier:

$$t_j = \sigma_j/\sigma_{tot} \qquad (3.4)$$

As discussed in the previous chapter, the pyrochlore structure has a number of empty interstitial sites which would be viewed as oxygen vacancies in the defect fluorite structure. Oxygen ions located at 48f sites can be exchanged with empty interstitial 8b sites at high temperature as observed in neutron diffraction work on YZT in Fig. 2.10 [Heremans, 1993]. This exchange creates anion Frenkel defects consisting of an oxygen interstitial - vacancy pair as described below:

$$O_o \leftrightarrow O_i'' + V_O^{\bullet\bullet} \qquad (3.5)$$

The mass action product K_F for this reaction is:

$$K_F = [V_O^{\bullet\bullet}][O_i''] = K_{FO} \exp(-E_F/kT) \qquad (3.6)$$

where E_F represents the Frenkel formation energy. In the case of ordered GT

where E_F is high, acceptor dopants such as Ca on Gd sites compensate the oxygen vacancy concentration in place of oxygen interstitials. Schottky defects and cation Frenkel defects are neglected due to the high formation energy of these defects [Catlow, 1989].

Oxygen ions in the lattice maintain equilibrium with oxygen in the gaseous phase. This redox reaction involves the annihilation of oxygen vacancies and the creation of holes when oxygen is absorbed on the surface of pyrochlore and transformed into oxygen ions:

$$V_O^{\bullet\bullet} + 1/2 \; O_2 \leftrightarrow O_o + 2h^{\bullet} \tag{3.7}$$

The mass action product for this oxidation reaction K_{ox} is:

$$K_{ox} = p^2 [V_O^{\bullet\bullet}]^{-1} P_{O2}^{-1/2} = K_{oxo} \exp(-E_{ox}/kT) \tag{3.8}$$

where E_{ox} represents the oxidation energy.

Electrons excited thermally from levels at the top of the valence band into levels at the bottom of the conduction band give rise to a free electron in the conduction band and a free hole in the valence band. This intrinsic electron-hole pair generation is given as:

$$nil \leftrightarrow e' + h^{\bullet} \tag{3.9}$$

The mass action product K_e is:

$$K_e = np = K_{eo} \exp(-E_g/kT) \tag{3.10}$$

where E_g represents the thermal band gap.

Electroneutrality requires a balance of charge species. This is represented by:

$$2[V_o^{\bullet\bullet}] + p + [D^\bullet] = [A'] + n + 2[O_i'']$$ (3.11)

in which A' and $D^\bullet$ represent singly ionized acceptors and donors.

Combining Eq. (3.6), (3.8), (3.10) and (3.11) and solving for $[V_o^{\bullet\bullet}]$, n and p yields:

$$[V_o^{\bullet\bullet}] = 0.25 [I + (I^2 + 16K_F)^{1/2}] = R$$ (3.12)

$$n = K_e(K_{ox}R)^{-1/2}P_{O2}^{-1/4}$$ (3.13)

$$p = (K_{ox}R)^{1/2}P_{O2}^{1/4}$$ (3.14)

where $I = [A']- [D^\bullet]$ is the net acceptor concentration

The ion mobility is a thermally activated process given by:

$$\mu_i = \mu_i^o/T \, exp(-E_m/kT)$$ (3.15)

where E_m is the migration energy of the ion.

The mobility of electrons and holes depends on whether they are localized around core ions or non-localized. For narrow band conduction, where carriers need to be excited from localized sites, the mobilities of electrons and holes are represented as follows:

$$\mu_e = \mu_{eo}/T \; \exp(-E_{h,e}/kT) \tag{3.16}$$

$$\mu_h = \mu_{ho}/T \; \exp(-E_{h,h}/kT) \tag{3.17}$$

$E_{h,e}$ and $E_{h,h}$ represent a hopping energy for electrons and holes respectively.

For the three mobile species, the partial conductivities are obtained by multiplying Eq. (3.12), (3.13) and (3.14) by their effective charges and mobilities:

$$\begin{aligned} \sigma_i &= 2q[V_O^{\bullet\bullet}]\mu_i \\ &= 2Re\mu_i \end{aligned} \tag{3.18}$$

$$\begin{aligned} \sigma_e &= qn\mu_e \\ &= K_e(K_{ox}R)^{-1/2}P_{O2}^{-1/4}e\mu_e \end{aligned} \tag{3.19}$$

$$\begin{aligned} \sigma_h &= qp\mu_h \\ &= (K_{ox}R)^{1/2}P_{O2}^{1/4}e\mu_h \end{aligned} \tag{3.20}$$

For intrinsic ionic conduction, where $[V_O^{\bullet\bullet}] = [O_i'']$, the activation energies for conduction are given by:

$$E_{ion} = E_{F/2} + E_m \tag{3.21}$$

$$E_{electron} = E_g - E_{ox/2} - E_{F/4} + E_{h,e} \tag{3.22}$$

$$E_{hole} = E_{ox/2} + E_{F/4} + E_{h,h} \tag{3.23}$$

where one assumes ionic conduction is dominated by oxygen vacancies.

For extrinsic ionic conduction, where $2[V_O^{\bullet\bullet}] = I$, the E_F is removed, and:

$$E_{ion} = E_m \qquad (3.24)$$

$$E_{electron} = E_g - E_{ox/2} + E_{h,e} \qquad (3.25)$$

$$E_{hole} = E_{ox/2} + E_{h,h} \qquad (3.26)$$

E_m and E_F can be obtained from Eq. (3.18) by deriving K_F and μ_i at each of the isotherms of a σ_i versus dopant concentration, I, dependence. E_g can be obtained from the sum of $E_{electron}$ and E_{hole} in Eq. (3.22) and (3.23) for intrinsic case or Eq. (3.25) and (3.26) for extrinsic case if hopping energy, $E_{h,e}$ and $E_{h,h}$ are negligible as observed in $Y_2Ti_2O_7$ [Goldschmidt, 1986]:

$$E_g = E_{electron} + E_{hole} \qquad (3.27)$$

In the case of GZT, Moon and Tuller [Moon, 1988a] observed that the increase in ionic conduction with increasing Zr content is largely related to an increase in σ_o rather than change in E_j in Eq. (3.3). By employing an atomistic model for the ionic conduction, an expression for σ_o is obtained [Facktor, 1984]:

$$\sigma_o = (4ae^2\nu d^2 N_o \exp[S_m/k] K_{FO}^{1/2})/k \qquad (3.28)$$

where a = geometrical factor

　　e = elementary charge

　　ν = attempt frequency

　　d = jump distance

　　N_o = oxygen 48f site concentration

S_m = migration entropy

K_{FO} = pre-exponential factor of the Frenkel constant

k = Boltzmann constant

Combining Eq (3.18)-(3.20) above gives an expression for the total conductivity:

$$\sigma_{tot} = \sigma_i + \sigma_e + \sigma_h = A + B(P_{O_2})^{-1/4} + C(P_{O_2})^{1/4} \tag{3.29}$$

Fig. 3.1 shows a fit between experimental data and Eq. (3.29) for $Gd_2(Zr_{0.2}Sn_{0.8})_2O_7$. As shown in the figure, the defect chemical model allows one to predict and obtain the P_{O_2} and temperature dependence of the electrical conductivity of each carrier.

For the ionic conductivity, Eq. (3.18) gives:

$$\log \sigma_i = \log \{0.5[I + (I^2 + 16K_F)^{1/2}]e\mu_i\} \tag{3.30}$$

Eq. (3.30) shows that one can obtain the Frenkel constant and oxygen vacancy mobility from a measurement of the ionic conductivity as a function of dopant concentration by fitting the experimental data to Eq. (3.30) using the iterative least square minimization routine.

3.2 Complex Impedance

The electrical conductivity of polycrystalline ceramics consists of bulk, grain boundary and electrode components. Complex impedance spectroscopy enables one to distinguish between bulk, grain boundary and electrode conductivity by obtaining an AC frequency dependent response over a wide

61
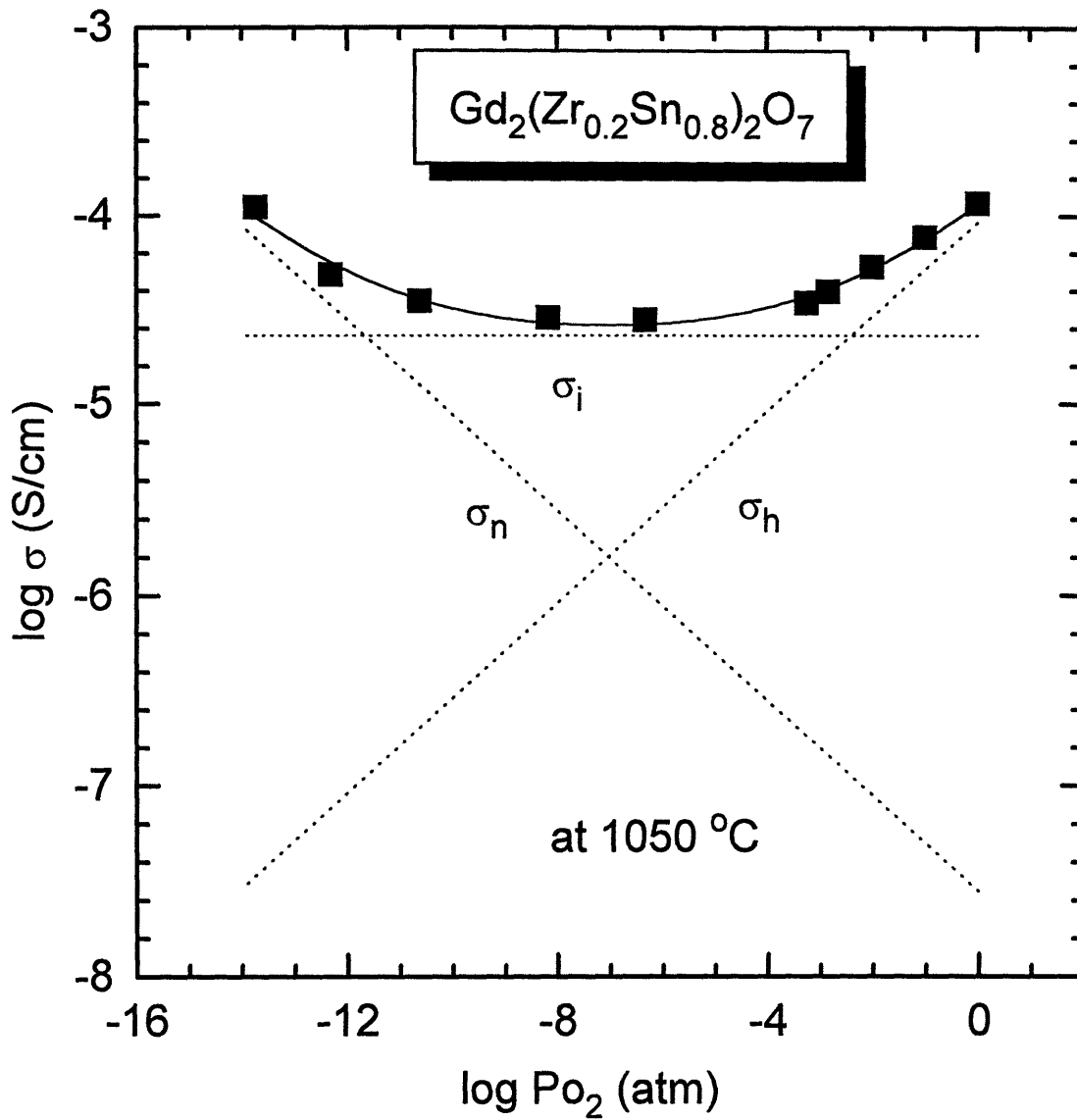
Fig. 3.1 log σ versus log Po₂ for Gd₂(Zr₀.₂Sn₀.₈)₂O₇ showing the least squares fit of Eq. (3.29) to the experimental data.

range of frequencies. Each of the components can be modeled by a parallel resistor-capacitor (RC) network corresponding to its own dielectric relaxation process as described in Fig. 3.2. Since these dielectric relaxation processes give rise to different characteristic time constants (τ_0 = RC), each network generates a complex impedance spectrum corresponding to its time constant.

For a single RC circuit as presented in Fig. 3.2, the impedance is given by:

$$Z = \frac{1}{1/R + j(2\pi f)C} \qquad (3.31)$$

where Z = overall impedance

      R = resistance of resistive element

      j = square root of -1

      f = frequency

      C = capacitance of capacitive element

Eq. (3.31) can be separated into its real (Z') and imaginary (Z") parts:

$$Z = Z' + Z'' \qquad (3.32)$$

with

$$Z' = \frac{1/R}{(1/R)^2 + (2\pi fC)^2} \qquad (3.33)$$

and

$$Z'' = \frac{2\pi fC}{(1/R)^2 + (2\pi fC)^2} \qquad (3.34)$$
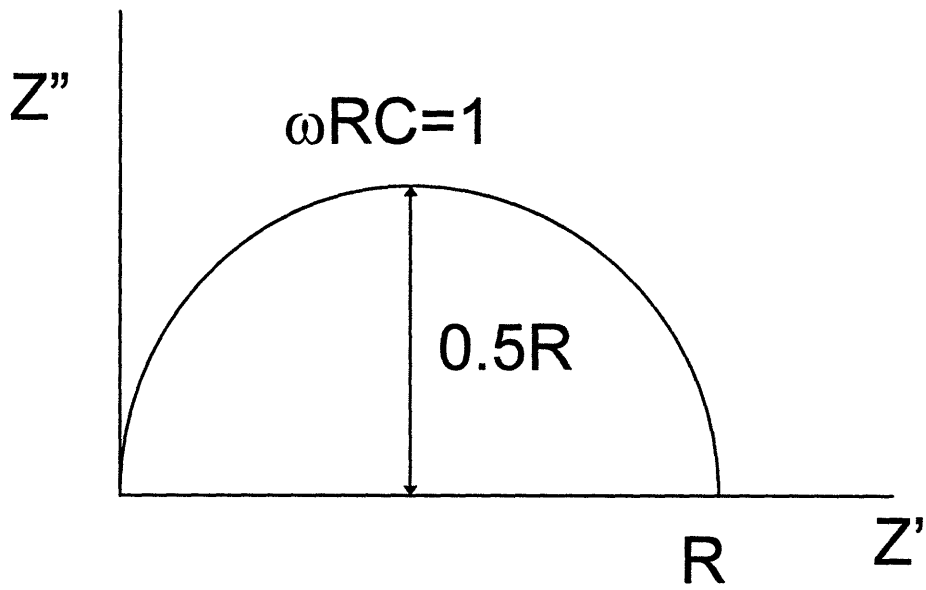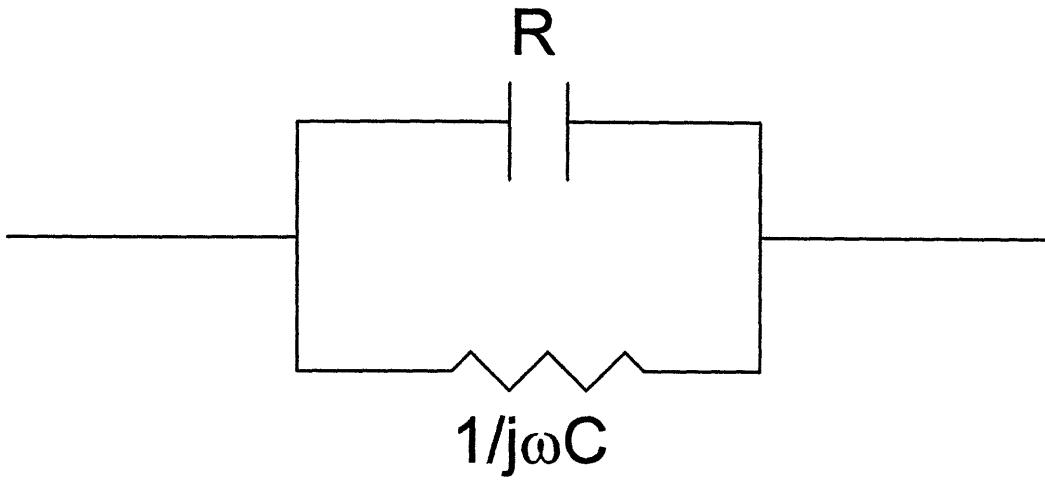
Fig. 3.2 Single R-C circuit and corresponding semi-circle in a complex impedance plane plot.

When Z'' versus Z' is plotted on a linear scale, the data takes the form of a semicircle as shown in Fig. 3.2. The semi-circle has intercepts on the Z axis at zero and R and the maximum of the semi-circle equals 0.5R and occurs at the frequency of:

$$2\pi f = 1/RC \qquad\qquad (3.35)$$

If the relaxation frequencies of the three distinctive processes are far apart, a series of semi-circles will be observed corresponding the bulk, grain boundary and electrode component as shown in Fig. 3.3.

However, not all of impedance spectra give ideal semicircles which enable the easy separation of the bulk resistivity from the grain boundary and electrode effects. Spiral shapes of can be obtained for highly conductive sample as shown in Fig. 3.4 due e.g. to lead inductance. The overlap of semicircles or sample heterogeneity related to a statistical distribution of relaxation processes [Kramer, 1994] can generate a depressed rather than the ideal semicircle. If the interpretation of impedance data is impossible, 4-probe DC measurements can assist in separating the electrode contribution from the total resistivity.

3.3 Ionic Conductivity Measurement

At low P_{O_2} where electronic conduction governs the total conductivity, it is difficult to observe the ionic conductivity. However, the absolute value of σ_i may still be high compared to that in other materials. In that case, it is important to separate the ionic conductivity from electronic conductivity to examine MIEC. One method is by the use of blocking electrodes which remove the undesired majority charge carriers such as electrons. This can be
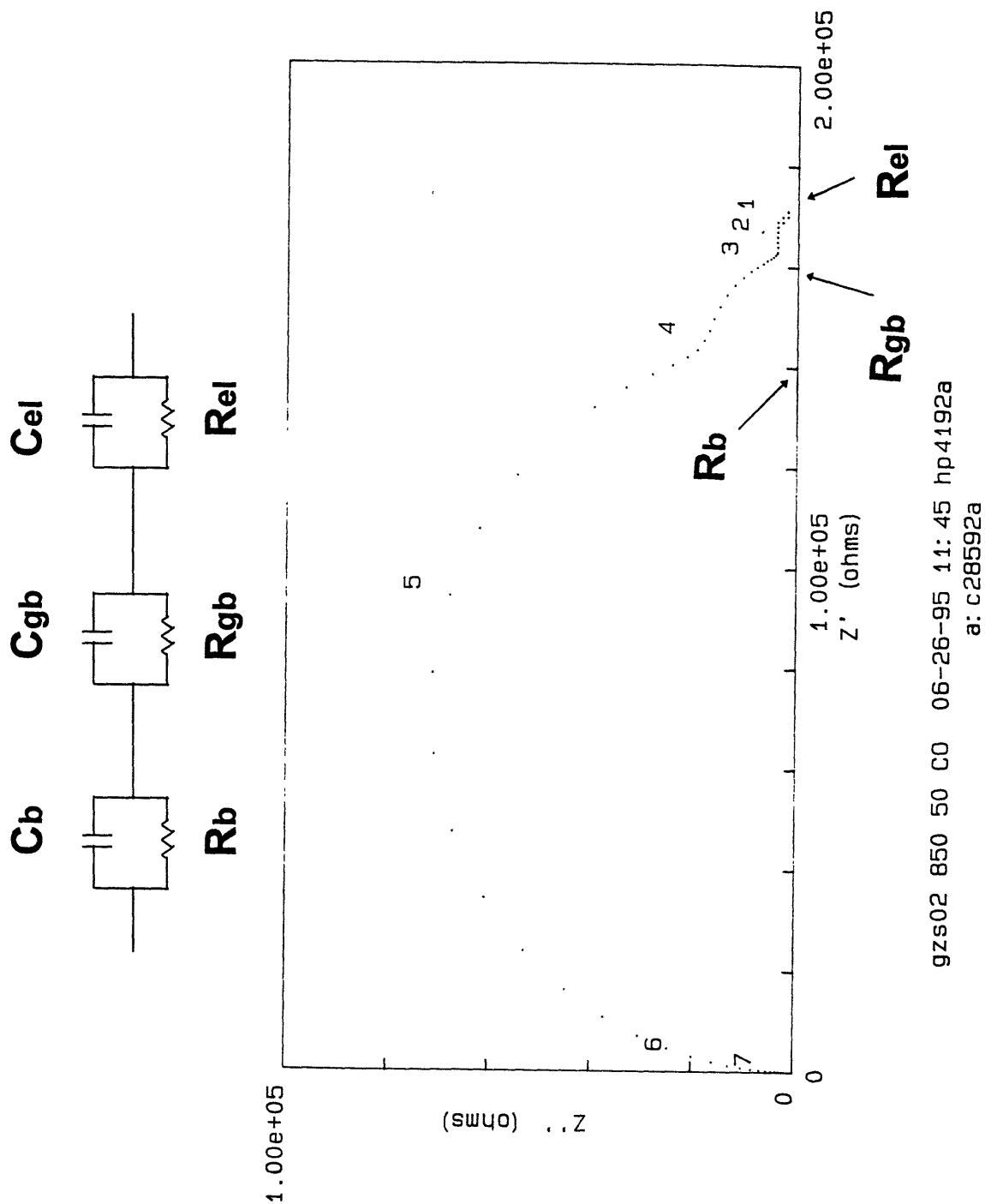
Fig. 3.3 Three R-C circuit in series corresponding the bulk, grain boundary and electrode and a complex impedance plot of $Gd_2(Zr_{0.6}Sn_{0.4})_2O_7$ at 800 °C showing the assignment of bulk, grain boundary and electrode resistance.
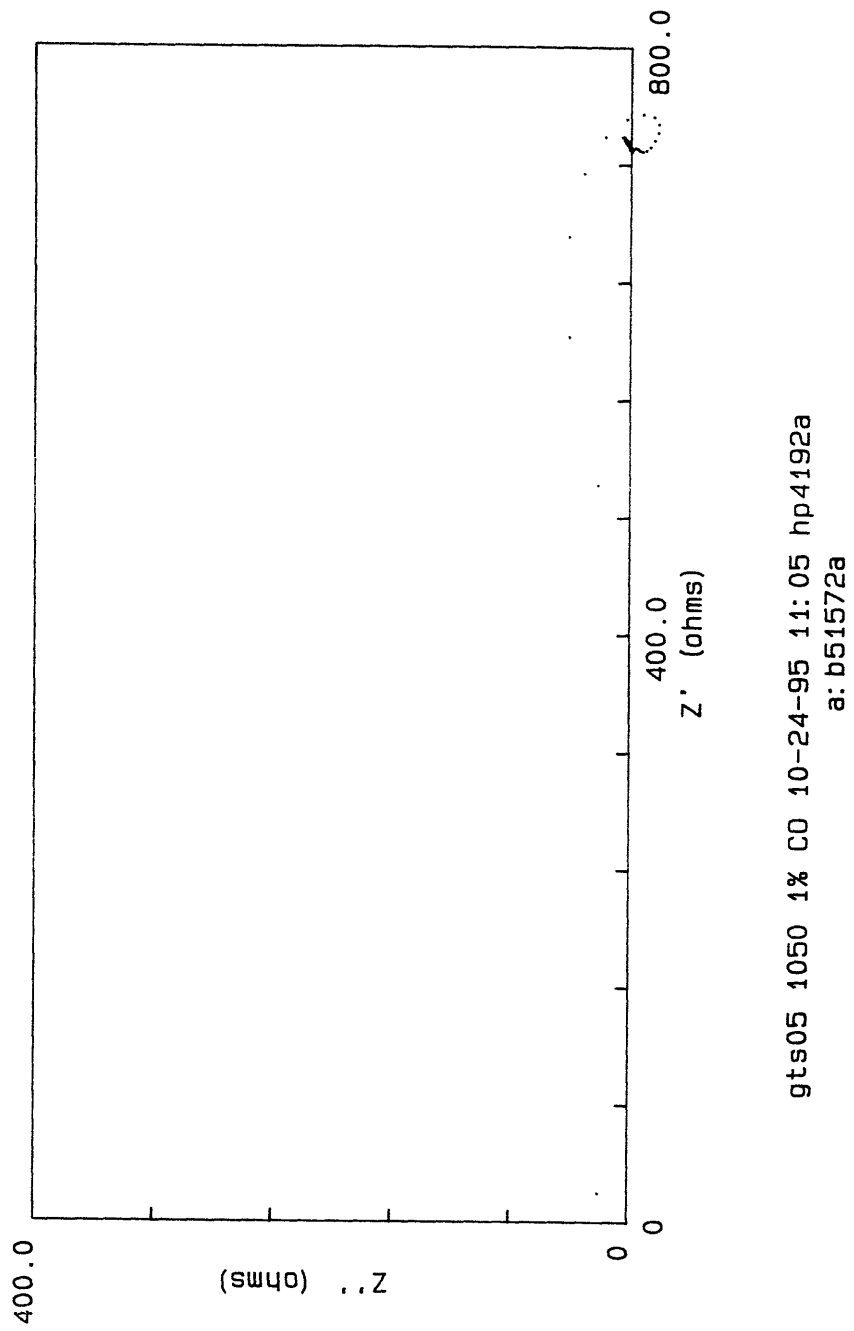
Fig. 3.4 A complex impedance plot of $Gd_2(Ti_{0.85}Sn_{0.15})_2O_7$ showing apparent inductive character.

achieved by placing a purely ionic conductor such as YSZ in series with the specimen. The situation is simplified if the ionic conductivity of the electrolyte is much higher than that of the sample under test. Then, when a current flows, the voltage drop across it can neglected. This method has some drawbacks such as leakage of oxygen and interactions between the electrodes and the sample [Riess, 1994]. If there are cracks or open pores in the electrolyte or the sample, neutral oxygen gas can diffuse through these routes and combine with electrons to become oxygen ions. When this is the case, the current in the external circuit measures the rate of diffusion of the neutral species instead of the oxygen ion current. If the free surface of the MIEC reacts with the oxygen gas, this can distort the distribution of the electrochemical potential of oxygen ion. When there is a decomposition of the MIEC near the electrode, the measured current reflects the decomposition rate rather than the ionic current.

In this research two different methods have been tried to obtain values for the ionic conductivity. The first one is an open circuit voltage measurement and the other one is a short circuit method.

3.3.1 Open Circuit Voltage Measurement

One way to distinguish the ionic current from the electronic current in an oxide is to derive the ionic transference number, t_i, from open circuit voltage measurements. This involves applying a P_{O_2} gradient across the sample while measuring the open circuit voltage which is proportional to the t_i. The derivation of the open circuit voltage as a function of t_i begins with examination of the electrochemical potential of the charge carriers [Tuller, 1981]. The electrochemical potential of the jth species is given by:

$$\eta_j = \bar{\mu}_j + Z_j q \phi \qquad (3.36)$$

which consists of the chemical potential, $\bar{\mu}_j$, and the electrostatic potential, ϕ. The current density of the jth species is given by:

$$j_j = c_j Z_j q \upsilon_j = \left(-\frac{\sigma_j}{Z_j q}\right)\left(\frac{\partial \eta_j}{\partial x}\right) \qquad (3.37)$$

where σ_j is the conductivity of jth species as explained in Eq. (3.1), $Z_j q$ the effective charge and υ_j the drift velocity. When there is no external current flow in the system, all partial currents sum to zero for the open circuit condition as described below:

$$\sum_j j_j = \sum_j \frac{\sigma_j}{Z_j q} \frac{\partial \eta_j}{\partial x} = 0 \qquad (3.38)$$

Combining with Eq. (3.2) gives:

$$\sum_j \frac{t_j}{Z_j} \frac{\partial \eta_j}{\partial x} = 0 \qquad (3.39)$$

Considering the equilibrium of the ionization of the neutral species, the electrochemical potential of neutral species can be separated into the electrochemical potential of the ionized species and that of electrons:

$$\bar{\mu}_j^* \text{ (neutral)} = \eta_j^{Z+} + Z_j \eta_e \qquad (3.40)$$

Combining this equation with Eq. (3.39) gives:

$$\frac{\partial \eta_e}{\partial x} = \sum_j \frac{t_j}{Z_j} \frac{\partial \overline{\mu}_j^*}{\partial x} \qquad (3.41)$$

The potential drop across the cell is equal to the corresponding difference in the electrochemical potential for electrons, which can be calculated by the integration between points I and II:

$$E = -\frac{1}{q} \int_{II}^{I} d\eta_e = -\frac{1}{q} \int_{II}^{I} \sum_j \frac{t_j}{Z_j} d\overline{\mu}_j^* \qquad (3.42)$$

For a binary oxide, M_xO_y, Eq. (3.42) gives the expression as follows with the aid of the Gibbs-Duhem relation:

$$E = \frac{kT}{4q} \cdot \int_{II}^{I} t_{ion} d\ln Po_2 \qquad (3.43)$$

When t_i reaches 1, i. e. pure ionic conduction, the voltage in the Eq. (3.43) becomes the Nernst voltage, V_N. By fixing $Po_2{}^I$ on one side of the oxide as a reference gas and varying $Po_2{}^{II}$ on the other side in the Eq. (3.43), one can get the t_i by differentiating Eq (3.43) with respect to the reference $Po_2{}^I$:

$$t_{ion} (Po_2^{II}) = \frac{4q}{kT} \left(\frac{\partial E}{\partial \ln Po_2} \right)_{Po_2 = Po_2^{II}} \qquad (3.44)$$

Therefore t_i can be calculated at a given $Po_2{}^{II}$ by evaluating the slope of the E-versus-$\ln Po_2{}^{II}$ curve with constant $Po_2{}^I$.

3.3.2 Short Circuit Method

The new method, proposed by Riess [Riess, 1991], enables the determination of the partial conductivity of ions and electrons without the use of blocking electrodes. This is possible by simply shorting the external circuit which eliminates the electrochemical potential gradient of electrons as shown in Fig. 3.5. However, the ionic current remains due to the oxygen partial pressure gradient which generates the driving force for ionic current flow. Riess derived an expression for the total current I_t, flowing through a MIEC:

$$I_t = \frac{\left(V_N - V\right)}{\left(R_i + R_{i,c}\right)} - \frac{V}{\left(R_e + R_{e,c}\right)} \tag{3.45}$$

where V_N is the Nernst voltage due to the P_{O_2} gradient, V is the measured voltage across the cell, R_i and R_e are the ionic and electronic resistance of the MIEC and $R_{i,c}$ and $R_{e,c}$ the respective ionic and electronic contact resistances at the electrodes. By short circuiting the cell, one eliminates V:

$$I_{sc} = \frac{V_N}{\left(R_i + R_{i,c}\right)} \tag{3.46}$$

where the short circuit current, I_{sc}, is now solely the ionic current. Under condition of negligible $R_{i,c}$:

$$R_i = \frac{V_N}{I_{sc}} \tag{3.47}$$

Therefore σ_i can be obtained even in a predominantly electronic conduction region.

71
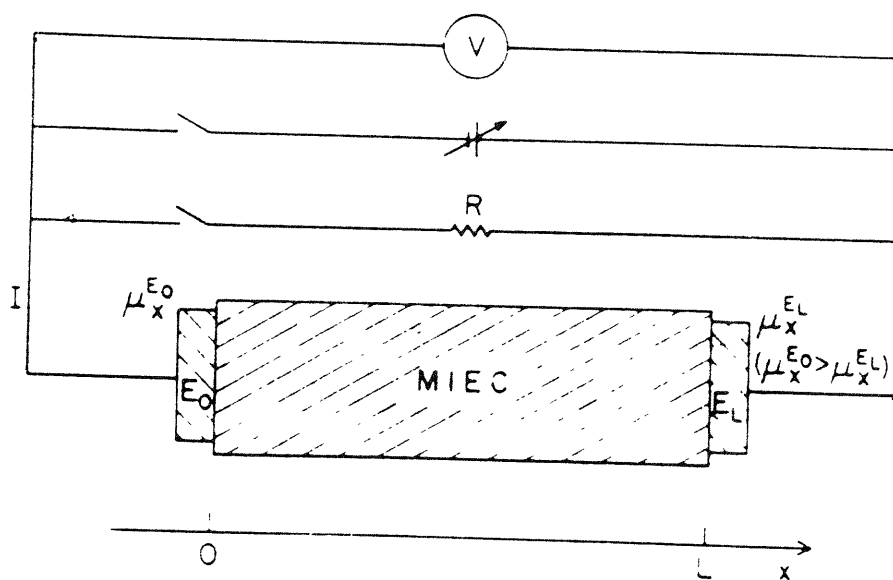
Fig. 3.5 A schematic diagram for the short circuit cell [Riess, 1991].

An equivalent circuit diagram is shown in Fig. 3.6. There are two paths for current flow, I_e for the electronic flow and I_i for the ionic flow. When the circuit is shorted, there is no driving force for electrons in I_e but the driving force for ionic flow in I_i remains due to a P_{O_2} gradient across the sample. Thus accurate measurements of P_{O_2} gradients and ionic currents allow one to obtain the ionic conductivity of the sample. Experimental details are discussed in the next chapter.
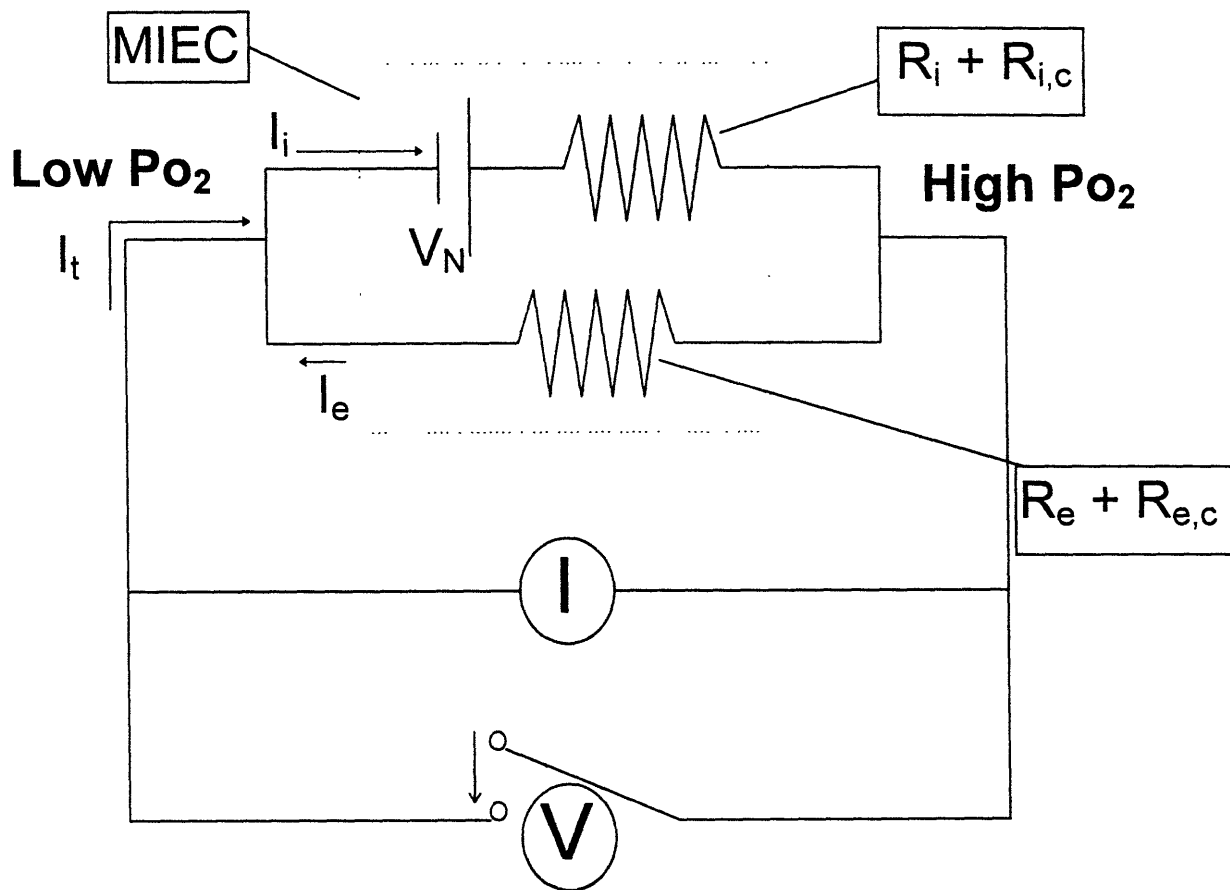
Fig. 3.6 Equivalent circuit diagram for the short circuit cell.

4 Experimental Work

4.1 Sample Preparation

4. 1. 1 Powder Preparation

Powder preparation was done by a "liquid-mix" technique developed by Pechini [Pechini, 1967]. The Pechini process allows one to produce ceramic powder with well-defined cation mole ratios and near atomic scale mixing. The traditional method of preparing ceramic powder requires the calcination of a mechanically-ground mixture of metal oxides and/or carbonates in definite proportions. The solid state reaction requires intimacy of reacting species to obtain a completely reacted and uniform product. However, this mechanical grinding does not permit homogeneous mixing of each species especially when a small amount of dopant is involved. Furthermore, prolonged calcination at high temperature to overcome inhomogeneous mixing leads to crystallite growth which is undesirable for dense and fine-grained ceramics. Contamination from abrasive materials can also be introduced during the milling and grinding stage.

The Pechini process starts with the dissolution of metal-organic compounds in a citric acid-ethylene glycol mixture. The metal -organic compound and citric acid forms polybasic acid chelates which undergo polyesterification upon heating with ethylene glycol. Each Gd, Ti, Zr and Sn citrate stock solution was made, assayed and mixed in the proper proportions to produce the desired oxide compound. Details regarding making Gd, Ti, Zr citrate can be found in other literature [Moon, 1988a; Spears, 1995]. The procedure for making Sn citrate is similar to that of Zr citrate. The preparation of Ca citrate was not successful. Therefore dry $CaCO_3$ powder

75

was added and dissolved in pre-mixed Gd and Sn citrate solutions. The mixing of two or three different citrates at ~100 °C for several hours ensures atom mixing between different cations. The next step is to heat the solution at 150-200 °C to condense the acid and alcohol groups and thus to form the polyester through dehydration. Further heating drives off water and excess ethylene glycol, which results in a hard polymeric solid. These resin intermediates contain the metal atom bonded through oxygen to organic radicals comprising the cross-linked network. The resin is charred at 400 °C to burn off the organic material followed by communition of the solid into powder. This powder is calcined at 800-900 °C to form the appropriate oxide phase. Fig. 4.1 shows flowcharts of making citrate stock solution and processing the ceramic powder. YTS powder was produced by Onnerud and Eberman in Prof. Wuensch's group.

4.1.2. Pellet Preparation

Calcined powder was formed into disk-shapes with a 0.75″ stainless steel die at 4000 psi. The pellets were carefully wrapped in plastic film wrap and isopressed at 40 Kpsi in a rubber pressing bag, followed by polishing of the sample surface with No. 600-1200 SiC paper. The samples were loaded into an alumina boat with platinum foil separating the pellet from the bottom of the boat and covered with packing powder of similar composition to prevent evaporation of Sn. The samples were then sintered at ~1570 °C with a heating rate of 15 °C/min for 16 hrs, annealed at 1200 °C for 3 hrs and cooled down to room temperature at a rate of 3 °C/min.

The density of the samples was measured by the Archimedes method. Samples sintered with a slow heating rate of 3 °C/min showed densities of ~78-85%. Faster heating rates of ~15 °C/min increased the density of the

```
                    Gd                              Ti, Zr, Sn

    ┌──────────┐  ┌──────────┐
    │ Ammonia  │  │ Acid Salt│
    └────┬─────┘  └────┬─────┘
         │             │
    ┌────▼─────────────▼──┐  ┌──────────┐      ┌──────────┐  ┌──────────┐
    │     Hydroxide       │  │Citric Acid│     │Citric Acid│  │ Alkoxide │
    └─────────┬───────────┘  └────┬──────┘     └────┬──────┘  └────┬─────┘
              │                   │                 │              │
    ┌─────────▼───────────────────▼──┐     ┌────────▼──────────────▼───┐
    │        Ethylene Glycol         │     │      Ethylene Glycol      │
    └──────────────┬─────────────────┘     └────────────┬──────────────┘
                   │                                     │
    ┌──────────────▼─────────────────┐     ┌─────────────▼─────────────┐
    │        Stock Solution          │     │       Stock Solution      │
    └────────────────────────────────┘     └───────────────────────────┘
```

Ternary
(GTS, etc)

```
┌──────────────────────┐   ┌──────────────────────┐   ┌──────────────────────┐
│ Cation Stock Solution│   │ Cation Stock Solution│   │ Cation Stock Solution│
└───────────┬──────────┘   └──────────┬───────────┘   └──────────┬───────────┘
            └─────────────────┐       │       ┌──────────────────┘
                              ▼       ▼       ▼
                          ┌───────────────────┐
                          │    Stir to mix    │
                          └─────────┬─────────┘
                                    ▼
                          ┌───────────────────┐
                          │     Polymerize    │
                          └─────────┬─────────┘
                                    ▼
                          ┌───────────────────┐
                          │       Char        │
                          └─────────┬─────────┘
                                    ▼
                          ┌───────────────────┐
                          │       Crush       │
                          └─────────┬─────────┘
                                    ▼
                          ┌───────────────────┐
                          │      Calcine      │
                          └─────────┬─────────┘
                                    ▼
                        ┌───────────────────────┐
                        │ Press, Sinter, Anneal │
                        └───────────────────────┘
```
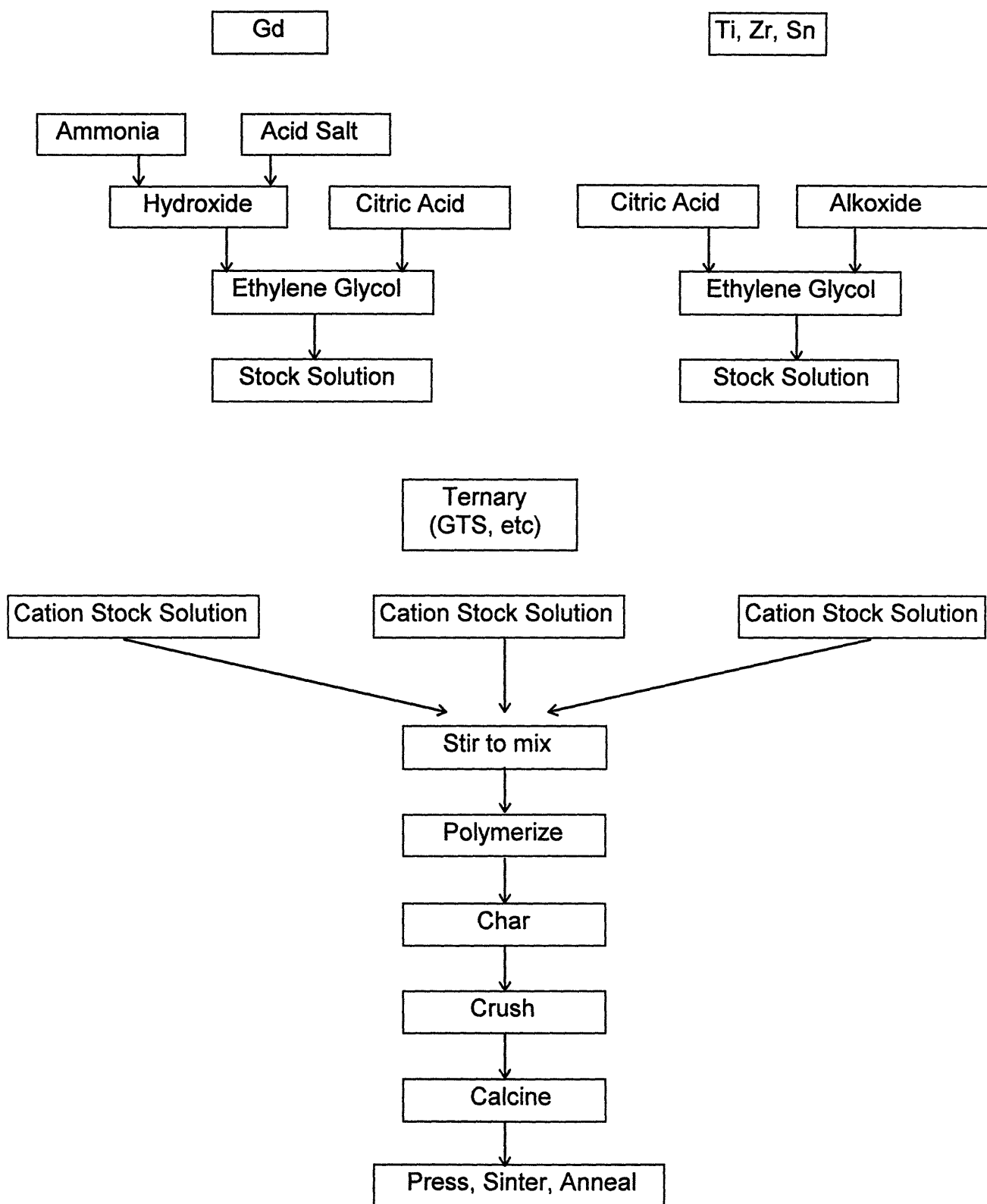
Fig. 4.1 Flowchart of sample preparation process.

samples up to ~93-95%. This can be explained by various diffusion mechanism depending on the different temperature regime [Kingery, 1976]. At relatively low temperature, a surface diffusion and/or evaporation - condensation process occurs, which does not lead to the densification of the sample. But as the temperature increases up to the sintering stage, the sample undergoes the densification process by a lattice diffusion process. Therefore, by increasing the heating rate in the sintering process, one can increase the density of the sample by minimizing the time spent in the non-densification process at low temperatures.

4.2. Microstructure and Compositional Analysis

X-ray diffraction measurements were performed using a Rigaku RU-300 diffractometer to examine the phases composing the samples. Typical operating parameters were λ=CuKα, a graphite diffracted beam monochromator, X-ray tube voltage of 50kV, tube current of 200 mA, scan rate of 2° 2θ/min and a scan range of 20° to 100°. The Rietvelt refinement was performed on GTS by Prof. Wuensch's group at M. I. T. [Onnerud, 1996].

Figs. 4.2 and 4.3 shows SEM micrograph of fractured samples of YTS and GZS. The figures show that there are isolated pores in the samples but that the overall apparent density of the samples is more than 90%. The grain size of the YTS sample is roughly 3μm with no evidence of a second phase. Generally we were able to obtain highly dense samples by increasing the heating rate as mentioned above.

Microprobe analysis was performed on samples of GZS and GTS to examine the impurity levels of the samples and stoichiometry of each of the cations in the samples. No major impurities above 50 ppm were found in
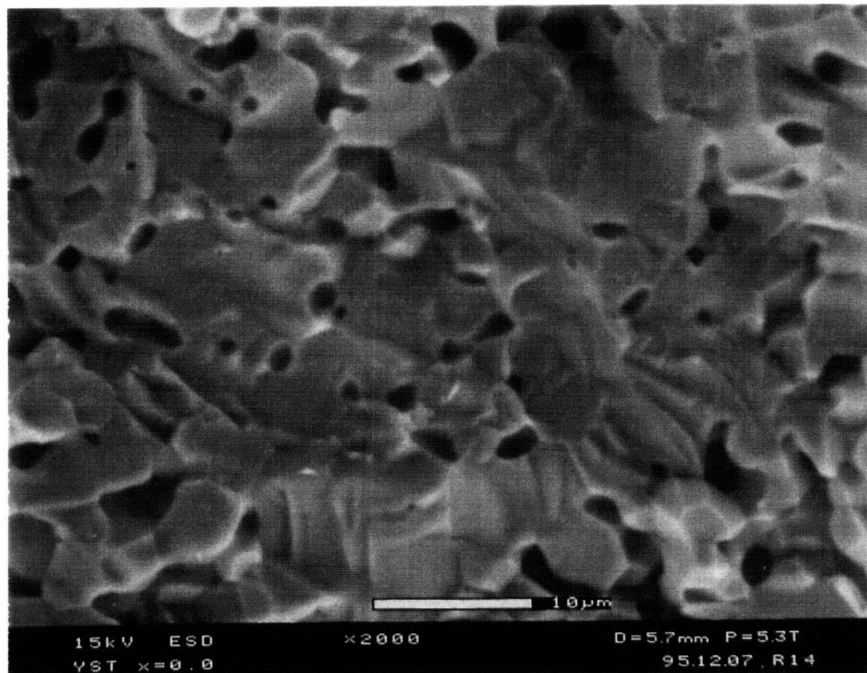
Fig. 4.2 Environmental scanning electron micrographs of fractured sample of
Y$_2$Ti$_2$O$_7$ [Performed by P. Onnerud, at M. I. T. 1996].

15kV   ESD   x6300   D=7.9mm P=5.1T
Welds in the Base Metal (MIT)   96.04.19 R10

2 µm
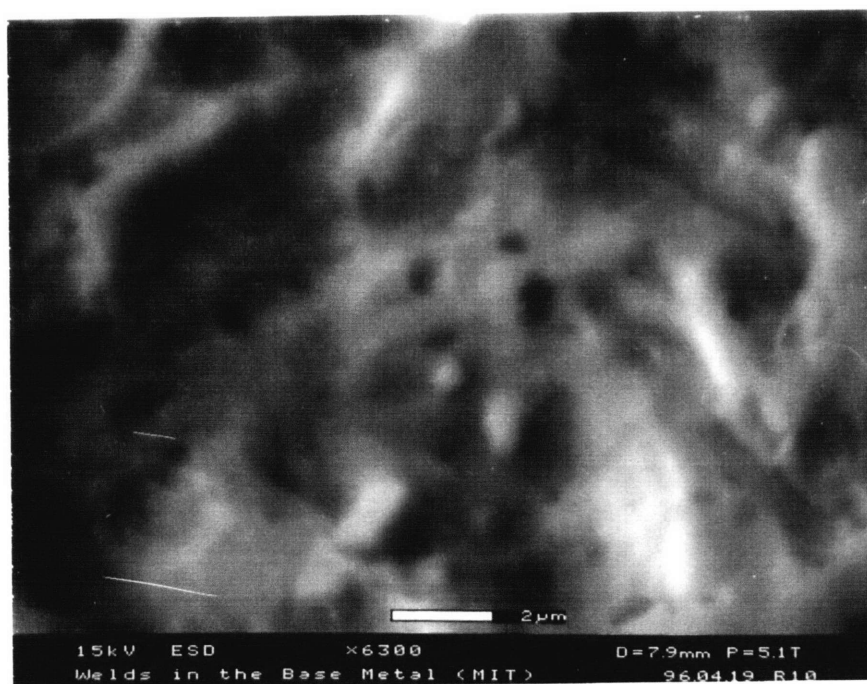
Fig. 4.3 Environmental scanning electron micrographs of fractured sample of
$Gd_2(Zr_{0.6}Sn_{0.4})_2O_7$ [Performed by P. Onnerud, at M. I. T. 1996].

those samples. Table 4.1 summarizes the compositional analysis for these samples. It appears that the Ca concentration in the A site of GTS is ~7% consistent with the solubility limit of Ca reported by Kramer et al. for GT [Kramer, 1994]. The difference in calculated and measured value in Ti and Sn in $(Gd_{0.9}Ca_{0.1})_2(Ti_{0.8}Sn_{0.2})_2O_7$ might be attributed to the overlap of Ti and Sn peaks in microprobe analysis.

Composition	Atomic % in cations (calculated)	Atomic % in cations (measured)
$Gd_2(Zr_{0.6}Sn_{0.4})_2O_7$	Gd 50.00 Zr 30.00 Sn 20.00	Gd 49.42 Zr 29.95 Sn 20.63
$(Gd_{0.9}Ca_{0.1})_2(Ti_{0.8}Sn_{0.2})_2O_7$	Gd 45.00 Ca 5.00 Ti 40.00 Sn 10.00	Gd 47.49 Ca 3.22 (6.35% on A site) Ti 37.94 Sn 11.35

Table 4.1 Microprobe analysis on $Gd_2(Zr_{0.6}Sn_{0.4})_2O_7$ and $(Gd_{0.9}Ca_{0.1})_2(Ti_{0.8}Sn_{0.2})_2O_7$.

4.3. Electrical Conductivity Measurements

The vast majority of the electrical conductivity measurements were made on bar-shaped samples with the 4 probe configuration. After sintering, the pellets were cut into bar-shapes with shallow grooves cut on the surface of each sample with a diamond saw. The typical dimensions of the samples after cutting were 2 mm by 2mm by 8mm. Platinum paste (Engelhard 6082) was applied in the grooves after sputtering of platinum onto the grooves. Platinum wire (0.001" in diameter) was then tightly wrapped around the grooves in the sample. Platinum paste was painted again onto the platinum wires and the grooves to ensure contact between the sample and wires. The sample was then sintered at ~850 °C for 3~4 hrs for a cure of platinum paste which contains bismuth as a fluxing agent.

The sample holder, consisting of 3 parallel alumina 4-bore tubes, accommodated the bar shaped samples. Platinum wires were passed through the bores in the alumina tubes and were then spot welded to the wires around the samples. One of the alumina tubes was used to accommodate the thermocouple consisting of pure platinum and 10% Rh/Pt wire (S type) to measure the temperature of the cell. The description of the sample holder is represented in Fig. 4.4.

The 2 and 4 probe DC conductivity measurements were performed on these bar shaped samples with an HP4140b picoammeter and Keithley 188 nanovoltmeter. The 2 probe AC impedance spectroscopy measurements, as discussed in the Section 3.2, were also performed in the same cell using an HP 4192a impedance analyzer. The temperature range examined was from 750 °C-1050 °C with 50 °C increments and the P_{O_2} ranged from $1\text{-}10^{-20}$ atm. For P_{O_2} control, pre-mixed O_2/Ar and CO/CO_2 mixtures were used for the high

6-bore Al_2O_3 tube

Cajon fitting

O-Ring

Copper tube

Bronze flange

Gasket

Al_2O_3 tube

Pt wires

Sample

6-bore Al_2O_3 tube

Type S thermocouple
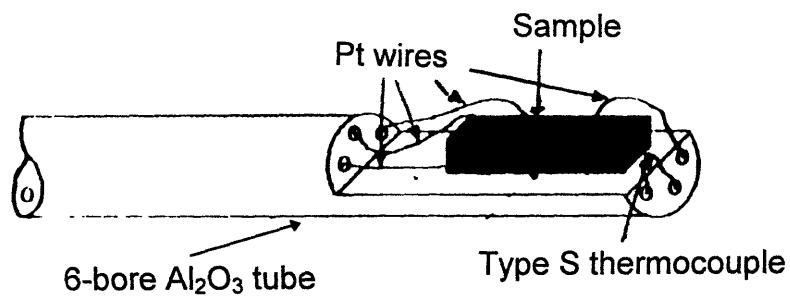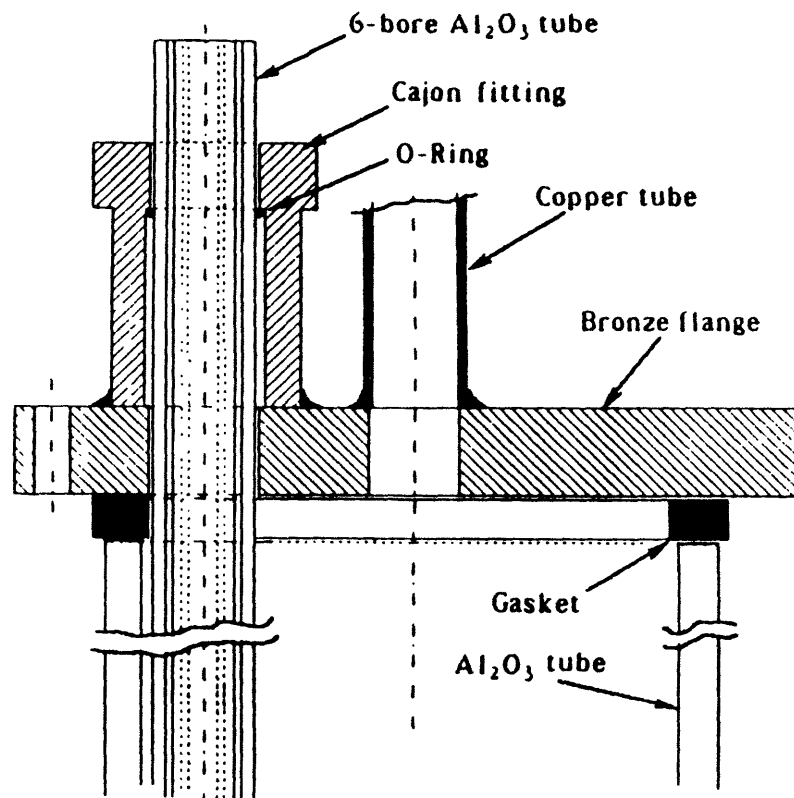
Fig. 4.4 Sample holder configuration for 4-probe DC and 2-probe AC conductivity with multiple samples [Tsai, 1991].

Po_2 and low Po_2 ranges respectively and a stabilized ZrO_2 cell was used to monitor the fugacity of Po_2.

4.4. Short Circuit Cell

As mentioned in chapter III, the short circuit method can separate ionic from electronic conductivity in a mixed ionic-electronic conduction region. Several experimental factors should be considered before determining σ_i . First, if the resistance of the ammeter, R, for measuring the total current I is large, V is not identically zero and the electronic current does not vanish. Care must be taken so that the resistance R of the ammeter should be much smaller than both $R_i + R_{ic}$ and $R_{el} + R_{e,c}$. R values between 10-500 ohms were found to be suitable for GZT. Second, adequate sealing of the sample chamber for the desired Po_2 gradient is critical. Eqs. (3.45) and (3.46) assume that a well defined chemical potential or equilibrium partial pressure of oxygen exists at each electrode-sample interface. Riess et al. [Riess, 1992] found some gas leakage in their cell and thus cold not define an exact value of V_N, in their calculations, which leads to errors in the determination of σ_i. More than 90% theoretical density in the samples is required to remove open pore channels that can be the source of leakage. Finally if the contact resistance, $R_{i,c}$, becomes significant, one should use 4-probe measurements to account for potential drops at the electrodes [Riess, 1991].

Fig. 4.5 shows the experimental set-up for short circuit measurements. Open circuit voltage measurements were also performed in this cell. The cell is made of two quartz tubes of different thickness. 10 mm thick quartz tube was welded with 3mm thick quartz tubes on both sides. The pellet was spring-loaded against a thick quartz tube in the center with support of an
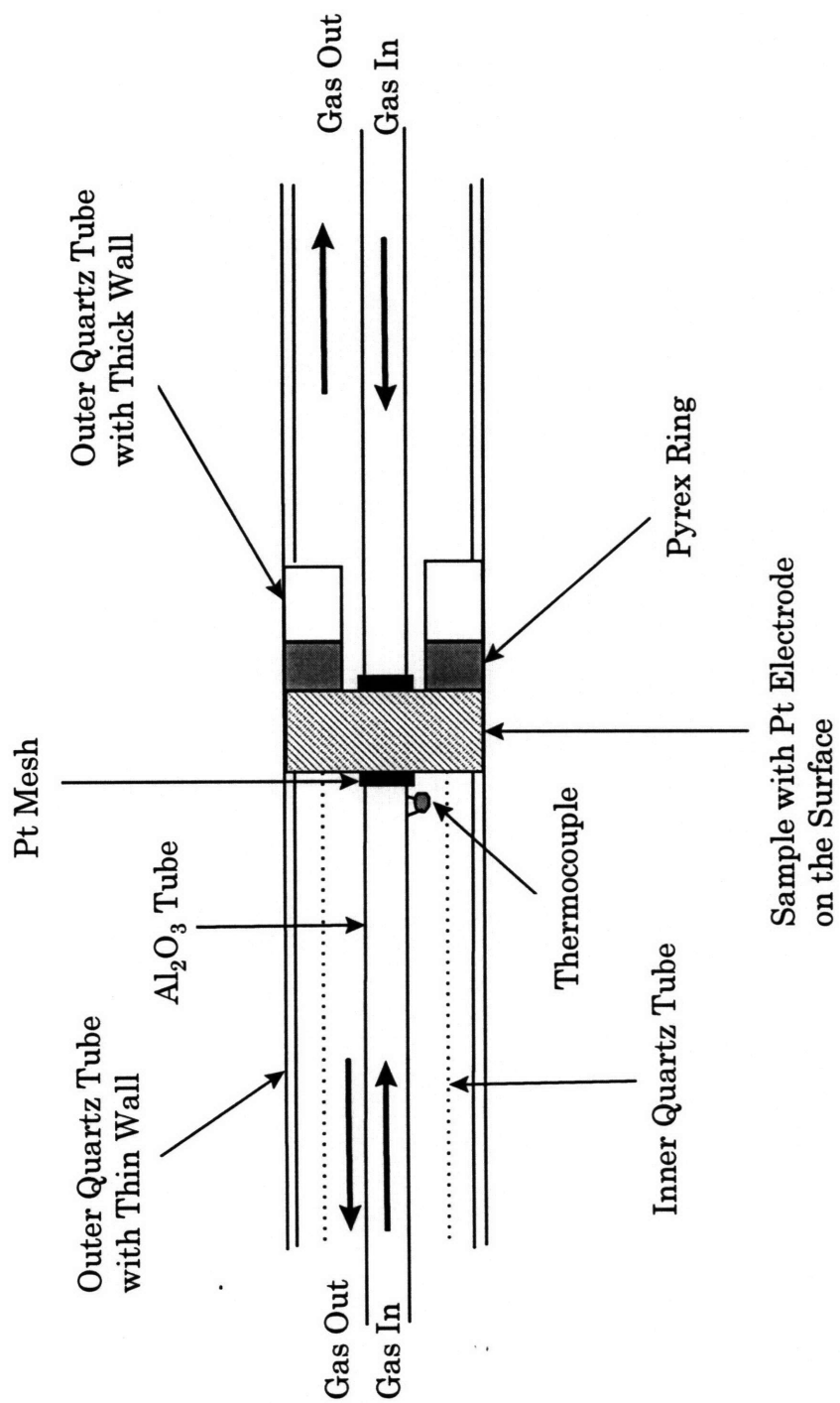
Fig. 4.5 The short circuit cell diagram.

85

inner quartz tube and two different P_{O_2} gases were passed over each face of the pellet to generate a P_{O_2} gradient cross the sample. A pyrex ring gasket was placed next to the pellet, which softened at high temperatures and thus prevented gas leakage across the sample. After sintering, the pellet was polished with No. 1000 SiC paper and 1mm of diamond paste to make a flat surface and thus achieve better sealing between the surface of the sample and the pyrex ring gasket. The pellet was painted with platinum paste followed by curing of the paste at high temperature. Since the platinum electrode is subject to scratching when contacted with a platinum lead wire or mesh, painting and curing processes were repeated 2~3 times to ensure the mechanical strength of the electrode. Platinum mesh welded to platinum wires were pressed onto each side of the pellet through a 4-bore alumina tube which contained the S-type thermocouples near the platinum mesh to monitor the temperature.

5 Results

The results section begins with X-ray diffraction data obtained for GS and GTS and follows the electrical conductivity data for undoped GS, Ca doped GS and the solid solution of GTS, GZS and YTS systems. The last section contains the results on short circuit and open circuit cell measurements on the GTS system.

5.1 X ray diffraction

Fig. 5.1 shows the X-ray diffraction pattern for undoped GS after sintering at 1570 °C. All observed peaks were identified as pyrochlore peaks without any evidence of a second phase. There are superstructure peaks with relatively small intensities which distinguish the pyrochlore phase from the fluorite phase. The powder of the same composition calcined at 850 °C, before sintering, was also examined with X-ray diffraction as shown in Fig. 5.2. Compared with Fig. 5.1, it is clear that those superstructure peaks shown in the sintered pellet decrease or disappear in the calcined powder indicating that the calcination alone does not achieve the equilibrium pyrochlore phase.

Sintered GS and GTS samples were annealed in reducing condition and quenched. The X-ray diffraction pattern for GS after annealed at 900 °C, 10^{-14} atm of P_{O_2} is shown in Fig. 5.3. The figure shows that the pyrochlore phase has completely decomposed into other phases. The major phase appears to be Gd_2SnO_5 which is not listed in the JCPDS files. Instead, Gd_2SiO_5 peak data was used to identify this phase. Other second phases include Gd_2O_3 and SnO. Fig. 5.4 and 5.5 shows GTS with x=0.2 and 0.15 after annealing and quenching at 1000 °C, 10^{-14} atm of P_{O_2}. The samples contain Gd_2TiO_5 and Gd_2O_3 as second phases while maintaining pyrochlore
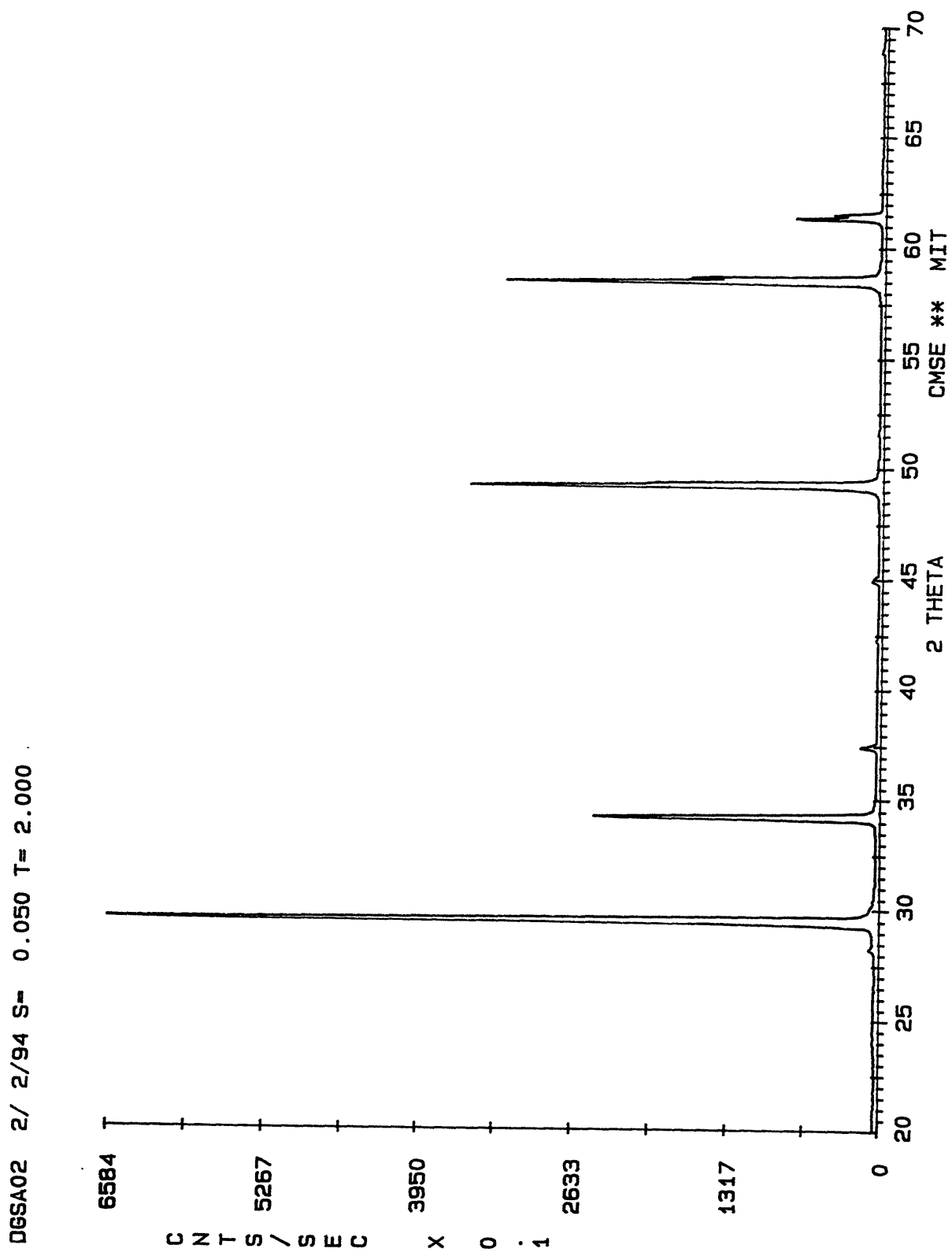
Fig. 5.1 X-ray diffraction pattern for $Gd_2Sn_2O_7$ for sintered at 1570 °C.
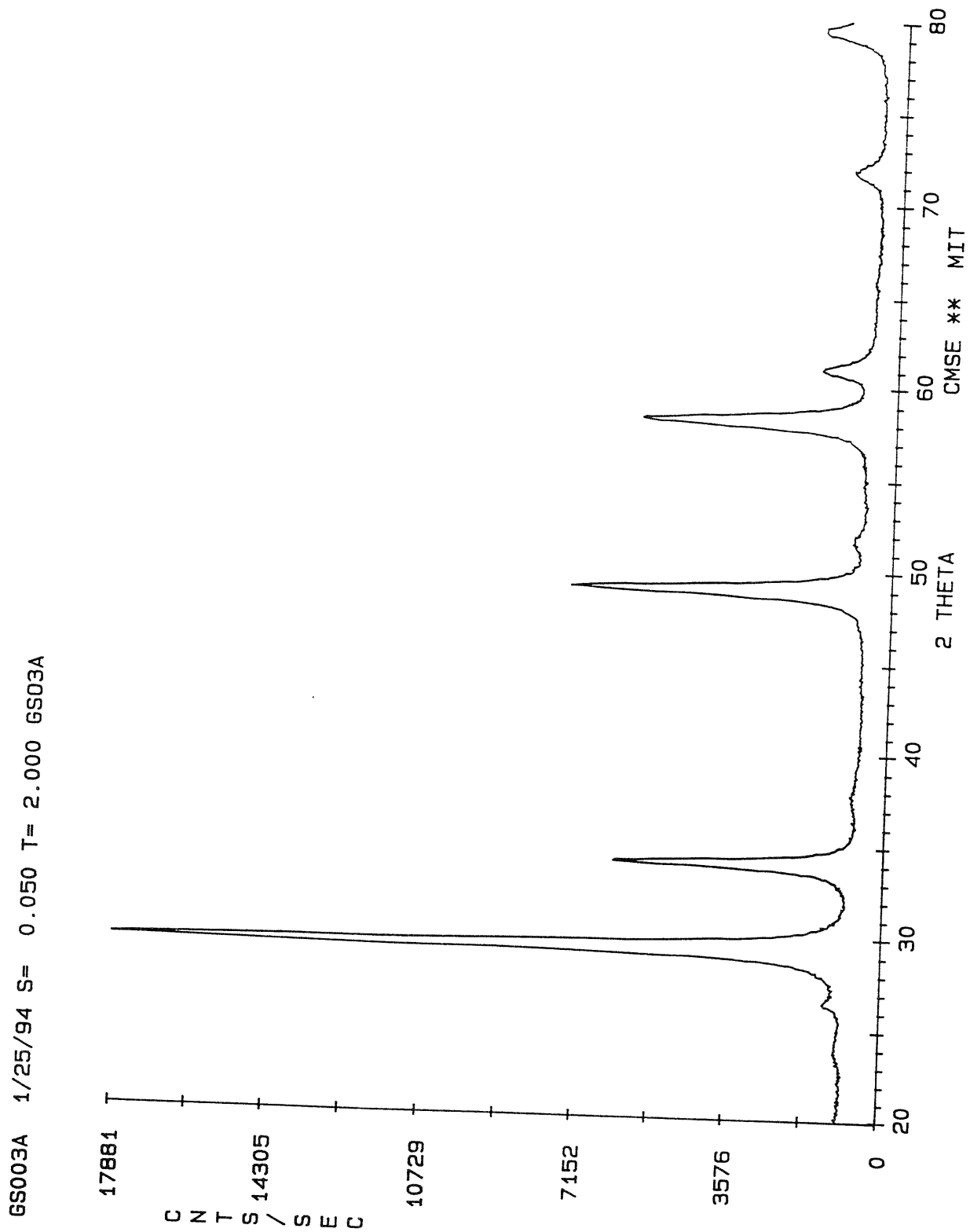
Fig. 5.2 X-ray diffraction pattern for $Gd_2Sn_2O_7$ for calcined at 850 °C.
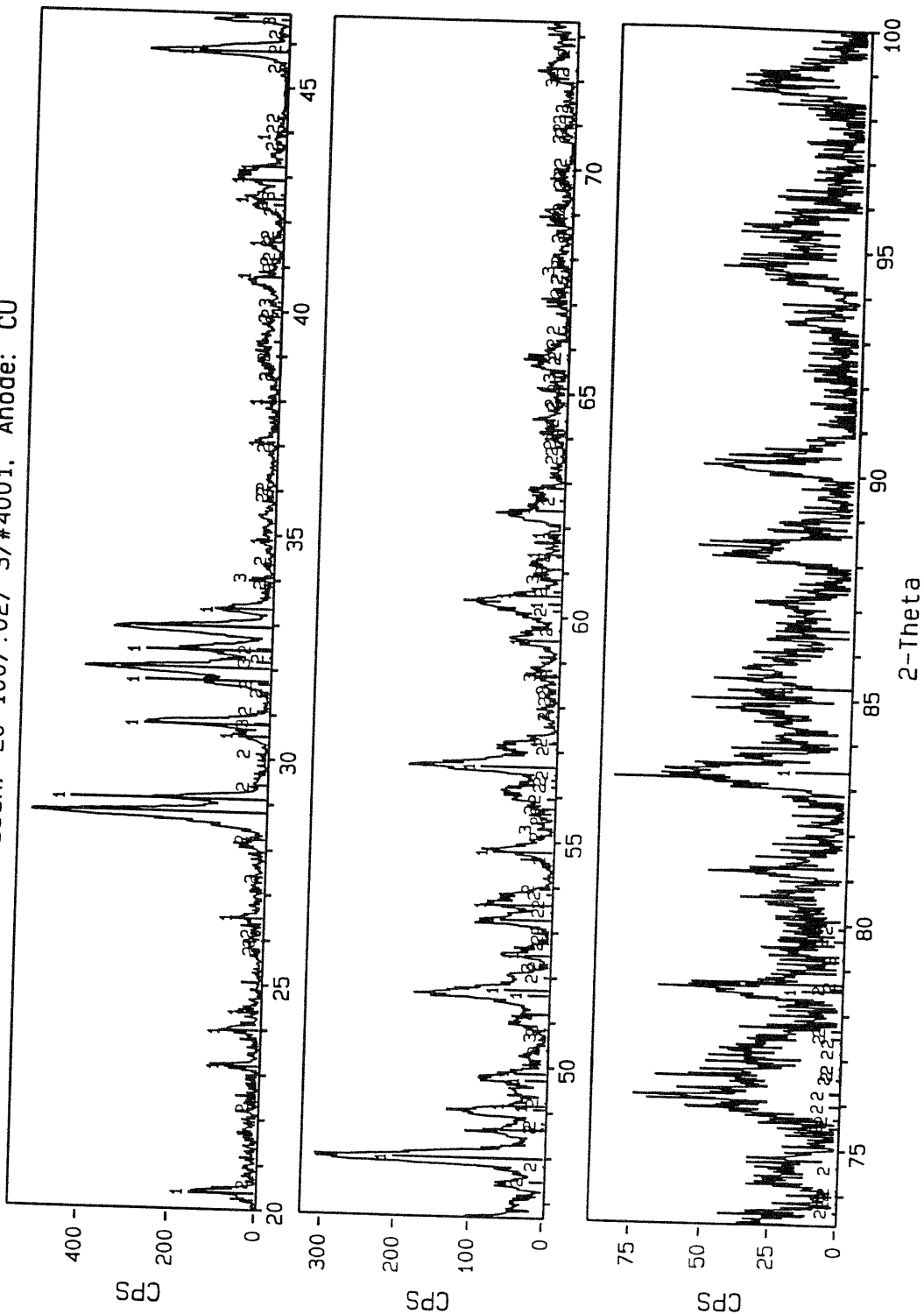
Fig. 5.3 X-ray diffraction pattern for Gd₂Sn₂O₇ for reduced and quenched at 900 °C.
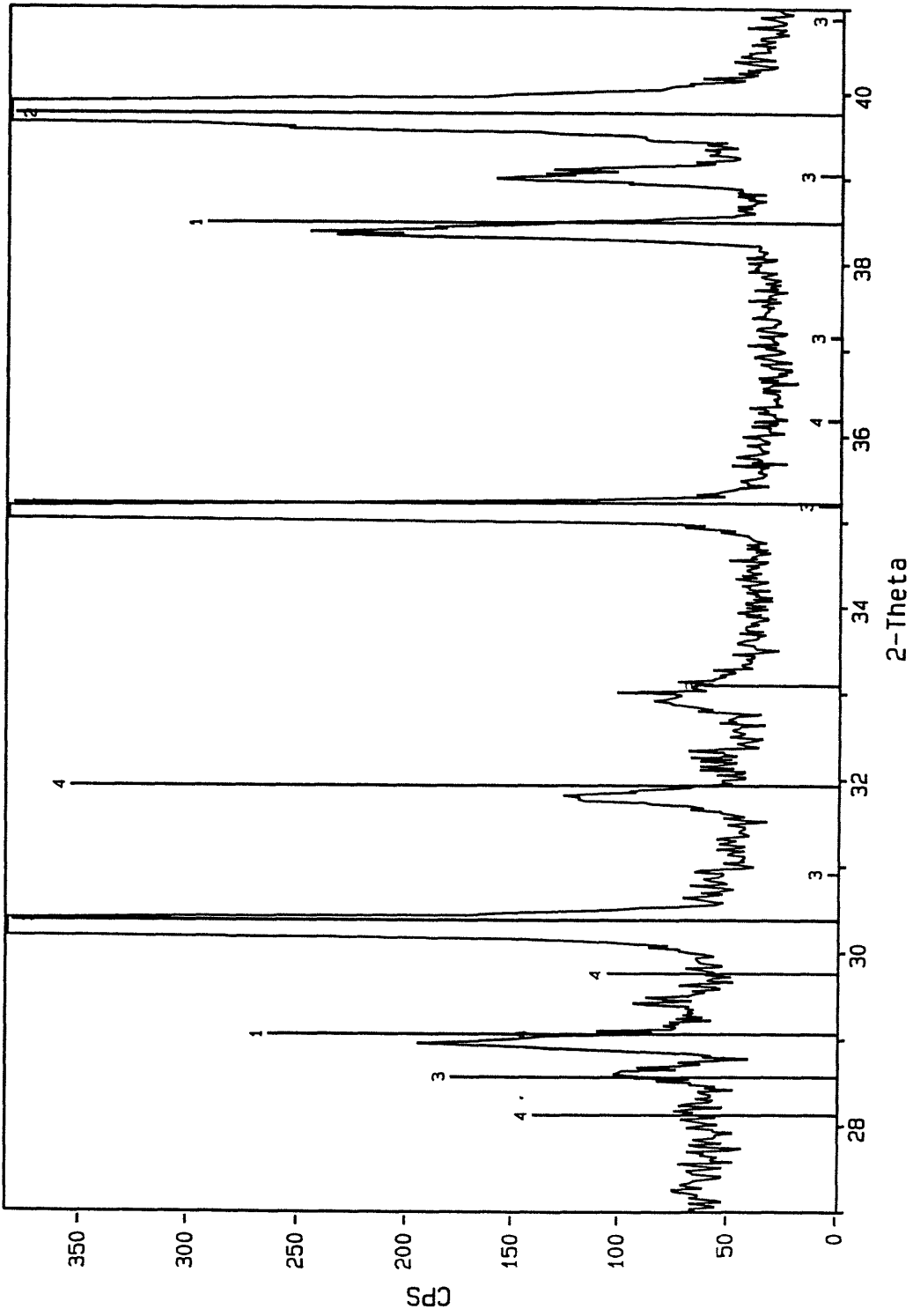
Fig. 5.4 X-ray diffraction pattern for $Gd_2(Ti_{0.8}Sn_{0.2})_2O_7$ for reduced and
quenched at 1000 °C. Pt phase represents electrodes for
conductivity measurements.
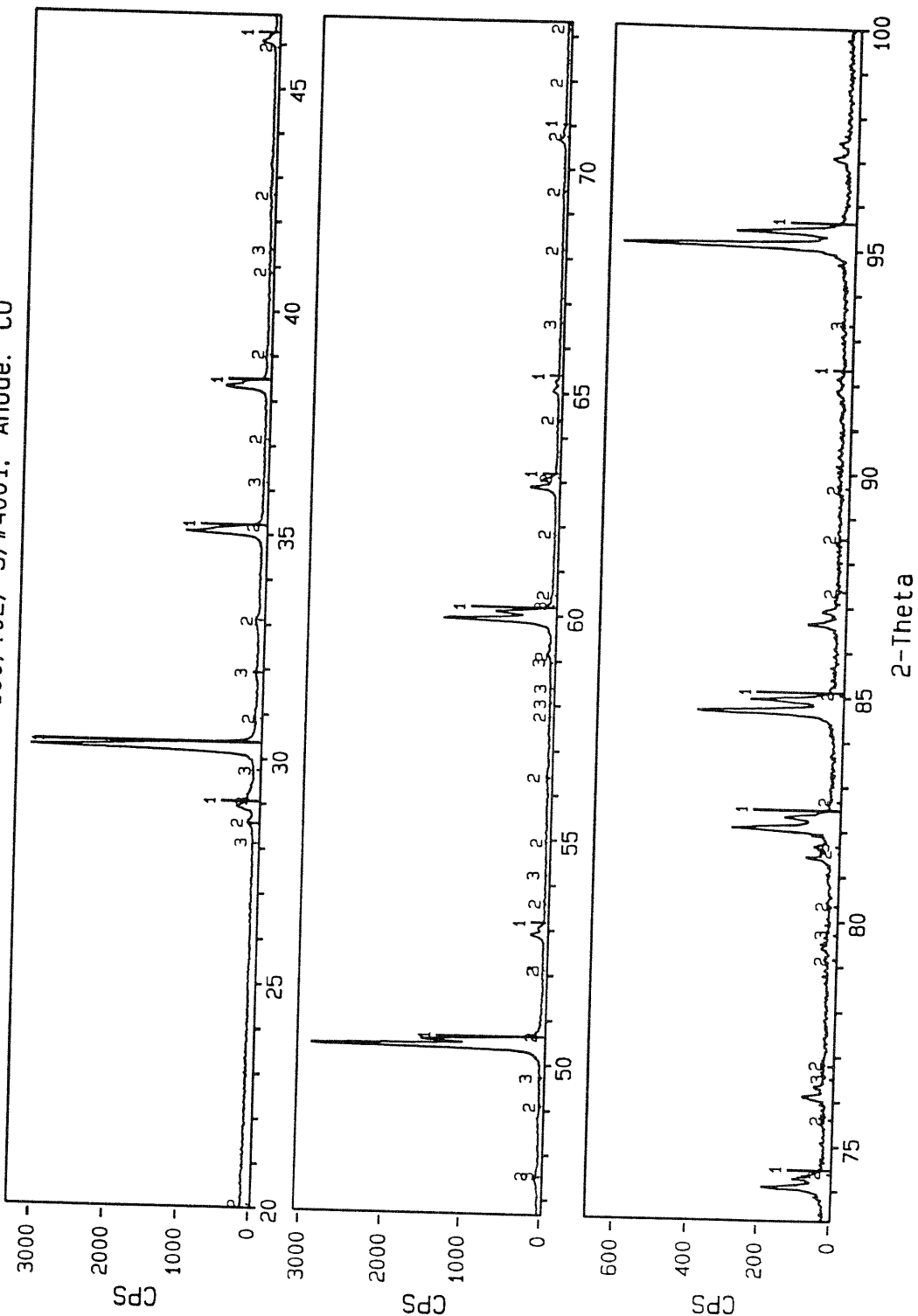
Fig. 5.5 X-ray diffraction pattern for $Gd_2(Ti_{0.85}Sn_{0.15})_2O_7$ for reduced and quenched at 1000 °C.

as a major phase. However when this sample was annealed and quenched at a higher temperature of 1400 °C, 10^{-14} atm of P_{O_2}, the Gd_2SnO_5 phase forms as well as shown in Fig. 5.6. From these quenching experiments, it is clear that single phase pyrochlore is not maintained for pure GS and GTS samples under reducing atmosphere but rather than the monoclinic phases of Gd_2SnO_5 and Gd_2TiO_5 form as second phases, which becomes more apparent at elevated temperature.

X-ray diffraction patterns on GTS (x=0.8, 0.6, 0.4, 0.2) were refined by Onnerud et al. [Onnerud, 1996]. The lattice constant, anion and cation site occupancy factors and thermal parameters for each ion were calculated. The lattice constant is shown plotted in Fig. 5.7 as a function of Sn fraction. It shows a linear dependence on composition indicating the formation of a complete solid solution. Oxygen ions (48f and 8a) were found to occupy essentially 100% of their own sites. However, since the oxygen ion has a much lower scattering power for X-rays relative to that of cations, pyrochlore peaks related to oxygen ions in the diffraction patterns (~45 °, 57° etc. in Fig. 5.1) were not significant, resulting in standard deviations for anion occupancy of ~1-3% depending on composition. A site cation occupancy for Gd was calculated from the scattering factor of the A site and plotted in Fig. 5.8. Since there are three cations for two different sites, it is impossible to determine the distribution of each of the three cations over the A and B sites from a single set of diffraction data. Thus the occupancy of Gd in the A site in Fig. 5.8 is based on an assumption that equal amounts of Ti and Sn proportional to their stoichiometric ratio move to the A site. It is more likely that the larger Sn relative to Ti would move more readily to the A site. In that case, Gd occupancy would decrease more rapidly than in Fig. 5.8, since the larger scattering factor of Sn relative to Ti requires more Gd to move to the B site for a measured scattering factor in A site. Nevertheless, the figure shows the trend of increasing cation disorder with increasing Sn content
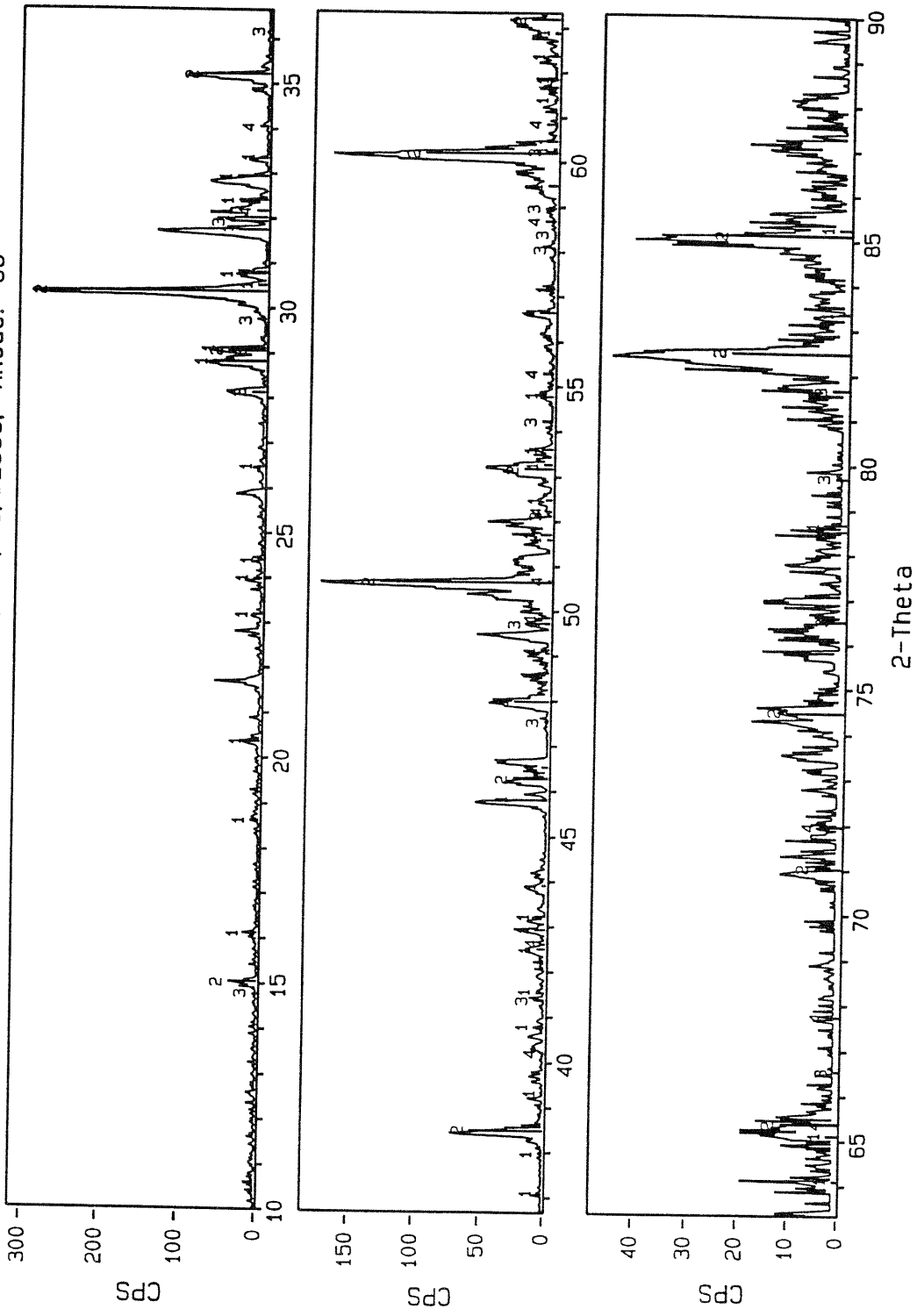
Fig. 5.6 X-ray diffraction pattern for $Gd_2(Ti_{0.8}Sn_{0.2})_2O_7$ for reduced and quenched at 1400 °C.
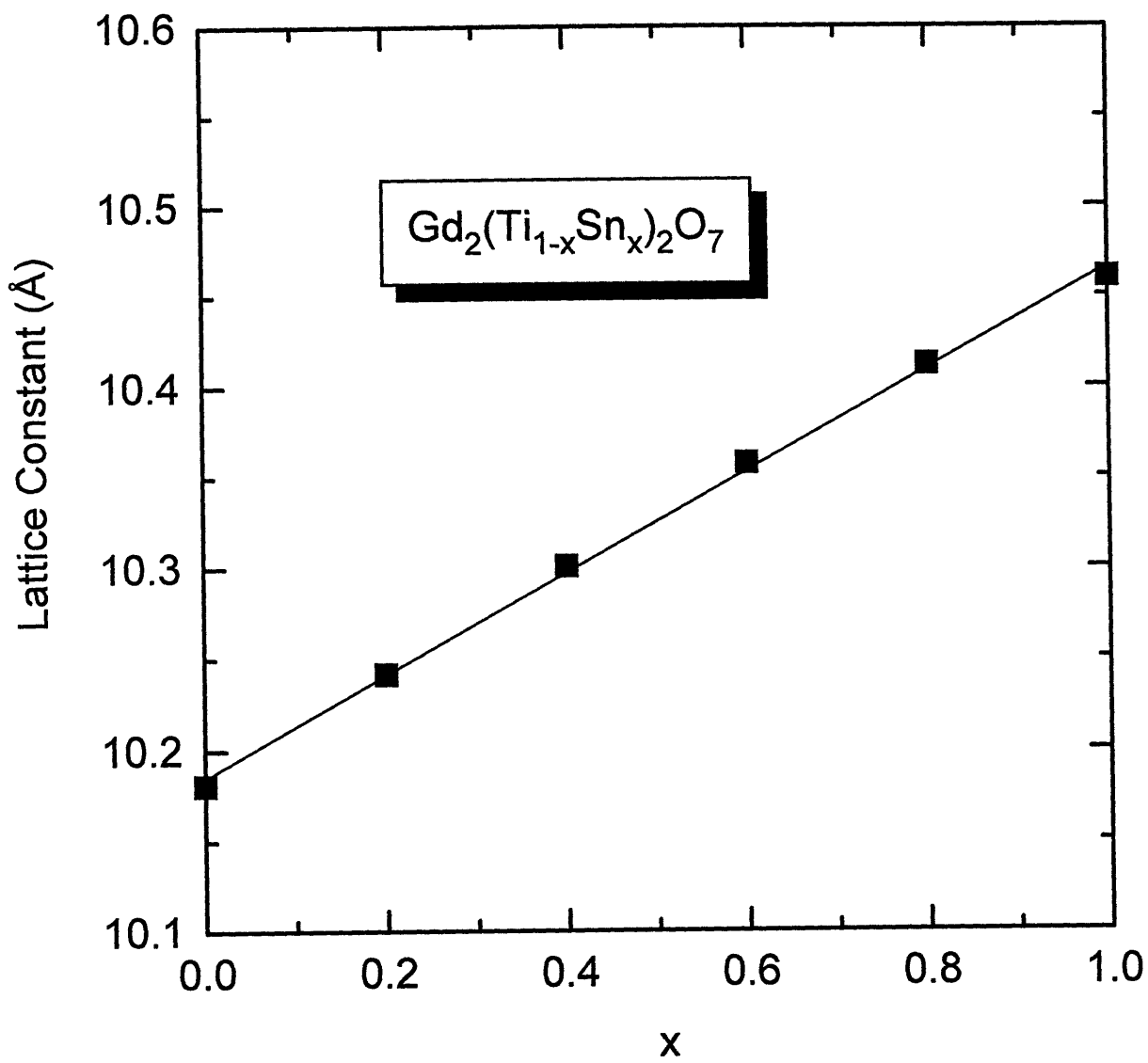
Fig. 5.7 The lattice parameter as a function of composition for
Gd$_2$(Ti$_{1-x}$Sn$_x$)$_2$O$_7$ [Onnerud, 1996].
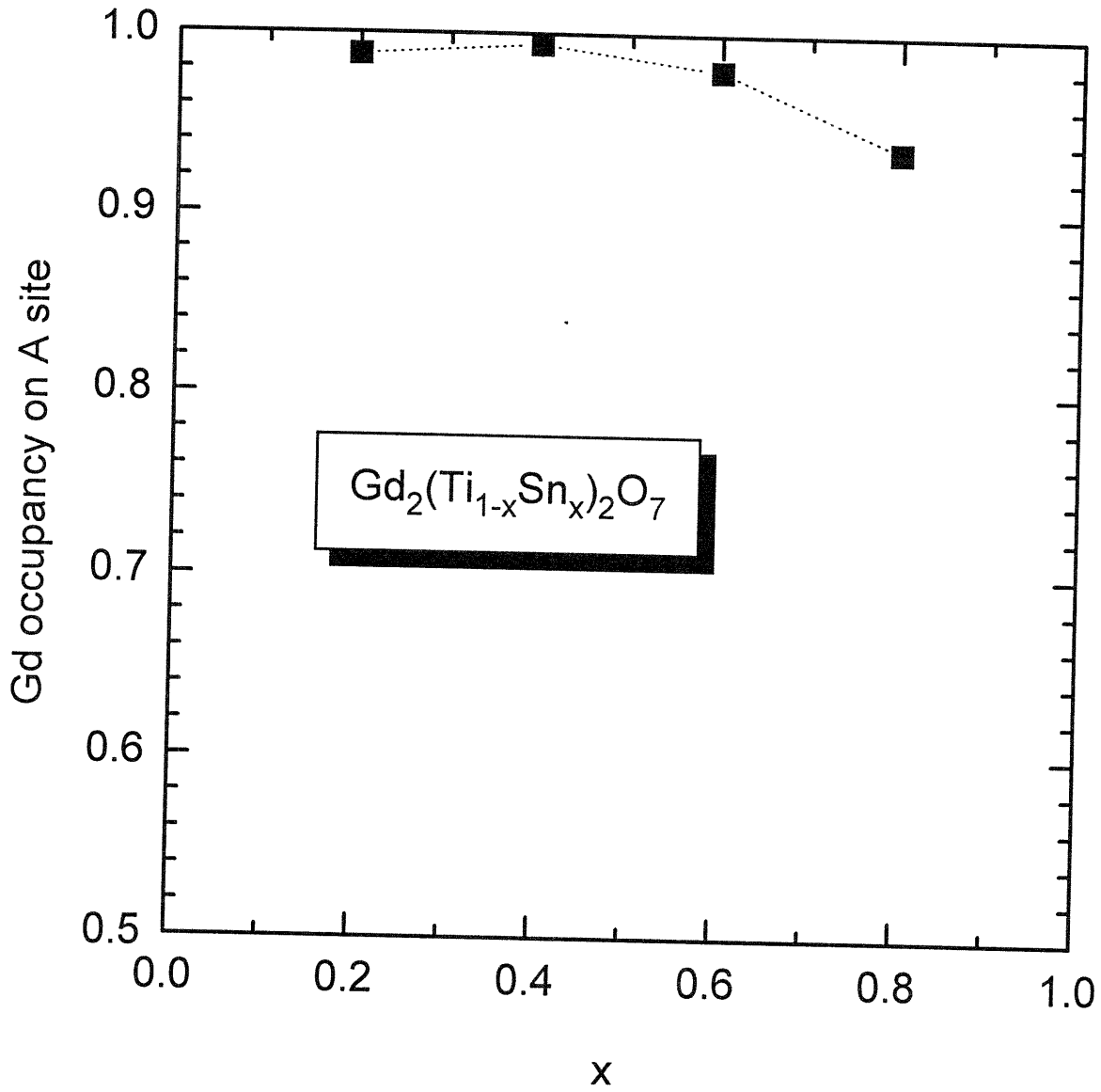
Fig. 5.8 Gd occupancy on A site in $Gd_2(Ti_{1-x}Sn_x)_2O_7$ [Onnerud, 1996].

except for x=0.4 in GTS. A similar trend of decreasing cation order parameter with increasing Zr content was reported in GZT as shown in Fig. 2.8. Standard deviations for cation occupancies was ~0.5% which is lower that those for anion occupancy. We assume that the cation disorder determined by X-ray is in quasi-equilibrium with the sintering temperature, ~1600 °C. It is unlikely that significant cation exchange occurs at lower than the sintering temperature due to low cation mobility in pyrochlores. In a closely related fluorite system of calcia-stabilized zirconia, for example, cation diffusion coefficient was found to be lower than that in anion by 10^6 [Rhodes, 1966]. On the other hand, the anion disorder is expected to maintain equilibrium in pyrochores in the temperature range of ~800-1000 °C where conductivity measurements were performed.

5.2 $(Gd_{1-x}Ca_x)_2Sn_2O_7$ system

Fig. 5.9 gives the P_{O_2}-dependence of the total conductivity of GS for a number of isotherms. The data were fitted to Eq. (3.29) by least square analysis to extract the parameters A, B and C which were used to produce the solid curves shown in the figure. P-type conduction with a $P_{O_2}^{1/4}$ dependence at high P_{O_2} is observed followed by a P_{O_2}-independent plateau at low P_{O_2} which is attributed to ionic conduction. This ionic conduction is observed down to a P_{O_2} of 10^{-15} atm at 800 °C. Exposure to more reducing atmospheres resulted in decomposition of the phase as evidenced by X-ray diffraction and a sharp decrease in conductivity. Compared with GZT (x=0.8) as shown in Fig. 2.14, pure GS has an ionic conductivity lower by two orders of magnitude than that of GZT. This is an unexpected result for the stannate pyrochlore considering the assumption that disorder increases with increasing average B site cation radius. Significant p-type conduction at high
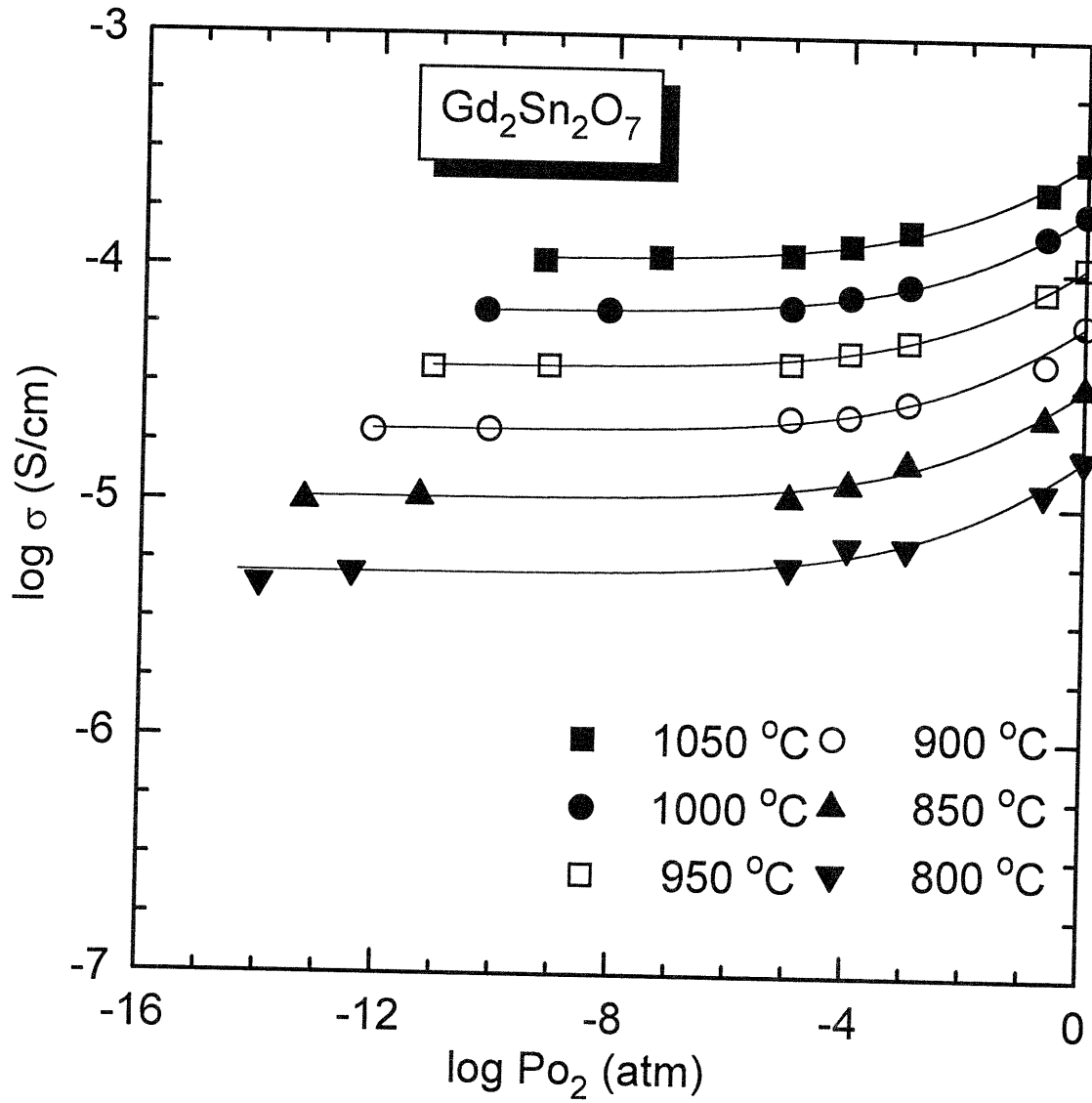
Fig. 5.9 The log conductivity as a function of log oxygen partial pressure for Gd$_2$Sn$_2$O$_7$.

Po$_2$ is also a distinctive difference as compared with GZT which exhibited weak or no p-type conduction at high Po$_2$.

Figs. 5.10 to 5.12 shows the total conductivity of (Gd$_{1-x}$Ca$_x$)$_2$Sn$_2$O$_7$ (x=0.02, 0.05 and 0.1). The figures show that GS specimens doped with Ca exhibit a similar dependence of total conductivity on Po$_2$ as does pure GS. The ionic component of the total conductivity, extracted from the log σ versus log Po$_2$ data for each of these compositions including undoped GS with the aid of Eq. (3.29), is shown plotted versus reciprocal temperature in Fig. 5.13. Note that while the specimens with x=0.02 and x=0.05 show only small increases in ionic conductivity over undoped GS, the specimen with x=0.1 exhibits an ionic conductivity approximately 12 times greater in magnitude.

The E$_i$, and σ_o for the bulk ionic conductivity were calculated using Eq. (3.3) for these compositions and are shown plotted in Figs. 5.14 and 5.15. The derived E$_i$ which range from 1.52~1.61 eV, are approximately double those found for ionic conduction in GZT. The σ_o increases with increasing Ca content above x=0.02 reaching ~10^{-6} S/cmK at GS with 10% Ca whereas the E$_i$ are relatively insensitive to the Ca dopant concentration.

The isothermal composition dependence of the ionic conductivity of GS on Ca content is shown plotted in Fig. 5.16. These data were first fit to Eq. (3.30) in an attempt to extract values for K$_F$ and μ_i. The fit was found to be unsatisfactory particularly with regard to replicating the expected curvature. Eq. (3.30) is based on a model which assumes non-interacting defects [Moon, 1988a]. We suspect results for the specimen with x=0.1 to deviate most strongly from these simplifying assumptions. The solid curve in Fig. 5.16, therefore, represents the best fit of Eq. (3.30) to only the first three compositions. Extrapolation of this curve to x=0.1 shows it to underestimate the measured conductivity. Figs. 5.17 and 5.18 represent the derived value of
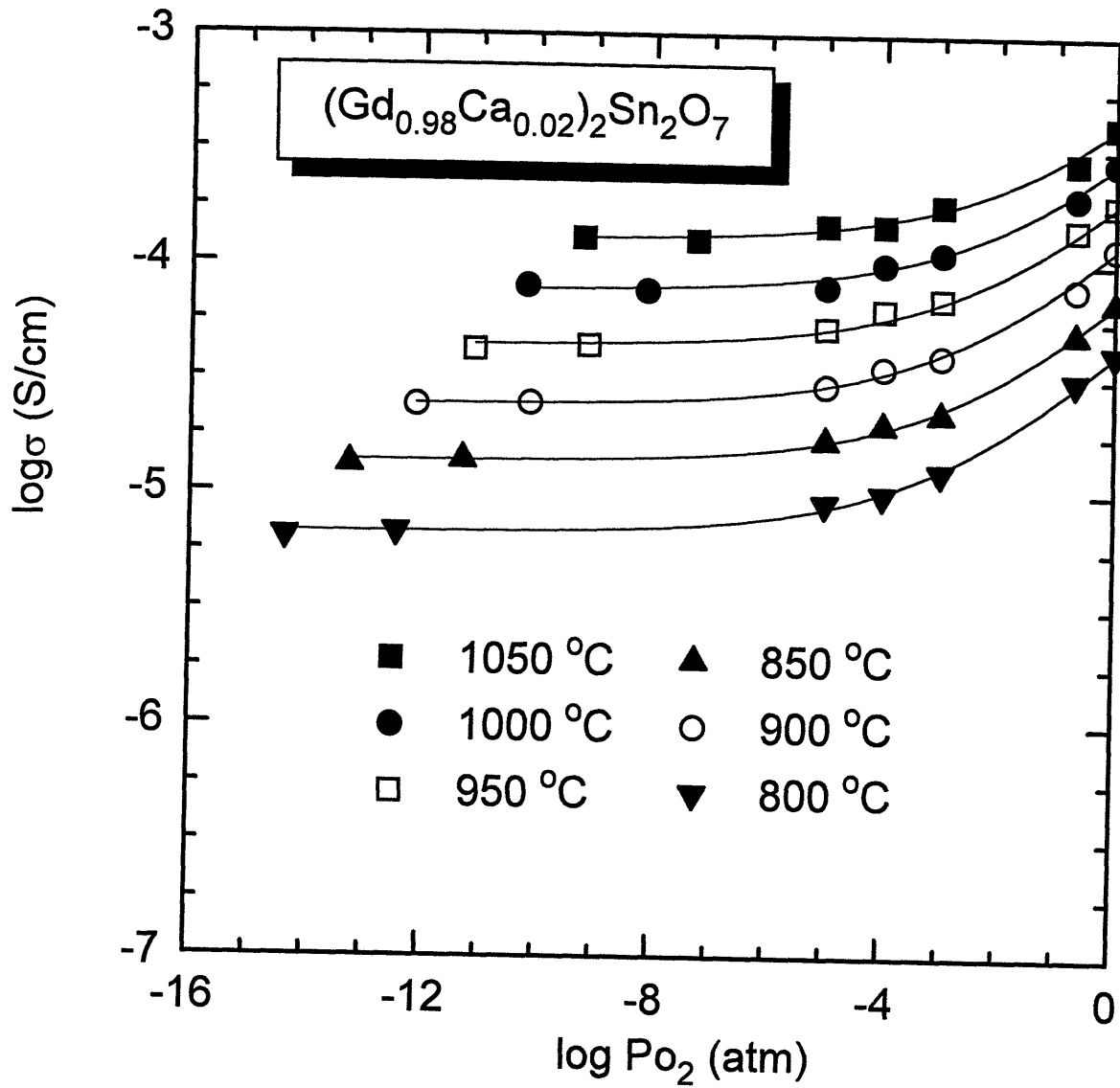
Fig. 5.10 The log conductivity as a function of log oxygen partial pressure for $(Gd_{1-x}Ca_x)_2Sn_2O_7$ with x=0.02.
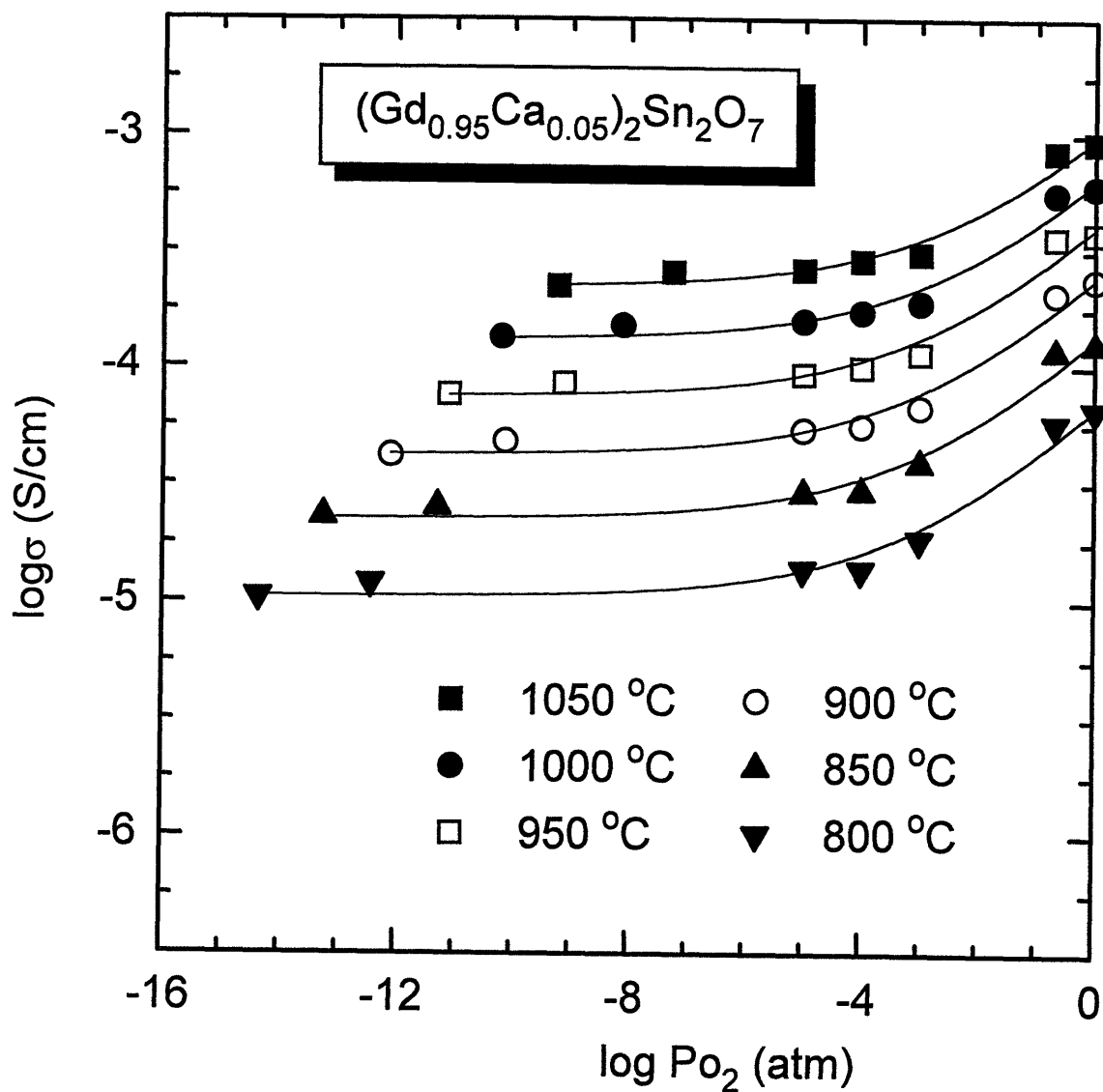
Fig. 5.11 The log conductivity as a function of log oxygen partial pressure for
$(Gd_{1-x}Ca_x)_2Sn_2O_7$ with x=0.05.
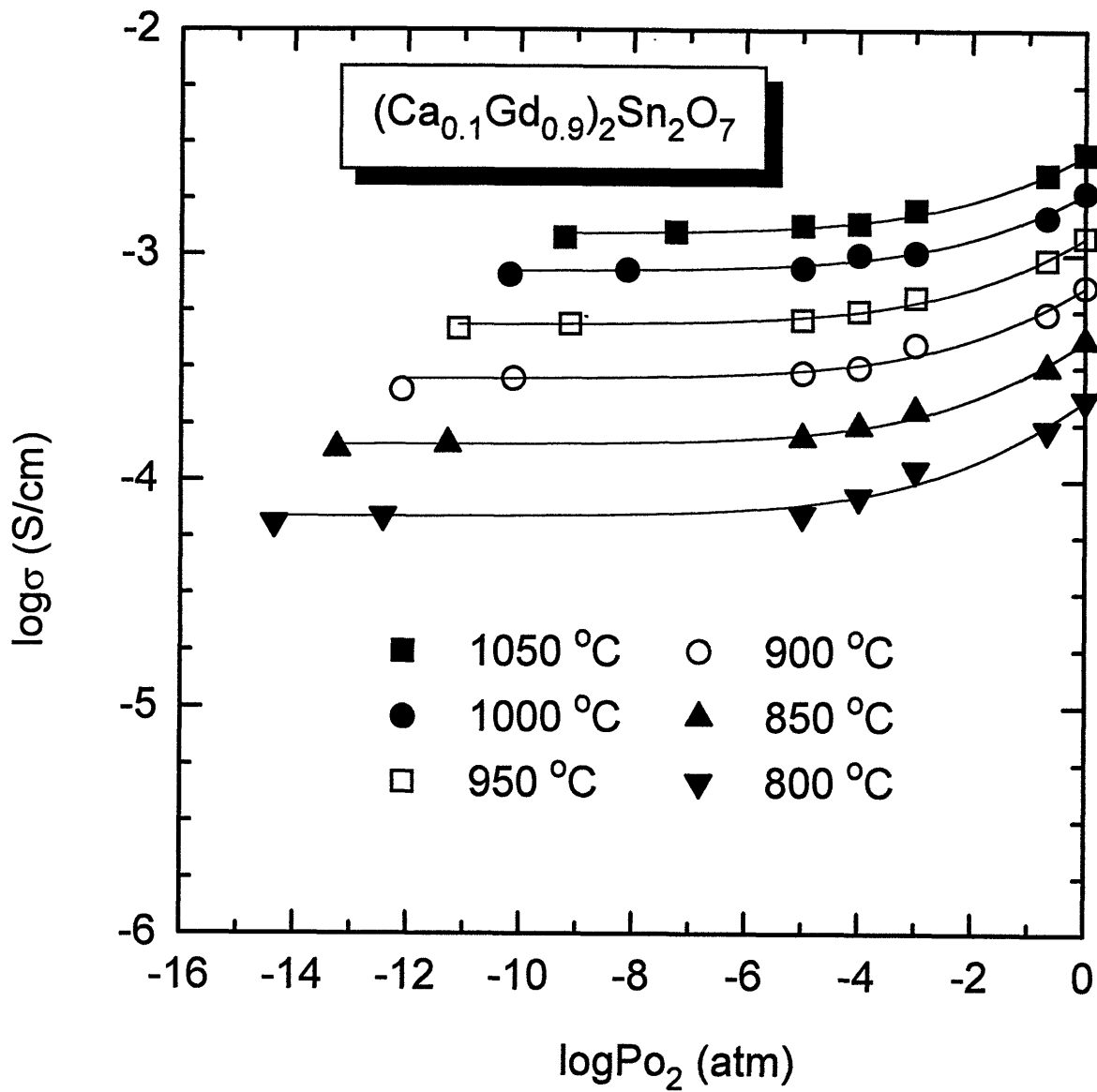
Fig. 5.12 The log conductivity as a function of log oxygen partial pressure for
$(Gd_{1-x}Ca_x)_2Sn_2O_7$ with x=0.1.
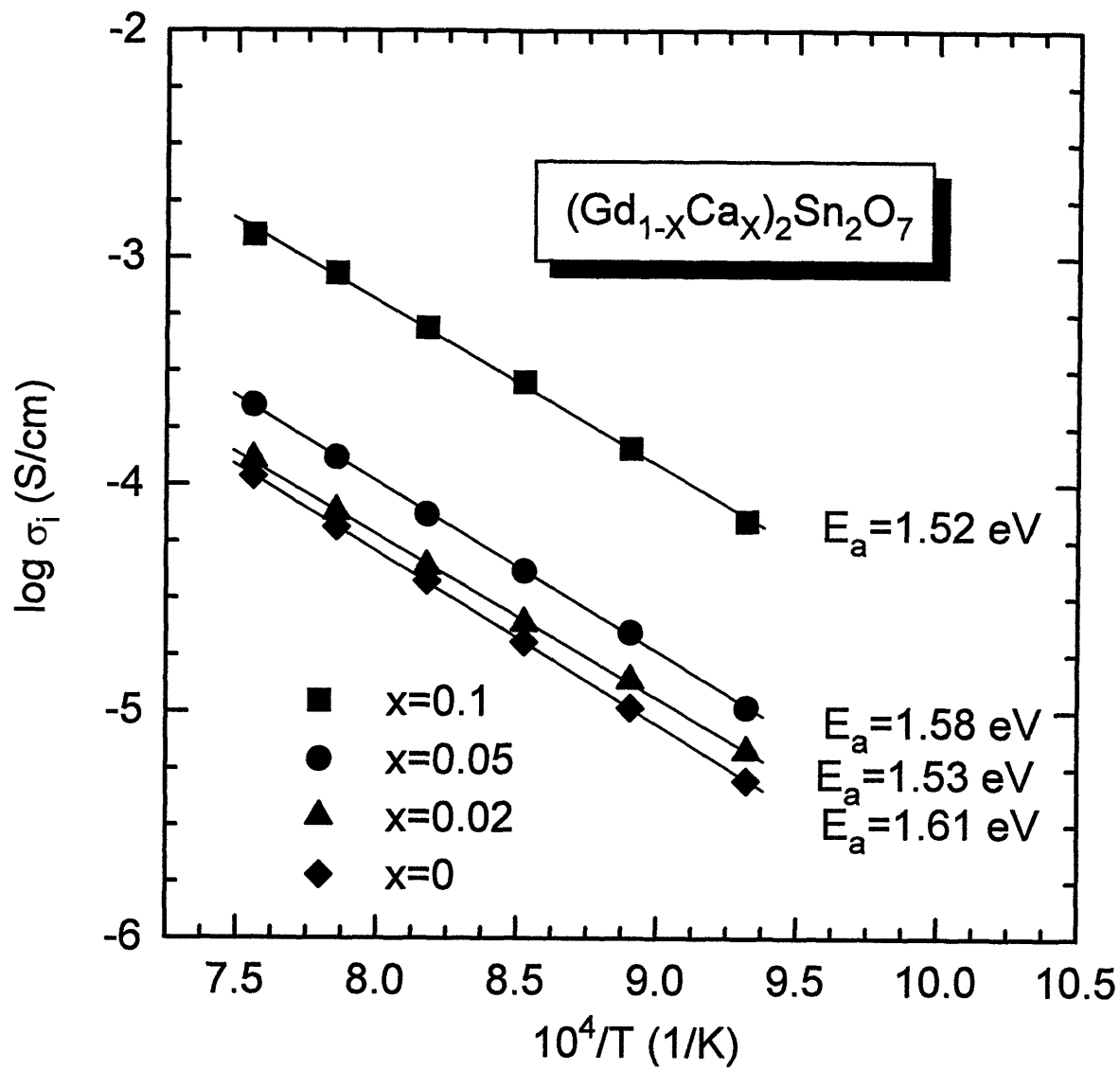
Fig. 5.13 The temperature dependence of ionic conductivity for $(Gd_{1-x}Ca_x)_2Sn_2O_7$.
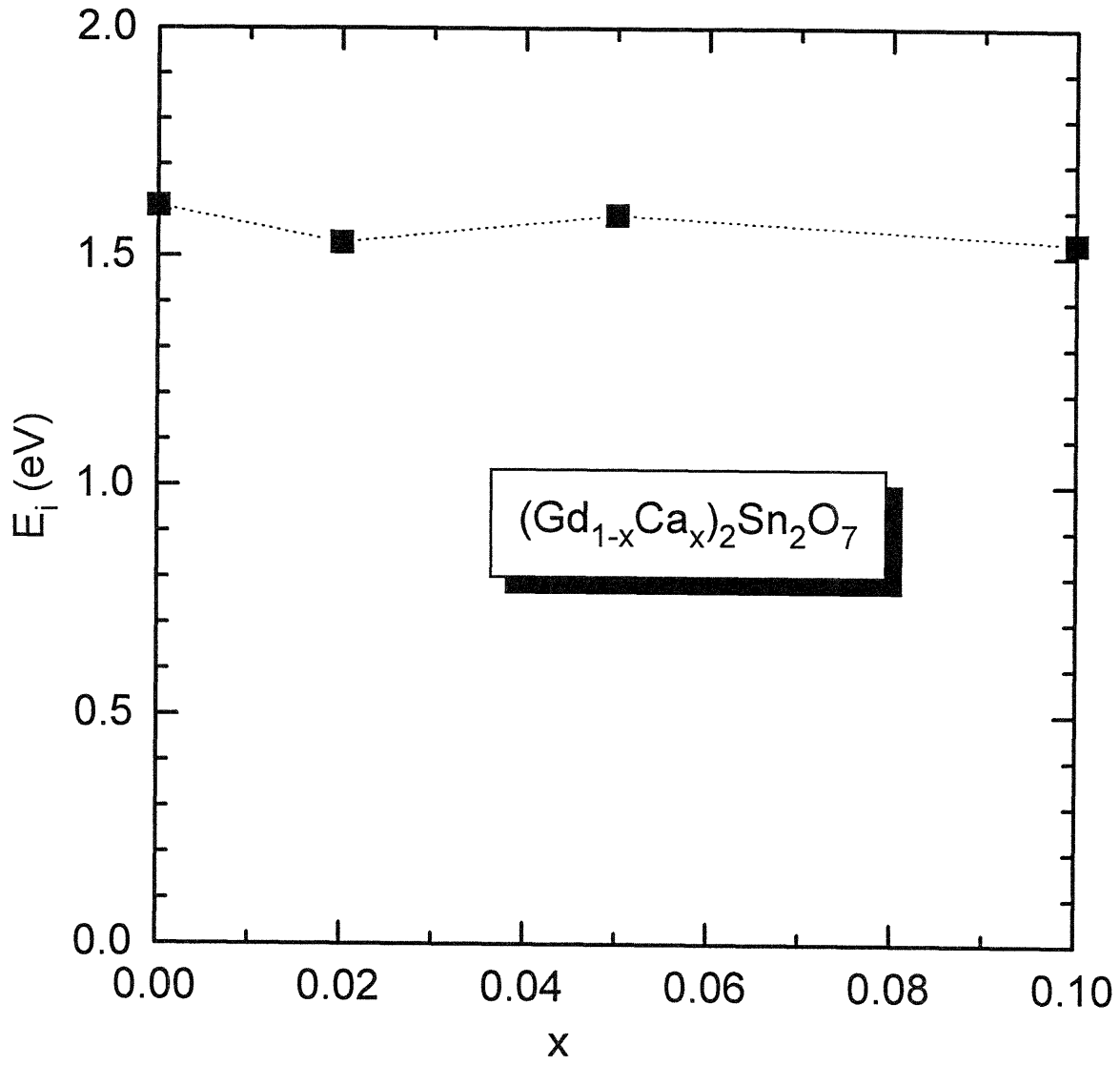
Fig. 5.14 The activation energy for ionic conduction for $(Gd_{1-x}Ca_x)_2Sn_2O_7$.

104
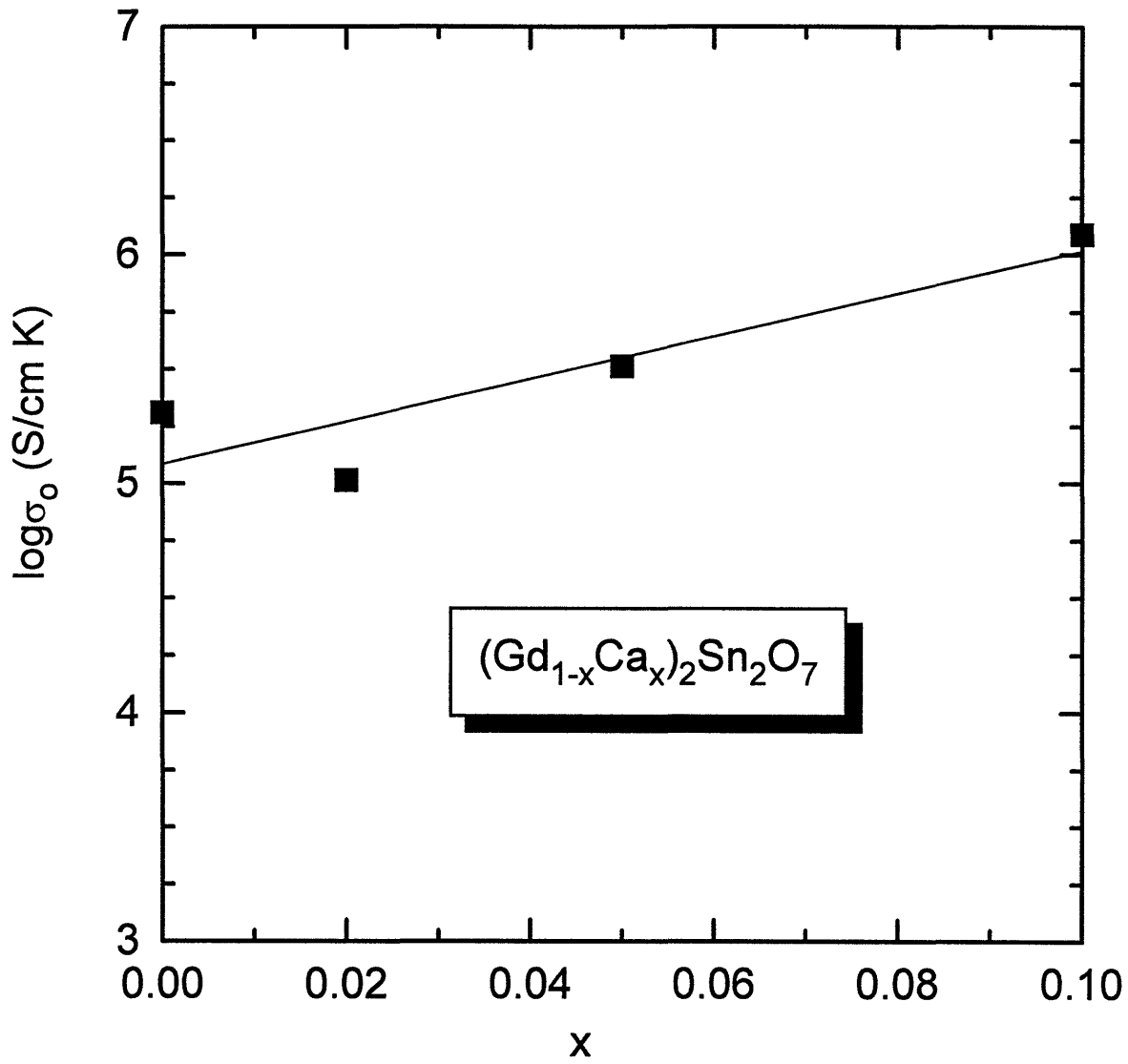
Fig. 5.15 The pre-exponential constant for ionic conduction for
$(Gd_{1-x}Ca_x)_2Sn_2O_7$.
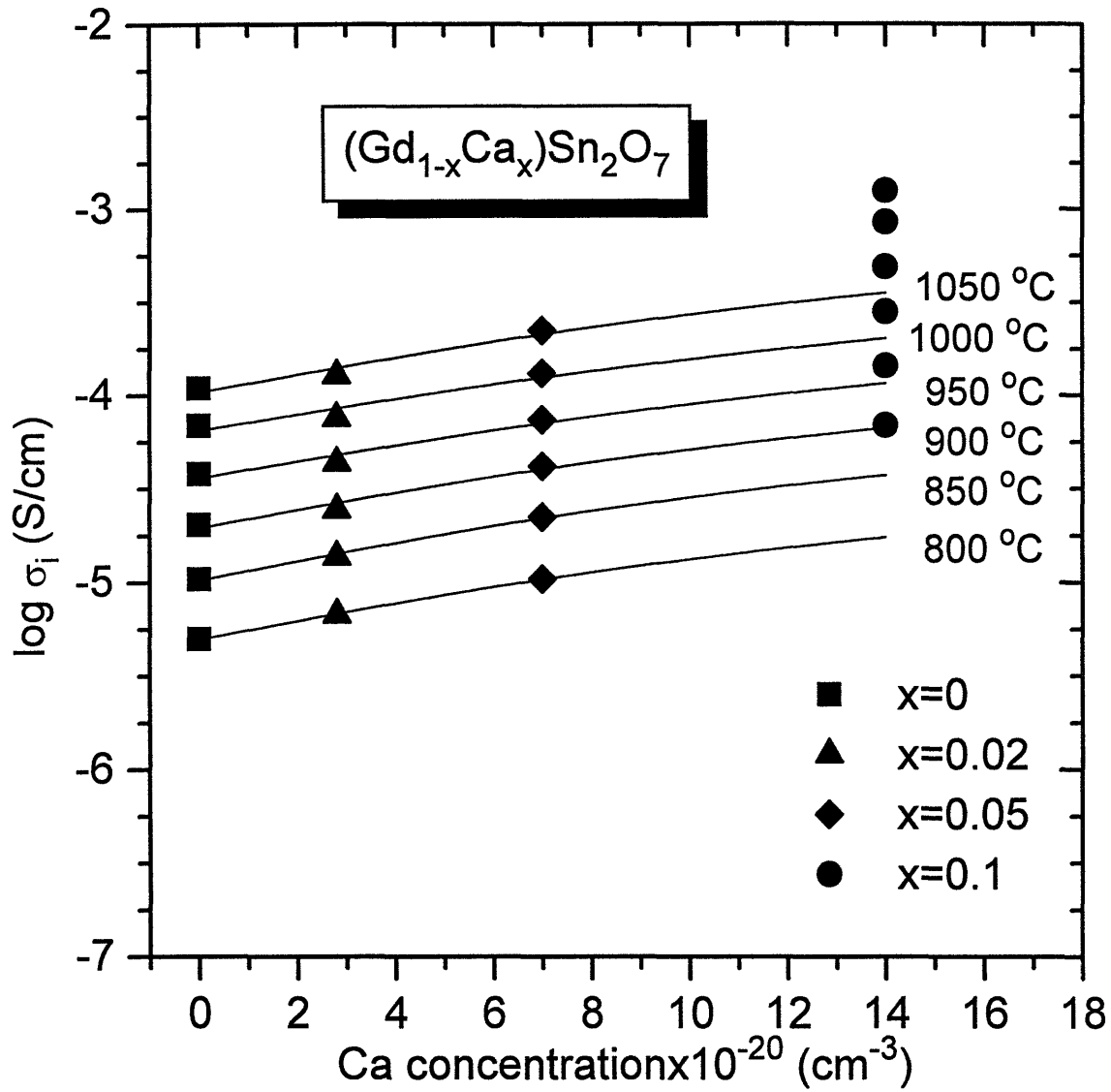
Fig. 5.16 The log ionic conductivity as a function of Ca concentration for $(Gd_{1-x}Ca_x)_2Sn_2O_7$. The lines are the least square fits of Eq. (3.30) to the data limited to x=0, 0.02 and 0.05.

106
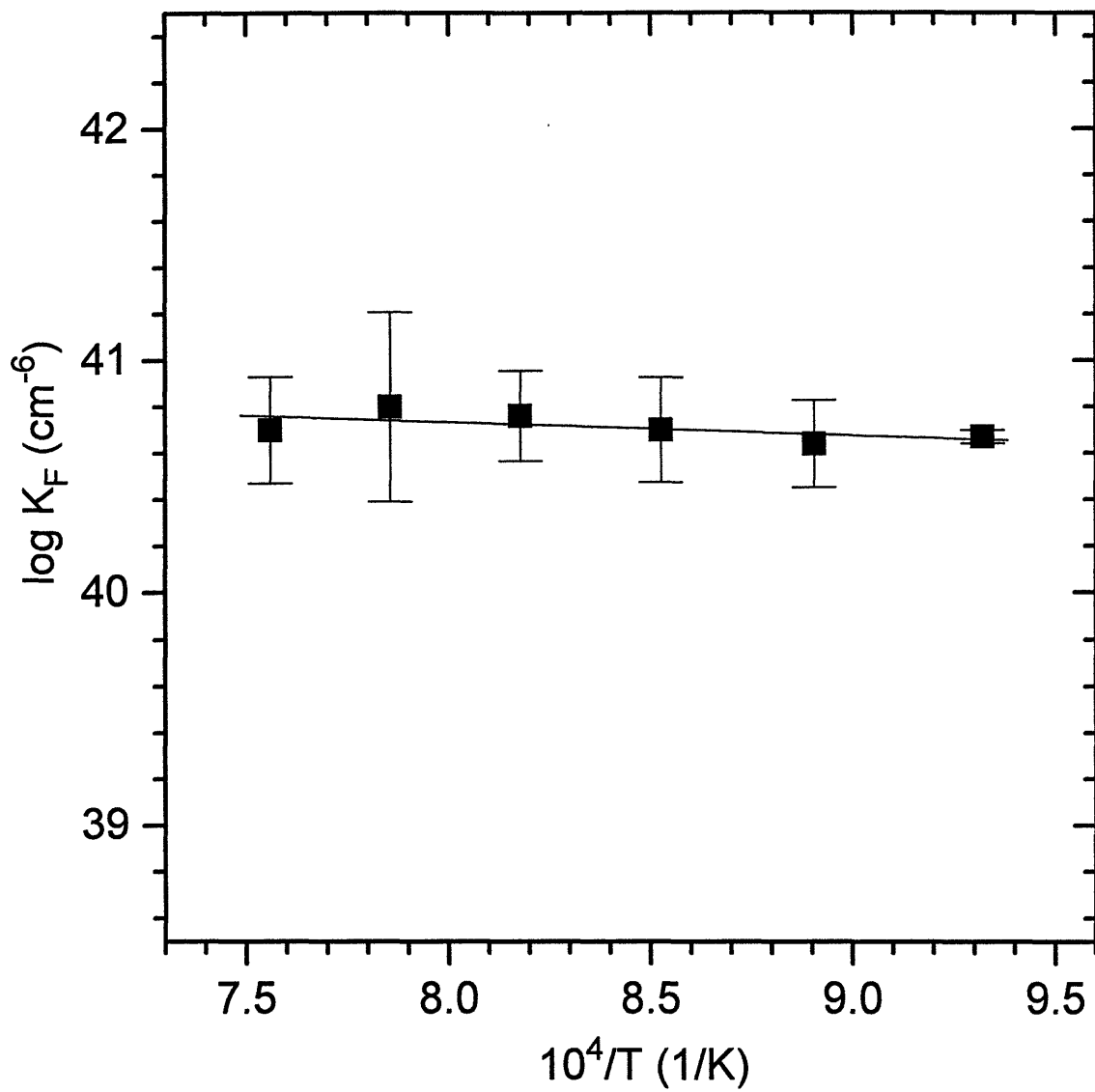
Fig. 5.17 Calculated values for the Frenkel constant in $Gd_2Sn_2O_7$ as a function of $1/T$.
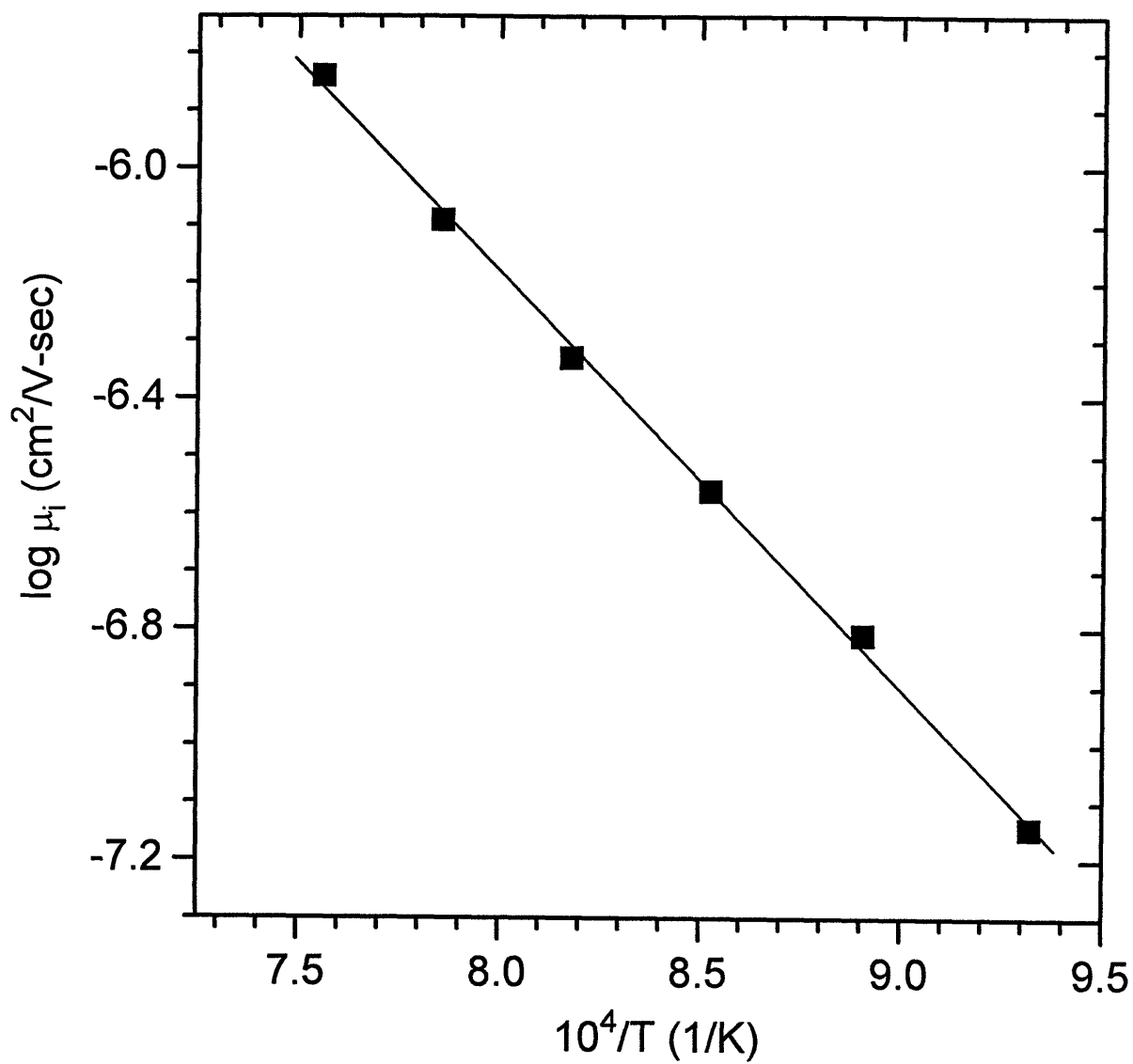
Fig. 5.18 Calculated values for the oxygen vacancy mobility in $Gd_2Sn_2O_7$ as a function of 1/T.

K_F and μ_i at each of the isotherms and the fits through these data result in the following expressions.

$$K_F = 1.55 \times 10^{41} \exp(-0.11 \pm 0.06 \text{ eV/kT}) \text{ cm}^{-6}$$

$$\mu_i = \frac{1317.7}{T} \exp(-1.54 \pm 0.03 \text{ eV/kT}) \text{ cm}^2/\text{Vsec}$$

The p-type conductivity is shown plotted versus reciprocal temperature in Fig. 5.19 at P_{O_2}=1 atm for pure GS and Ca doped GS. While the activation energies for p-type conduction, E_h, range from 1.13-1.49 eV, they typically fall within the range of 1.35 ± 0.15 eV. Fig. 5.20 shows the isothermal composition dependence of the p-type conductivity, σ_h, of GS on Ca content at 1000 °C. The magnitude of the p-type conductivity increases with increasing Ca content.

5.3 $Gd_2(Ti_{1-x}Sn_x)_2O_7$ System

Fig. 5.21 shows the total conductivity plotted versus P_{O_2} for GTS (x= 0.8). A p-type conductivity is seen at high P_{O_2}, a P_{O_2}-independent ionic conductivity at intermediate P_{O_2} and an n-type conductivity at low P_{O_2} as predicted by Eq. (3.29). Note that for this composition, the n-type conductivity appears at 10^{-16} atm, 800 °C whereas only ionic conductivity was observed in undoped GS down to 10^{-15} atm at 800 °C.

Fig. 5.22 to 5.27 presents the conductivity of GTS (x=0.6, 0.4, 0.2, 0.15, 0.1 and 0.05) as a function of P_{O_2} and temperature. The samples show several conduction regimes. At high P_{O_2}, the conductivity appears to change from p-type to ionic followed by a further increase at intermediate P_{O_2} to a conductivity plateau. At lower P_{O_2}, there is a further increase in conductivity

$(Gd_{1-x}Ca_x)_2Sn_2O_7$

$E_h = 1.23$ eV

$E_h = 1.37$ eV
$E_h = 1.13$ eV

$E_h = 1.49$ eV

▼ x=0
▲ x=0.02
● x=0.05
■ x=0.1

Figure showing $(Gd_{1-x}Ca_x)_2Sn_2O_7$ data plotted against Ca concentration $\times 10^{-20}$ (Cm^{-3}). Legend: $x=0$, $x=0.02$, $x=0.05$, $x=0.1$.
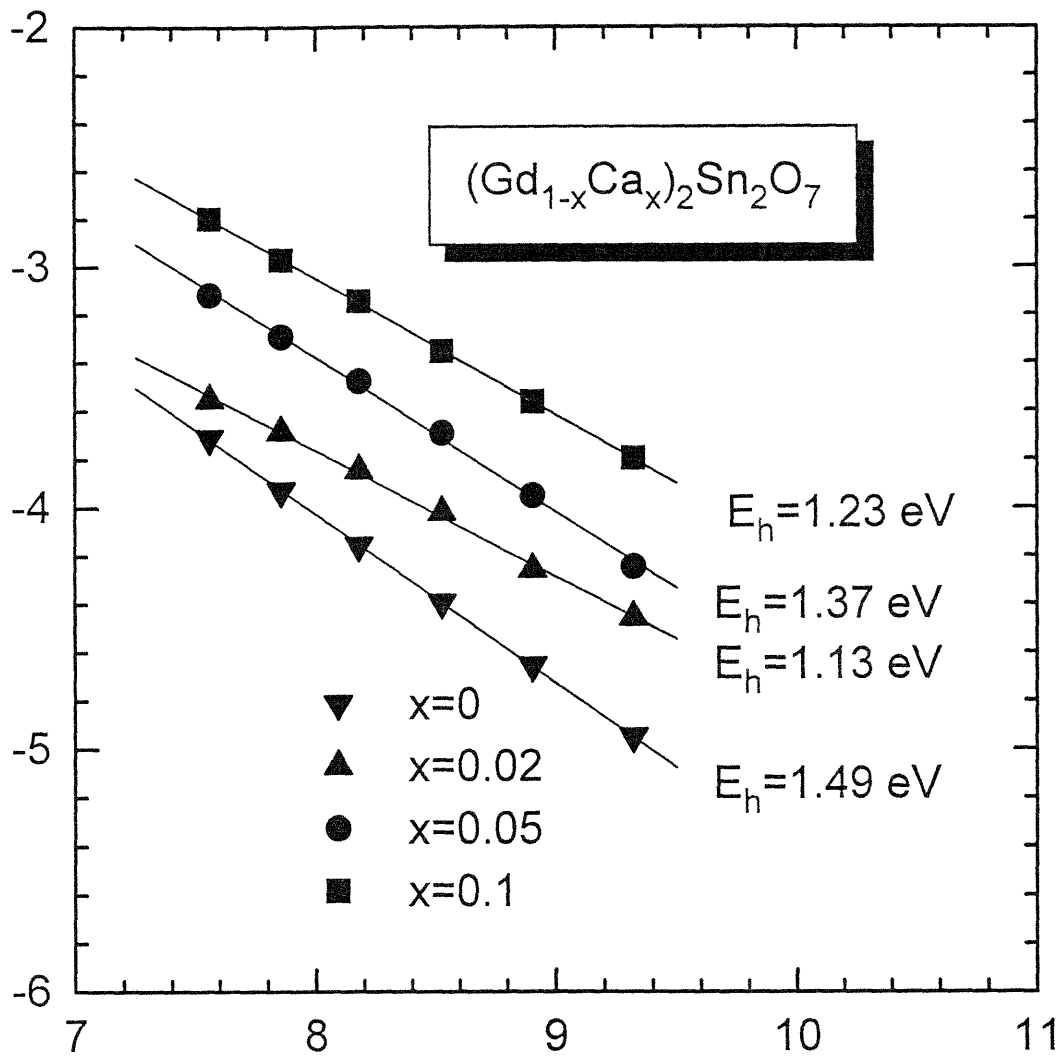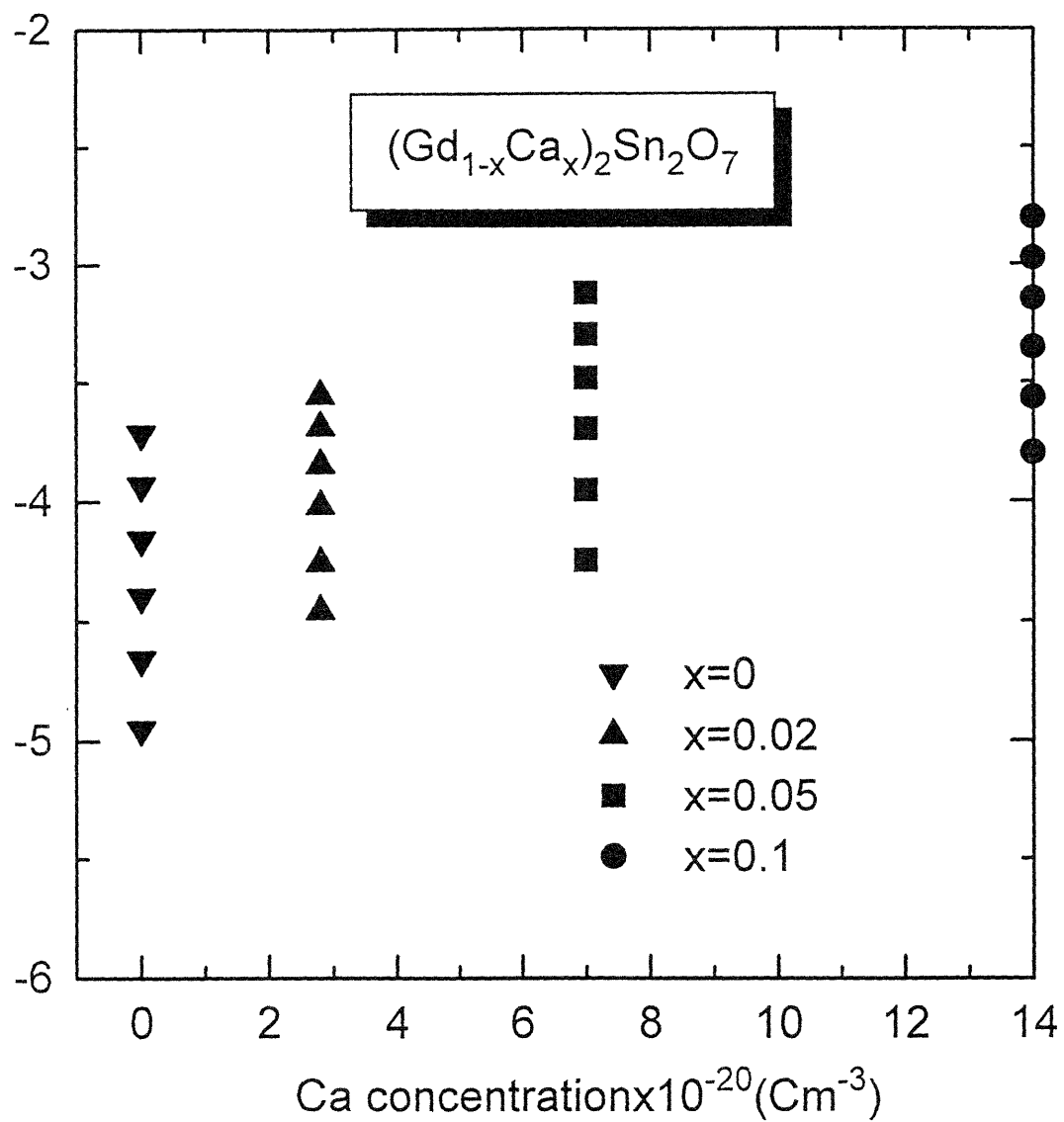
Fig. 5.21 The log conductivity as a function of log oxygen partial pressure for $Gd_2(Ti_{1-x}Sn_x)_2O_7$ with x=0.8.

Fig. 5.22 The log conductivity as a function of log oxygen partial pressure for
$Gd_2(Ti_{1-x}Sn_x)_2O_7$ with x=0.6.

Fig. 5.23 The log conductivity as a function of log oxygen partial pressure for
Gd$_2$(Ti$_{1-x}$Sn$_x$)$_2$O$_7$ with x=0.4.

Fig. 5.24 The log conductivity as a function of log oxygen partial pressure for
$Gd_2(Ti_{1-x}Sn_x)_2O_7$ with x=0.2.

Fig. 5.25 The log conductivity as a function of log oxygen partial pressure for $Gd_2(Ti_{1-x}Sn_x)_2O_7$ with x=0.15.

Fig. 5.26 The log conductivity as a function of log oxygen partial pressure for $Gd_2(Ti_{1-x}Sn_x)_2O_7$ with x=0.1.

Fig. 5.27 The log conductivity as a function of log oxygen partial pressure for $Gd_2(Ti_{1-x}Sn_x)_2O_7$ with x=0.05.

with a nominal $-\frac{1}{4}$ slope. The magnitude of the conductivity in the second plateaus, observed at low Po_2 in each sample, appears to increase with increasing Ti content in GTS. The fitting to Eq. (3.29) was performed piecewise at high and low Po_2 separately with different parameters. At low Po_2, the fit was performed setting C=0 in (3.29).

The ionic component of the conductivity evaluated at 1000 °C in the high Po_2 region is shown plotted in Fig. 5.28 as a function of the Sn fraction in GST. The ionic conductivity for the end member GT measured by Kramer et al. was also included in the figure. Since the oxygen vacancy concentration in GT is determined by background impurities, the ionic conductivity in GT ranges from $\sim10^{-4}$ to 10^{-6} S/cm depending on sample history [Moon, 1988a; Kramer, 1994]. A broad maximum, centered at approximately x=0.4 is observed.

Fig. 5.29 shows the corresponding E_i as a function of composition. There is a near linear increase in E_i from ~0.8 eV to 1.6 eV from x=0.2 to 1 in GTS. Note that, in contrast, E_i remains nearly constant, ~0.8-0.9 eV, in GZT for all x as shown in section 3.16. The drop in E_i from 1.04 eV at x=0.05 to 0.78 eV at x=0.15 is similar to one observed previously in GT doped with Ca as shown in Fig. 3.19. Fig. 5.30 shows the composition dependence of the σ_0. The value of σ_0 increases by over two orders of magnitude as x in GTS increases from 0.2 towards 1.0 similar to the trend observed previously in GZT (See Fig. 2.17).

In Fig. 5.31, the magnitude of conductivity at 1000 °C in the second plateau observed at low Po_2 is plotted as function of x in GTS. This is found to increase monotonically with increasing Ti content in GTS. Fig. 5.32 and 5.33 give corresponding activation energies and pre-exponential constants for
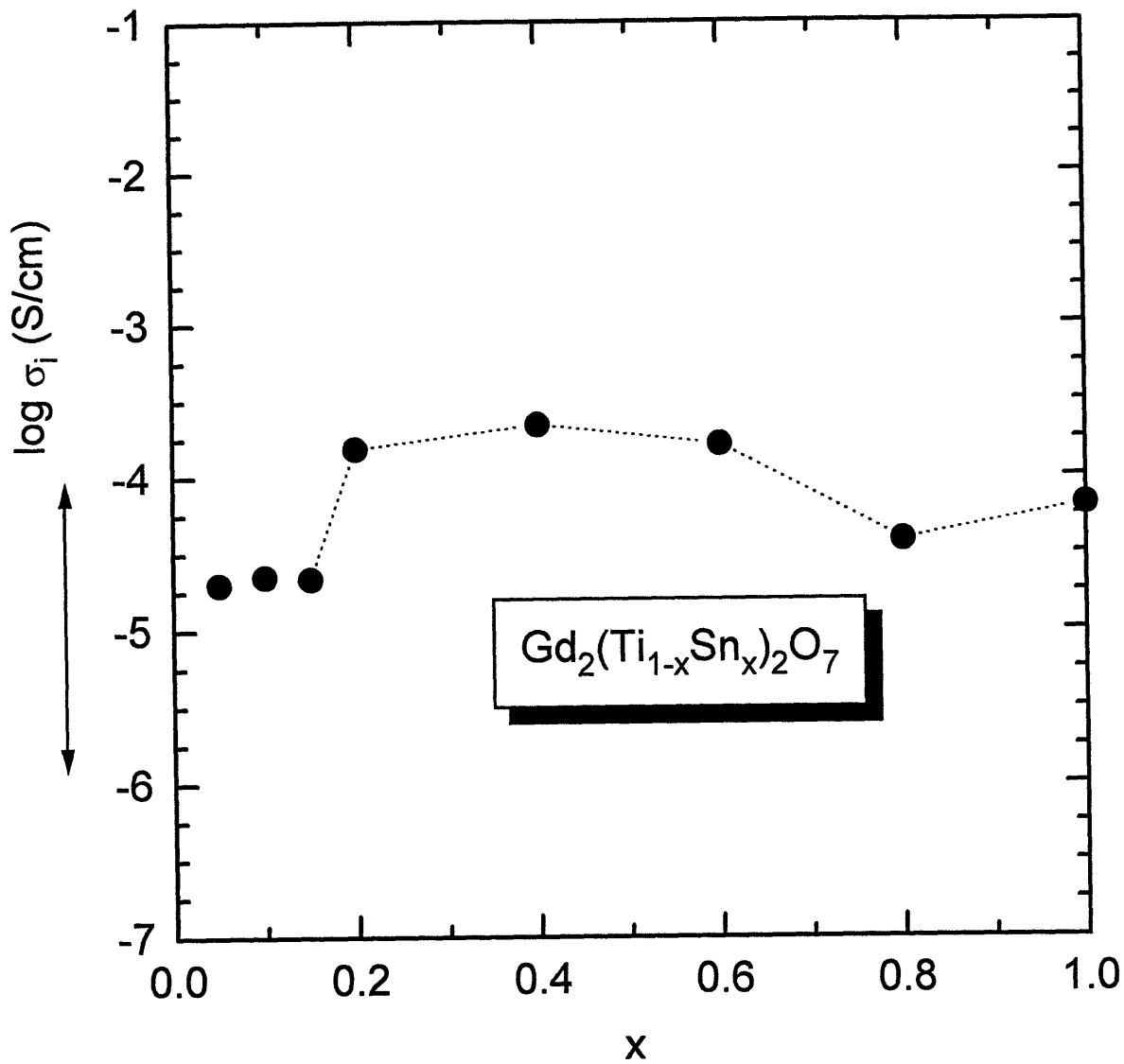
Fig. 5.28 The ionic conductivity as a function of composition at 1000 °C for
$Gd_2(Ti_{1-x}Sn_x)_2O_7$. The ionic conductivity of $Gd_2Ti_2O_7$ was observed
to range from $\sim 10^{-4}$ to 10^{-6} (S/cm) as represented by$\updownarrow$
[Moon, 1988a; Kramer, 1994]
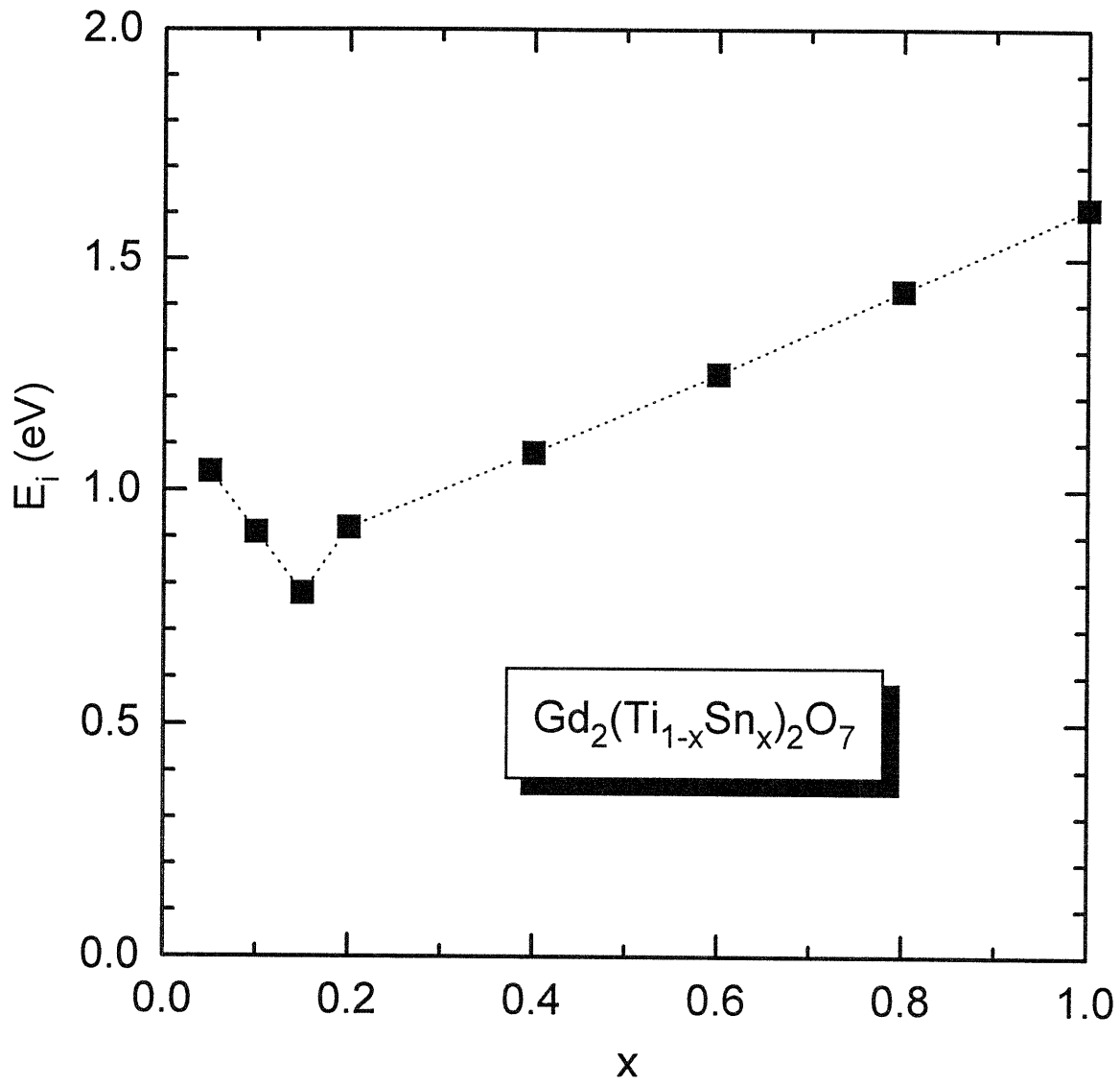
Fig. 5.29 The activation energy for ionic conduction for $Gd_2(Ti_{1-x}Sn_x)_2O_7$.
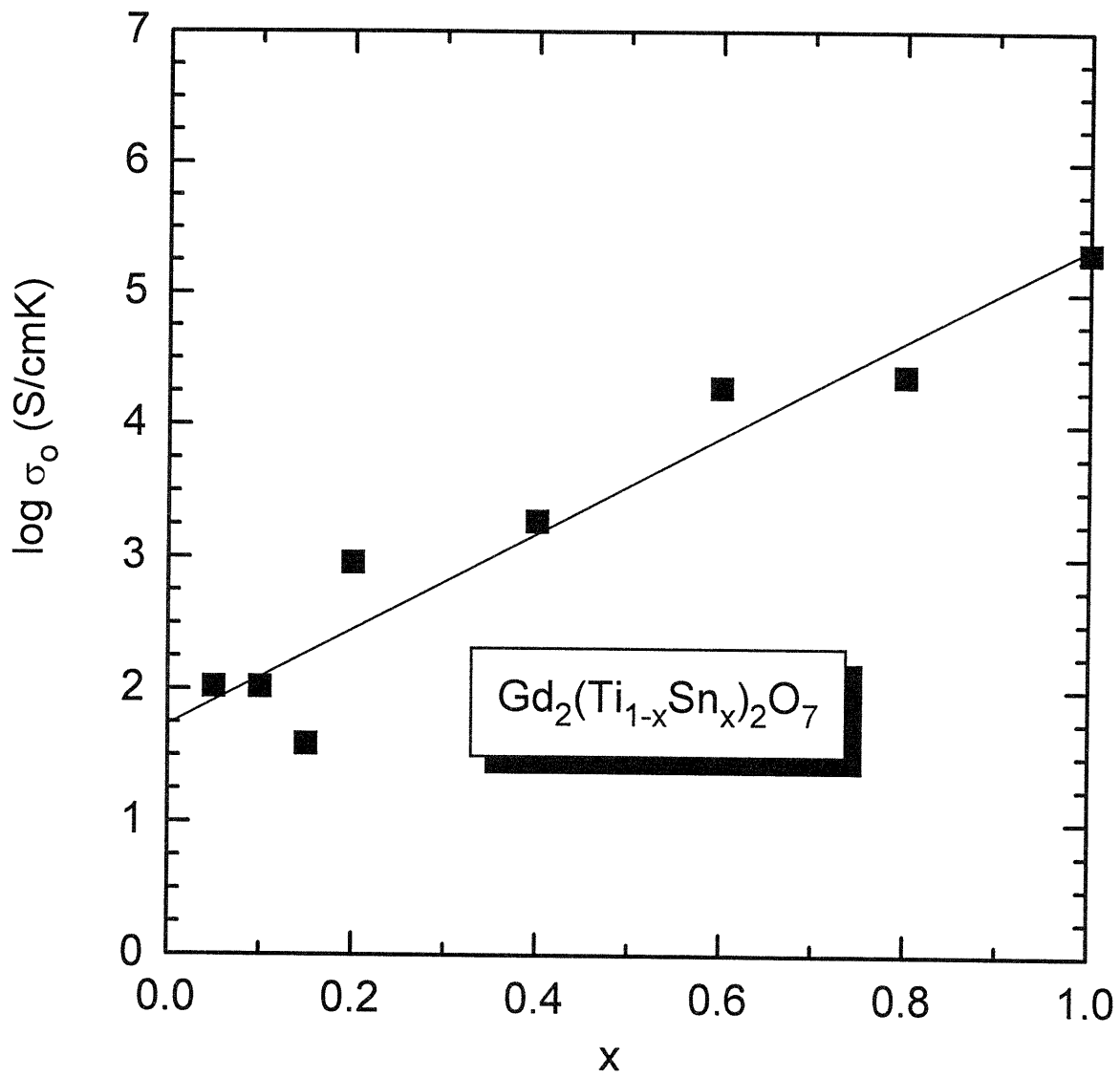
Fig. 5.30 The pre-exponential constant for ionic conduction for $Gd_2(Ti_{1-x}Sn_x)_2O_7$.
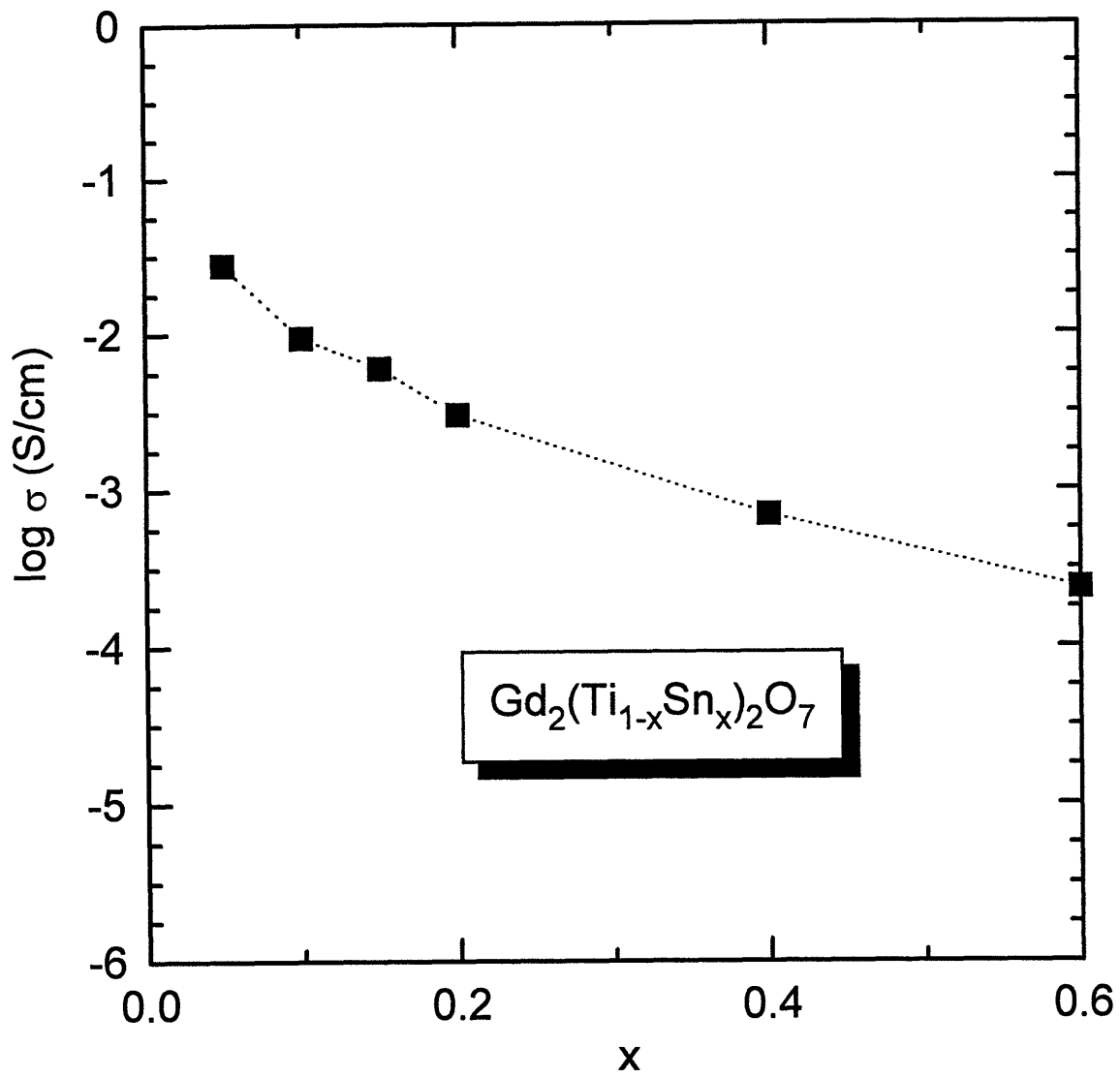
Fig. 5.31 The second electrical conductivity plateau observed at low P_{O_2} at 1000 °C for $Gd_2(Ti_{1-x}Sn_x)_2O_7$.
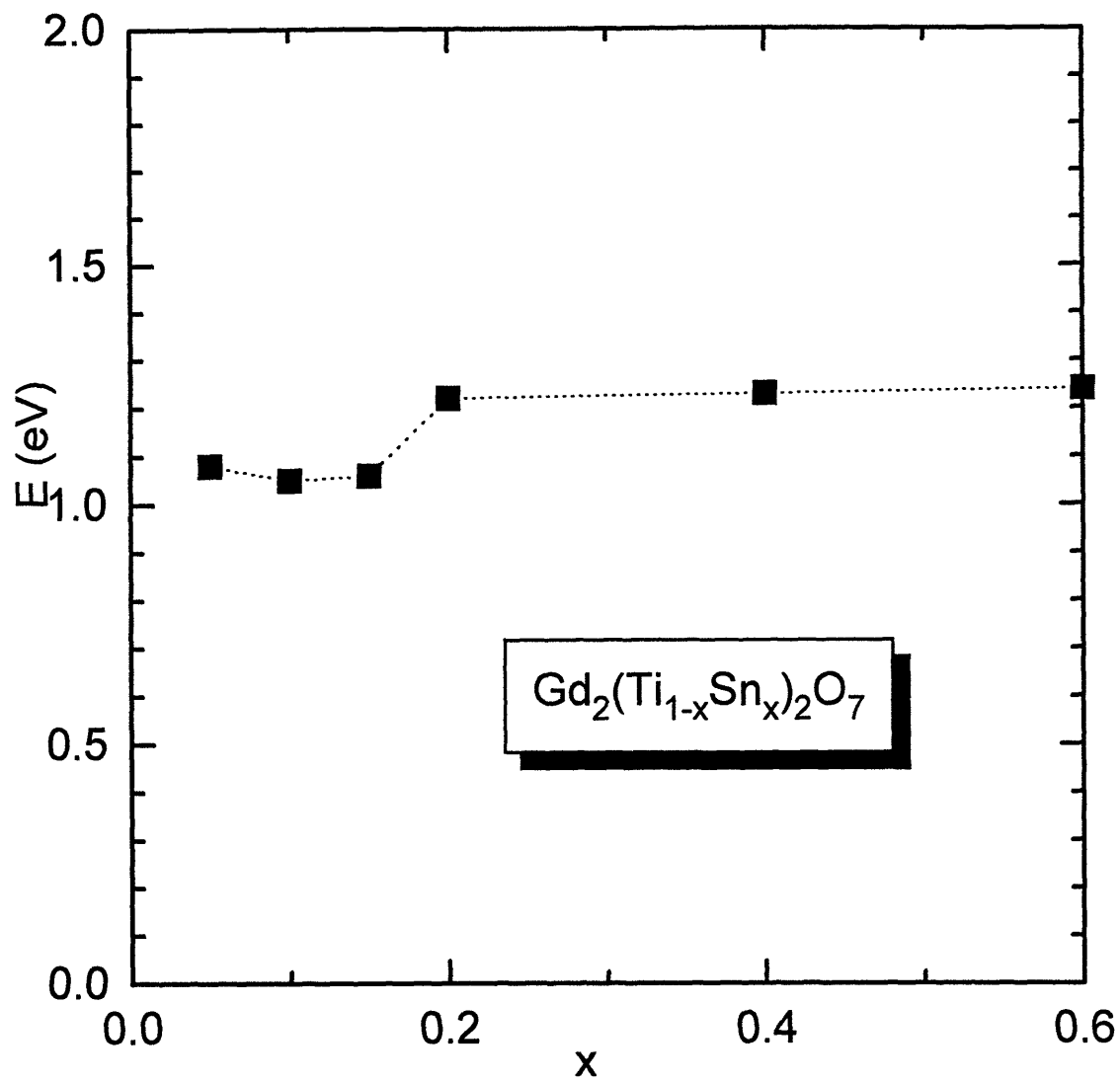
Fig. 5.32 The activation energy for the second conductivity plateau at low P_{O_2} for $Gd_2(Ti_{1-x}Sn_x)_2O_7$.
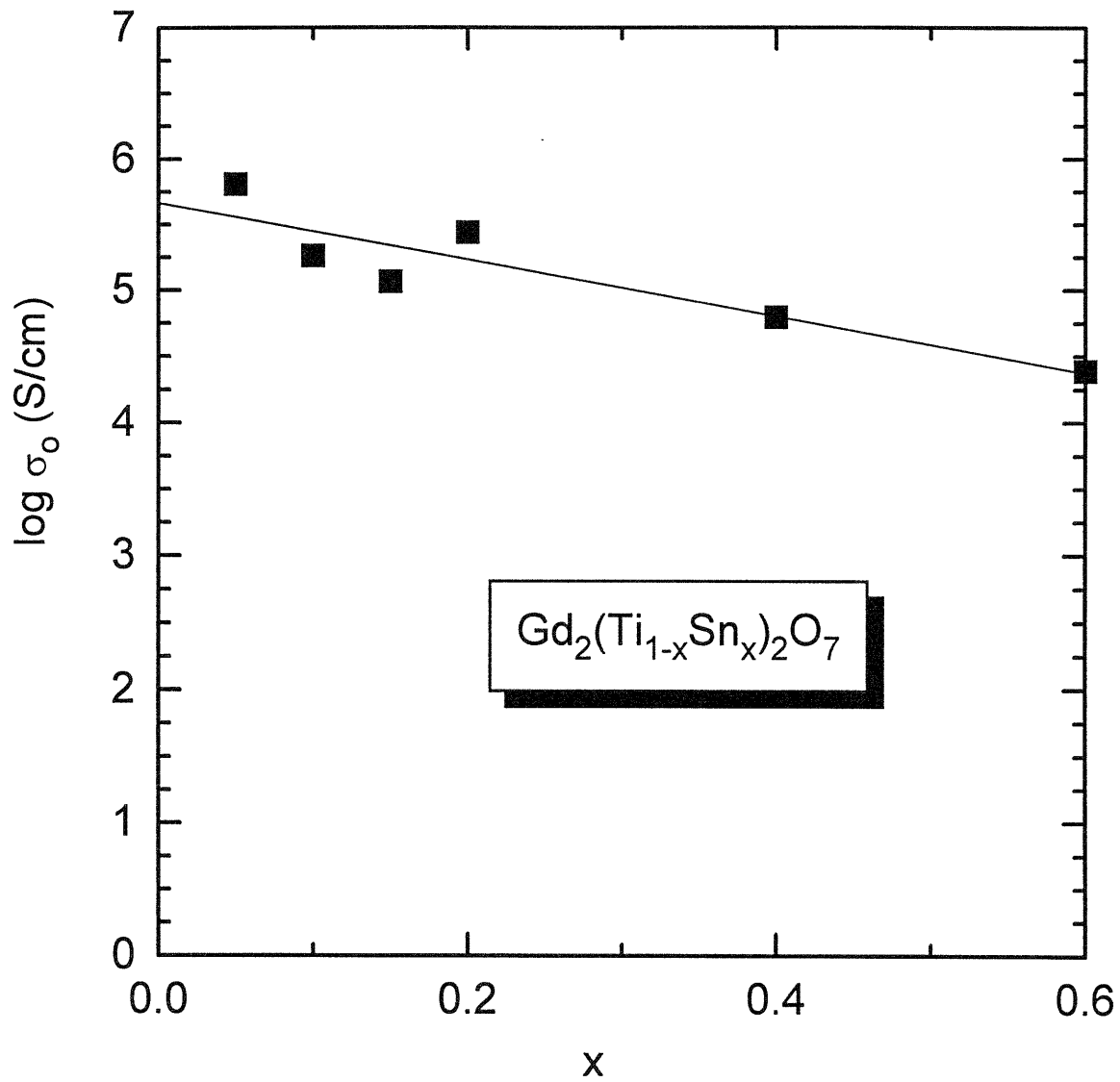
Fig. 5.33 The pre-exponential constant for the second conductivity plateau at low P_{O_2} for $Gd_2(Ti_{1-x}Sn_x)_2O_7$.

these systems. The activation energies appear to decrease slightly from ~1.2 eV to ~1 eV as x decreases but the pre-exponential constant decreases with increasing x in GTS.

5.4 $Gd_2(Zr_{1-x}Sn_x)_2O_7$ System

Fig. 5.34 represents the total conductivity plotted versus log Po_2 for GZS at x=0.2 in the temperature range from 750 °C to 1050 °C. The specimen shows a Po_2-independent conductivity indicating predominant ionic conduction over the entire range of Po_2 and temperature examined. The magnitude of the ionic conductive is comparable to that in GZT (x=0.7) as presented in Fig. 3.14.

Figs. 5.35 to 5.37 give the total conductivity of GZS with x=0.6, 0.4 and 0.2. Regions with $+\frac{1}{4}$ and $-\frac{1}{4}$ slopes corresponding to the p-type and n-type conduction at high and low Po_2 respectively begin to appear as x decreases in GZS. Fig. 5.38 presents the ionic conductivity obtained from Eq. (3.29) at 1000 °C as a function of the B site composition in these systems, including $Gd_2Zr_2O_7$ by Moon et al. [Moon, 1988a]. There is a increase in the ionic conductivity as Zr replaces Sn in the B site except for a slight decrease from x=1 to x=0.8. This fluctuation in GS and GZS (x≤0.8) may come from the processing condition as GS and GZS (x≤0.8) were processed in different citrate solution.

The corresponding E_i and σ_o for the ionic conductivity are presented in Fig. 5.39 and 5.40. The E_i is observed to drop from 1.62 eV at x=1 to 0.8 eV at x=0, which follows a similar trend to that observed in the GTS system. The σ_o on the other hand, shows only small changes with composition. The
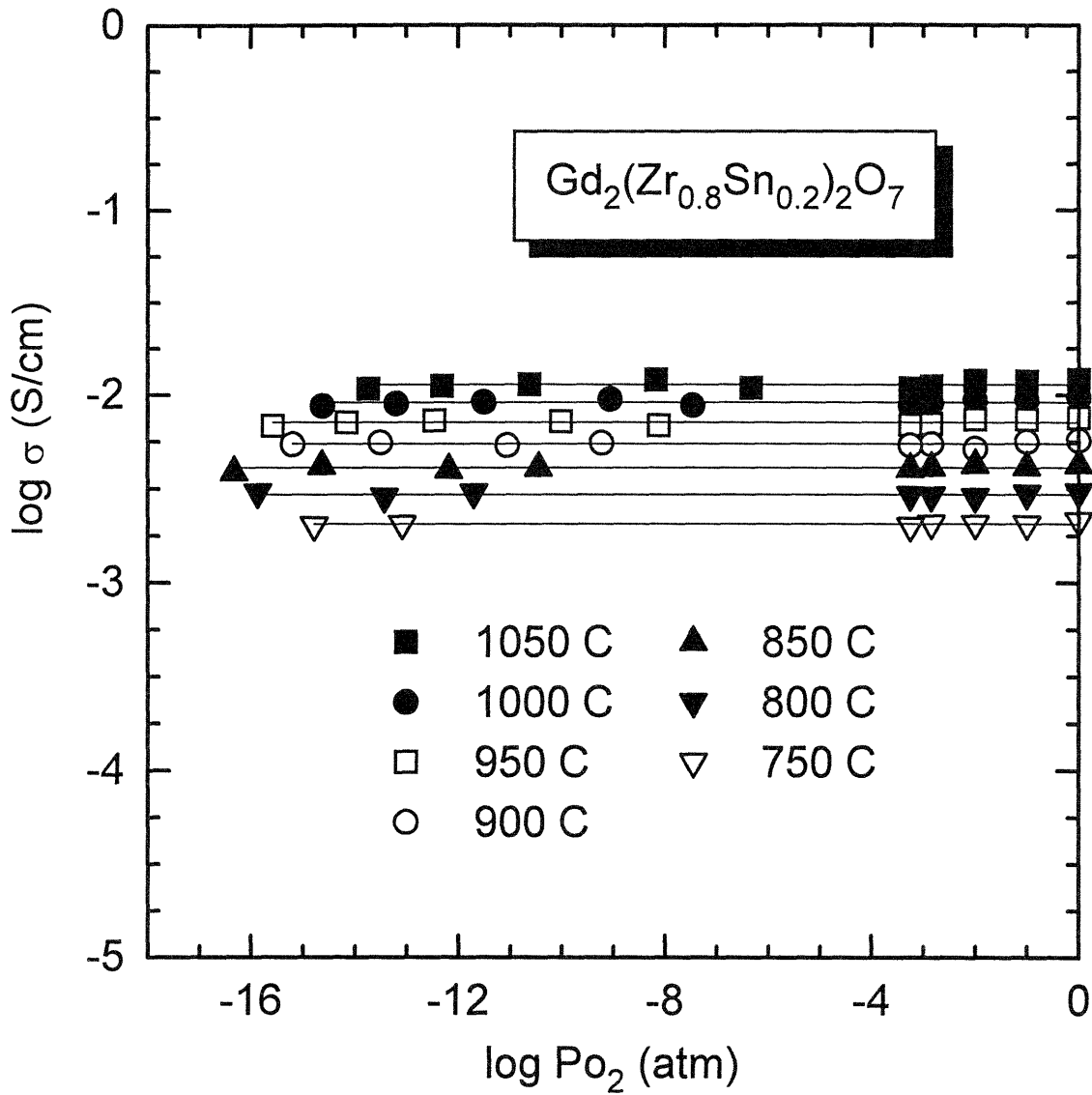
Fig. 5.34 The log conductivity as a function of log oxygen partial pressure for $Gd_2(Zr_{1-x}Sn_x)_2O_7$ with x=0.2.
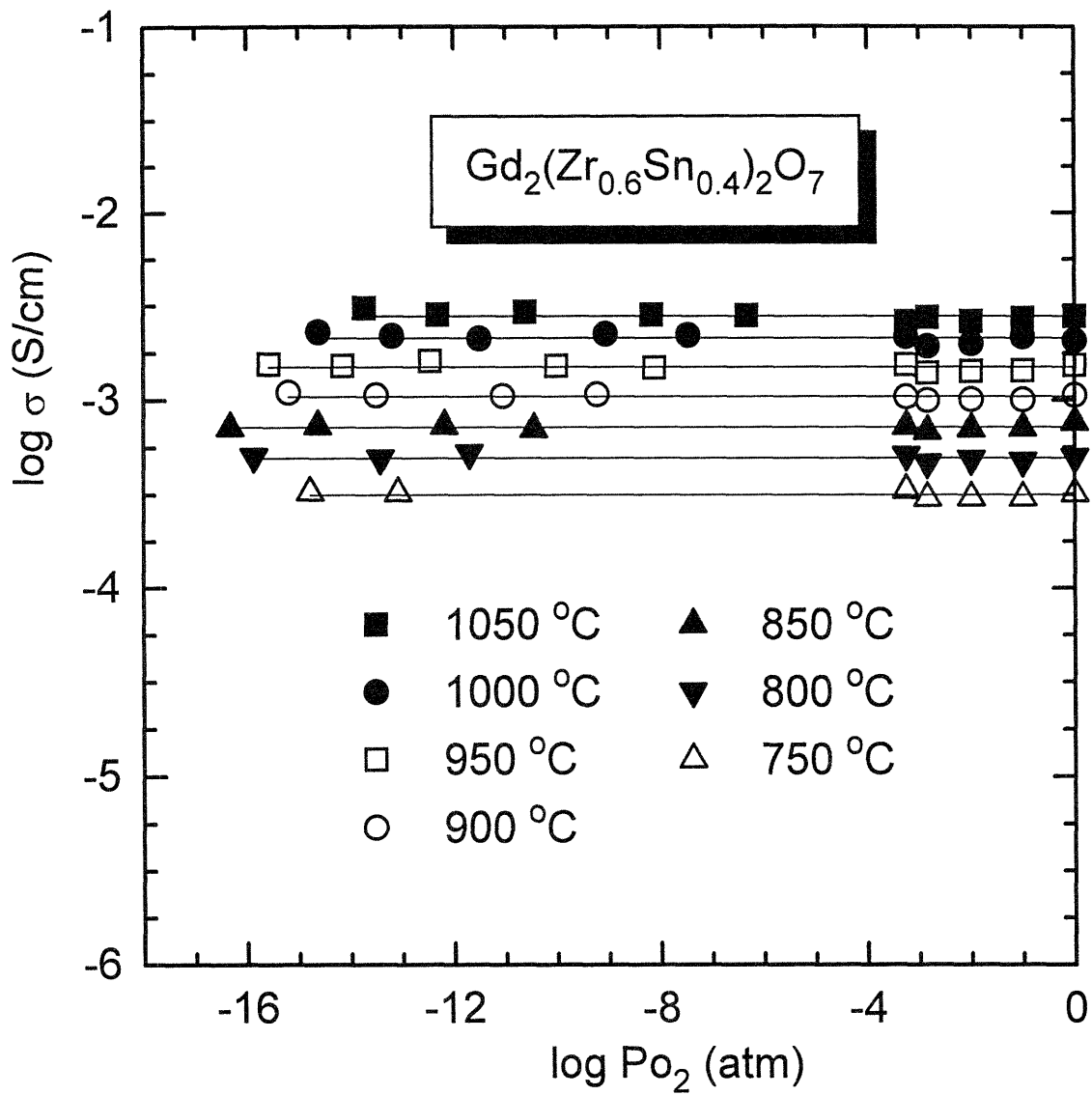
Fig. 5.35 The log conductivity as a function of log oxygen partial pressure for $Gd_2(Zr_{1-x}Sn_x)_2O_7$ with x=0.4.
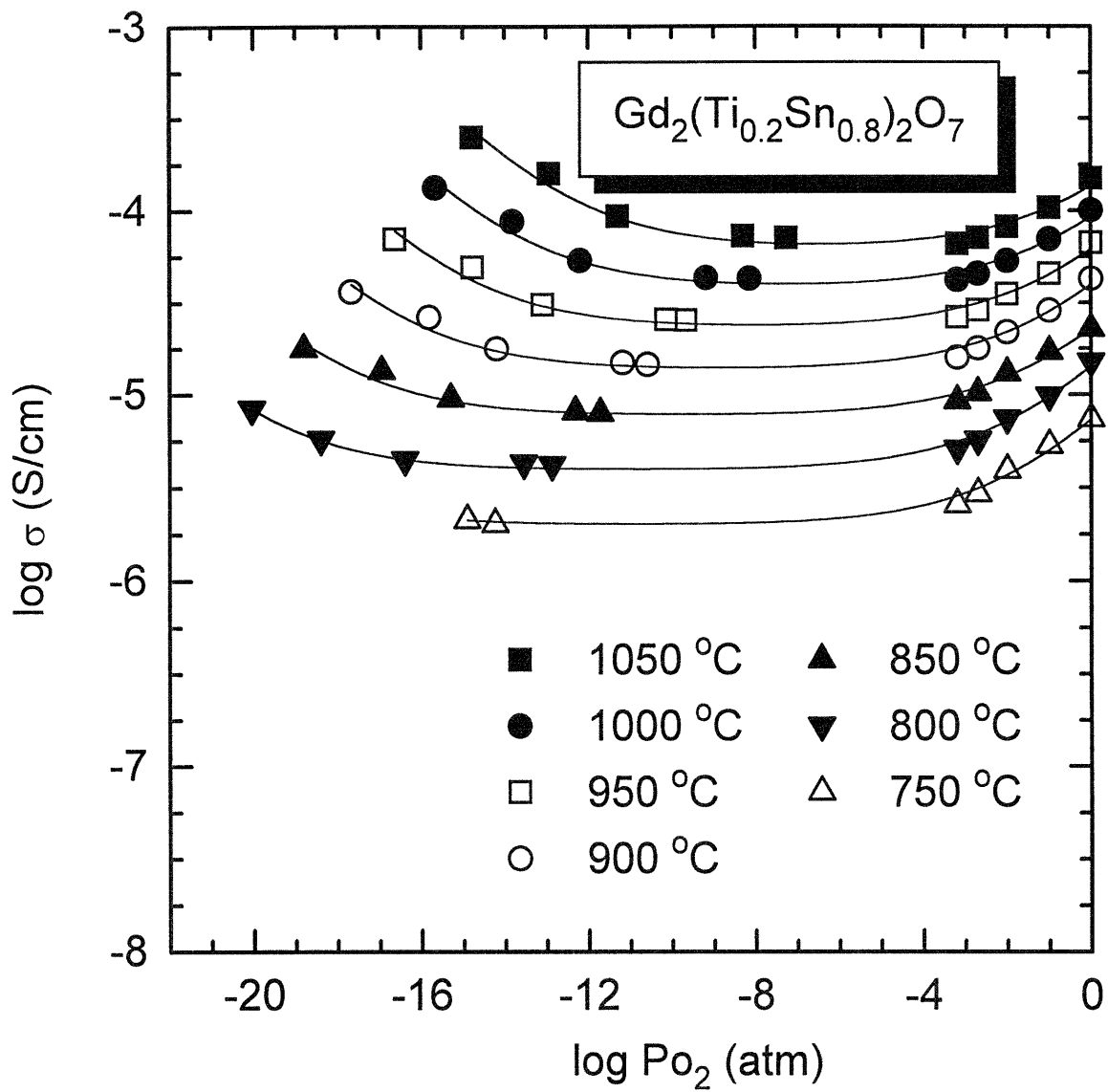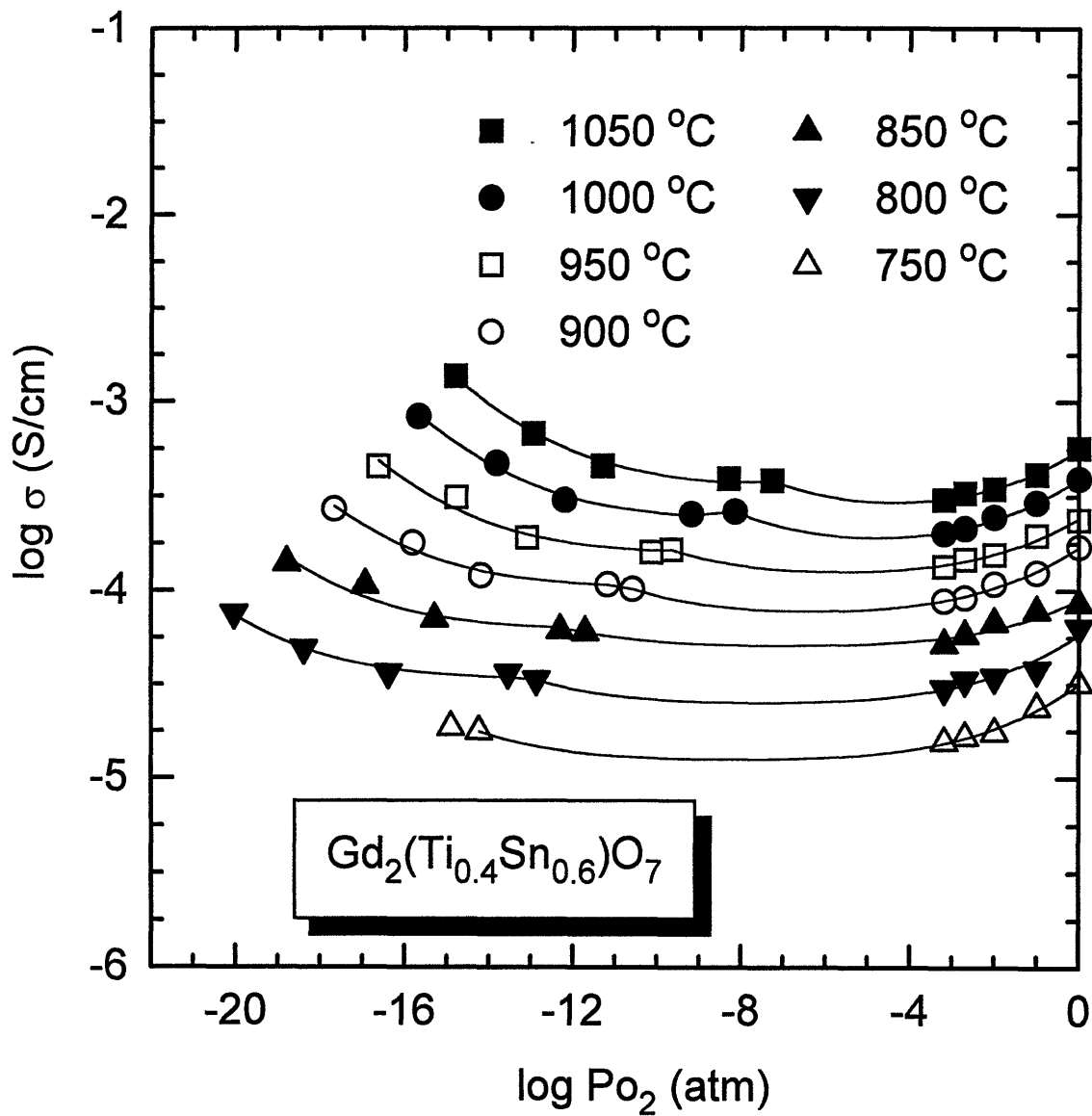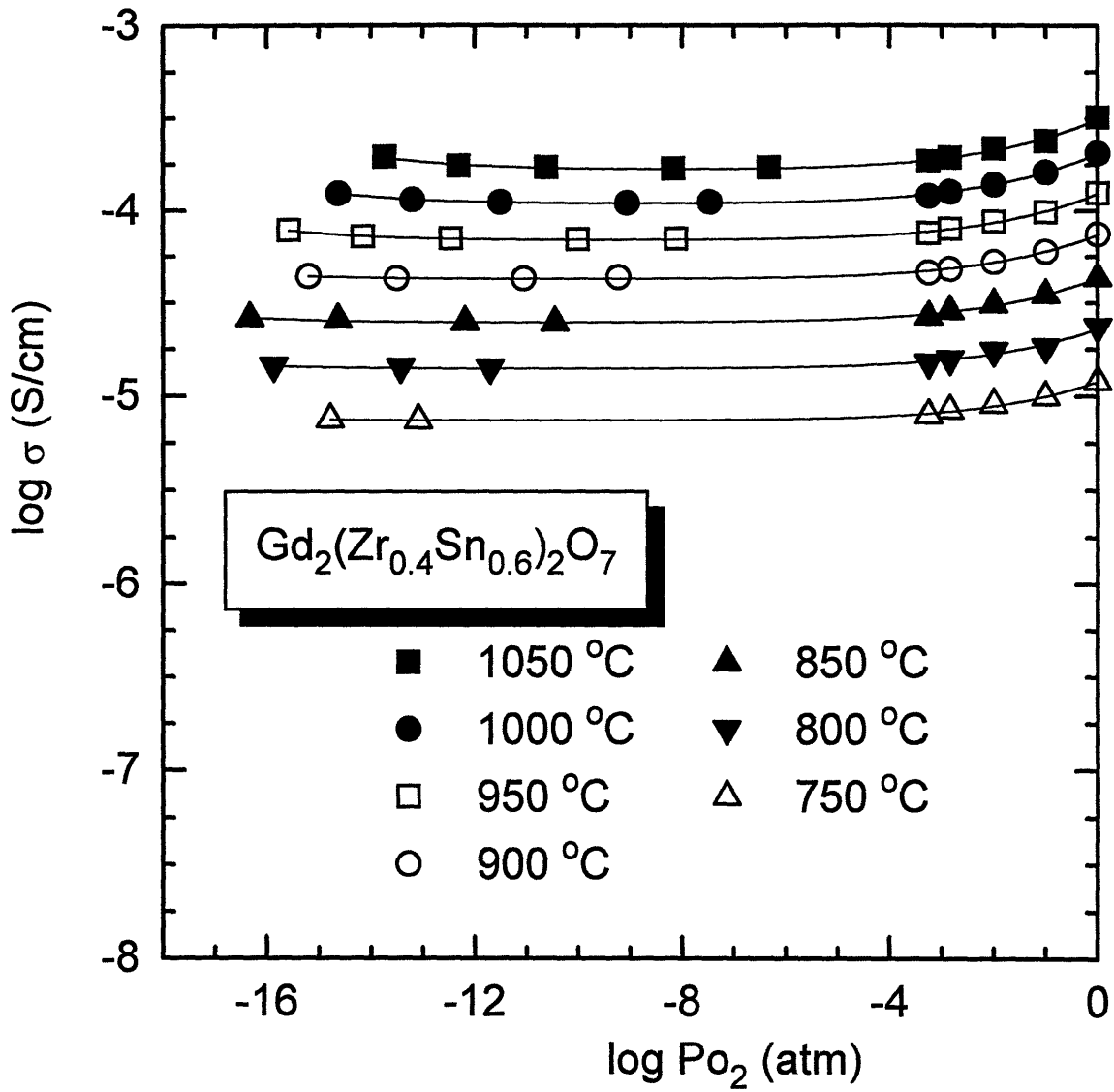
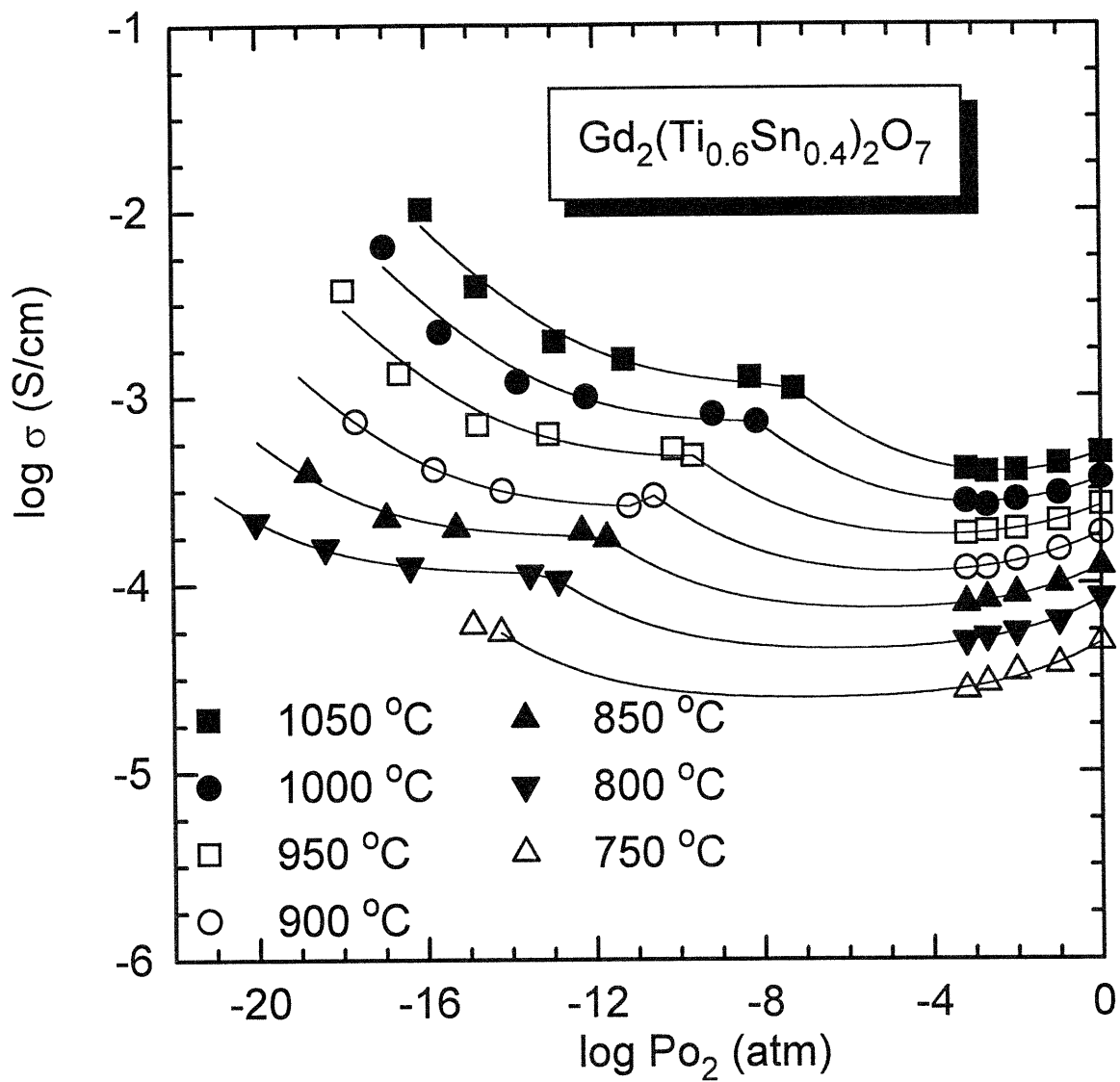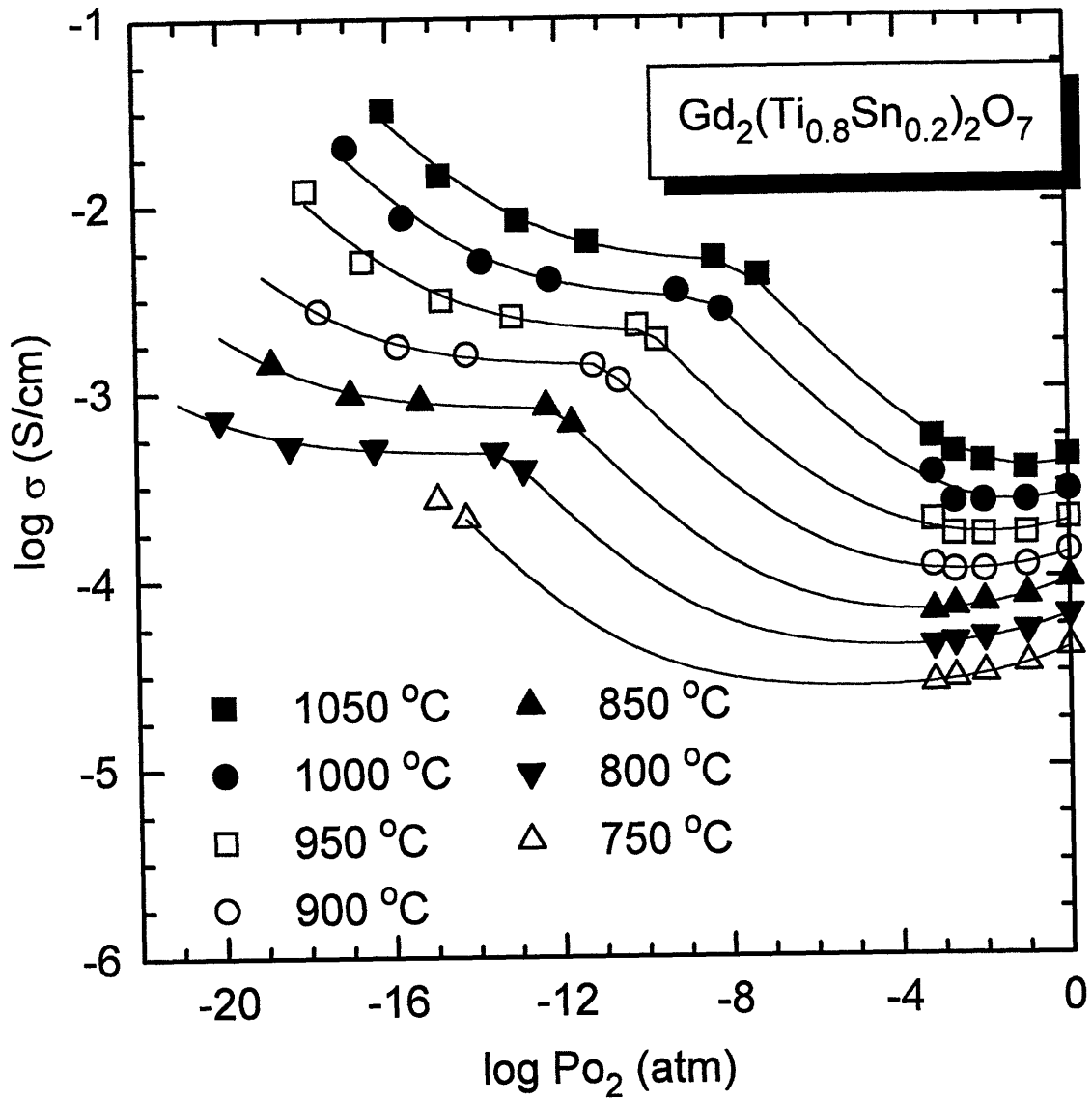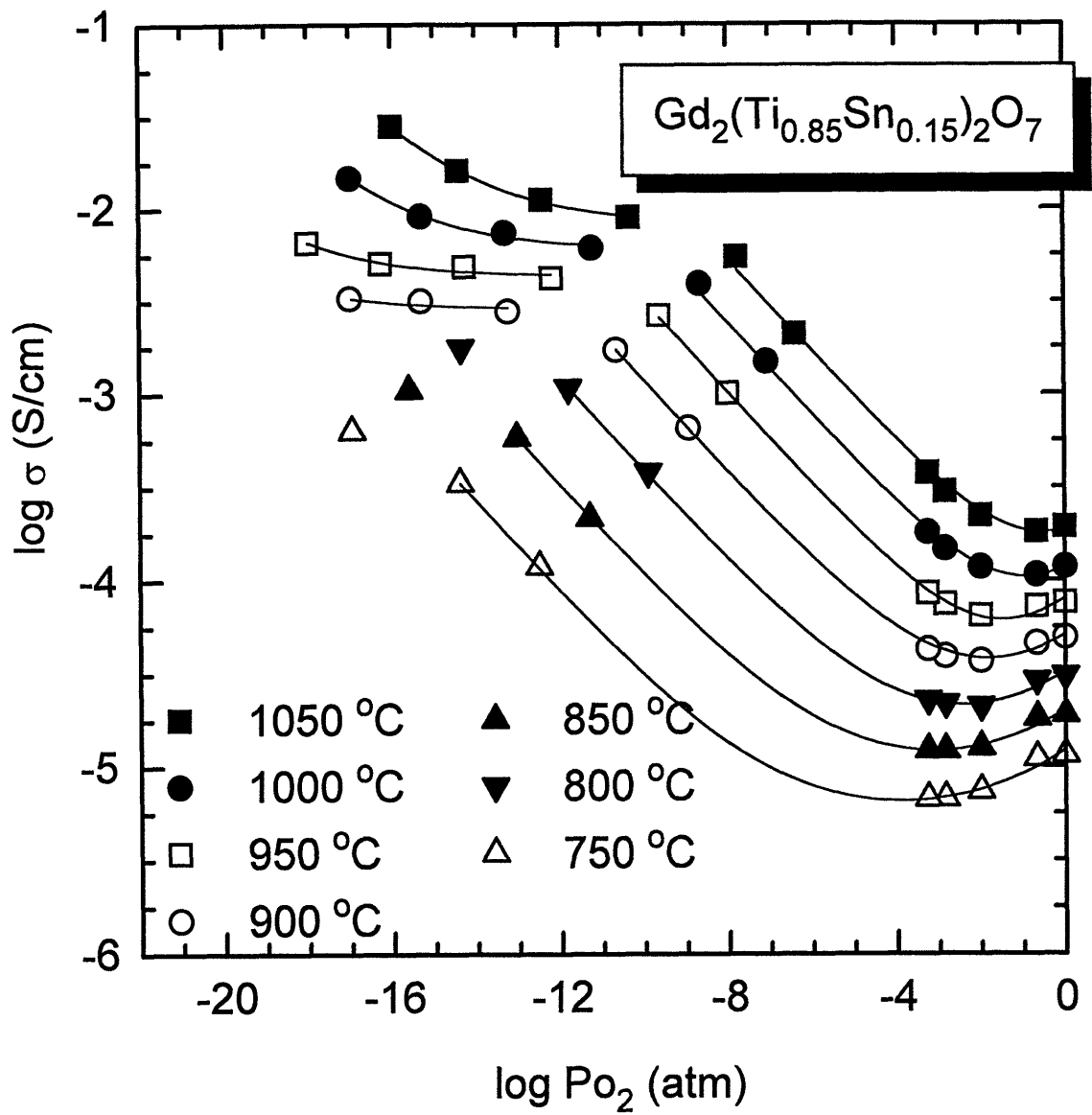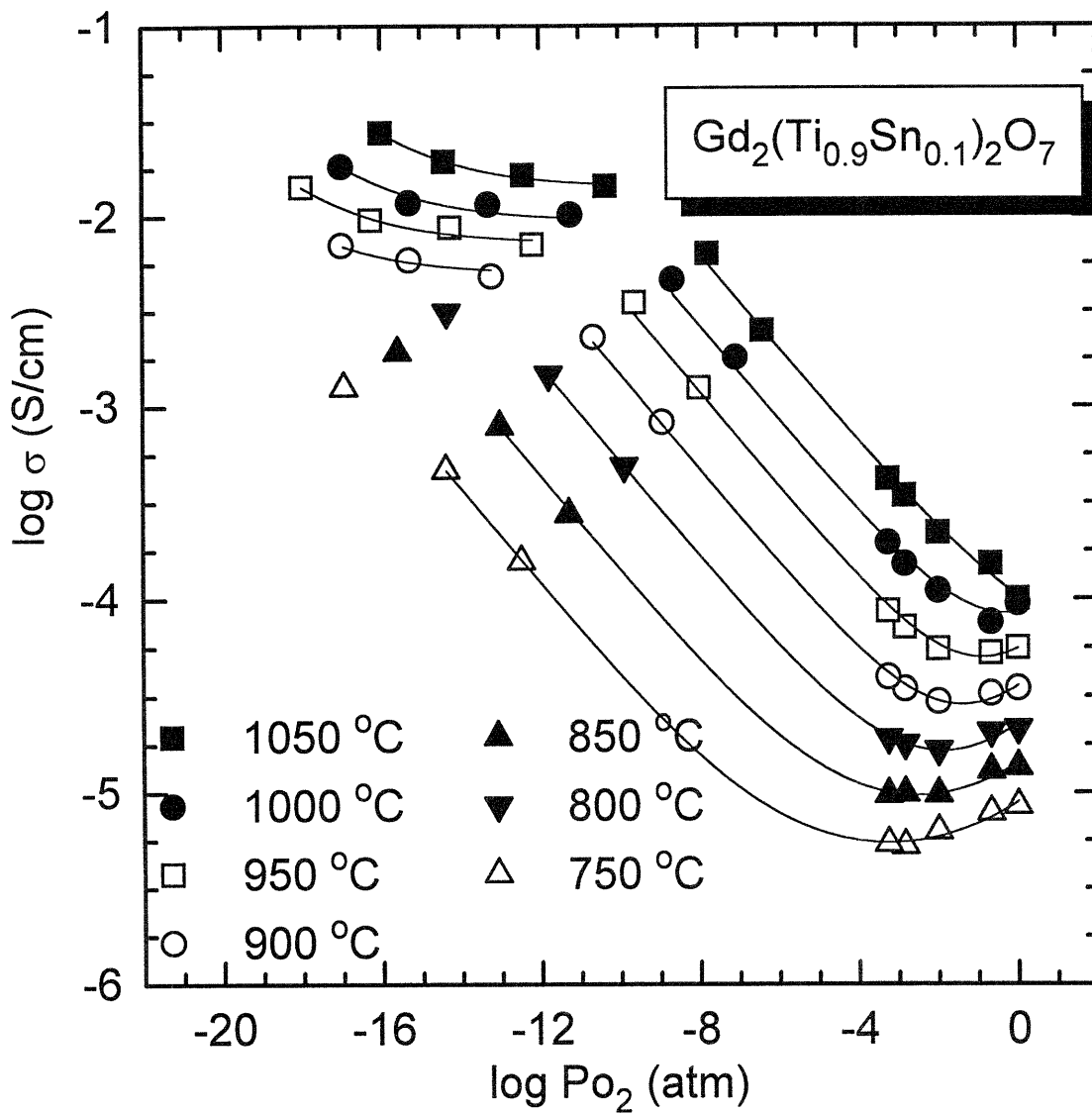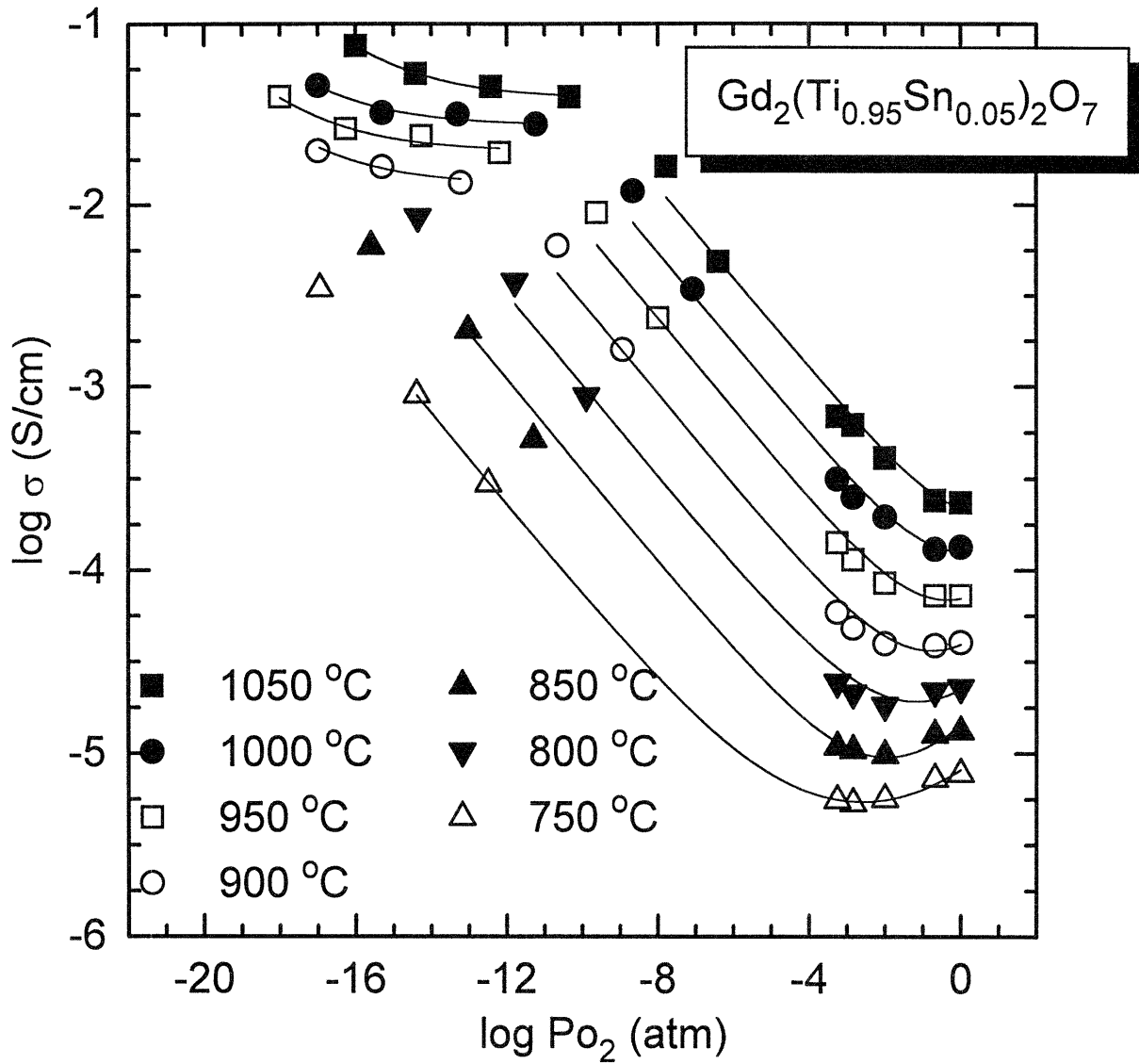Fig. 5.36 The log conductivity as a function of log oxygen partial pressure for $Gd_2(Zr_{1-x}Sn_x)_2O_7$ with x=0.6.
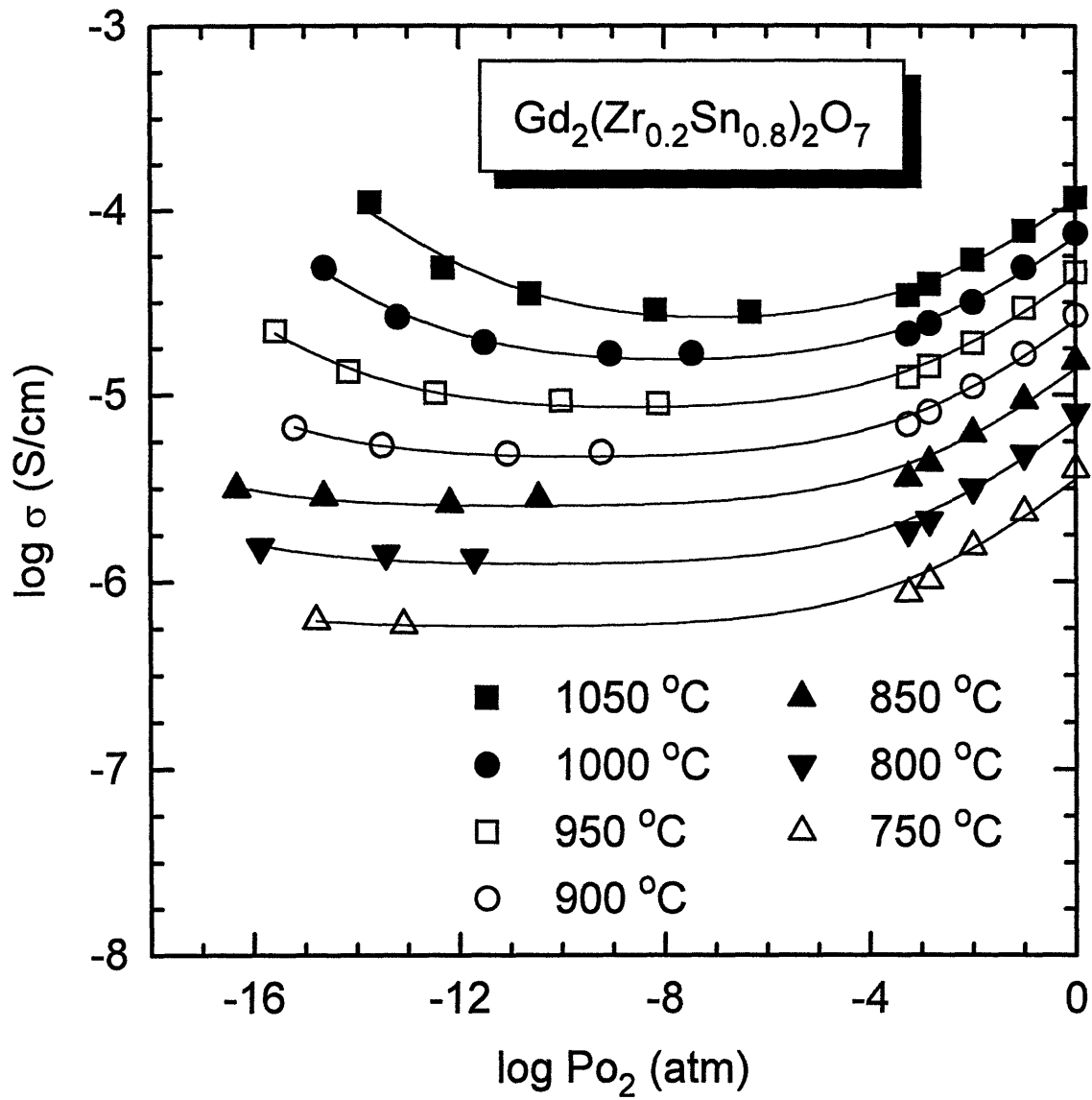
Fig. 5.37 The log conductivity as a function of log oxygen partial pressure for
$Gd_2(Zr_{1-x}Sn_x)_2O_7$ with x=0.8.
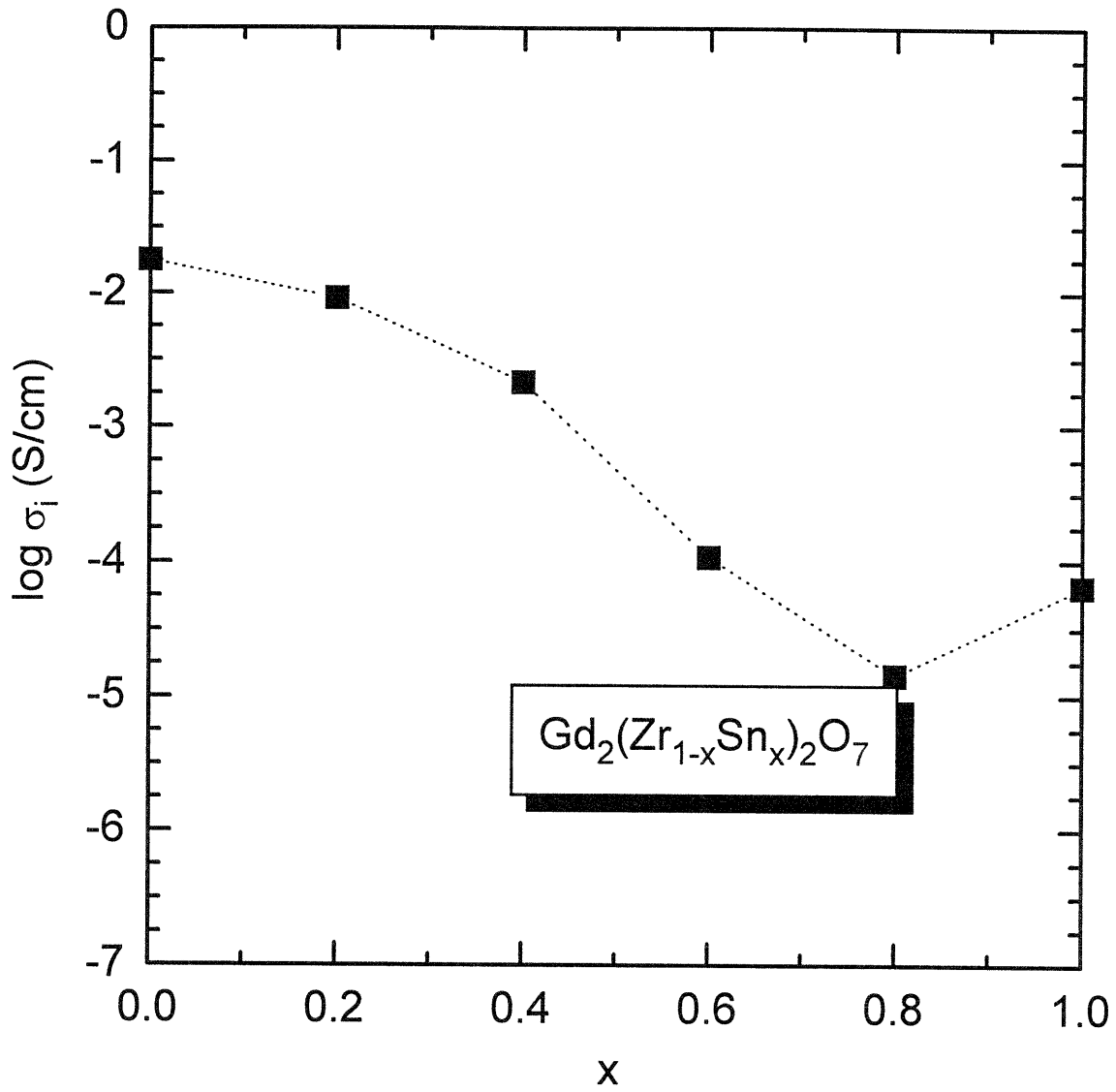
Fig. 5.38 The ionic conductivity as a function of composition at 1000 °C for $Gd_2(Zr_{1-x}Sn_x)_2O_7$. The value for $Gd_2Zr_2O_7$ is from [Moon, 1988a].
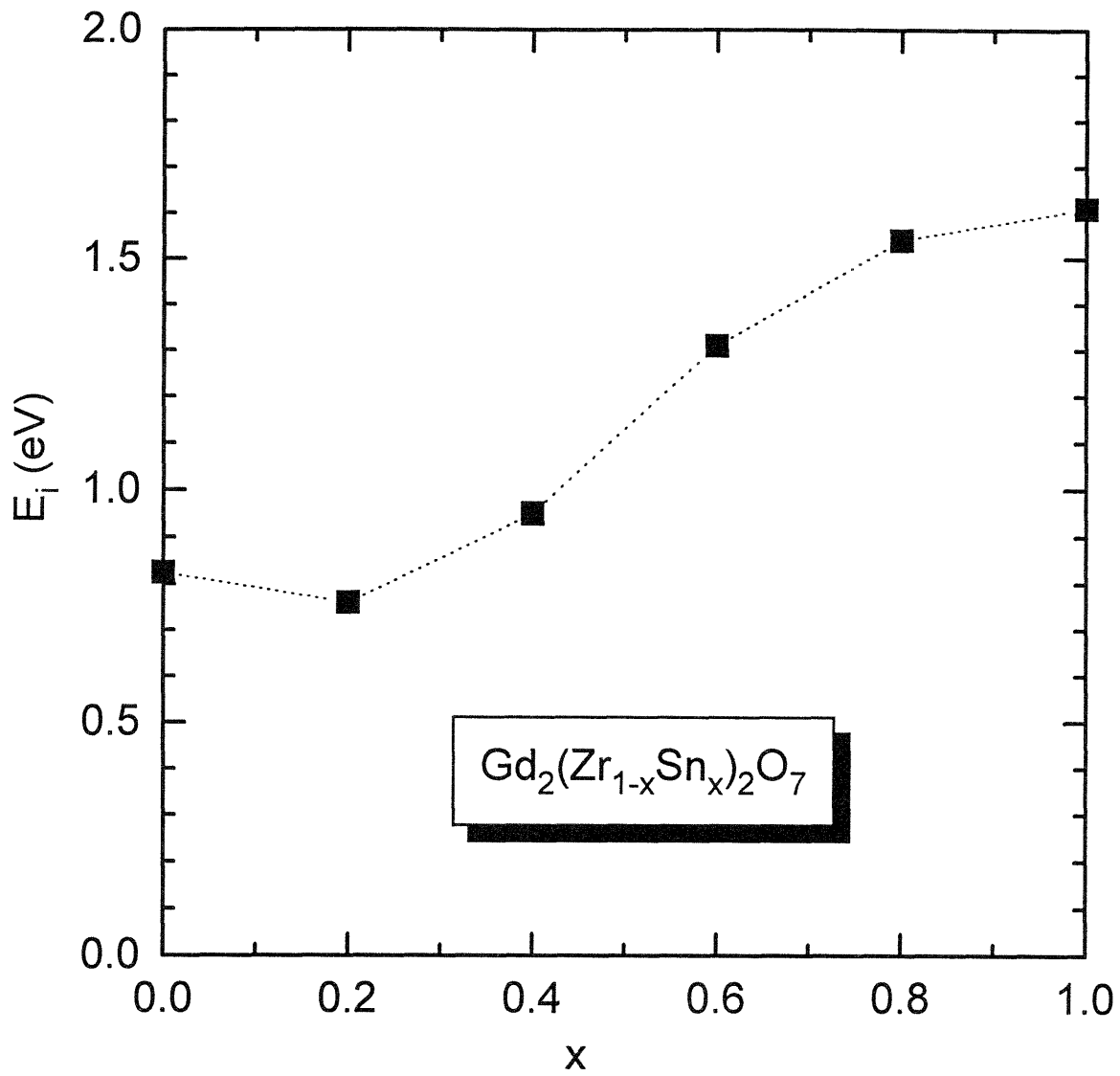
Fig. 5.39 The activation energy for ionic conduction for $Gd_2(Zr_{1-x}Sn_x)_2O_7$.
The value for $Gd_2Zr_2O_7$ is from [Moon, 1988a].
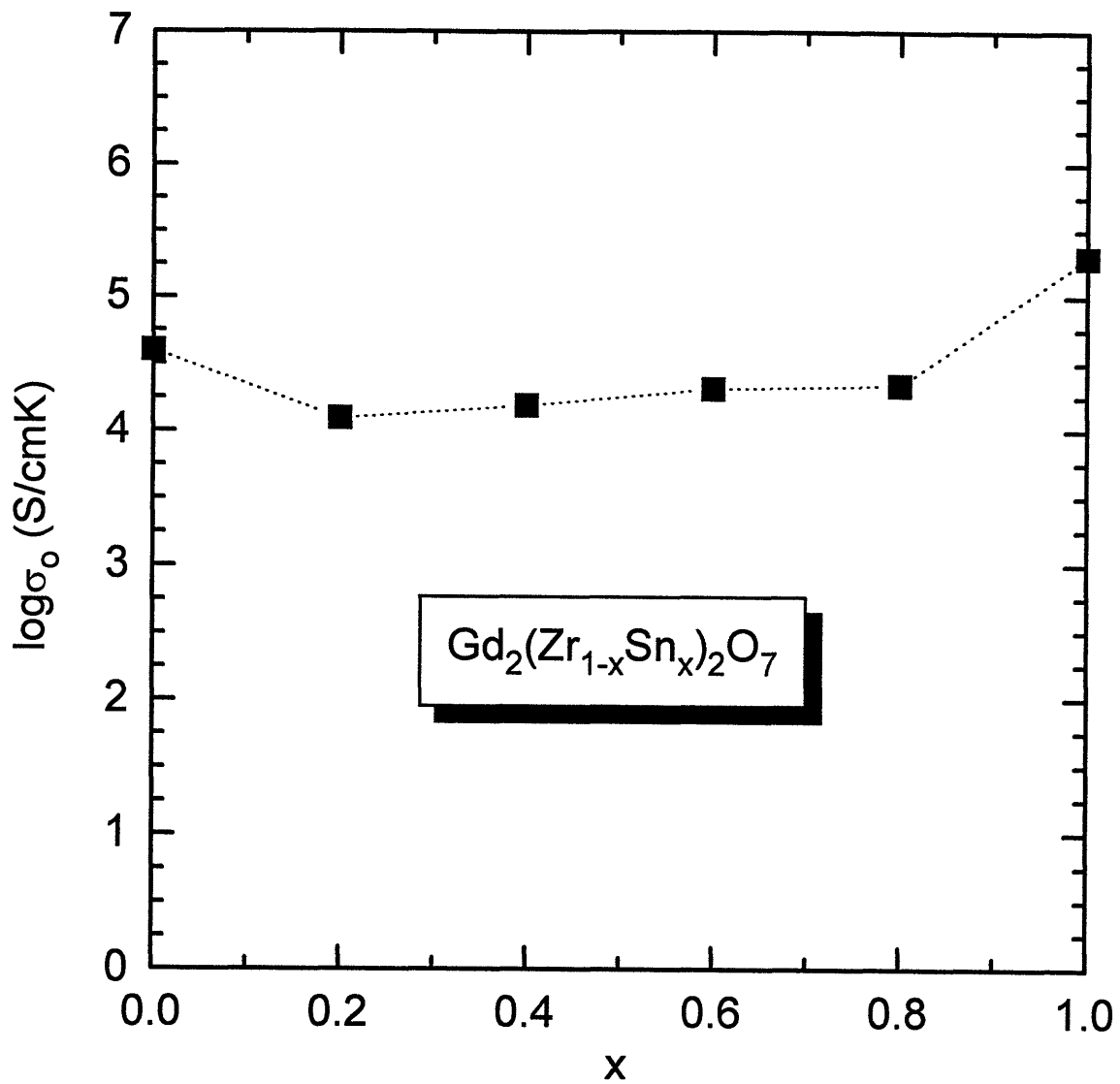
Fig. 5.40 The pre-exponential constant for ionic conduction for
Gd$_2$(Zr$_{1-x}$Sn$_x$)$_2$O$_7$. The value for Gd$_2$Zr$_2$O$_7$ is from [Moon, 1988a].

strong increase in the ionic conductivity in GZS with increasing Zr content appears, therefore, to be related largely to the decrease in E_i. On the contrary, it was σ_0 that induced the increase in the ionic conductivity in GZT as Zr replaced Ti while E_i remained nearly constant as discussed in section 2.2.1..

5.5 $Y_2(Ti_{1-x}Sn_x)_2O_7$ System

Figs. 5.41 to 5.45 represent the Po_2-dependence of the total conductivity of YST (x=0, 0.4, 0.6, 0.85, 1) for a number of isotherms. A p-type conductivity is observed for all compositions followed by predominant ionic conduction which is Po_2-independent at lower Po_2. N-type conduction was not observed for x=1 and 0.85 where the predominant ionic conductivity extends to a Po_2 of ~10^{-16} atm. For x less than 0.85 in YST, n-type conductivity appears at low Po_2 with a $-\frac{1}{4}$ dependence on Po_2 and increases with increasing Ti content in YTS.

It is surprising that $Y_2Ti_2O_7$ (YT) exhibits a significant ionic conduction at intermediate Po_2. Compared with YT and Ca doped YT data measured by Kramer et al. [Kramer, 1994], the magnitude of the ionic conductivity in YT in this measurement is the same as that in $(Y_{0.98}Ca_{0.02})_2Ti_2O_7$ rather than undoped YT. In fact, the two samples exhibit almost identical conductivities in terms of their Po_2 dependence and the magnitude of the conductivity at a given temperature. This similarity indicates that YT in this investigation has impurity levels equivalent to 2% acceptor dopant.

Fig. 5.46 shows the ionic component of the conductivity at 1000 °C as a function of the B site composition. A maximum is observed at x=0.4 as was
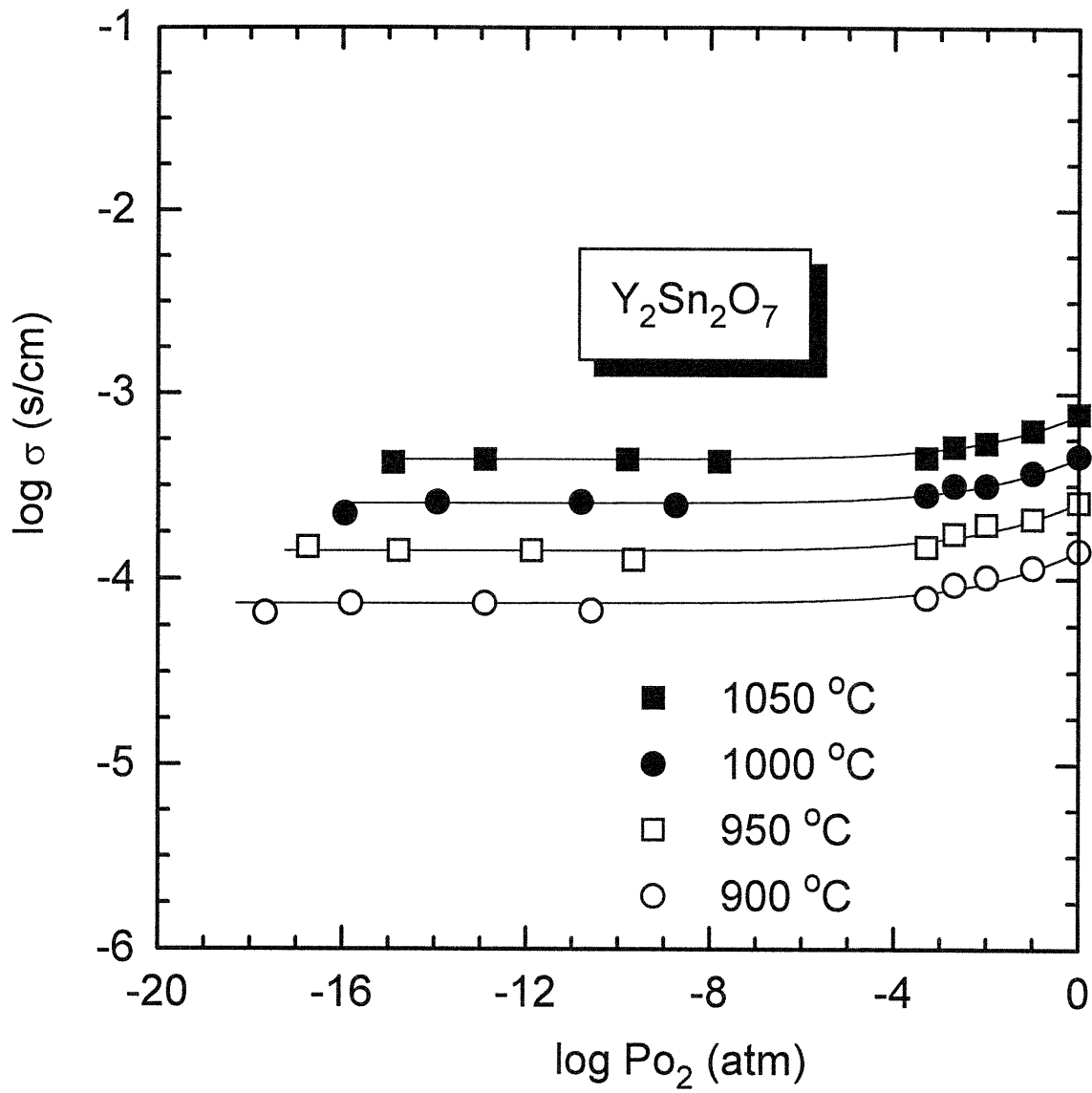
Fig. 5.41 The log conductivity as a function of log oxygen partial pressure for
$Y_2(Ti_{1-x}Sn_x)_2O_7$ with x=1.
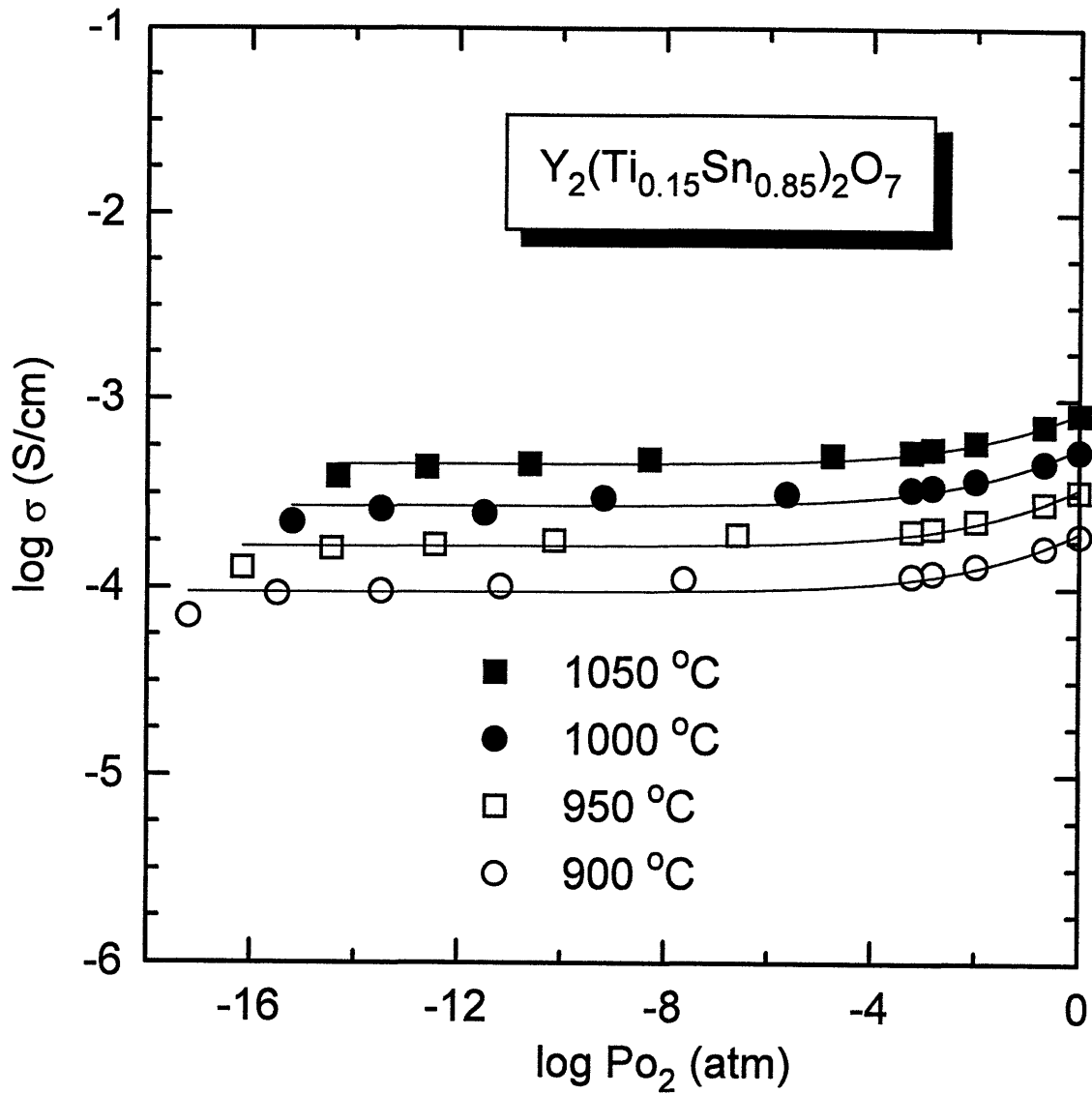
Fig. 5.42 The log conductivity as a function of log oxygen partial pressure for $Y_2(Ti_{1-x}Sn_x)_2O_7$ with x=0.85.
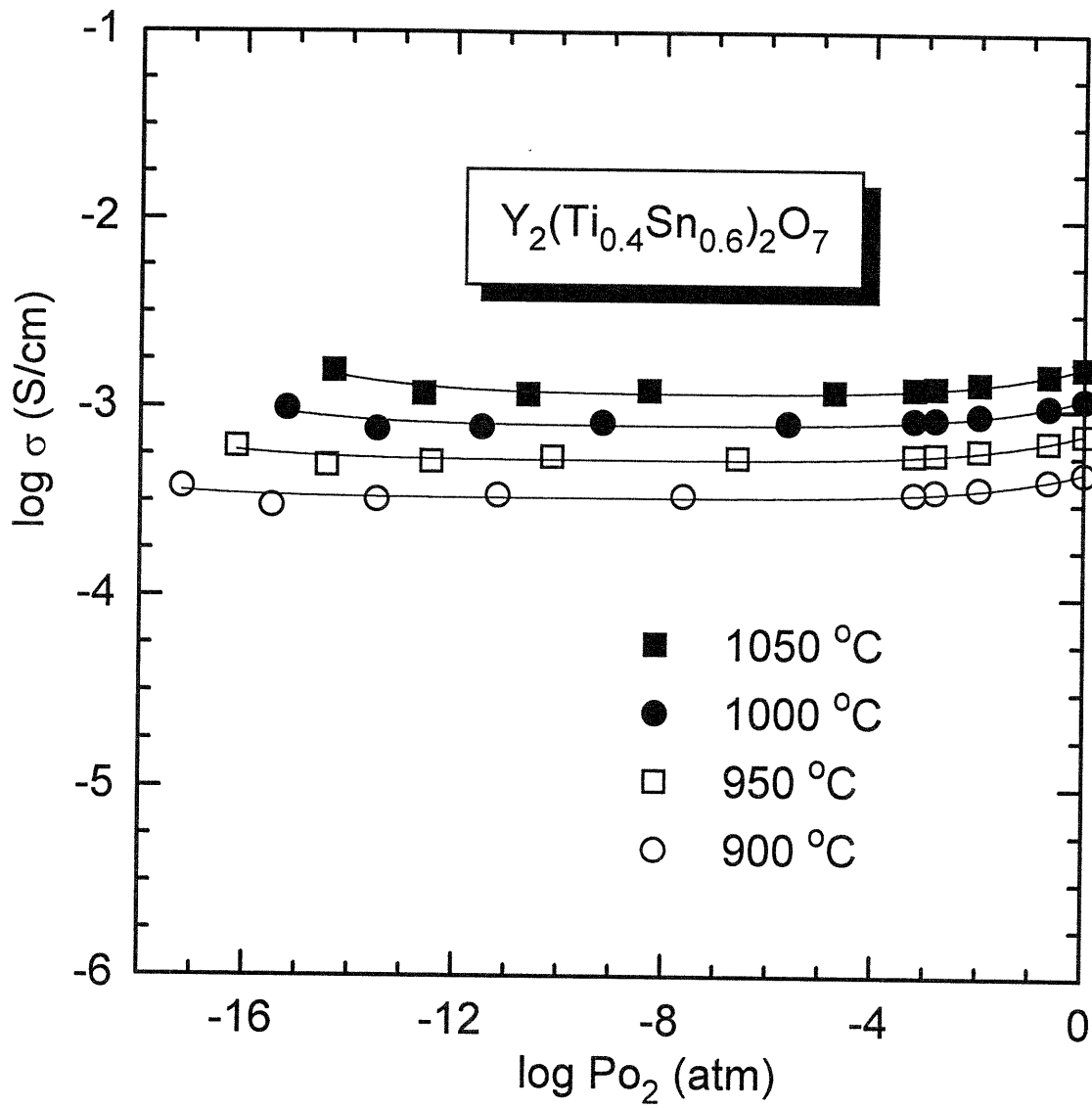
Fig. 5.43 The log conductivity as a function of log oxygen partial pressure for $Y_2(Ti_{1-x}Sn_x)_2O_7$ with x=0.6.
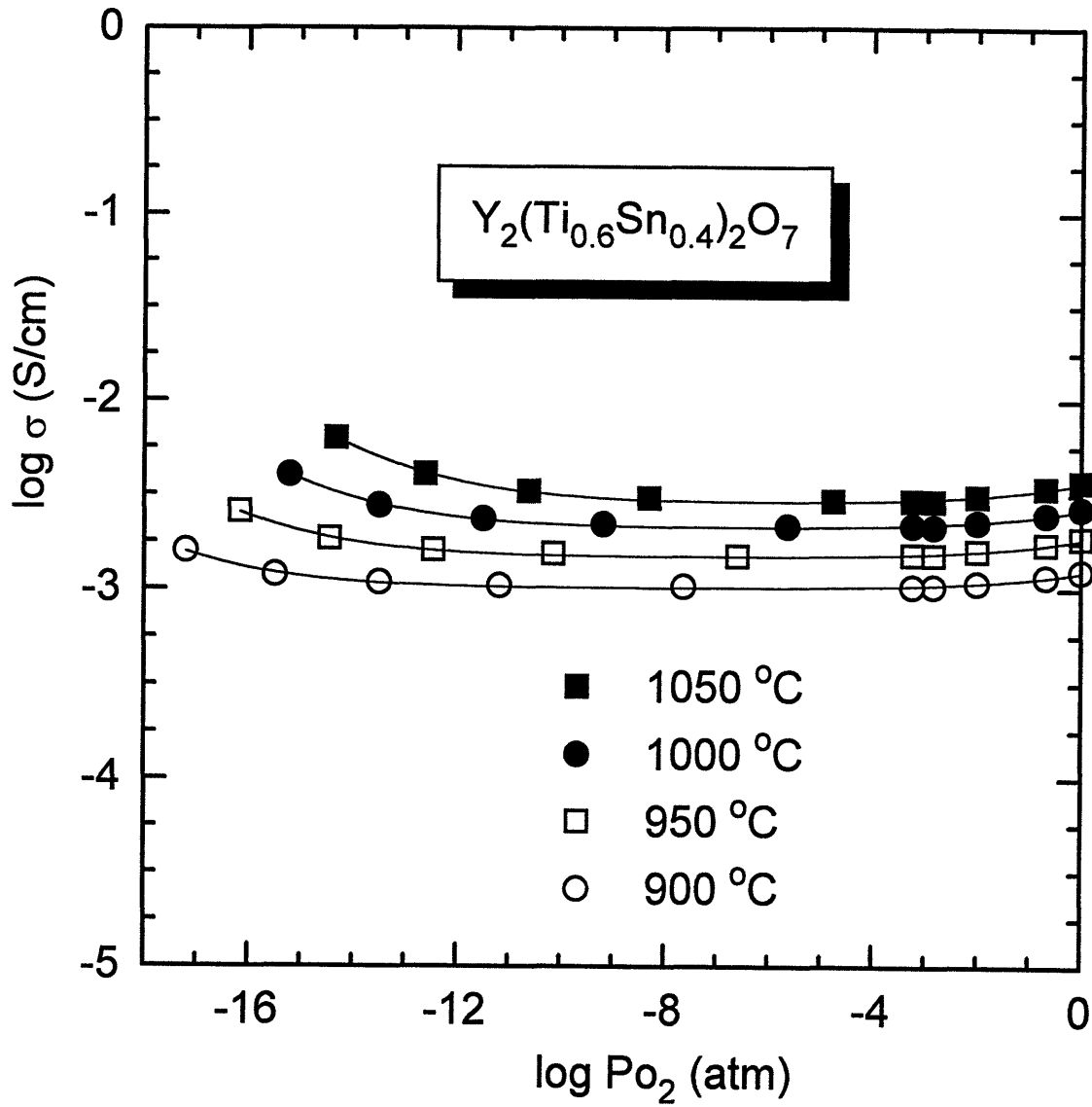
Fig. 5.44 The log conductivity as a function of log oxygen partial pressure for
Y$_2$(Ti$_{1-x}$Sn$_x$)$_2$O$_7$ with x=0.4.
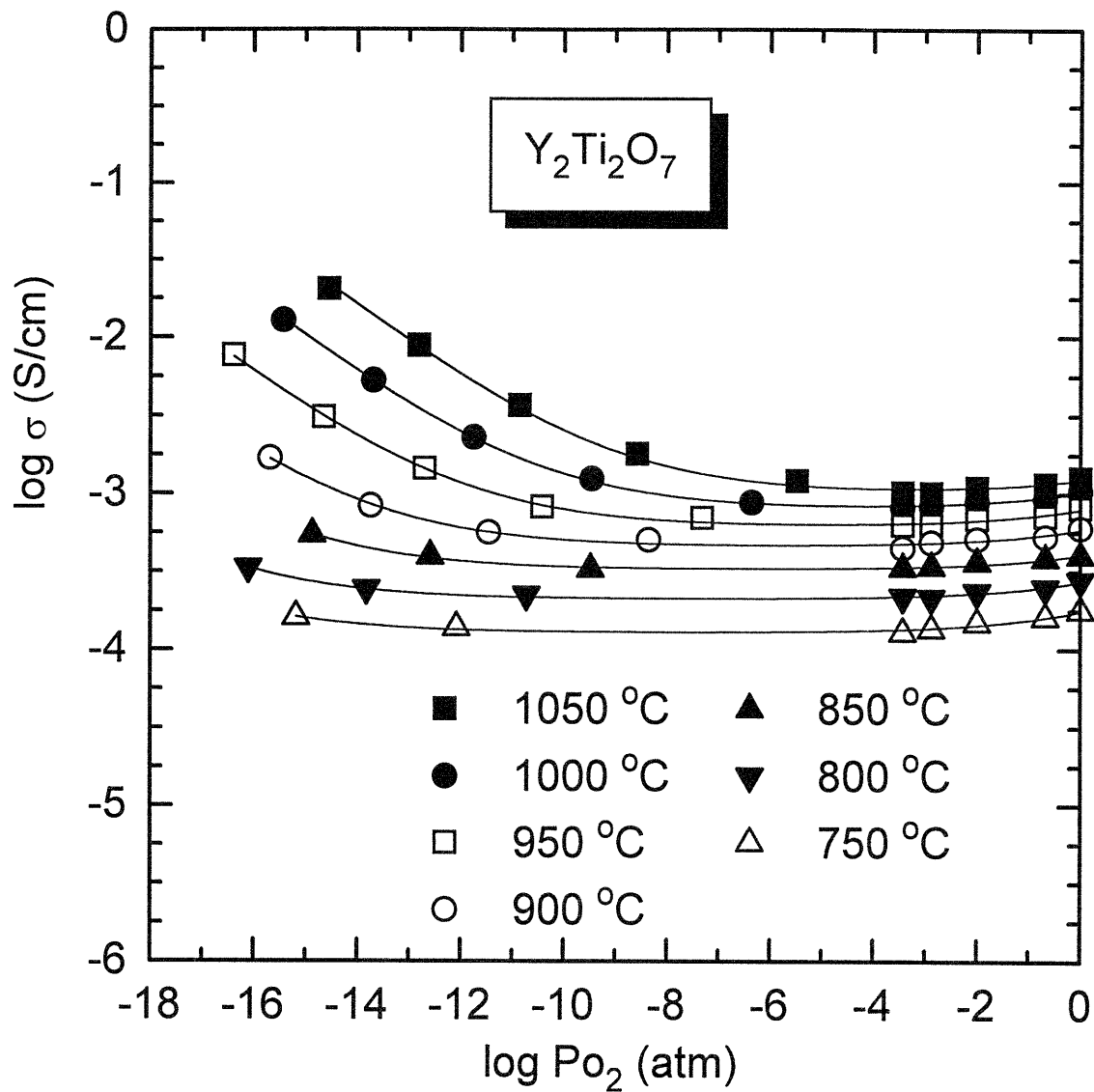
Fig. 5.45 The log conductivity as a function of log oxygen partial pressure for
$Y_2(Ti_{1-x}Sn_x)_2O_7$ with x=0.
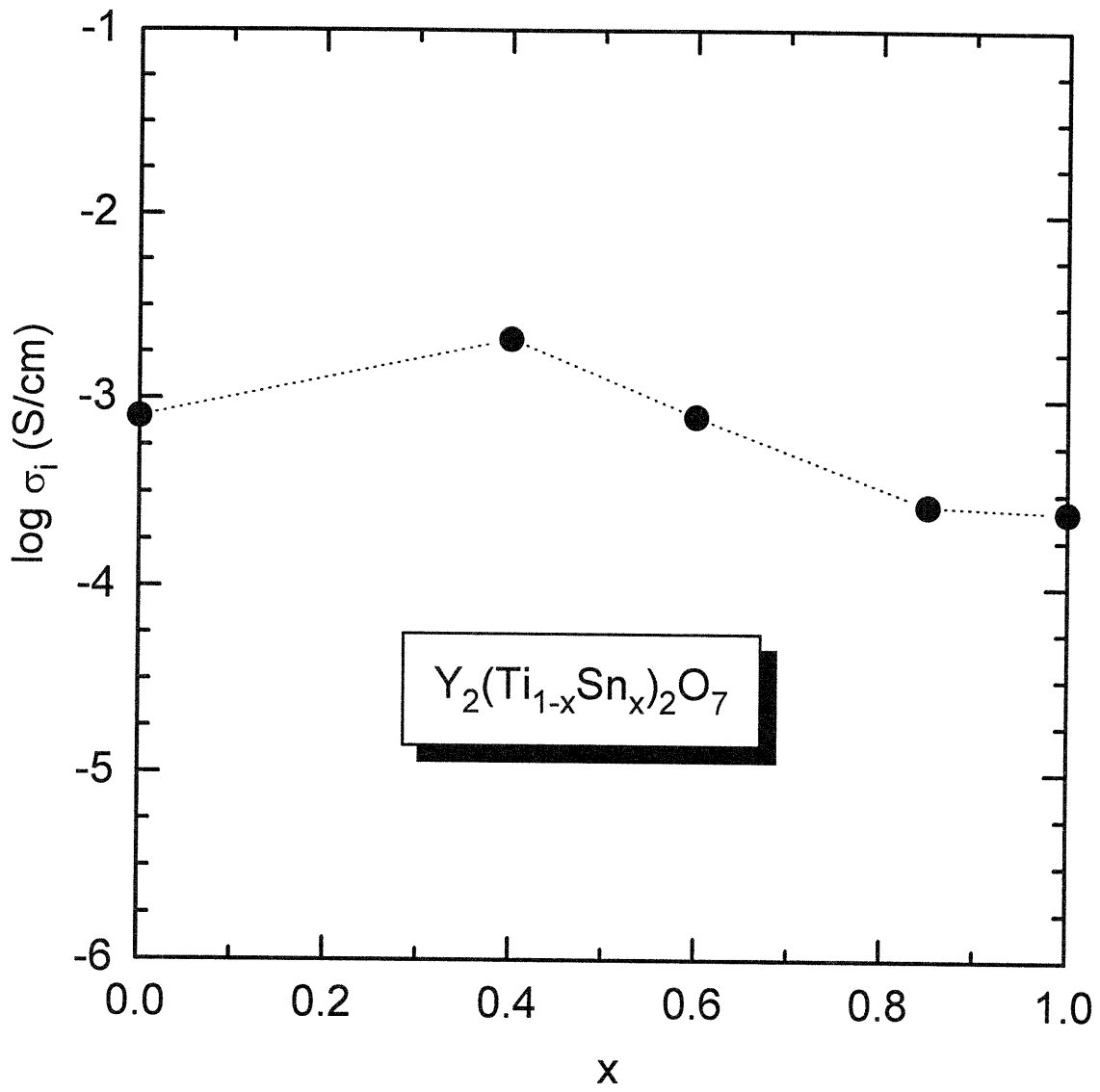
Fig. 5.46 The ionic conductivity as a function of composition and temperature for $Y_2(Ti_{1-x}Sn_x)_2O_7$.

observed in GTS. Generally the ionic conductivity in YTS is higher by one order of magnitude than that in GTS, which is opposite to the trend observed by Moon et al. on their GZT and YZT measurements.

Corresponding E_i and σ_o are presented in Figs. 5.47 and 5.48. Disregarding the end member, YTS (x=0 and 1), both E_i and σ_o seem to increase with increasing Sn content as in the case of GTS. Compared with that in GTS, it appears that higher ionic conductivity in YTS results from higher σ_o. In fact, the magnitude of E_i for YTS (x=0.4, 0.6, 0.85) increases linearly with x and matches well with those in GTS.

5.6 Hole and electronic conduction and the thermal bandgap

As discussed in section 3.1, it is possible to extract the energies of reduction, E_r, and oxidation, E_{ox}, from Eqs. (3.25) and (3.26) by calculating the activation energies for the n-type conduction, E_e, and p-type conduction, E_h, assuming that the hopping energy for electrons and holes is negligibly small. E_e and E_h are obtained from the temperature dependence of the n and p-type conductivities by fitting Eq. (3.29) to the total conductivity data. Table 5.1 tabulates the results of the calculations for the reduction and oxidation energies in the GTS and GZS systems. The thermal bandgaps are also included in the table, which can be calculated from Eq. (3.27). E_e could not be determined for compositions, GS and GZS (x < 0.6) while E_h could not be determined for compositions, GZS (x<0.6) due to the lack of measurable n and/or p-type conductivities. Fig. 5.49 presents E_g as a function of B site composition. E_g at x=0.05 in GTS is 3.62 eV, increasing to a maximum of 4.62 eV at x=0.8 in GZS and a value of 3.97 eV for further increasing Zr content in GZT. Even though E_g for pure GS could not be obtained due to the lack of a measurable n-type conductivity in the low P_{O_2} region, it appears
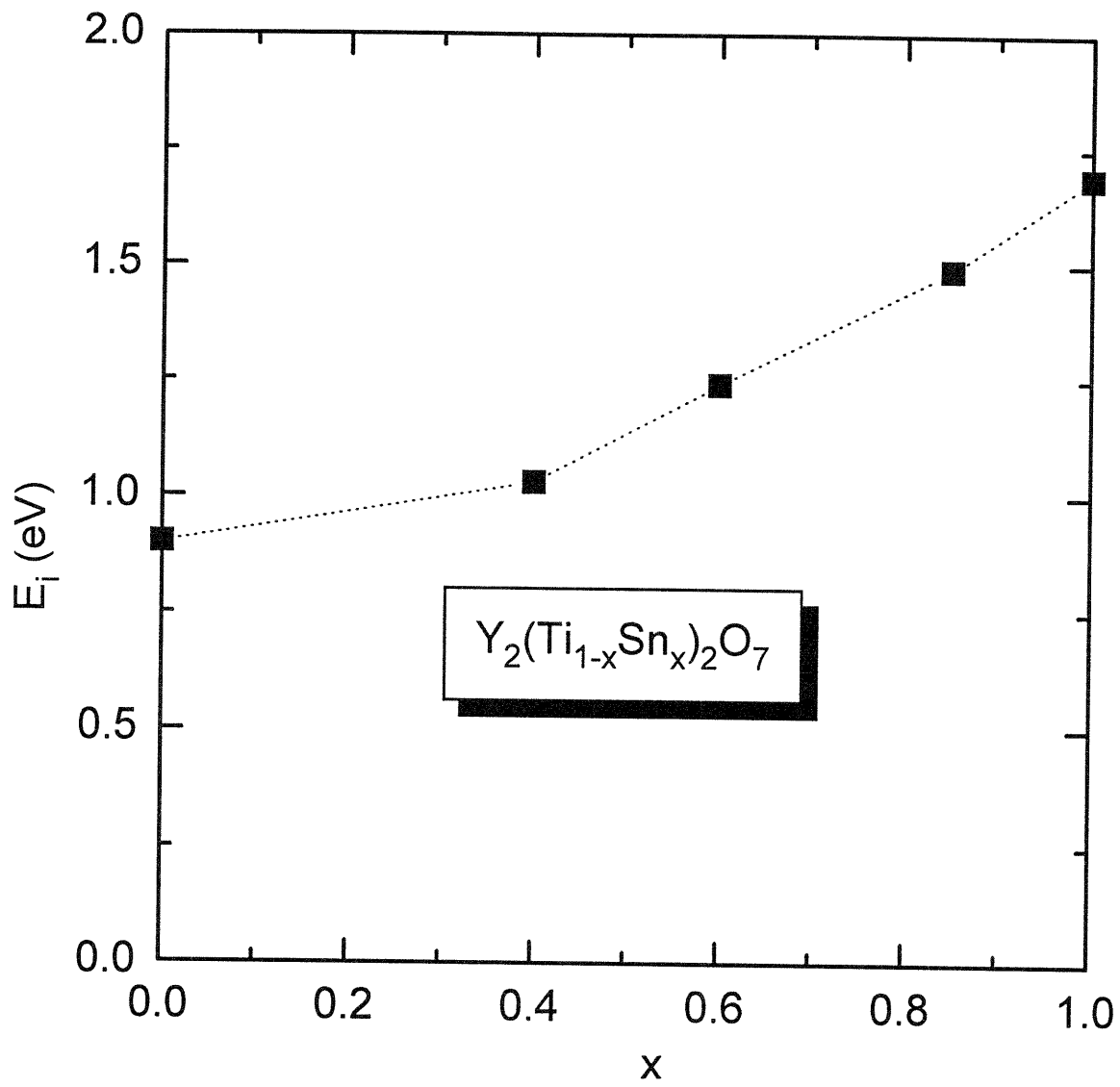
Fig. 5.47 The activation energy for ionic conduction for $Y_2(Ti_{1-x}Sn_x)_2O_7$.
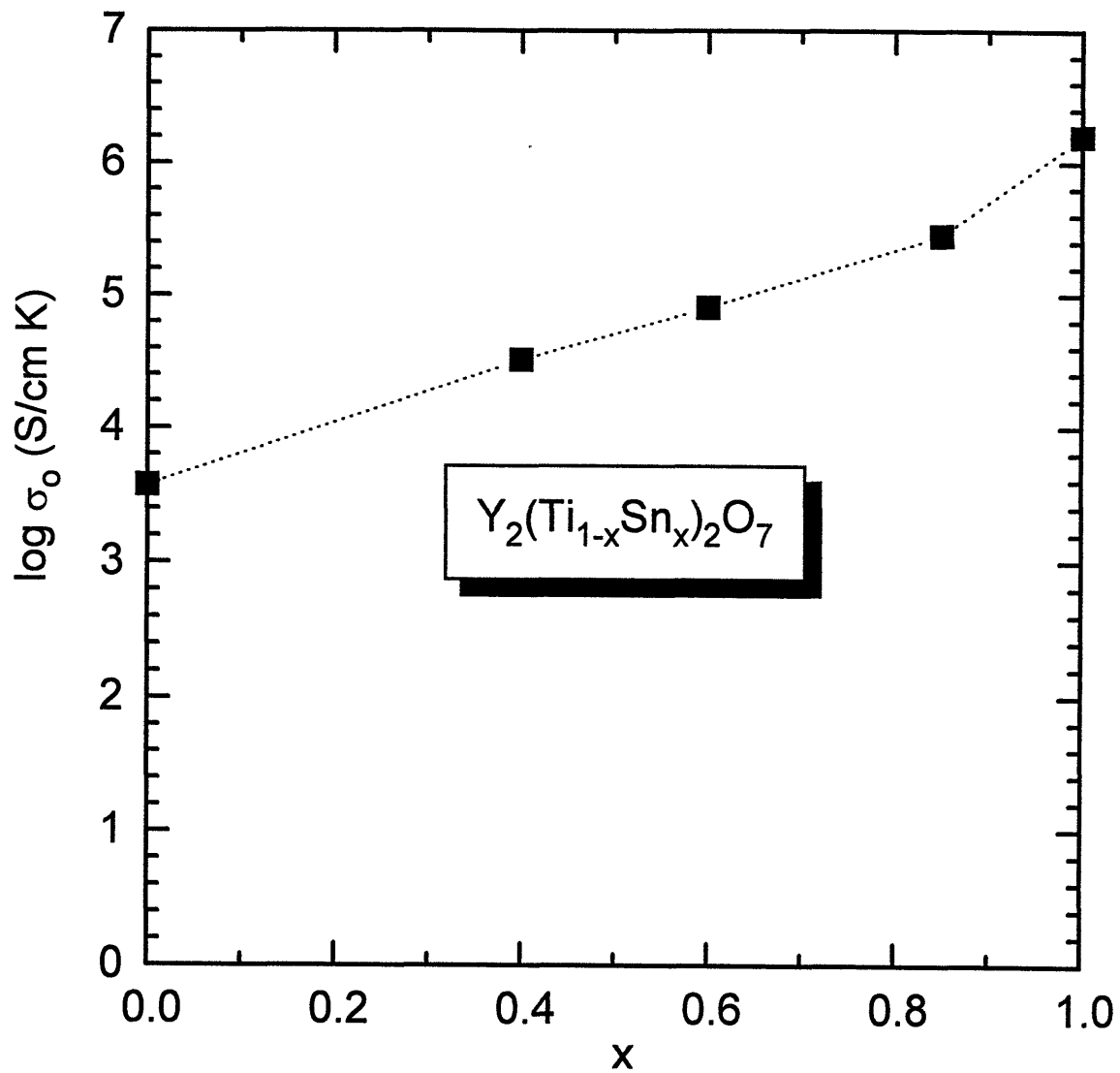
Fig. 5.48 The pre-exponential constant for ionic conduction for
$Y_2(Ti_{1-x}Sn_x)_2O_7$.
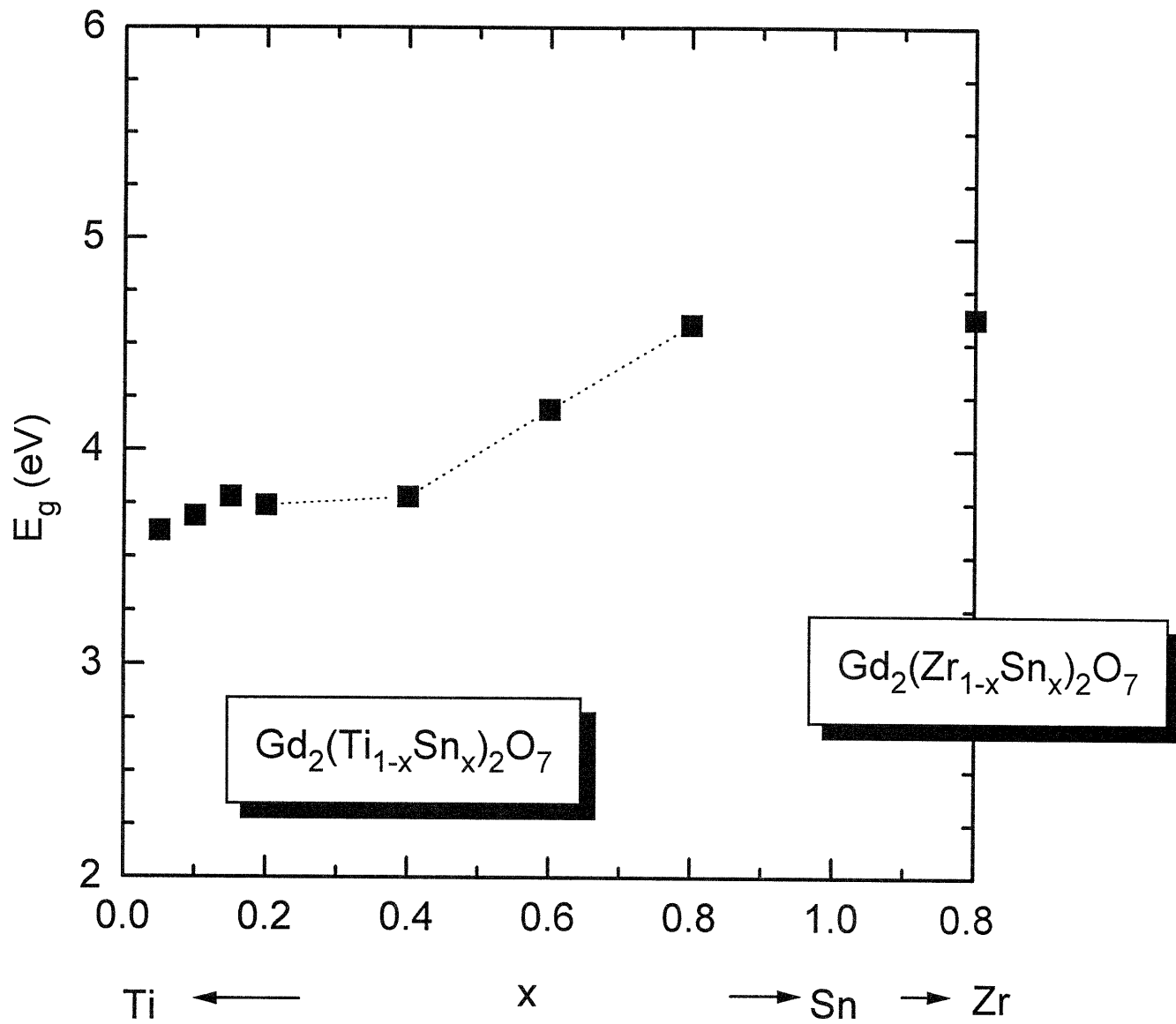
Fig. 5.49 The thermal bandgap as a function of composition in $Gd_2(Ti_{1-x}Sn_x)_2O_7$ and $Gd_2(Zr_{1-x}Sn_x)_2O_7$.

that E_g increases with either Sn or Zr replacing Ti in the GTS and GZS systems.

Composition	E_e (eV)	E_h (eV)	E_g (eV)	E_r (eV)	E_{ox} (eV)
GTS (x=0)	2.40	NA	NA	4.80	NA
GTS (x=0.05)	2.51	1.11	3.62	5.02	2.22
GTS (x=0.1)	2.55	1.14	3.69	5.1	2.28
GTS (x=0.15)	2.63	1.15	3.78	5.26	2.3
GTS (x=0.2)	2.82	0.92	3.74	5.64	1.84
GTS (x=0.4)	2.91	0.87	3.78	5.82	1.74
GTS (x=0.6)	2.99	1.2	4.19	5.98	2.4
GTS (x=0.8)	3.47	1.12	4.59	6.94	2.24
GTS (x=1)	NA	1.49	NA	NA	2.98
GZS (x=0.8)	3.19	1.43	4.62	6.38	2.86
GZS (x=0.6)	2.52	1.46	3.98	5.04	2.92

Table 5.1 The energy of reduction, oxidation and the thermal bandgap for $Gd_2(Ti_{1-x}Sn_x)_2O_7$, $Gd_2(Zr_{1-x}Sn_x)_2O_7$.

Table 5.2 tabulates E_r and E_{ox} in the YTS system from E_e and E_h. E_e could not be determined for compositions, YTS (x=0.85 and 1) due to the predominant ionic conductivity at low P_{O2}. As in the GTS and GZS systems, E_g appears to increase with Sn content.

Composition	E_e (eV)	E_h (eV)	E_g (eV)	E_r (eV)	E_{ox} (eV)
YTS (X=0)	3.08	0.82	3.90	6.16	1.64
YTS (X=0.4)	3.19	1.24	4.43	6.38	2.48
YTS (X=0.6)	3.76	1.28	5.04	7.52	2.56
YTS (X=0.85)	NA	1.33	NA	NA	2.66
YTS (X=1)	NA	1.23	NA	NA	2.46

Table 5.2 The energy of reduction, oxidation and the thermal bandgap for $Y_2(Ti_{1-x}Sn_x)_2O_7$.

σ_e and σ_h in GTS and YTS at 1000 °C, 1 atm is plotted in Figs. 5.50 and 5.51 as a function of Sn content. It appears that σ_e decreases readily and σ_h increases with Sn content though scatter in the data is observed possibly due to difficulties in separating out the small electronic conduction. Generally, sharp decreases in σ_e are accompanied by increases in E_e with increasing Sn content in GTS and YTS.
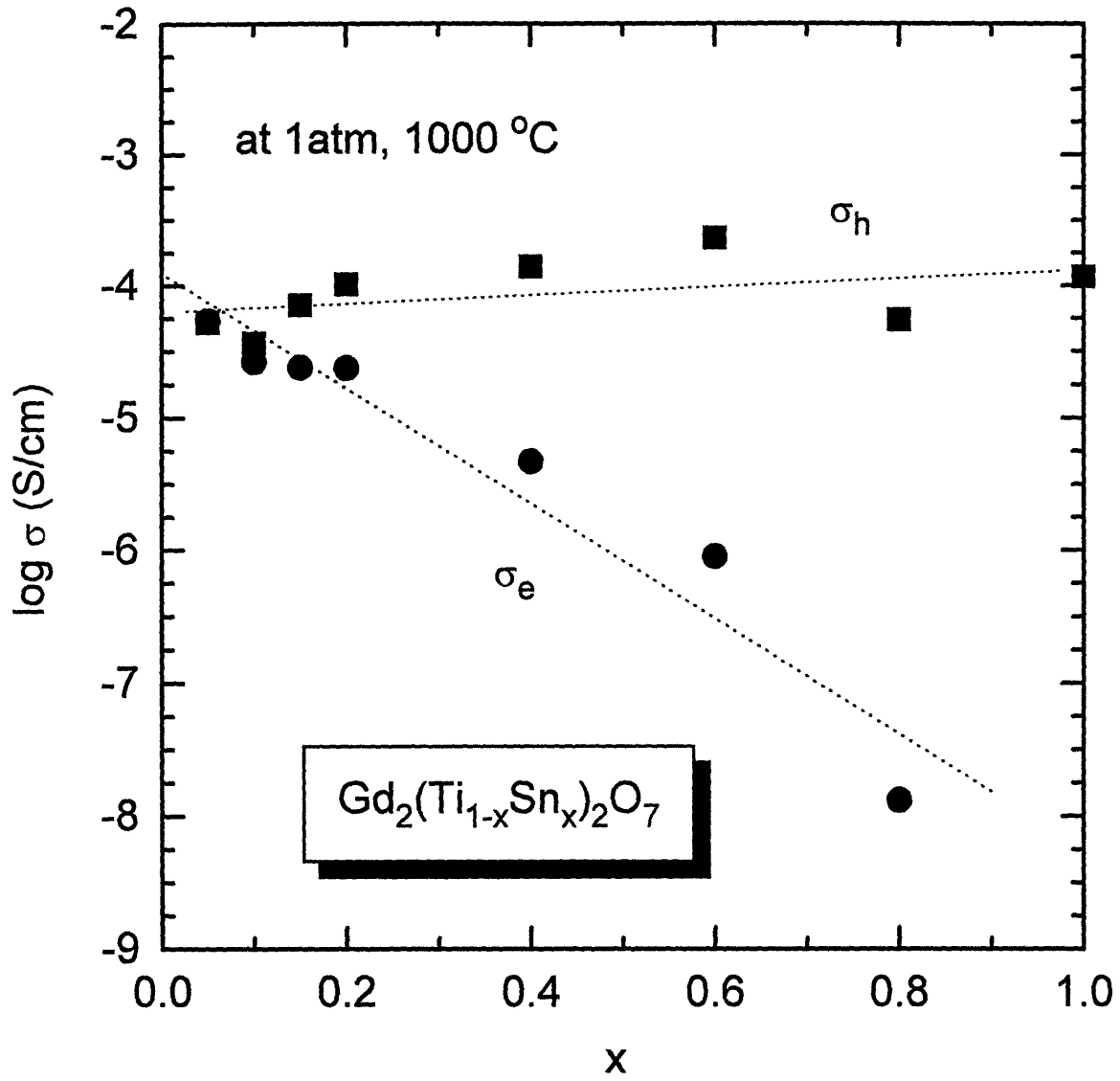
Fig. 5.50 The n-type and p-type conductivity at 1000 °C , 1 atm of Po2 in Gd2(Ti1-xSnx)2O7.
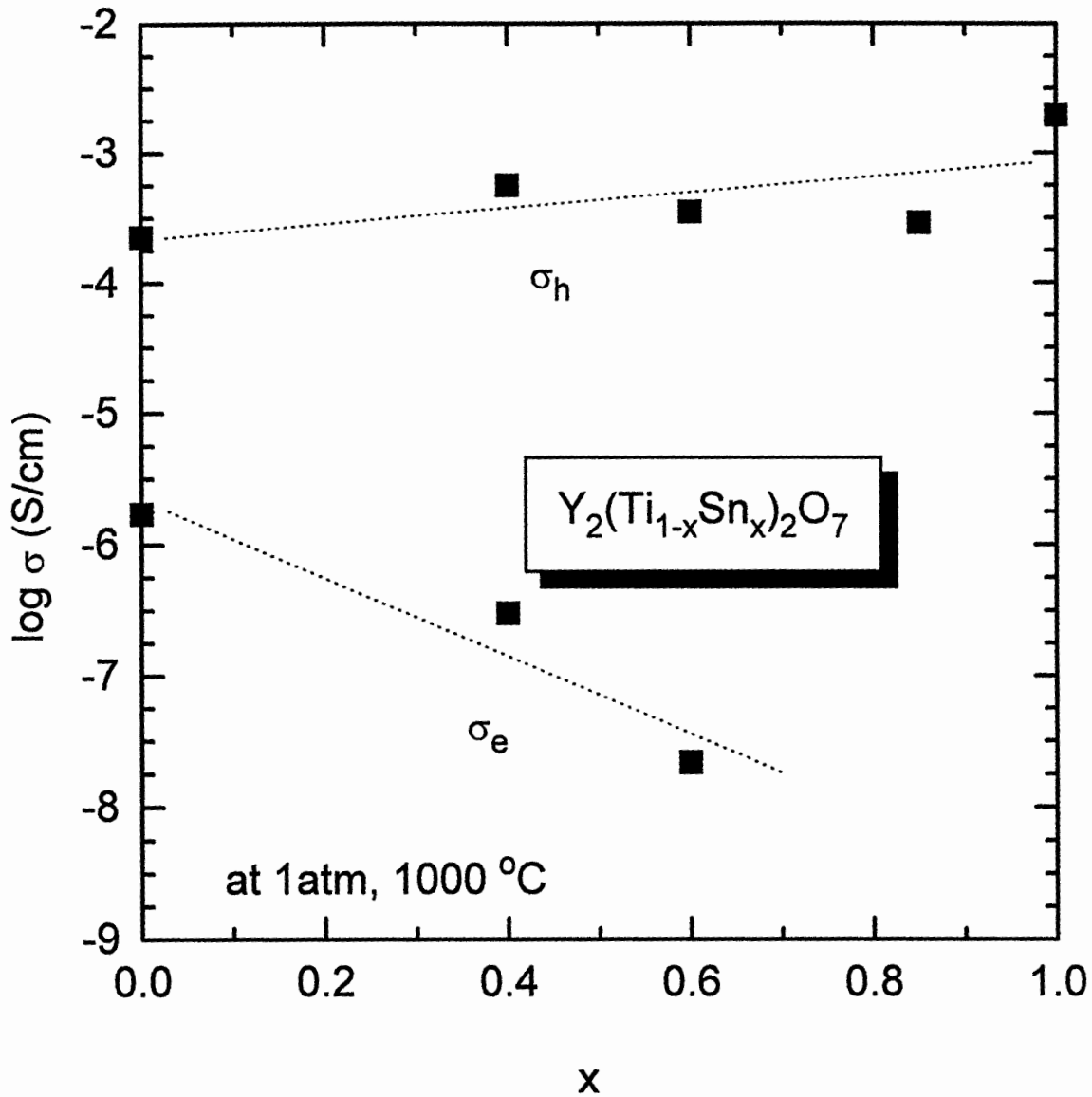
Fig. 5.51 The n-type and p-type conductivity at 1000 °C , 1 atm of P_{O_2} in $Y_2(Ti_{1-x}Sn_x)_2O_7$.

5.7 Dielectric Constant measurements

The dielectric constant was calculated using equation (3.35) for GTS (x=0.2, 0.4, 0.6, 0.8 and 1) from the frequency at the maximum of the bulk semicircle in the impedance spectrum. Disk shaped samples were used for the dielectric constant measurements since bar shaped samples are more strongly influenced by stray capacitance due to the smaller capacitance of the bar shape.

The average dielectric constant at 800 °C is plotted as a function of composition in Fig. 5.52. The figure shows that the dielectric constant decreases from ~80 at x=0.2 to ~30 at x=1. This trend is similar to that observed in the system, $Zr_xTi_ySn_zO_4$ (x+y+z=2) shown in Fig. 2.23. The dielectric constant measured by Moon in GZT ranges from 50 ~70 which is slightly lower than that in GTS (x=0.8). The dielectric constants in GTS appear to be roughly temperature-independent in the range of 800 ~ 600 °C even though there is a slight fluctuation in data as represented by the error bar in the figure. As proposed by Moon et al. [Moon, 1988a], this fluctuation might come from an artifact of the wide variation in measuring frequencies, the slight frequency dependence of the dielectric constant or the slight deviation of the experimental complex impedance plot from ideal semicircles.

5.8 Short Circuit Current Measurements

For GTS with x<0.8, the second conductivity plateaus were observed at low P_{O_2} where the second phases begin to form as confirmed from X-ray diffraction measurements. Since the defect model in Eq. (3.29) predicts the single ionic conductivity plateau at intermediate P_{O_2}, it is not clear what is the major carrier in this second conductivity plateau. Thus short circuit and
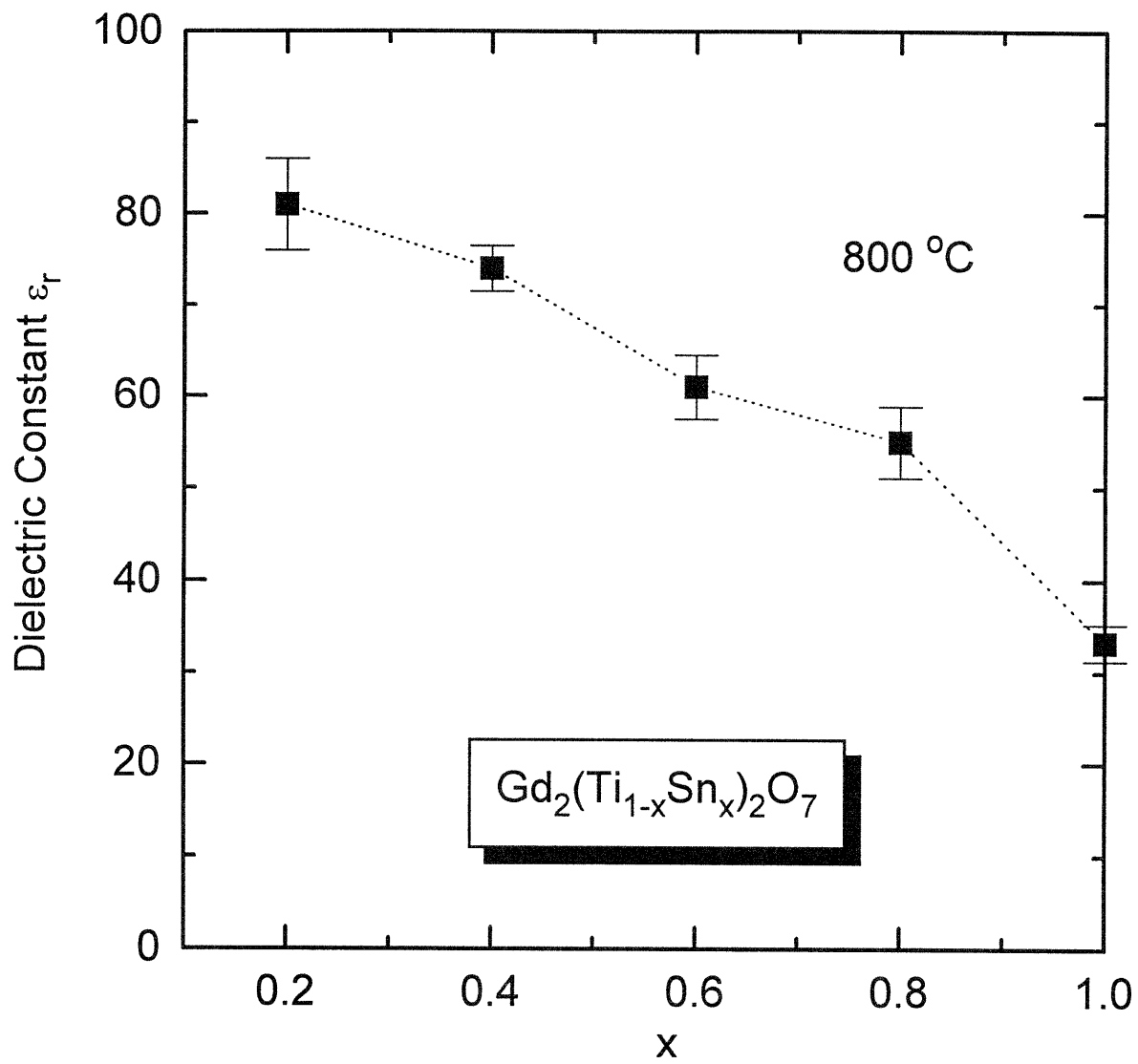
Fig. 5.52 The dielectric constant as a function of composition for
$Gd_2(Ti_{1-x}Sn_x)_2O_7$.

open circuit measurements were performed to examine the ionic conductivity as a function of P_{O_2}. Short circuit current measurements were performed for $Gd_2(Ti_{0.8}Sn_{0.2})_2O_7$ in the cell as described in Fig. 4.5 to obtain the ionic conductivity in the mixed ionic and electronic conduction regime. Fig. 5.53 shows the apparent ionic conductivity obtained by the short circuit method at 850 °C and total conductivity measured by 2-probe AC impedance spectroscopy. In the figure, the P_{O_2} indicated on the x-axis represents an average P_{O_2} as measured in the P_{O_2} gradient (i.e. $P_{O_2} = 0.5 \times (P_{O_2}{}^{I} + P_{O_2}{}^{II})$). The figure shows that the short circuit ionic conductivity remains relatively constant over the P_{O_2} region examined as predicted in the defect model in the Eq. (3.29) while the total conductivity exhibits a P_{O_2}-dependent behavior which includes electronic contributions. This results confirms that the second conductivity plateau at low P_{O_2} is mainly electronic. The magnitude of the ionic conductivity, however, is lower than that extracted from the total conductivity by 2-probe AC impedance spectroscopy. Fig. 5.54 shows the temperature dependence of the ionic conductivities extracted from the total conductivity measurement in the Fig. 5.24 using the defect model and the short circuit cell, respectively. The difference between the two measurements at 950 °C is about half an order of magnitude but increases as temperature decreases. The activation energy for the ionic conductivity as extracted from the short circuit cell is approximately double that extracted from the total conductivity measurement.

5.9 Open Circuit Voltage Measurements

Open circuit voltage measurements were performed on $Gd_2(Ti_{0.8}Sn_{0.2})_2O_7$ to obtain t_i in the mixed ionic and electronic regime as described earlier in section 3.3.1. A P_{O_2} gradient was applied across the sample by fixing $P_{O_2}{}^{I}$ on one side of the sample as the reference gas while

151
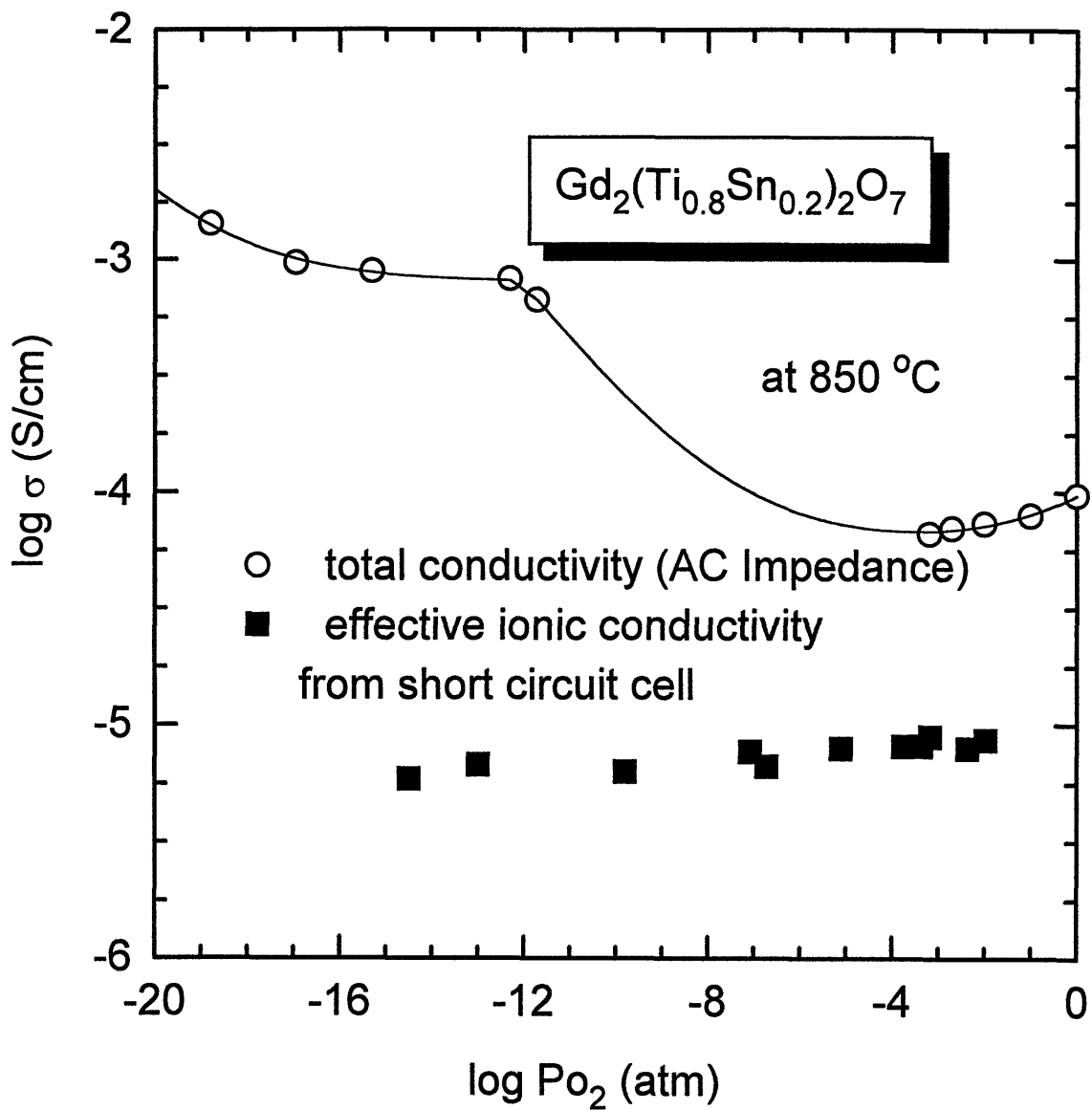
Fig. 5.53 The total conductivity from AC impedance and the apparent ionic
conductivity by the short circuit method at 850 °C for
$Gd_2(Ti_{0.8}Sn_{0.2})_2O_7$.
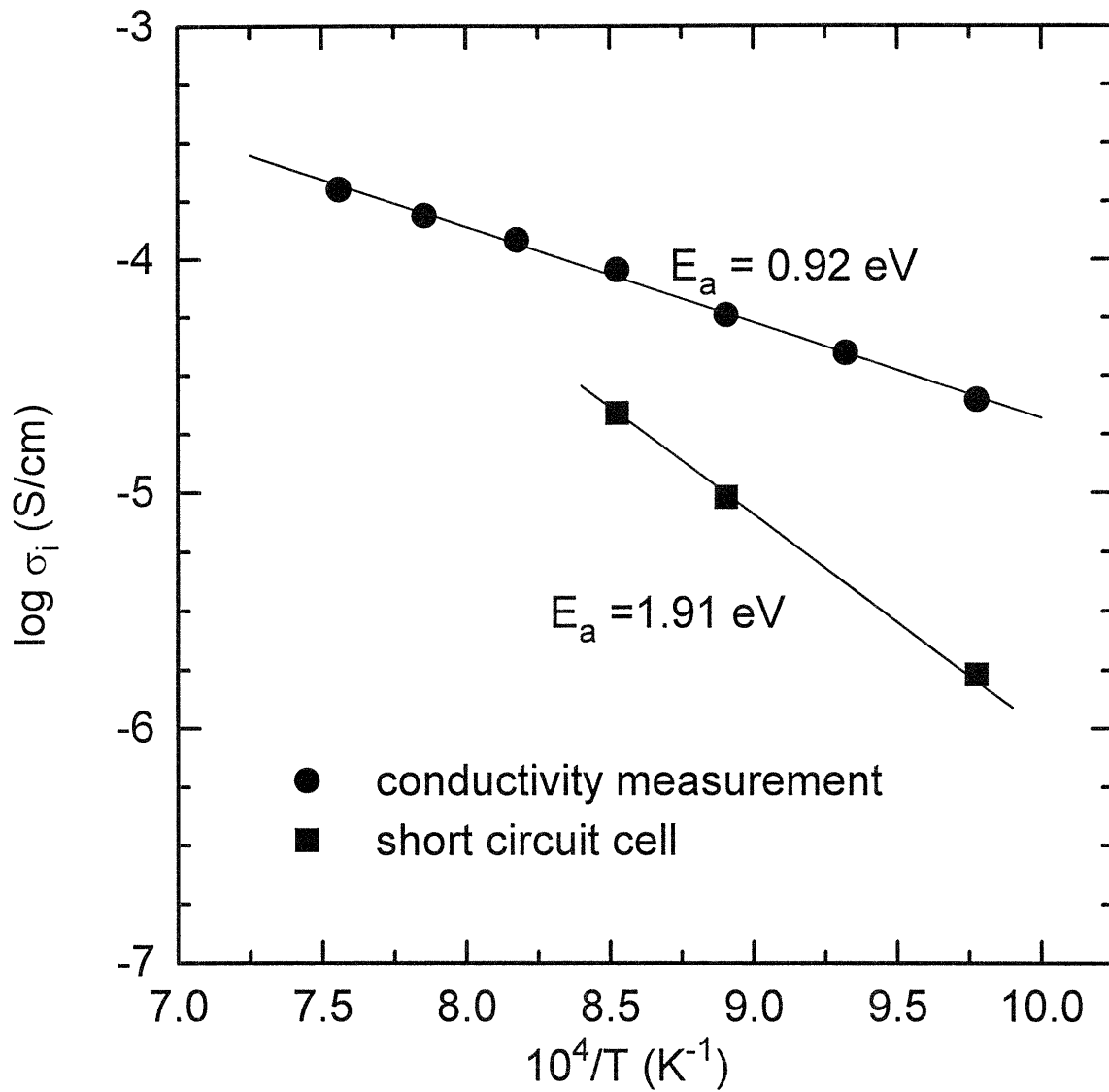
Fig. 5.54 Temperature dependence of the ionic conductivity in $Gd_2(Ti_{0.8}Sn_{0.2})_2O_7$ from the total conductivity measurement using Eq. (3.29) and the short circuit cell.

varying Po_2^{II} on the other side. Fig. 5.55 gives the open circuit voltage, V_{oc}, measured at various Po_2^{II} with Po_2^{I} fixed at 10^{-15} atm at 900 °C. Po_2^{II} was initially 10^{-15} atm which was gradually increased to 1 atm. V_{oc} is observed to initially slowly increase from 0 to ~60 mV at low Po_2^{II} up to 10^{-10} atm and then increase rapidly to ~450 mV at 1 atm. Fig. 5.56 shows the corresponding t_i obtained from Eq. (3.44) by differentiating V_{oc} with respect to $lnPo_2^{II}$. It appears that as Po_2 decreases from 1 atm, t_i increases reaching a maximum of ~0.8 between 10^{-4}~10^{-6} atm and then dropping down to ~ 0.1 at 10^{-12} atm. Fig. 5.57 gives t_i calculated from Fig. 5.24 for GTS (x=0.2) assuming that the first plateau at the high Po_2 region represents the "only" ionic conductivity of the sample and dividing it by the total conductivity as shown by the solid line in the figure. Comparing this calculated value t_i with the t_i determined from open circuit voltage measurements (Fig. 5.56), one finds good agreement suggesting that the plateau at high Po_2 represents ionic conduction while the second plateau at low Po_2 represents largely electronic conduction.

154
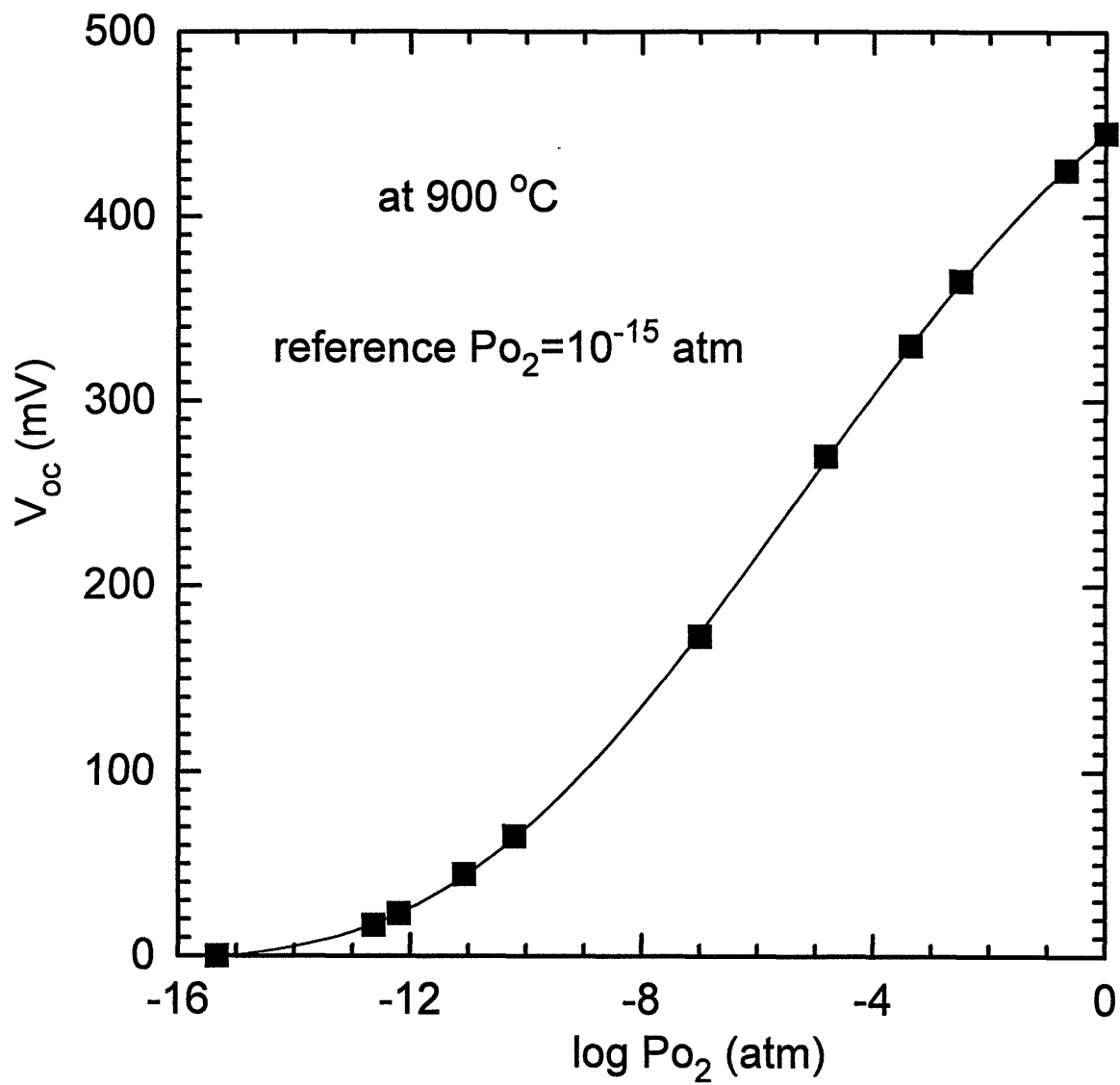
Fig. 5.55 The open circuit voltage as a function of Po_2^{II} for $Gd_2(Ti_{0.8}Sn_{0.2})_2O_7$ with a reference Po_2^I of 10^{-15} atm at 900 °C.
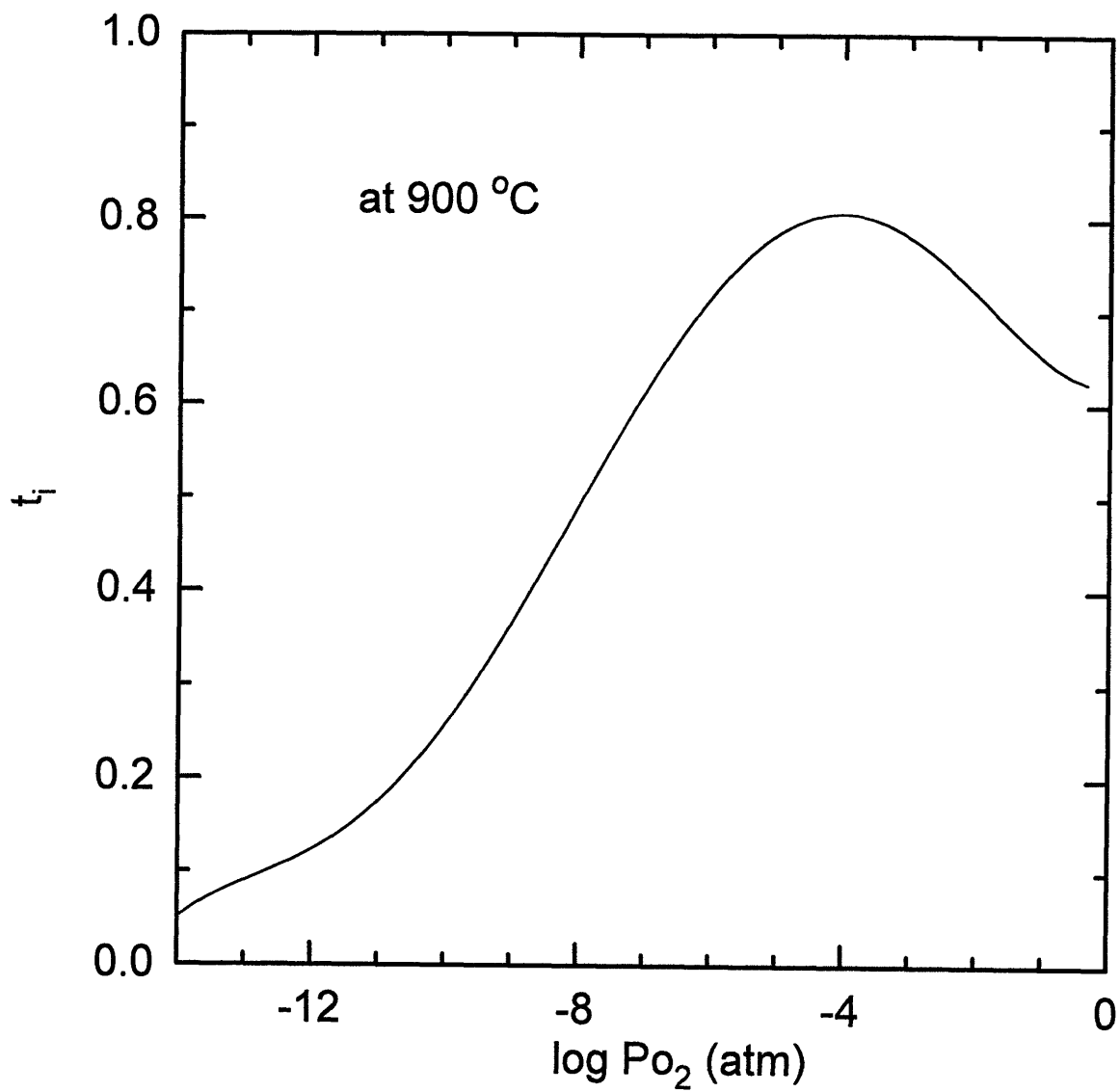
Fig. 5.56 The calculated ionic transference number as a function of oxygen partial pressure from the data in Fig. 5.55 using Eq. (3.44).
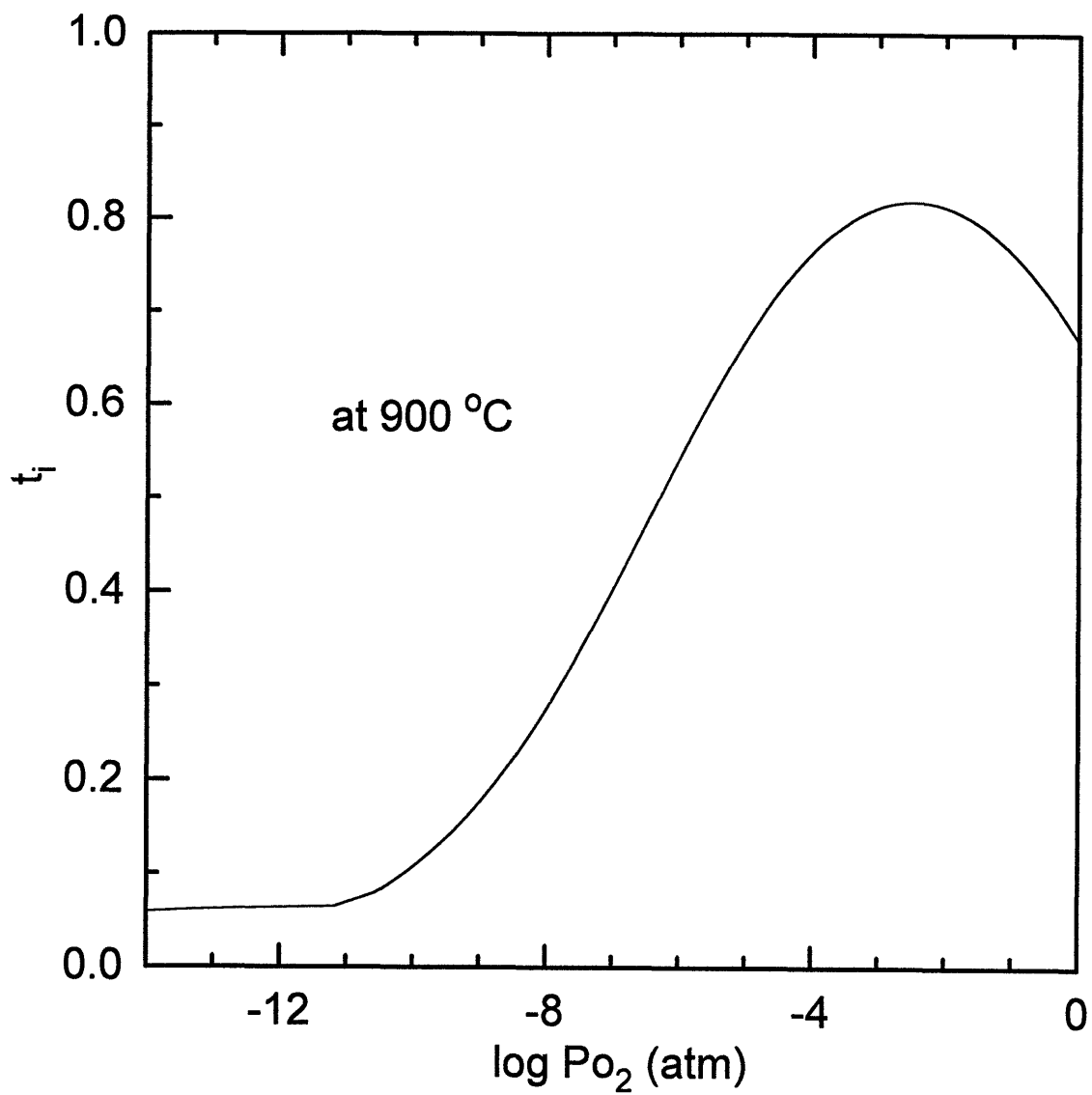
Fig. 5.57 The calculated ionic transference number as a function of oxygen
partial pressure from the data in Fig. 5.24 using Eq. (3.4) and
(3.29).

6 Discussion

This chapter begins with a discussion regarding the calculated K_F and μ_i in GS and the composition dependence of ionic conductivity in the GTS and GZS systems. X-ray diffraction analysis provides important input regarding structural disorder in GTS and its influence on the ionic conductivity. The electrical conductivity data of the GTS and YTS systems are then compared and discussed. The defect parameters such as the E_r and E_g are then examined followed by an analysis of the ionic conductivities derived by the short circuit and open circuit cell methods.

6.1 Disorder and Mobility in Stannate Pyrochlores

Fig. 5.13 and Fig. 2.14 show that the magnitude of the P_{O_2} independent-ionic conductivity in GS is very low (~10^{-4} S/cm at 1000 °C) relative to that in GZT with high Zr content. The question arises as to the source of this low ionic conductivity in GS. As shown in Eq. (3.1), the ionic conductivity consists of two parts - carrier concentration and mobility.

We first examine the carrier concentration, which is the oxygen vacancy concentration in the case of pyrochlores. As mentioned in chapter II, the r_A/r_B ratio was found to be an important factor in determining intrinsic disorder in GZT. From a lattice constant comparison, $Gd_2(Ti_{0.2}Zr_{0.8})_2O_7$ has the same average B site cation radius as GS as discussed in section 2.3. It has been estimated from σ_0 that the oxygen vacancy density is ~0.3 % in $Gd_2(Ti_{0.2}Zr_{0.8})_2O_7$ [Moon, 1988a]. This value was obtained by utilizing Eq. (3.29) with calculated values of σ_0 derived from the ionic conductivity data. This procedure, however, was based on a comparison of σ_0 in GZT (x=0.3 and 0.8), which considered the E_F of 0.25 eV in GZT (x=0.3) twice in calculation of

the oxygen vacancy concentration resulting in a lower estimation of the actual oxygen vacancy concentration. Our re-analysis points to a somewhat higher value of ~0.85 % with a migration entropy, $\exp(S_m/k)$ of 2.

Fig. 5.13 shows that the ionic conductivity of GS is increased only by half an order of magnitude with 5% Ca^{2+} doping. This is contrasted with the Ca doped GT in Fig. 2.18. In this system, only 1% Ca doping on the A site of GT increased the ionic conductivity by orders of magnitude by introducing extrinsically generated oxygen vacancies into the highly ordered anion lattice. This contrast indicates that the highly disordered lattice in GS already has a large number of oxygen vacancies, comparable to several percent Ca doping. Fig. 5.14 shows that E_i remains relatively insensitive to Ca doping in GS. Thus as shown in Fig. 5.15, the increases in the ionic conductivity with Ca doping is, therefore, related to increases in σ_o. The derived expression, in section 5.2, for the K_F from Fig. 5.17 with the defect model in Eq. (3.30) gives a quantitative value for the anion disorder in GS. The high value of 5.69×10^{40} cm^{-6} obtained for the K_F at 1000 °C shows that GS is indeed intrinsically highly disordered. From Eq. (3.6), an oxygen vacancy density of 0.57 % is obtained, which is in very good agreement with that of 0.85% estimated for $Gd_2(Ti_{0.2}Zr_{0.8})_2O_7$, which would have lower value if the E_F is considered in that composition. Therefore we may conclude that the high level of intrinsic anion disorder in GS is consistent with expectations based on the ionic radius ratio issue. The magnitude of pre-exponent of the Frenkel constant, K_{FO}, of 1.55×10^{41} cm^{-6} was found to be lower than the product of oxygen lattice and interstitial sites (48f and 8b sites) of 2.932×10^{44} cm^{-6}. Since two values should be equal in the ideal case where the concentration of defects is sufficiently small enough to neglect the interaction between defect species and volume of the crystal is held at constant volume in the formation of defect species [Greenwood, 1968], a high concentration of oxygen vacancy and interstitials in GS appears not to follow the ideal case.

Fig. 6.1 shows the E_F as a function of r_A/r_B ratio. The E_F of 0.11 eV calculated from the GS data follows the decreasing trend in E_F with decreasing r_A/r_B in $A_2B_2O_7$ pyrochlores, i.e. 0.44 eV in GZT (x=0.25) and 0.24 eV in GZT (x=0.3) [Moon, 1989; Kramer, 1994]. This trend confirms that oxygen vacancies in the pyrochlores can be easily generated with particularly low values of E_F as the average r_B approaches r_A in magnitude.

We have also found that the defect model described in Eq. (3.30) breaks down at x values > 0.05 for which we find that σ_i (x=0.1) is higher than predictions. This suggests that either K_F or μ_i increases as the Ca doping level increases. Since the defect model in the Eq. (3.30) is based on the use of relatively low dopant concentration and a dopant-independent ion mobility [Moon, 1988a], GS with 10% of Ca appears not to follow those assumptions due to the large concentration of defect species. Generally, at high dopant concentrations, E_i increases with dopant concentration due to the long range ordering of vacancies [Hohnke, 1979]. This seems not to apply to the 10% Ca doped GS composition given that E_i is observed to be insensitive to the Ca concentration (see Fig. 5.14). This suggests that the migration energy, E_m, remains insensitive to doping concentration. One distinction between 10% Ca doped GS and pure GS is that the latter exhibits intrinsic ionic conductivity while in the former, the ionic conductivity is determined by oxygen vacancies generated extrinsically by Ca doping. Thus Ca'_{Gd} dopants might increase the magnitude of σ_o by enhancing the migration entropy.

Since anion disorder in GS is significant, one must conclude that the source of the lower ionic conductivity of GS versus that of $Gd_2(Ti_{0.2}Zr_{0.8})_2O_7$ must be due to a lower oxygen vacancy mobility. At 1000 °C, GS is calculated to have an oxygen vacancy mobility of 8.6×10^{-7} $cm^2V^{-1}S^{-1}$. This is remarkably low for pyrochlore oxides. The calculated value for oxygen vacancy mobility
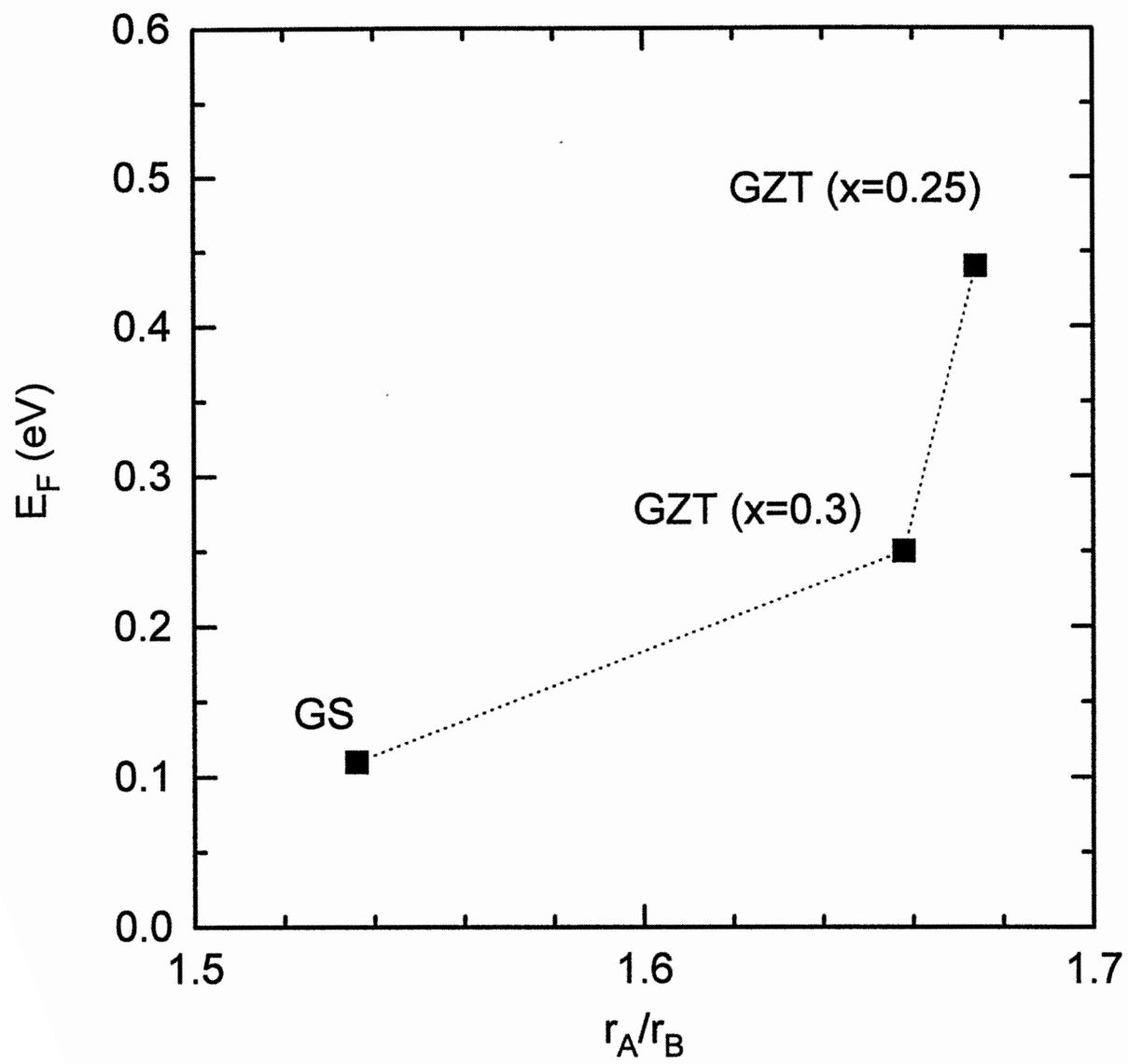
6.1 The Frenkel energy as a function of r_A/r_B in $A_2B_2O_7$ pyrochlores.

in GZT at x=0.3 at 1000 °C is 1.2×10^{-4} $cm^2V^{-1}S^{-1}$ with an activation energy of 0.74 eV [Moon, 1989], less than half of that in GS of 1.54 eV. This high value of the oxygen vacancy migration energy is rather unexpected considering that pyrochlores are more ordered relative to fluorites, leading to improved oxygen vacancy mobility as discussed in section 2.2. The high oxygen vacancy migration energy (~ 1.5 eV) resulted in much lower ionic conductivities as compared with GZT (x=0.8). The low conductivity in GS indicates the possible importance of local bonding on mobility. In contrast, disorder appears to be more clearly tied to the relative size of the ions.

One possible explanation for the low oxygen vacancy mobility in GS is the local bonding between Sn and O. As mentioned in section 2.3.1, Vandenborre et al. [Vandenborre, 1983] suggested that the Sn-O bonding is more rigid and covalent compared with that between Ti-O as reflected in the strong force field in Sn-O bonding. From the refinement of Raman spectra in pyrochlores, the stretching constant between the B cation and oxygen ion was found to be 1.27×10^2 Nm^{-1} for $Gd_2Ti_2O_7$ and 1.73×10^2 Nm^{-1} for $Gd_2Sn_2O_7$. The authors attributed a part of the increase to the higher electronegativity of Sn^{4+} in comparison with the Ti^{4+} and Zr^{4+} cations. From the electronic structure calculations by Svane and Antoncik [Svane, 1987], an appreciable degree of covalency in the bonding was observed for SnO_2 in contrast to the significant ionic character in TiO_2. Since oxygen ions have to overcome the potential barriers induced by the cations to migrate through the lattice, it is expected that the bonding characteristics between cation and anion can impact the mobility significantly. The other possibility for the low mobility of the oxygen vacancy is the ionic polarizability of the Sn ion. This will be discussed in relation to the dielectric constant measurements in later section.

6.2 Ionic Conductivity in $Gd_2(Ti_{1-x}Sn_x)_2O_7$, $Gd_2(Zr_{1-x}Sn_x)_2O_7$ and $Y_2(Ti_{1-x}Sn_x)_2O_7$ systems

The ionic conductivity dependence on the B site composition in the solid solutions of GTS and GZS is evaluated in terms of its impact on the oxygen vacancy concentration and mobility.

The expected trend of oxygen vacancy concentration, its mobility and ionic conductivity as a function of B site cations is shown in Fig. 6.2. From the observation in GS, it was found that GS was intrinsically disordered with low ionic mobility. Thus it appears that the oxygen vacancy concentration increases with increasing Sn content in GTS and YTS due to increasing disorder as larger Sn replaces smaller Ti ion. On the other hand, ionic mobility decreases with increasing Sn content. Since ionic conductivity is a product of the oxygen vacancy concentration and mobility, it is expected that a maximum ionic conductivity be observed at an intermediate composition in GTS and YTS. In the case of GZS, the ionic conductivity is expected to increase with increasing Zr content since ionic mobility increases with higher Zr content while oxygen vacancy concentration remains high regardless of x due to the similar ionic radii of Sn and Zr. These expectations are well observed in the ionic conductivity data.

As shown in Figs. 5.38 and 5.40, the ionic conductivity generally increases with increasing Zr content in GZS while σ_0 remains nearly constant. Considering that σ_0 reflects the oxygen vacancy concentration, this suggests that disorder remains invariable with nearly constant r_B for GZS. Then the measured increase in E_i with increasing Sn levels in GZS is attributed to the increase in migration energy since E_F of ~0.1 eV is negligible The large increases in ionic conductivity in GZS with decreasing Sn content, therefore, results form the increasing ion mobility with higher Zr

GTS & YTS
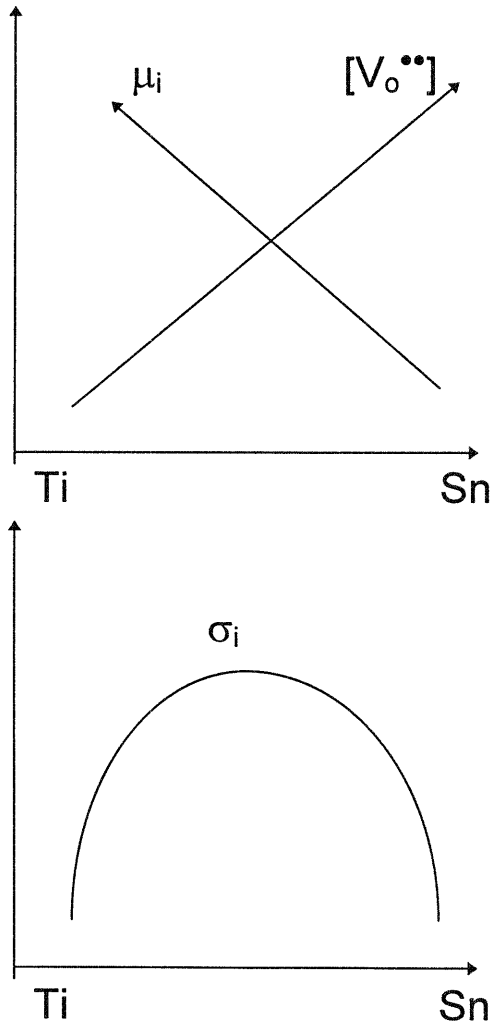
GZS
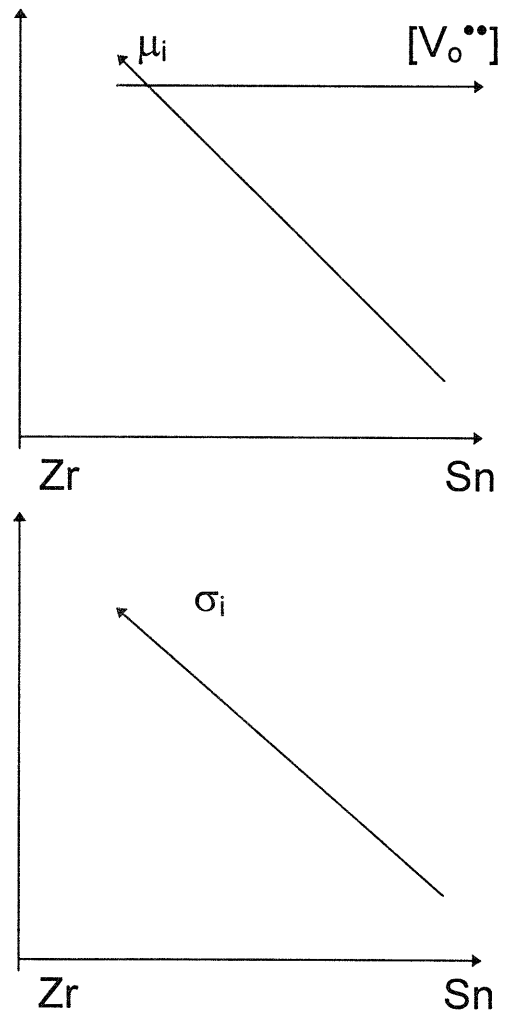
Fig. 6.2 Expected trend of mobility, oxygen vacancy concentration and ionic conductivity as a function of B site composition in GTS, YTS and GZS.

content in GZS where the structure is already disordered regardless of the B site composition.

The composition dependence of the oxygen vacancy mobility in GZS is in contrast to an almost constant oxygen vacancy mobility in GZT as suggested by Moon et al. [Moon, 1988a]. They calculated the oxygen vacancy mobility of GT from the data for GT with 10% of Ca assuming that the oxygen vacancy concentration is fixed by the Ca dopant. The oxygen vacancy mobility was found to be 1.2×10^{-4} cm^2/Vs at 1000 °C, which is in good agreement with the value for GZT (x=0.3) of 1.1×10^{-4} cm^2/Vs at the same temperature. In addition to that, the E_i found for compositions for x $\geq$ 0.4 in the GZT system was nearly constant indicating composition-independent oxygen vacancy mobility across the entire GZT system.

GTS shows a somewhat different behavior from GZS. As shown in Fig. 5.30, σ_0 increases over two orders of magnitude as Sn replaces Ti on the B site. Since the ionic radius of Sn is larger that that of Ti, this increase in σ_0 can be understood due to increasing disorder as a result of the decrease in r_A/r_B with higher Sn content in GTS. At the same time, E_i increases from ~0.8 eV to ~1.6 eV from GT to GS, similar to that observed in GZS, pointing to a decrease in mobility due to an increase in migration energy. Therefore there are two different features depending on the B site composition in GTS, disorder and mobility. The former increases with higher Sn content but the latter increases with higher Ti content. The broad conductivity maximum observed in the Fig 5.28 at x=0.4 in GTS can be described by the competing effects of increasing disorder and decreasing ion mobility upon Sn substitution for Ti.

It appears that the ionic conductivity drops rapidly below x=0.2 in GTS. The oxygen vacancy concentrations in Ti rich compositions are

influenced by background impurities. For Zr less than 20% in GZT and YZT as shown in Figs. 2.16 and 2.17, the oxygen vacancy concentration was fixed by background impurities due to low intrinsic disorder in the lattice. Thus we suspect that impurities also control Ti rich compositions in GTS where intrinsic disorder is insufficient to overcome background impurities. The initial decrease in E_i with increasing Sn at low x might be attributed to the electrostatic interaction of impurities with oxygen vacancies similar to that observed in Ca doped GT as shown in Fig. 2.19.

The second plateau at low P_{O_2} in GTS was not predicted from the simple defect model. It was found that monoclinic Gd_2TiO_5 and Gd_2SnO_5 phases form instead of the homogeneous pyrochlore phase as samples are reduced as confirmed from the X-ray diffraction spectra. Since the ratio of A to B cations is 2:1 in the monoclinic phase, the pyrochlore phase might be Gd-deficient by the formation of these second phases. If this is the case, additional donors may be created in the form of $Ti_{Gd}^{\bullet}$ thereby enhancing the electronic conductivity at low P_{O_2}. Activation energies for these second plateaus are ~1.1 eV (Fig. 5.32) which should be considered as the donor ionization energies. In the case of Nb doped GT, $Nb_{Ti}^{\bullet}$ was found to be a deep donor creating a conductivity plateau at low P_{O_2} with an activation energy of ~1.6-2 eV [Kosacki, 1995].

The similarity in the magnitude of electrical conductivity of YT in this investigation and that of 2% Ca doped YT by Kramer et al. [Kramer, 1994] may be due to the off-stoichiometry of the Y and Ti cations since a 2% background acceptor is very unlikely. Possible errors in assaying the Y citrate or Ti citrate could result in Y excess YT resulting in 2% acceptor doped YT. As in the case of GT, YT is expected to exhibit sensitivity to background impurities or cations off-stoichiometry due to its highly ordered lattice.

Disregarding YT, we discuss the remaining YTS compositions which were produced by traditional solid state mixing techniques. The broad conductivity maximum at x=0.4 in YTS can be understood in the same way as in GTS where the two competing effects of disorder and mobility resulted in a conductivity maximum at intermediate compositions. Let us examine σ_0 and E_i of YTS in relation to GTS. Figs. 6.3 and 6.4 present σ_0 and E_i in GTS and YTS. σ_0 in YTS increases linearly with increasing Sn content. YTS has a larger value of σ_0 relative to GTS for a given Sn content by approximately one order of magnitude. Assuming that σ_0 indicates disorder in the system as discussed in the case of GTS, this is consistent with the expectation based on r_A/r_B. Since YTS has a smaller value of r_A/r_B than GTS for a given x, more charge carriers are formed due to disorder in the structure. The difference in σ_0 between GZT and YZT was about an order and a half, which is somewhat larger than the difference between GTS and YTS. E_i also increases with increasing Sn content in YTS as in the case of GTS suggesting a decrease in oxygen vacancy mobility. The good agreement between the magnitude of E_i of YTS and GTS for a given x is distinct from that observed in YZT and GZT. In YZT, E_i was found to be much greater than that in GZT resulting in lower ionic conductivities in YZT despite the larger values of σ_0 as shown in Fig. 2.16 and 2.17. Moon et al.[Moon, 1988a] attributed the higher E_i in YZT to the decrease in oxygen vacancy mobility due to either defect association or the loss of optimal transport pathways caused by the cation disorder. In the cases of GST and YST, it appears that the role of the Sn ion is the main factor in determining oxygen vacancy mobility.

6.3 X-ray Diffraction Analysis on $Gd_2(Ti_{1-x}Sn_x)_2O_7$

Gd occupancy on the A site calculated from the refinement of the X-ray diffraction patterns were found to be decrease with increasing Sn content suggesting increasing cation disorder. This is consistent with the trend
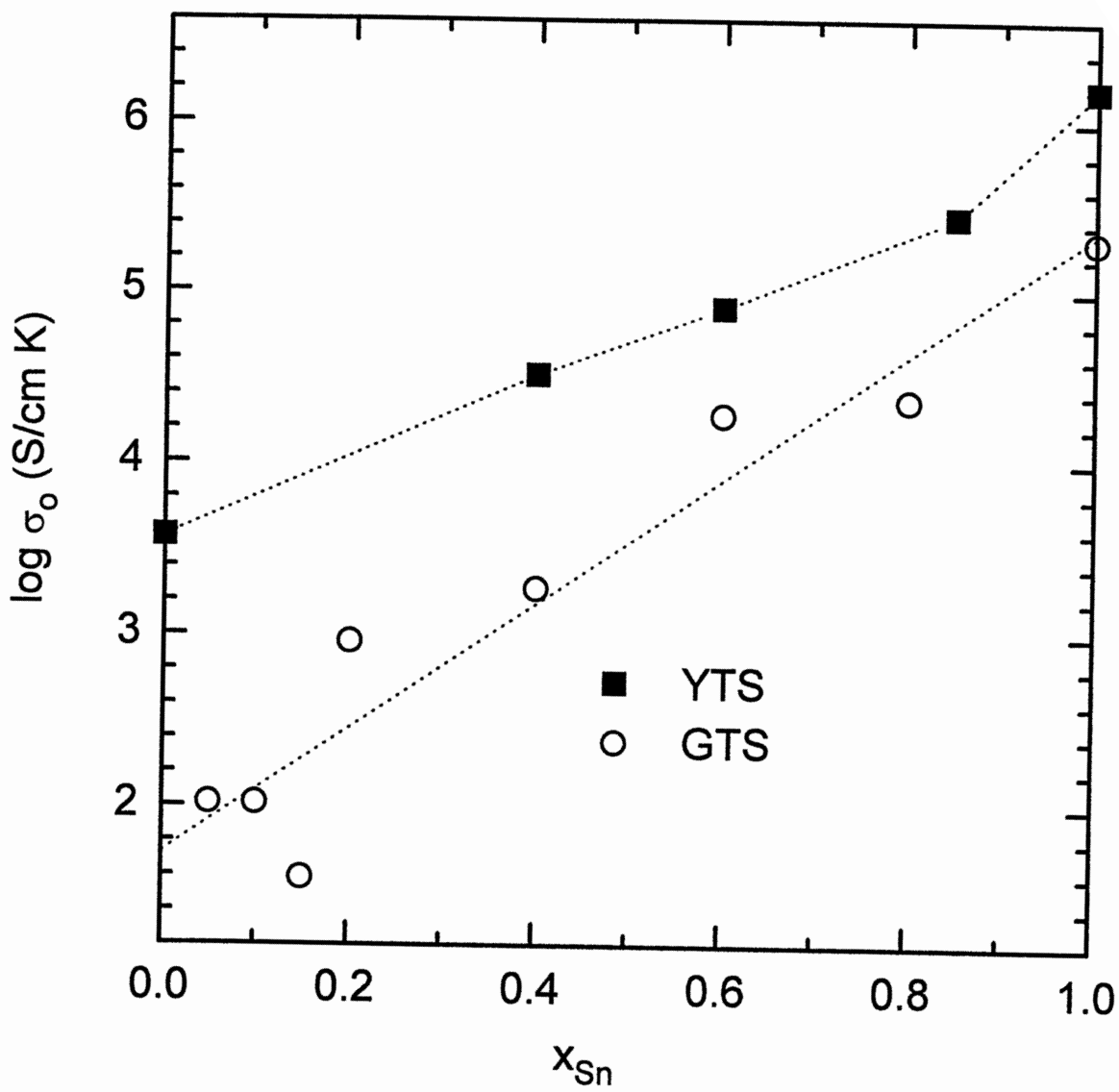
Fig. 6.3 The pre-exponential constant for ionic conduction for $Gd_2(Ti_{1-x}Sn_x)_2O_7$ and $Y_2(Ti_{1-x}Sn_x)_2O_7$.
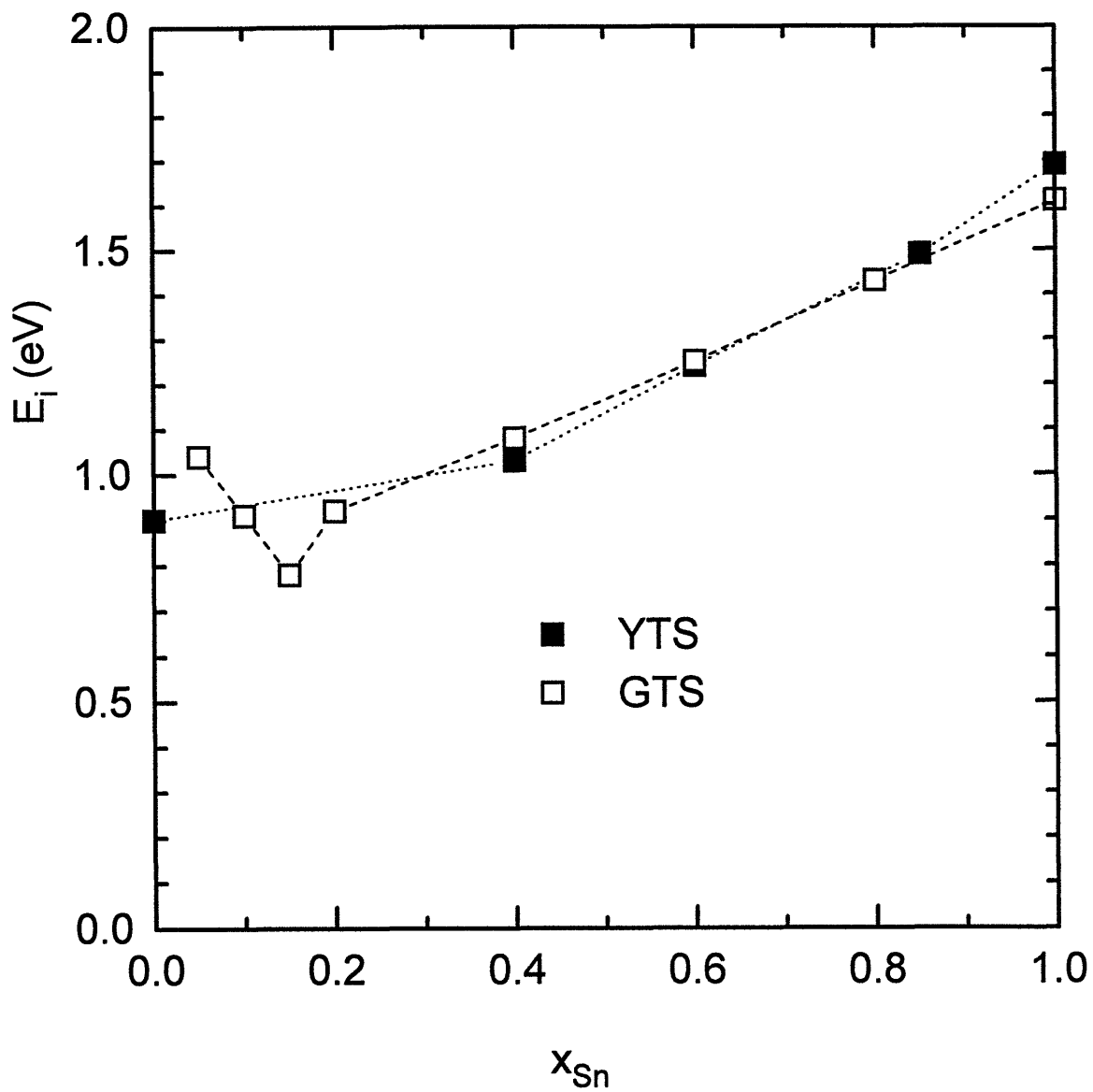
Fig. 6.4 The activation energy for ionic conduction for $Gd_2(Zr_{1-x}Sn_x)_2O_7$ and $Y_2(Zr_{1-x}Sn_x)_2O_7$.

observed in GZT of increasing cation disorder with increasing Zr content as shown in Fig. 2.8 despite the limitations as discussed in section 2.1.3.

On the other hand, according to the X-ray analysis, the anion lattice did not exhibit structural disorder in the entire GTS composition. It should be noted that the standard deviation in the calculation of anion occupancy with X-ray diffraction can be larger than the degree of anion disorder. As calculated from the conductivity data on Ca doped GS, the structural disorder in the anion lattice is found to be ~0.6% which is less than the standard deviation of several percent characteristic of X-ray diffraction analysis. Furthermore, disorder in the anion array can be more sensitive to the thermal history of the samples than the cation array since the anion mobility is larger relative to those of the cations. Since X-ray diffraction was performed at room temperature on samples which were not quenched from elevated temperature, it is possible that the samples may not have the anion structural disorder corresponding to the high temperature phase. In-situ measurements of neutron diffraction at high temperature can show the degree of anion disorder more clearly without the effect of thermal history.

Wilde and Catlow [Catlow, 1996] emphasized the importance of cation disorder for generating anion disorder in the pyrochlore system. From their calculations, it was found that cation disorder causes the environment of the 48f and 8b oxygen ions to become more similar, which induces a corresponding drastic decrease in the E_F. From this calculation along with the increase in cation disorder with higher Sn content in GTS, one can conclude that anion disorder increases with higher Sn content in GTS, which is consistent with increases in σ_o with increasing Sn content. It is, however, not clear which lattice initiates the disordering process in GTS. It is possible that cations disorder first induces the anion disorder by providing similar environments for 48f and 8b sites. Neutron diffraction analysis on YZT

[Heremans, 1993], however, revealed that anions disorder at Zr levels for which the cations still remain completely ordered.

6.4 Dielectric Constant and Ionic Polarizability in $Gd_2(Ti_{1-x}Sn_x)_2O_7$

Since the oxygen 48f sites are believed to form a continuous channel for oxygen ion migration and are surrounded by two A site cations and the two B site cations, the polarizability of cations can influence the oxygen migration mobility. Ionic polarizability indicates how readily the ions can be displaced from their equilibrium positions. For oxygen ions in the 48f sites to migrate, the surrounding cations must displace from their equilibrium positions to provide a optimal pathway for oxygen ion migration. This process can be enhanced by increasing the ionic polarizabilities. Spears [Spears, 1995] suggested that the B site cations may have a stronger interaction with the 48f oxygen sites than the A site cations if the 48f sites are displaced towards the B site cations reflected in large positional parameter x. Since the positional parameter x is higher than 0.375, as confirmed in neutron diffraction analysis [Brisse, 1968], the 48f site oxygen ions are closer to the B site than the A site cations in stannate pyrochlores. Thus, we can expect that the oxygen vacancy mobility is more sensitive to the B site cation composition.

The decrease in the dielectric constant with increasing Sn content in GTS in Fig. 5.52 indicates that the polarizability decreases as Sn replaces Ti on the B site. The trend of decreasing dielectric constant with Sn content in GST was also observed in $Zr_xTi_ySn_zO_4$ (x+y+z=2) system as shown in Fig. 2.23. One must note that this polarizability consists of electronic as well as ionic contributions. The electronic polarizability is a measure of how easily electrons in various shells are deformed under the electric field whereas ionic

171

polarizability represents the displacement of the ion itself [Omar, 1975]. The importance of electronic polarizability shows up in Ag, Bi and Pb ions with large electronic polarizabilities thereby contributing to increases in ion mobility [Kleppmann, 1976; Ratner, 1988]. Since Sn is larger and more covalent that Ti [Svane, 1987], we expect Sn to have a larger electronic polarizability than Ti [Ashcroft, 1976]. Nevertheless, the dielectric constant decreases with higher Sn content pointing to a larger ionic polarizability of the Ti ion relative to the Sn ion. This decrease in ionic polarizability with increasing Sn content explains the observed oxygen vacancy mobility decrease with Sn content in GTS. One can conclude that the oxygen vacancy mobility in pyrochlores is more sensitive to the bonding characteristics of the B site cations including polarizability rather that ionic radius.

6.5 N and P type conduction with thermal bandgap in Stannate Pyrochlores

As shown in Fig. 5.9, clear p-type conduction has been observed in GS up to $P_{O2} = 10^{-4}$ atm with a 1/4 slope dependence of log σ on log P_{O2}. It is surprising that GS exhibits a strong p-type conduction at high P_{O2} considering that SnO_2 is known to be difficult to oxidize with a calculated oxidation energy of 5.53 eV [Freeman, 1990]. P-type conduction in GS indicates that the highly disordered state in GS accommodates oxygen easily in contrast to SnO_2 which exhibits low intrinsic disorder. The activation energies measured for p type conduction in Ca doped GS, GTS and GZS range from 0.87~1.49 eV which are similar to those in GZT [Moon, 1988a]. The increase in p-type conductivity with higher Ca content in GS in Fig. 5.20 is consistent with the defect model discussed in section 3.1 since the increase in negatively charged acceptor concentration (Ca'_{Gd}) increases hole concentration as well as oxygen vacancies. The p-type conduction was often difficult to

determine in GZT (x<0.6) due to the higher ionic conduction which serves to mask the p-type conduction in GZT.

The E_r, appears to increase with Sn or Zr content relative to Ti in the GTS, GZS and YTS systems (We disregard x=0.6 in GZS and YTS in the discussion due to negligible electronic conduction dominated by ionic conductivity at low Po_2). In the GZT system, E_r was observed to increase with increasing Zr content [Moon, 1988a]. From these observations, it was concluded that Ti on the B site of pyrochlores is easier to reduce than Sn or Zr. It is known that titanates are generally easier to reduce than zirconates. We expected that the magnitude of electronic conductivity at low Po_2 in GS would be larger than that in GT from the fact that SnO_2 has a better electronic mobility relative to TiO_2 due to broad band conduction which doesn't involve a thermally activated hopping process [Kohnke, 1962; Breckenridge, 1953]. However it turned out that electronic conductivity is negligible in stannate pyrochlores due to large values of E_r. Ti^{4+} is known to be reduced into Ti^{3+} under reducing condition. The small polaron conduction of electrons in reduced TiO_2 indicates the association of Ti^{4+} with electrons. In contrast, we expect reduced SnO_2 contains Sn^{2+} which requires a higher energy for reduction than Ti^{3+} from Ti^{4+}. Form the analysis of the optical spectra, the difference in ionization energy between Sn^{2+} and Sn^{4+} was found to be ~29.1 eV while the difference between Ti^{3+} and Ti^{4+} is ~15.8 eV [Moore, 1949]. A more reducible Ti ion than Sn ion under reducing conditions can be, therefore, one possible source for the increase in E_r with higher Sn content in GTS. It appears that we can increase the electronic conductivity by donor doping thereby increasing the number of free electrons for electronic conduction provided that the electronic mobility is higher in stannates relative to titanates.

The E_g in GTS and YTS appears to increase with increasing Sn content. This is consistent with the observed difference in the bandgap of SnO_2 and TiO_2 system i. e., E_g is ~3.0 eV for TiO_2 and ~3.5 eV for SnO_2 [Cronemeyer, 1952; Fonstad, 1971; Svane, 1987].

6.6 The short circuit and open circuit voltage measurements

As mentioned in section 3.3. the short circuit cell enables one to measure the ionic conductivity of a mixed conductor without the use of blocking electrodes. The 2-probe short circuit current measurement demonstrated that the apparent ionic conductivity can be obtained from the cell as shown as P_{O_2}-independent conductivity. The magnitude of the bulk ionic conductivity of the sample was, however, lower than the true ionic conductivity extracted from 2-probe AC impedance spectroscopy. This difference appears to be largely due to electrode polarization or $R_{i,c}$ since this 2-probe short circuit measurement cannot isolate bulk R_i from $R_{i,c}$. A similar observation was made by Riess et al. [Riess, 1992] in the short circuit measurement on the $Gd_2Ti_2O_7$ doped with 0.25% Ca where large deviations were observed between the apparent ionic conductivity by the short circuit cell and the one extracted from AC impedance spectroscopy using a defect model as temperature decreases.

For the isolation of the bulk resistance from the electrode polarization, it is recommended that a 4-probe configuration be designed where solid electrolytes are used for the inner electrodes. Solid electrolytes can measure the electrochemical potential gradient of oxygen ions by blocking electronic current. This potential gradient of oxygen ions can give the bulk ionic conductivity when combined with the ionic current measured from outer electrodes. Since no current is involved in measuring the potential gradient

174

of oxygen ions with a solid electrolytes, there is no IR drop at the inner electrodes eliminating the contribution from $R_{i,c}$.

Open circuit voltage measurements showed that the t_i reaches a maximum of ~0.8 at intermediate P_{O_2}. This is consistent with the total conductivity measurements which shows a conductivity plateau at intermediate P_{O_2} indicating predominant ionic conductivity. This observation also confirms that the second plateau at low P_{O_2} in GTS is, indeed, electronic conduction where the single pyrochlore phase was decomposed into monoclinic phases such as Gd_2SnO_5 and Gd_2TiO_5.

7 Conclusion

The electrical conductivity of the stannate pyrochlores $(Gd_{1-x}Ca_x)_2Sn_2O_7$, $Gd_2(Ti_{1-x}Sn_x)_2O_7$, $Gd_2(Zr_{1-x}Sn_x)_2O_7$ and $Y_2(Ti_{1-x}Sn_x)_2O_7$ were measured as a function of Po_2 and temperature so as to examine the role of the Sn ion on structural disorder and oxygen ion conductivity. The following observations have been made:

1. From Ca doping of $Gd_2Sn_2O_7$, $Gd_2Sn_2O_7$ was found to have an intrinsic anion disorder corresponding to ~0.6% of the oxygen sites. This value is in good agreement with that observed previously in $Gd_2(Ti_{1-x}Zr_x)_2O_7$ (x=0.8) with the same r_A/r_B ratio thereby confirming the importance of the cation radii in influencing structural disorder in pyrochlores.

2. The intrinsic Frenkel activation energy, E_F, was found to be 0.11 eV, in $Gd_2Sn_2O_7$ as compared with 0.44 eV in $Gd_2(Ti_{1-x}Zr_x)_2O_7$ (x=0.25) and 0.24 eV in $Gd_2(Ti_{1-x}Zr_x)_2O_7$ (x=0.3). This follows the trend of decreasing E_F with decreasing r_A/r_B ratio.

3. The oxygen vacancy mobility in Sn-rich solid solutions was found to be much lower than that in $Gd_2(Ti_{1-x}Zr_x)_2O_7$. The activation energy of ~1.5 eV in GS is double that in $Gd_2(Ti_{1-x}Zr_x)_2O_7$ resulting in two orders of magnitude lower ionic conductivity than that in $Gd_2(Ti_{1-x}Zr_x)_2O_7$ (x=0.8). The B site chemistry is important in influencing the oxygen vacancy mobility while intrinsic oxygen disorder is determined largely by the relative ionic radii of the cations.

4. A likely source of low oxygen vacancy mobility is the lower polarizability of the Sn ion relative to the Ti ion as reflected in the continuous decrease in

dielectric constant with higher Sn content in $Gd_2(Ti_{1-x}Sn_x)_2O_7$. Increased covalent character of the bonding between Sn and O contributes to the lower oxygen vacancy mobility.

5. The two competing effects of decreasing mobility and increasing disorder with x in $Gd_2(Ti_{1-x}Sn_x)_2O_7$ resulted in a broad maximum in ionic conductivity at x=0.4 of $Gd_2(Ti_{1-x}Sn_x)_2O_7$. In $Gd_2(Zr_{1-x}Sn_x)_2O_7$, where disorder remains high regardless of composition, the ionic conductivity increased with Zr content due to increases in oxygen vacancy mobility

6. X-ray diffraction studies on $Gd_2(Ti_{1-x}Sn_x)_2O_7$ confirmed that the cation lattice disorders substantially with increasing Sn content. This is expected to lead to increased anion disorder by providing similar environments for 48f and 8b sites. Anion disorder, however, could not be observed in $Gd_2(Ti_{1-x}Sn_x)_2O_7$ by X-ray diffraction due to large standard deviations in the site occupancies.

7. $Y_2(Ti_{1-x}Sn_x)_2O_7$ like $Gd_2(Ti_{1-x}Sn_x)_2O_7$ exhibited a maximum in ionic conductivity at intermediate compositions. The magnitude of conductivity was higher than that in $Gd_2(Ti_{1-x}Sn_x)_2O_7$ presumably due to larger lattice disorder induced by the smaller Y relative to the Gd ion.

8. A P_{O2}-independent ionic conductivity was obtained by short circuit cell measurements. The magnitude of the conductivity was, however, lower than the bulk ionic conductivity of the sample with larger activation energy due to electrode polarization. Open circuit voltage measurements revealed that the ionic transference number, t_i, reaches a maximum at intermediate P_{O2} confirming that the second conductivity plateaus at low P_{O2} in $Gd_2(Ti_{1-x}Sn_x)_2O_7$ (x<0.8) are largely electronic conductivity.

8 Future Work

1. From X-ray diffraction analysis, it was found to be difficult to determine the anion disorder due to the low scattering power of oxygen ions. Furthermore, these measurements were performed at room temperature where disorder may not be in a quasi-equilibrium state as at high temperature. In-situ neutron diffraction measurements on $Y_2(Ti_{1-x}Sn_x)_2O_7$ is, therefore, recommended to investigate anion as well as cation disorder in these pyrochlores as a function of temperature as the structure disorder more readily as temperature increases.

2. From Ca doping of $Gd_2Sn_2O_7$, an effective Frenkel constant and oxygen vacancy mobility were obtained using the defect models. The same approach on $Y_2Sn_2O_7$ is suggested to examine the degree of anion disorder and its mobility in these pyrochlores and to compare them with those in GS.

3. Stannate pyrochlores were observed to exhibit low electronic conductivity at low P_{O_2} with large reduction energy. It is expected that stannates provide better electronic mobility than titanates by broad band conduction. If this is the case, the electronic conductivity can be improved by extrinsic generation of electrons by donor doping. Donor doping in stannates such as by W or Nb is suggested to increase the number of free electrons thereby improving electronic conduction. By fixing the electron density, one can also obtain the quantitative value of the electronic mobility.

4. A molecular dynamics calculation of the migration energy in stannates would be useful to confirm the experimental observation that migration energy increases with increasing Sn content in $Gd_2(Ti_{1-x}Sn_x)_2O_7$, $Y_2(Ti_{1-x}Sn_x)_2O_7$ and $Gd_2(Zr_{1-x}Sn_x)_2O_7$.

5. Sn^{2+} is found to occupy the A site due to the large ionic radius, forming (2,5) pyrochlores such as $Sn_2Ta_2O_7$, $Sn_2Nb_2O_7$. Neutron diffraction and Mössbauer spectroscopy revealed that these composition have significant non-stoichiometry indicating large amounts of oxygen vacancies. In particular, a potion of the Sn ion was found to occupy the B site in the form of Sn^{4+}. It is, therefore, suggested to investigate the electrical properties of these pyrochlores and to examine the oxygen vacancy concentration and ionic mobility.

6. 2-probe short circuit cell measurements showed that electrode polarization is dominant and largely masks the bulk ionic conductivity. A 4-probe configuration is recommended to separate out the electrode contribution from the bulk part using a solid electrolyte as the inner electrodes. One can also investigate the electrode polarization phenomena more extensively from the results of two different configurations.

Reference

L. H. Ahrens, "Use of Ionization Potentials. I. Ionic Radii of the Elements", Geochim. Cosmochim. Acta, **2**, 155-169 (1952).

N. W. Ashcroft and N. D. Mermin, in Solid State Physics, (Saunders College Publishing, Orlando, FL, 1976).

L. M. Belyaev, I. S. Lyubutin, L. N. Dem'yanets, T. V. Dmitrieva and L. P. Mitina, "Mössbauer Effect in Rare-Earth Stannates $R_2Sn_2O_7$", Soviet Physics-Solid State, **11**, 424-426 (1969).

T. Birchall and A. W. Sleight, "Nonstoichiometric Phase in the Sn-Nb-O and Sn-Ta-O Systems Having Pyrochlore-Related Structures", J. Sol. St. Chem., **13**, 118-130 (1975).

R. G. Breckenridge and W. R. Hosler, "Electrical Properties of Titanium Dioxide Semiconductors", Physical Review, **91**(4), 793-802 (1953).

F. Brisse and O. Knop, "Pyrochlores. III. X-ray, Neutron, Infrared, and Dielectric Studies of $A_2Sn_2O_7$ Stannates", Canadian Journal of Chemistry, **46**, 859-873 (1968).

A. J. Burggraaf, T. van Dijk and M. J. Verkerk, "Structure and Conductivity of Pyrochlore and Fluorite Type Solid Solutions", Solid State Ionics, **5**, 519-522 (1981).

Y. Calage and J. Pannetier, "Electric Field Gradients in Pyrochlore Compounds", J. Phys. Chem. Solids, **38**, 711-718 (1977).

C. R. A. Catlow and R. James, "Disorder in TiO_{2-x}," Proc. R. Soc. Lond. A, **384**, 157-173 (1982).

C. R. A. Catlow, "Superionic Fluorites", in Superionic Solids and Solid Electrolytes: Recent Trends", ed. by A. L. Laskar and S. Chandra, (Academic Press, New York, 1989) p. 339-378.

R. A. Chapman, D. B. Meadowcroft and A. J. Walkden, "Some Properties of Zirconates and Stannates with the Pyrochlore Structure", J. Phys. D: Appl. Phys., **3**, 307-319 (1970).

D. C. Cronemeyer, "Electrical and Optical Properties of Rutile Single Crystals", Physical Review, **87**(5), 876-886 (1952).

J. D. Facktor, "A Study of Oxygen Ion Conductivity in the System $Nd_2Zr_2O_7$-$Nd_2Ce_2O_7$ and Related Materials", Ph. D. Thesis at the Imperial College of Science and Technology, University of London, (1984).

C. M. Freeman and C. R. A. Catlow, "A Computer Modeling Study of Defect and Dopant States in SnO_2", J. Sol. State Chem., **85**, 65-75 (1990).

C. G. Fonstad and R. H. Rediker, "Electrical Properties of High-Quality Stannic Oxide Crystals", J. Appl. Phys., **42(7)**, 2911-2918 (1971).

D. Goldschmidt and H. L. Tuller, "Small-Polaron Conduction in $Y_2Ti_2O_7$", Physical Review B, **34**, 5558-5561 (1986).

N. N. Greenwood, in Ionic Crystals, Lattice Defects and Nonstoichiometry, (Butterworth & CO., London, 1968).

S. M. Haile, B. J. Wuensch and E. Prince, "Neutron Rietvelt Analysis of Anion and Cation Disorder in the Fast-Ion Conducting Pyrochlore System $Y_2(Zr_xTi_{1-x})_2O_7$", in Proc. Symp. Neutron Scattering for Materials Science, 166, ed. by S. M. Shapiro, S. C. Moss and J. D. Jorgensen, (Mat. Res. Soc., Pittsburgh, PA, 1990) p. 81-86.

C. Heremans, "Fast-Ion Conductors: Single Crystal Growth of Copper and Silver Halides and Structural Determination of $Y_2(Zr_yTi_{1-y})_2O_7$ Pyrochlores", Ph. D. Thesis, Massachusetts Institute of Technology, Cambridge, (1993).

D. K. Hohnke, "Ionic Conduction in Doped Zirconia", in Fast Ion Transport in Solids, ed. P. Vashishta, J. N. Mundy and G. K. Shenoy, (North Holland, New York) (1979) p. 669-672.

W. D. Kingery, H. K. Bowen and D. R. Uhlmann, in Introduction to Ceramics: Second Edition, (John-Wiley and Sons, New York, 1976).

W. G. Kleppmann and H. Bilz, "Effect of Quadrupolar Deformability of the Ionic Conductivity of Silver Salts", Communications on Physics, **1**, 105-110 (1976).

O. Knop and F. Brisse and L. Castelliz, "Pyrochlore V. Thermoanalytic, X-ray, Neutron, Infrared and Dielectric Studies of $A_2Ti_2O_7$ Titanates", Canadian Journal of Chemistry, **47**, 971-990 (1969).

E. E. Kohnke, "Electrical And Optical Properties of Natural Stannic Oxide Crystals", J. Phys. Chem. Solids, **23**, 1557-1562 (1962).

I. Kosacki and H. L. Tuller, "Donor-Doped $Gd_2Ti_2O_7$ as a Semiconductor-Type Oxygen Sensor", Sensor and Actuators B, **24-25**, 370-374 (1995).

S. Kramer, "Mixed Ionic-Electronic Conduction in Rare Earth Titanate/Zirconate Pyrochlore Compounds", Ph. D. Thesis, Massachusetts Institute of Technology, Cambridge, (1994).

H. M. Loebenstein, R. Zilber and H. Zmora, "Mössbauer Effect and X-ray Analysis of Rare Earth Stannates", Physics Letters, **33A**, 453-454 (1970).

J. M. Longo, P.M. Raccah and J. B. Goodenough, "$Pb_2M_2O_{7-x}$ (M = Ru, Ir, Re)-Preparation and Properties of Oxygen Deficient Pyrochlores", Mat. Res. Bull., 4, 191-202 (1969).

P. K. Moon, "Electrical Conductivity and Structural Disorder in $Gd_2Ti_2O_7$-$Gd_2Zr_2O_7$ and $Y_2Ti_2O_7$-$Y_2Zr_2O_7$ Solid Solutions", Ph. D. Thesis, Massachusetts Institute of Technology, Cambridge, (1988).

P. K. Moon and H. L. Tuller, "Ionic Conduction in the $Gd_2Ti_2O_7$-$Gd_2Zr_2O_7$ System", Solid State Ionics, **28-30**, 470-474 (1988).

P. K. Moon and H. L. Tuller, "Intrinsic Fast Oxygen Ionic Conductivity in the $Gd_2(Zr_{1-x}Ti_x)_2O_7$ and $Y_2(Zr_{1-x}Ti_x)_2O_7$ Pyrochlore Systems," in Solid State Ionics, edited by G. Nazri, R. A. Huggins, and D. F. Shriver, (Mat. Res. Soc. Symp. Proc. 135, Pittsburgh, PA, 1989) p. 149-163.

C. E. Moore, "Atomic Energy Levels as Derived from the Analysis of Optical Spectra", in Circular of the National Bureau of Standards 467 vol. III, (Government Printing Office, Washington, D. C., 1949-1958).

M. A. Omar, in Elementary Solid State Physics, (Addison-Wesley Publishing Company, Reading, MA, 1975).

P. Onnerud, K. Eberman and B. J. Wuensch, unpublished work, Massachusetts Institute of Technology, Cambridge (1996).

M. P. Pechini, "Method of Preparing Lead and Alkaline Earth Titanates and Niobates and Coating Method Using the Same to Form a Capacitor", US Patent No. 3,330,697 (1967).

M. A. Ratner and A. Nitzan, "Fast Ion Conduction: Some Theoretical Issues", Solid State Ionics, **28-30**, 3-33 (1988).

P. J. Rentzeperis, "The Crystal Structure of the Anhydrous Stannous Sulphate", Z. Krist., **117**, 431-436 (1962).

W. H. Rhodes and R. E. Carter, "Cationic Self-Diffusion in Calcia-Stabilized Zirconia", Journal of American Ceramic Society, **49(5)**, 244-249 (1966).

I. Riess, "Measurements of Electronic and Ionic Partial Conductivities in Mixed Conductors, without the Use of Blocking Electrodes", Solid State Ionics, **44**, 207-214 (1991).

I. Riess, S. Kramer and H. L. Tuller, "Measurement of Ionic Conductivity in Mixed Conducting Pyrochlores by the Short Circuit Current Method", in Solid State Ionics, ed. by M. Balkanski, T. Takahashi and H. L. Tuller, (Elsevier Sc. Publ., Amsterdam, 1992) p. 499-505.

I. Riess, "Critical Review of Methods for Measuring Partial Conductivities in Mixed Ionic Electronic Conductors", in Ionic and Mixed Conducting Ceramics, ed. by T. Ramanarayanan, W. L. Worrell and H. L. Tuller, (The Electrochemical Society Proc. 94-12, Pennington, NJ, 1994) p. 286.

R. B. Roth, "Pyrochlore-Type Compounds Containing Double Oxides of Trivalent and Tetravalent Ions," Journal of Research of the National Bureau of Standards, **56**, 17-25 (1956).

R. D. Shannon and C. T. Prewitt, "Effective Ionic Radii in Oxides and Fluorides", Acta Cryst., **B25**, 925-946 (1969).

M. Spears, "Defect Chemistry and Electrical Properties of Ruthenium-and Bismuth-Substituted Gadolinium Titanate Pyrochlore", Ph. D. Thesis, Massachusetts Institute of Technology, Cambridge, (1995).

M. Spears, S. Kramer, H. L. Tuller and P. K. Moon, "Mixed Ionic-Electronic Conduction in some Pyrochlore Oxides", in Ionic and Mixed Conducting Ceramics, ed. by T. A. Ramanarayanan and H. L. Tuller, (The Electrochemical Society Proc. 91-12, Pennington, NJ, 1991) p. 32-45.

D. J. Stewart, O. Knop, R. E. Meads and W. G. Parker, "Pyrochlores. IX. Partially Oxidized $Sn_2Nb_2O_7$ and $Sn_2Ta_2O_7$: A Mössbauer Study of Sn(II, IV) Compounds", Can. J. Chem., **51**, 1041-1049 (1973).

T. G. Stratton, D. Reed and H. L. Tuller, "Study of Boundary Effects in Stabilized Zirconia Electrolytes", in Grain Boundary Phenomena in Electronic Ceramics, ed. L. M. Levinson, (Am. Ceram. Soc., Columbus, Ohio, 1981) p. 114.

M. A. Subramanian, G. Aravamudan and G. V. Subba Rao, "Oxide Pyrochlores - A Review", Progress in Solid State Chemistry, **15**, 55-143 (1983).

A. Svane and E. Antoncik, " Electronic Structure of Rutile SnO_2, GeO_2 and TeO_2", J. Phys. Chem. Solids, **48**, 171-180 (1987).

M.-J. Tsai, "The Defect Structure and Transport Properties of Some High T_c Superconductors", Ph. D. Thesis, Massachusetts Institute of Technology, Cambridge, (1991).

H. L. Tuller, "Mixed Conduction in Nonstoichiometric Oxides", in Nonstoichiometric Oxides, ed. O. T. Sørensen, (Academic Press, NY, 1981) p. 275-335

T. Uehara, K. Koto, F. Kanamaru and H. Horiuchi, "Stability and Antiphase Domain Structure of the Pyrochlore Solid Solution in the ZrO_2-Gd_2O_3 System", Solid State Ionics, **23**, 137-143 (1987).

M. T. Vandenborre, E. Husson, J. P. Chartry and D. Michel, "Rare-earth Titanates and Stannates of Pyrochlore Structure; Vibrational Spectra and Force Fields", J. Raman Spectroscopy, **14**, 63-71 (1983).

T. van Dijk, K. J. de Vries and A. J. Burggraaf, "Electrical Conductivity of Fluorite and Pyrochlore $Ln_xZr_{1-x}O_{2-x/2}$ (Ln = Gd, Nd) Solid Solutions", Phys. Stat. Sol., **A58**, 115-125 (1980).

M. P. van Dijk, A. J. Burggraaf, A. N. Cormack and C. R. A. Catlow, "Defect Structures and Migration Mechanisms in Oxides Pyrochlores", Solid State Ionics, **17**, 159-167 (1985).

G. Wagner and H. Binder, "Untersuchung der binaren Systeme BaO-SnO_2 und BaO-PbO_2. II" "Kristallstrukturbestimmungen", Z. Anorg. Allegem. Chem., **298**, 12-21 (1959).

N. Wakiya, S. Nishiyama, K. Shinozaki and N. Mizutani, "Electrical Conduction of New Compounds $(Ca,Ce)_2Sn_2O_7$ and $(Sr,Ce)_2Sn_2O_7$ with Pyrochlore Structure", J. Sol. St. Chem., **102**, 349-353 (1993).

D. Y. Wang, D. S. Park, J. Griffith and A. S. Nowick, "Oxygen-Ion Conduction and Defect Interactions in Yttrium-Doped Ceria", Solid State Ionics, **2**, 95-105 (1981).

A. F. Wells, in Structural Inorganic Chemistry, (Clarendon Press, Oxford, Fifth Edition, 1987).

P. J. Wilde and C. R. A. Catlow, "Defects and Diffusion in Pyrochlore Structured Oxides", to be published in Solid State Ionics.

G. Wolfram and H. E. Göbel, "Existence Range, Structural and Dielectric Properties of $Zr_xTi_ySn_zO_4$ Ceramics (x+y+Z=2)", Mat. Res. Bull., **16**, 1455-1463 (1981).